DECLARATION BY AUTHOR OF THE THESIS

Name of Author in Full (Block Letters) VICTOR HUGO DEL VALLE MUÑOZ.

Faculty Board PHYSICAL SCIENCES.

Title of thesis as approved by the Faculty Board

Note

(*a*) A candidate wishing to amend the title previously approved by the faculty board must apply to the faculty board for permission to do so.

(*b*) The title stated here must be precisely the same as that stated on the title page of the thesis submitted.

FLOW BOILING NEAR THE CRITICAL HEAT FLUX.

1. I understand that I am the owner of the copyright of this thesis and that the copyright rests with me unless I specifically transfer it to another person.

2. I understand that the University requires that I shall deposit one copy of my thesis in the Bodleian Library where it shall be available for consultation and that photocopies of it may be made available to those who wish to consult it elsewhere.* I understand that the Library, before allowing the thesis to be consulted either in the original or in a photocopy, will require each person wishing to consult it to sign a declaration that he recognizes that the copyright of the thesis belongs to me and that no quotation from it and no information derived from it may be published without my prior written consent.

3. I agree that my thesis shall be available for consultation in accordance with paragraph 2 above.

SIGNED [signature] DATE 15th FEBRUARY, 1980.

*(a) A candidate who, for good reason, does not wish his thesis or part of it to be made available for consultation or to be photocopied, may apply to the relevant Faculty board for dispensation from this requirement. Any such application should state, with full reasons, both the nature and the period of the dispensation requested, and should be sent with this form to the Graduate Studies Office, University Offices, Wellington Square, Oxford.

Notes

(i) Dispensation for a period will always be granted in cases where confidentiality has been made a condition of access to material which is subsequently incorporated in a thesis.

(ii) Where confidential material forms only a small part of a thesis and the force of the thesis will not be seriously impaired by the removal of such material, the faculty board may grant permission for the confidential material to be deposited separately from the thesis, on the understanding that the thesis will be available for consultation or photocopying but access to the confidential material will be restricted.

(b) A candidate who wishes to be informed of the names of persons consulting his thesis should write separately to Bodley's Librarian, The Bodleian Library, Oxford.

1000: 3.79
KIGS

Microfilmed by NLL

D 34321/81

FLOW BOILING NEAR THE CRITICAL HEAT FLUX

Victor Hugo Del Valle Muñoz

BODLEIAN LIBRARY OXFORD
DEPOSITED
THESIS
8-(-)-80

Dissertation submitted to the Faculty of

Physical Sciences at the University of Oxford

for the degree of Doctor of Philosophy

Lincoln College

February 1980

To

Silvia,

Mauricio

and

Alejandro

FLOW BOILING NEAR THE CRITICAL HEAT FLUX

V. H. DEL VALLE M.

UNIVERSITY OF OXFORD
LINCOLN COLLEGE
HILARY TERM 1980

D. PHIL. THESIS

ABSTRACT

An experimental investigation of the flow boiling of water at atmospheric pressure was undertaken, including a high-speed cine photographic study of the flow structure near the Critical Heat Flux (CHF). Experimental tests from single-phase forced convection to burnout were conducted at different flow velocities and inlet subcoolings for water flowing upwards through a vertical channel of rectangular cross-section electrically heated on one wall with a glass window forming the opposite wall. The test surfaces were stainless steel strips of constant dimensions, except that wall thickness ranged from 0.08 mm to 0.20 mm.

Quantitative measurements of the bubble parameters for the same heating surface under the same operating conditions with varying levels of heat flux (70% to 95% of CHF) were carried out. A nucleation site deactivation/reactivation process was observed with increasing heat flux. A proposed site deactivation mechanism explained this behaviour. A nucleate boiling heat transfer model was proposed for the fully-developed nucleate boiling region, with allowance made for the overlapping areas of bubble influence. It compared favourably with the experimental data.

The effect of wall thickness on CHF was investigated: increases in CHF as between the 0.08 mm and the 0.20 mm wall thickness ranging from 38% to 57% were observed. An empirical expression for CHF, including wall thickness as a parameter was developed, correlating the experimental data to within 15% and indicating a limiting value for wall thickness affecting CHF. The flow regimes near burnout were identified as bubbly and slug, these being independent of wall thickness.

Other models proposed for the CHF mechanism were tested against the detailed experimental observations at high subcoolings. They were found to be inconsistent with the experimental evidence. A possible alternative for the CHF mechanism points towards stabilisation/growth of a vapour patch following bubble coalescence as a most likely cause for burnout.

ACKNOWLEDGEMENTS

I am very grateful to :

My supervisor, Dr. D. B. R. Kenning for his teaching, help and advice throughout.

The Consejo Nacional de Ciencia y Tecnologia (CONACYT) México, whose financial support enabled me to carry out the present study.

The United Kingdom Atomic Energy Authority (Harwell) for having funded the photographic study.

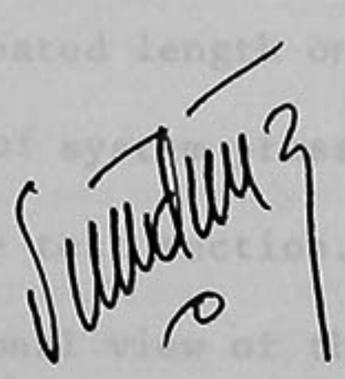
The staff of the main workshop of the Department of Engineering Science of the University of Oxford for their help in building the experimental equipment.

Mrs. E. Rose, Mrs. J. Takacs, Mr. J. Mooney, Mr. J. McMillan, Sr. Lic. R. Cánovas T. and particularly Mr. Paul Cammack for their assistance with different aspects of the work.

Miss. Debbie Gladstone for having efficiently and kindly typed the manuscript.

My parents who have always been in my thoughts,

and most particularly to my wife Silvia for her enthusiasm, help and support. Together with our sons Mauricio and Alejandro she has been a source of constant encouragement.



Victor Hugo Del Valle M.

LIST OF FIGURES

Figure No.	Title	Page
1	Qualitative representation of the Boiling Curve.	2
2	Nucleate boiling heat transfer models.	6
3	The microlayer in hemispherical bubbles (Cooper [23]).	13
4	Model of Graham and Hendricks for nucleate boiling heat transfer [12].	13
5	Fraction of dry surface area under a bubble as a function of percentage of CHF [12].	19
6	Model of Judd and Hwang for nucleate pool boiling heat transfer [28].	19
7	Chang's model for CHF [39].	23
8	Tong's model for CHF [41].	25
9	Bankoff's model for CHF [8].	25
10	Liquid film thickness under a bubble layer as a function of heat flux [44].	29
11	Model of Fiori and Bergles for CHF [40].	31
12	Surface temperature trace at CHF in slug flow [40].	31
13	Isolation of liquid by bubble coalescence [49].	34
14	The effect of inlet subcooling on CHF [45,50].	37
15	Effect of mass-velocity on CHF [51].	39
16	Effect of tube diameter on CHF [51].	39
17	Effect of heated length on CHF [52,50].	41
18	The effect of system pressure on CHF [31].	42
19	Views of the test section.	49
20	Cross-sectional view of the test section channel.	51
21	An assembled test section.	52

22	Test section bolted onto the sindanyo plate; stainless steel plate and stainless steel clamping plate.	54
23(a)	Front view of the test section channel.	55
23(b)	Rear view of the test section channel.	56
24	Schematic diagram of the forced-convection boiling rig.	58
25	High-speed cine-photography equipment.	61
26	Set-up of the high-speed cine-photography equipment.	62
27	Temperature profile along the heated surface.	66
28	Single-phase forced convection heat transfer data.	67
29	Experimental flow boiling curves, v = 0.8 m/sec.	71
30	Experimental flow boiling curves, v = 1.7 m/sec.	72
31	Experimental flow boiling curves, v = 2.0 m/sec.	73
32	Typical roughness profiles of the test surfaces.	76
33	Gas nucleation site density as a function of ΔP.	78
34	Effect of wall thickness on nucleate pool boiling (Grigoriev et al [75].	80
35	Heat flux against temperature difference $T_w - \overline{T}_b$.	83
36	The effect of inlet subcooling on nucleate boiling heat transfer.	85
37	Nucleate boiling heat flux vs. wall superheat: typical flow velocity effect.	87
38	Nucleate boiling heat flux vs. wall superheat: typical wall thickness effect.	88
39	Nucleate boiling heat flux vs. wall superheat: typical subcooling effect.	89
40	The effect of heat flux on bubble parameters.	94

41	Bubble diameter as a function of time.	96
42	Heat flux as a function of active nucleation site density.	99
43	Spatial distribution of nucleation sites; Run 4, 70% and 80% of the CHF.	100
44	Spatial distribution of nucleation sites; Run 4, 90% and 95% of the CHF.	101
45	Maximum bubble diameter data under two different grouping criteria, Run 4.	105
46	Maximum bubble diameter data on probability paper, run 4.	106
47	Normal distribution fitting curves for maximum bubble diameter data, run-film 4-90.	108
48	Normal distribution fitting curve for the total number of maximum bubble diameter data. Run 4, 70% to 95% CHF.	110
49	Frequency distribution polygons for bubble life time data, run 4.	112
50	Normal distribution fitting curves for waiting time data, run 4.	113
51	Distributions of separation distance between pairs of nearest neighbour nucleation sites, run 4.	117
52	Spatial distribution of local active nucleation sites at Z = 100 and Z = 25; run-film 4-70.	119
53	Local active nucleation site densities; run 4, 70% to 95% CHF.	120
54	Probability distributions of local active nucleation sites.	121
55	Spatial distribution and individual site activation histories; run 4, 70% to 95% CHF.	125
56	Deactivation/reactivation of nucleation sites by thermal interference.	127
57	Flow patterns near the CHF.	134
58	Idealized picture of the flow patterns near the CHF in a channel of rectangular cross-section viewed from above.	135
59	Transition from bubbly to slug flow regimes. Run 15.	137

60	Present flow-regime map (water/stainless steel).	138
61	Comparison between flow-regime maps for water/stainless steel in vertical up-flow.	140
62	Comparison between the present flow-regime map (vertical upflow) and that of Bergles et al [86] (horizontal flow).	141
63	A bubble coalescence sequence of Type 1. Run 21, 30% of CHF. (Front views).	143
64	Critical heat flux as a function of inlet subcooling.	149
65	Critical heat flux as a function of mass-velocity.	150
66	Critical heat flux as a function of test-section wall thickness.	152
67	Distribution of burnout location data.	154
68	Types of failure exhibited in destroyed test sections.	156
69	Idealized picture of types of failure.	158
70	Distribution of types of failure.	159
71	Critical heat flux against $1/\delta$.	162
72	Normalized critical heat flux η as a function of wall thickness.	163
73	Calculated maximum critical heat flux $\emptyset_\infty$, as a function of inlet subcooling.	165
74	Comparison between experimental critical heat fluxes and those predicted by the present correlation, eq. (4-14).	167
75	Bubble shape variation with t^+. (Cooper et al[27]).	173
76	Initial microlayer thickness as a function of t^+_g (Cooper et al [27]).	173
77	Heat transfer from the wall associated with hemispherical bubble growth-collapse.	176
78	Graphical approximation used to derive the numerical value of constant C_3.	177

79	Actual fraction of boiling area as a function of K.	186
80	Ratio x of actual boiling area to nominal boiling area against nominal fraction of boiling area β.	187
81	Actual fraction of boiling area β_a against nominal fraction of boiling area β.	187
82	Actual fraction of boiling area at K = 4.8 for run 4 at 70% and 80% of the CHF.	189
83	Actual fraction of boiling area at K = 4.8 for run 4 at 90% and 95% of the CHF.	190
84	Areas of operation for the proposed nucleate boiling heat transfer model.	194
85	Comparison between experimental total heat fluxes and those predicted by the present model.	196
86	Apparent decrease in the parameter K with increasing heat flux.	201
87	Reduction in boiling flux due to overlap.	203
88	Temperature distribution in a solid with internal heat generation subjected to sudden insulation.	215
89	Wall temperature rise at the heater surface as a function of time.	216
90(a)	The effect of wall thickness on the first maximum wall temperature.	218
90(b)	The effect of wall thickness on the first quenching wall temperature.	218
91(a)	Wall superheat as a function of effective cavity radii.	221
91(b)	Effective cavity radius as a function of time.	221
91(c)	Experimental gas nucleation density data.	221
92(a)	Bubble projected area as a function of time.	222
92(b)	Number of bubbles growing per unit of area as a function of time.	222
92(c)	Fraction of surface area covered as a function of time.	222

LIST OF TABLES

Table No..	Title	Page
1	Range of experimental data.	70
2	Difference in wall superheats at constant heat flux and difference in heat fluxes at constant wall superheats for two surfaces of different thickness.	81
3	Experimental conditions for the cine films analysed. Run 4.	90
4	Average bubble parameters as a function of heat flux; Run 4.	93
5	Statistical measures of central tendencies for maximum bubble diameter data under two different grouping criteria. Run 4.	107
6	Harmonic and arithmetical means and degree of distortion for the frequency of bubble emission data. Run 4.	115
7	Nucleation site activation histories. Run 4.	124
8	Deactivation/activation of nucleation sites during heat flux increments. Run 4.	128
9	Classification of deactivated sites during heat flux variations.	130
10	Comparison between observed and predicted fraction of deactivated sites during heat flux intervals.	130
11	Bubble coalescence data for run 4.	142
12	Critical heat flux results.	147
13	Comparison between the pool boiling critical heat fluxes predicted by the present correlation and those predicted by well-known pool boiling burnout correlations.	169
14	Values calculated for t^+ based on t_L	172
15	Values measured for the true fraction of boiling area.	188

16	Physical properties of water and experimetal data.	191
17	Calculated heat transfer under bubbles. Run 4.	192
18	Total heat fluxes predicted by equation (5-56) at various values of K. Run 4.	195
19	Total heat fluxes predicted by the modified models of nucleate boiling heat transfer.	199

NOMENCLATURE†

English symbols:

a	Local area, equation (3-19).
A	Aspect channel parameter, equation (3-1).
A_b	Maximum bubble projected area.
$A_b(t)$	Bubble projected area as a function of time.
A_i	Area of bubble influence, equation (1-6).
A_T	Total surface area.
b	Parameter defined by equation (5-2).
CHF	Critical heat flux.
C_p	Specific heat at constant pressure.
C_2	Constant in equation (1-11).
C_3	Constant defined by equation (5-11).
C_4	Parameter defined by equation (5-22).
d_r	Dryout diameter.
D	Bubble or tube diameter.
D_H	Hydraulic or equivalent diameter of a channel.
D_i	Diameter of bubble influence, equation (3-20).
D_{in}	Internal diameter of a tube.
D_m	Maximum bubble diameter.
D_r	Fraction of dry surface under a bubble, d^2_r/D^2_m.
E	Dimensionless parameter defined by equation (5-46).
f	Frequency of bubble emission.
f'	Instantaneous surface area fraction affected by bubbles, equation (1-2).
f_o	Frequency of occurrence (number of data).
F	Periodically surface area fraction affected by bubbles, equation (1-3).
g	Acceleration due to the force of gravity

---

† Other symbols are defined in the text as necessary

g_c	Conversion factor from force to mass.
G	Mass-velocity of liquid.
h	Heat transfer coefficient.
H	Enthalpy.
H_e	Fluid enthalpy at exit, equation (1-22).
H_f	Enthalpy of saturated liquid.
ierfc	Complementary error function.
Ja	Jakob number, $\rho_l \ Cp_l \ (T_w-T_{sat})/\rho_v\lambda$.
k	Thermal conductivity.
K	Factor defining the area of bubble influence, equation (1-6).
L	Characteristic dimension, equation (5-10).
L_B	Burnout location (Distance from the downstream end of the heated surface to the burnout location).
L_H	Heated length.
n	Exponent in equation (3-5).
n_g	Gas nucleation site density.
n_o	Local active site density.
n_s	Nucleation site density.
N	Bubble population density.
N_c	Current bubble population.
N_G	Number of bubbles growing per unit of area at a given time, Figure 92(b).
Nu	Nusselt number, hD_H/k.
P	System pressure.
P_e	Exit pressure.
Pr	Prandtl number, $C_p\mu/k$.
P_s	Saturation pressure.
P_2	Overpressure in the gas nucleation tests, equation (3-8).
q	Heat flow.
$\dot{q}$	Internal heat generation rate per unit of volume.
r	Bubble radius.

r_e	Effective cavity radius, equation (3-7).
r_m	Maximum bubble radius.
r_r	Dried-out radius, Figure 3.
R	Maximum bubble radius.
Re	Reynolds number, $D_H v\rho/\mu$.
S	Separation distance between pairs of nearest-neighbour nucleation sites.
St	Stanton number, $h/v\rho C_p$.
t	Time.
t_c	Bubble cycle period.
t_d	Time defined by equation (5-6).
t_e	Microlayer evaporation time, equation (5-19).
t_g	Bubble growth time.
t_i	Insulation time (vapour patch life time).
t_L	Bubble life time.
t_w	Waiting time.
t_o	Time under consideration, equation (5-3).
t_1	Time defined by equation (1-11).
t_2	Time for conduction across the microlayer, equation (5-13).
T	Temperature.
T_b	Liquid bulk temperature.
T_{M_1}	First maximum surface wall temperature.
T_{Q_1}	First quenching surface wall temperature.
T_{sat}	Saturation temperature.
T_w	Wall temperature.
T_o	Initial temperature of a solid.
v	Flow velocity.
V_B	Bubble volume.
V_{fg}	Specific volume change of evaporation.
V_M	Volume of microlayer evaporated.
W	Dimensionless parameter defined by equation (5-15).

x	Ratio of true boiling area to nominal boiling area, equation (5-54).
x'	Characteristic length, page 175.
X	Thermodynamic mass-quality.
X_e	Thermodynamic mass-quality at exit, equation (1-21).
X_s	Characteristic thickness, equation (6-2).
Z	Number of local areas of magnitude a, equation (3-19).

Greek Symbols:

α	Thermal diffusivity.
β	Nominal fraction of boiling area, equation (1-14).
β_a	Actual fraction of boiling area.
β_o	Coefficient of volumetric expansion.
β_1	Constant in equation (1-1).
γ	Parameter defined by equation (5-45).
δ	Test section wall thickness.
δ'	Microlayer thickness.
δ'_o	Initial microlayer thickness.
ΔP	Pressure difference, P_s-P, equation (3-7).
ΔP_p	Prepressurisation level, P_2-P_s, equation (3-8).
ΔT	Temperature difference, T_w-T_b.
ΔT_{sat}	Wall superheat, T_w-T_{sat}.
ΔT_{sub}	Degree of subcooling, $T_{sat}-T_b$.
ΔT_w^+	Dimensionless temperature difference, equation (6-5).
ε	Dimensionless distance, equation (6-7).
η	Dimensionless parameter, equation (4-5).
θ	Bubble contact angle.
λ	Latent heat of vaporization.
μ	Absolute viscosity.
μ_r	Ratio of bulk to wall viscosity, equation (3-1).
ν	Kinematic viscosity, μ/ρ.
ξ	Parameter defined by equation (5-44).
ρ	Density.
σ	Surface tension.

τ	Dimensionless time, equation (5-10).
τ_i	Dimensionless insulation time, equation (6-6).
$\emptyset$	Heat flux.
$\emptyset_b$	Boiling flux.
$\emptyset_c$	Critical heat flux.
$\emptyset_{FC}$	Heat flux due to forced-convection.
$\emptyset_{FC_{(1-\beta)}}$	Forced convection contribution to heat flux, equation (5-38).
$\emptyset_{FC_{(1-\beta a)}}$	Increased forced convection contribution to heat flux due to an increase in the fraction of area not involved in boiling, equation (5-52).
$\emptyset_i$	Heat flux at the onset of boiling, equation (3-6).
$\emptyset_M$	Heat flux due to microlayer evaporation.
$\emptyset_{NB}$	Nucleate boiling heat flux.
$\emptyset_{NB_i}$	Nucleate boiling heat flux in the annular area illustrated in Figure 84.
$\emptyset_{NC}$	Natural convection contribution to heat flux.
$\emptyset_{ov}$	Heat flux in the overlapping areas of bubble influence, equation (5-49).
$\emptyset_T$	Total heat flux.
$\emptyset_{TE}$	Experimental total heat flux.
$\emptyset_{TP}$	Predicted total heat flux.
$\emptyset_{UB}$	Heat flow under bubbles per unit of time over the total surface area, equation (5-39).
χ	Statistical parameter (Chi).
ψ	Parameter defined in equation (3-5).

Subscripts:

f	Property evaluated at the film temperature, Tw+Tb/2
in	Inlet condition.
l	Liquid.
out	Outlet condition.
s	Solid.
v	Vapour.

Superscripts:

+	Dimensionless.
-	Average.

INDEX

		Page
	Abstract	i
	Acknowledgements	ii
	List of Figures	iii
	List of Tables	viii
	Nomenclature	x
Chapter One	Introduction	1
I	Boiling heat transfer: a brief survey.	1
1.	The boiling curve.	1
2.	Nucleate boiling heat-transfer mechanisms.	4
A.	Bubble-agitation model.	5
B.	Latent heat transport.	7
C.	Vapour-liquid exchange model.	8
D.	Enthalpy transport model.	9
E.	Evaporative model.	10
3.	Composite nucleate boiling heat transfer models.	12
A.	Han-Griffith and Mikic-Rohsenow models.	14
B.	Model of Graham and Hendricks.	15
C.	Model of Judd and Hwang.	17
II	The critical heat flux (CHF) phenomenon in subcooled flow boiling.	20
1.	Methods of investigating the CHF phenomenon.	21
A.	Empirical method.	21
B.	Semi-empirical method.	21
C.	Theoretical method.	22

		Page
2.	Models proposed for the mechanism of the ĊHF in subcooled flow boiling.	22
A.	Chang's model.	22
B.	Tong's model.	24
C.	Bankoff's model.	26
D.	Kutateladze's model.	26
E.	Kirby's (et. al) model.	27
F.	Fiori and Bergles's model.	30
G.	Model of van der Molen and Galjee.	33
H.	Concluding remarks on the proposed models for the CHF mechanism.	35
3.	Flow regimes and their relationship with the CHF.	35
4.	General trends in the parameters affecting the CHF.	36
A.	The main parameters effect.	36
a)	Effect of subcooling on CHF	38
b)	Effect of mass-velocity on CHF	38
c)	Effect of tube diameter on CHF	38
d)	Effect of heated length on CHF	40
e)	Effect of system pressure on CHF	40
B.	Secondary factors affecting the CHF	40
a)	Test section wall thickness effect on CHF.	40
b)	The effect of other parameters on CHF.	46
III	Purpose of the present study.	47

			Page
Chapter Two		Experimental equipment and test procedure	48
I		Experimental apparatus.	48
	1.	The test section.	48
	2.	Test section channel.	50
	3.	The forced-convection boiling rig.	53
	4.	The high speed cine-photography equipment.	59
II		Test procedure.	60
	1.	System preparation.	60
	2.	Test procedure.	63
Chapter Three		Experimental Results. Part I: Single phase forced-convection and Nucleate flow boiling.	65
I		Single phase forced-convection experiments.	65
II		Nucleate flow boiling experiments.	68
	1.	Experimental flow boiling curves.	68
	A.	Test section wall thickness effect.	74
	B.	Inlet subcooling effect.	82
	C.	Flow velocity effect.	84
	2.	Photographic study of the bubble parameters.	86
	A.	Method of Analysis.	91
	B.	The measured bubble parameters.	92
	a)	Maximum bubble diameter, D_m.	95
	b)	Waiting - (t_w), growth - (t_g) and life - (t_L) times; frequency of vapour bubble emission (f) and bubble population density (N).	95
	c)	Nucleation site density (n_s), spatial distribution of nucleation sites and separation distance from the nearest neighbouring nucleation site (S).	97

		Page
C.	Statistical analyses of the measured bubble parameters.	102
a)	Maximum bubble diameter.	103
b)	Bubble life time.	109
c)	Waiting time.	111
d)	Frequency of bubble emission.	111
e)	Separation distance from nearest-neighbour nucleation site.	114
f)	Spatial distribution of local active nucleation sites.	116
3.	Deactivation/reactivation of nucleation sites.	122
Chapter Four	Experimental Results. Part II: Critical Heat Flux	132
I	High-speed cine photographic observations.	132
1.	Flow patterns near the CHF.	132
2.	Bubble coalescence.	139
II	Critical heat flux experiments.	146
1.	Effect of inlet subcooling on CHF.	148
2.	Effect of mass-velocity on CHF.	148
3.	Effect of test-section wall thickness on CHF.	148
4.	Burnout location data.	153
5.	Types of failure exhibited in the destroyed test sections.	153
6.	Development of an empirical correlation for CHF.	160

		Page
Chapter Five	Analysis of Nucleate Flow Boiling Heat Transfer	170
I	Introduction.	170
II	A proposed model for nucleate flow boiling heat transfer.	170
1.	Basic assumptions.	170
2.	Heat transfer model neglecting overlap of areas of influence.	174
A.	Heat flow under bubbles per unit of time over the total surface area.	181
3.	Heat transfer model considering overlap of areas of influence.	183
A.	Analysis.	183
B.	Prediction of overlap.	185
III	Assessment of the proposed model for nucleate boiling heat transfer.	191
1.	Basic model.	191
2.	Modifications to the basic model.	197
3.	Effect of overlap on boiling heat flux.	200
Chapter Six	Analysis of Critical Heat Flux	204
I	Introduction	204
II	Critical heat flux models.	207
III	A possible alternative for the CHF mechanism.	211
1.	Analysis.	212
A.	Initial conditions.	213
B.	Insulation of the surface by a vapour patch.	213
C.	Quenching of the surface by the liquid bulk.	214
D.	Criterion to determine the cause for burnout.	217

		Page
Chapter Seven	Summary and Conclusions	225
I	Summary and conclusions.	225
1.	Single-phase forced convection.	225
2.	Nucleate boiling heat transfer.	226
3.	Critical heat flux.	229
II	Future work.	232
References		234
Appendices		
A.	Temperature drop across the test section wall.	240
B.	Estimates of experimental errors.	241
C.	Effective cavity radii as a function of ΔP.	242
D.	Observed flow patterns in the high-speed cine films.	243
E.	Critical heat flux data.	244
F.	Heat flow under bubbles per unit of time over the total surface area.	246
G.	Prediction of the ratio x of actual boiling area to nominal boiling area for an assumed random distribution of nucleation sites.	254
H.	Solution of the one-dimensional unsteady-state heat conduction equation for a solid with internal heat generation subjected to sudden insulation.	258

CHAPTER ONE

INTRODUCTION

I. Boiling heat transfer: a brief survey

Boiling can be defined as that process which involves a change in phase from liquid to vapour or the formation of vapour bubbles in a liquid, due to heat supply. The practical importance of boiling arises from the fact that it represents a very efficient cooling process for devices where very large quantities of heat are generated and have to be extracted at the equivalent rate of production. Typical examples of such high-flux operating devices are nuclear reactors and rocket engines whose ultimate performance can be dictated by boiling considerations.

The present study is concerned with boiling heat transfer on a uniformly heated solid surface which forms one wall of a channel of rectangular cross-section, placed vertically, through which water at atmospheric pressure and inlet temperatures below saturation is forced to flow upwards. Comprehensive reviews on boiling heat transfer can be found in references [1 to 5].

1. The Boiling curve

It has been customary to characterize the boiling phenomenon with a plot of heat flux against the temperature difference $T_w - T_{sat}$. This relationship, known as the boiling curve, is used to establish the different heat transfer regions. The results for pool boiling, where the heating surface is immersed in a large volume of initially stationary liquid, are generally employed to describe such boiling regimes. For the case of a temperature-controlled system, the well-established heat transfer modes, depicted in Fig. 1, are:

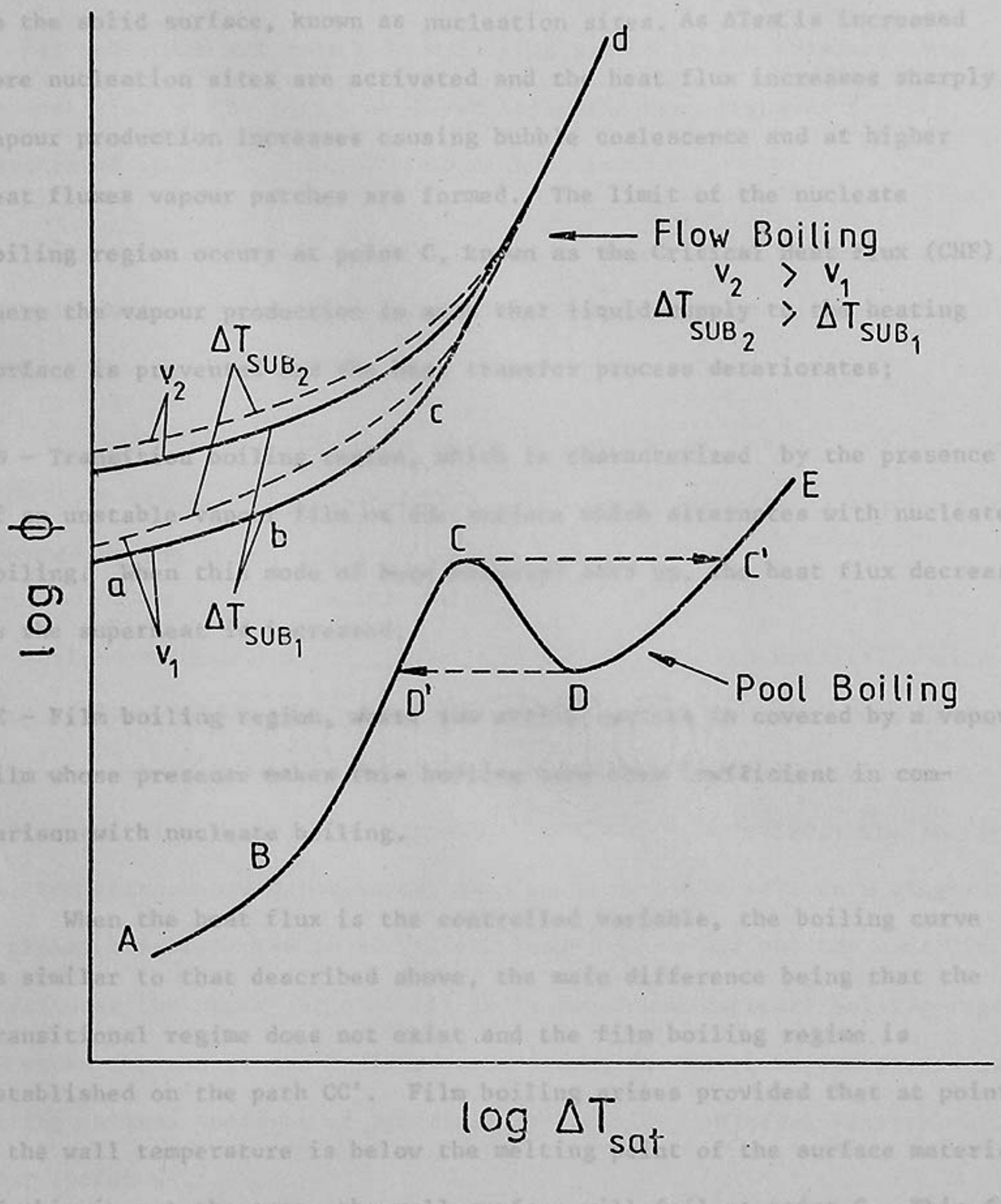


Figure 1 Qualitative representation of the Boiling Curve.

AB - Single-phase region, where the heat is removed by natural convection;

BC - Nucleate boiling region, where the wall superheat ΔT_{sat}, reaches the value necessary to promote vapour bubble production at localized spots on the solid surface, known as nucleation sites. As ΔT_{sat} is increased more nucleation sites are activated and the heat flux increases sharply. Vapour production increases causing bubble coalescence and at higher heat fluxes vapour patches are formed. The limit of the nucleate boiling region occurs at point C, known as the Critical Heat Flux (CHF), where the vapour production is such that liquid supply to the heating surface is prevented and the heat transfer process deteriorates;

CD - Transition boiling region, which is characterized by the presence of an unstable vapour film on the surface which alternates with nucleate boiling. When this mode of heat transfer sets up, the heat flux decreases as the superheat is increased;

DE - Film boiling region, where the entire surface is covered by a vapour film whose presence makes this boiling mode very inefficient in comparison with nucleate boiling.

When the heat flux is the controlled variable, the boiling curve is similar to that described above, the main difference being that the transitional regime does not exist and the film boiling regime is established on the path CC'. Film boiling arises provided that at point C the wall temperature is below the melting point of the surface material. If this is not the case, the wall surface will fail at point C. This fact has led to point C being referred to, among other names (first boiling crisis, departure from nucleate boiling, maximum heat flux), as the burn-out point. Once film boiling is set up a decrease in heat flux brings the nucleate boiling regime through the path C'DD'. Point D is generally

known as the Leidenfrost point, sometimes referred to as minimum film boiling superheat or second boiling crisis.

From an engineering point of view pool boiling lacks significance but the valuable information drawn from its investigation can be embodied in the study of the more complex process of flow boiling.

For subcooled water in a flow boiling system at low pressure when the heat flux is the independent variable, the heat transfer regions, illustrated in Fig. 1 , are described as follows:-

ab - Single-phase forced convection region, found up to the point where the wall surface temperature reaches the value required to cause nucleation;

bc - Partial boiling region, is characterized by the presence of few activated nucleation sites, and due to this fact, the heat transfer is strongly influenced by the single-phase convective process.

cd- Fully-developed boiling region, where the number of nucleation sites being activated increases with increasing heat flux and the contribution of single-phase convection is greatly diminished. In this region, subcooling and flow velocity do not appear to affect appreciably the surface wall temperature and experimental data lie reasonable well on a single line.

Point b is referred to as the incipience point and the CHF condition constitutes the upper limit of the fully-developed nucleate boiling region and marks the end of the boiling curve since, for water at low pressures boiling on most surfaces of practical application, physical failure will occur (point d).

2. Nucleate boiling heat-transfer mechanisms.

Since the ultimate purpose of the study of boiling is the design of efficient and safe-operating cooling processes, considerable effort has been directed towards the understanding of the nucleate boiling heat

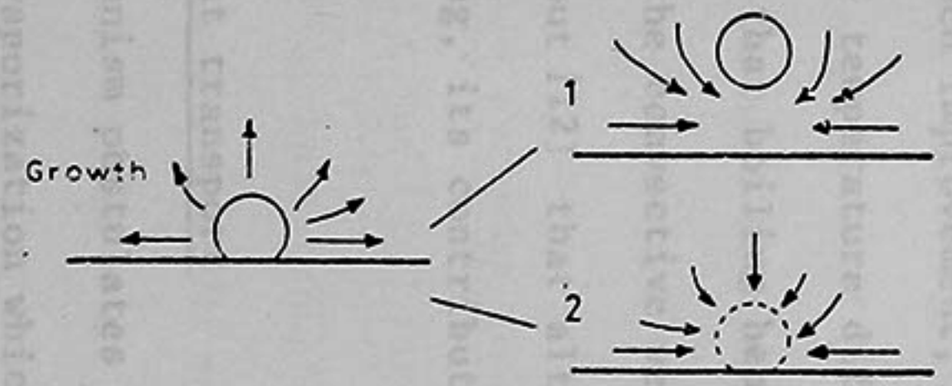
transfer mechanism (s). The following presentation is restricted to discussion of nucleate boiling heat transfer mechanisms derived for, or modifiable for incorporation in, flow boiling systems. Schematic representations of the models are shown in Fig. 2.

A. Bubble-agitation model (or micro-convection)

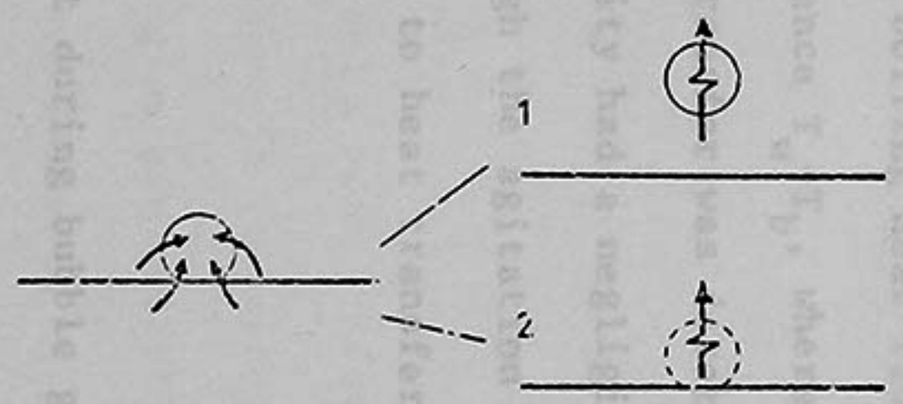
This mechanism of nucleate boiling heat transfer, perhaps the earliest, suggests that the growth and collapse (or detachment) of bubbles create micro-convection currents which induce turbulence, promoting heat transfer between the surface and the liquid. The observed increase in heat transfer when boiling starts is entirely attributed to the resulting agitation of the fluid in the vicinity of the heater wall. Jakob, quoted in [6], was one of the first experimenters to make this suggestion. Subsequently Rohsenow and Clark [6] adopted this concept, which became the basis for the development of several nucleate boiling correlations which considered the boiling phenomenon as a turbulent convective-type of process. Bubble parameters were incorporated in a definition of a bubble-Reynolds number and a well known Nusselt-Reynolds type correlation was developed [7]. However, the first theoretical approach using the micro-convection concept was formulated by Bankoff [8] who proposed a 3-step "sequential process" model for nucleate boiling heat transfer, the first of which considers the flow of heat from the heating surface to the layer adjacent to the heating surface containing bubbles, denominated the two-phase wall layer. Bankoff expressed the total heat flux as

$$\phi = 1.25\sqrt{(kc_p\rho)_1 t_L}\ \left[fn\left(\frac{t_c}{t_L}\right)\right] D_m^2\ N(T_w - T_b) + \beta_1\ (\rho C_p)_1\ \frac{D_m}{t_L}\ \left(\frac{2f'}{1-f'}\right)^{\frac{1}{2}}\ (1-F)\ (T_w - T_b) \qquad (1\text{-}1)$$

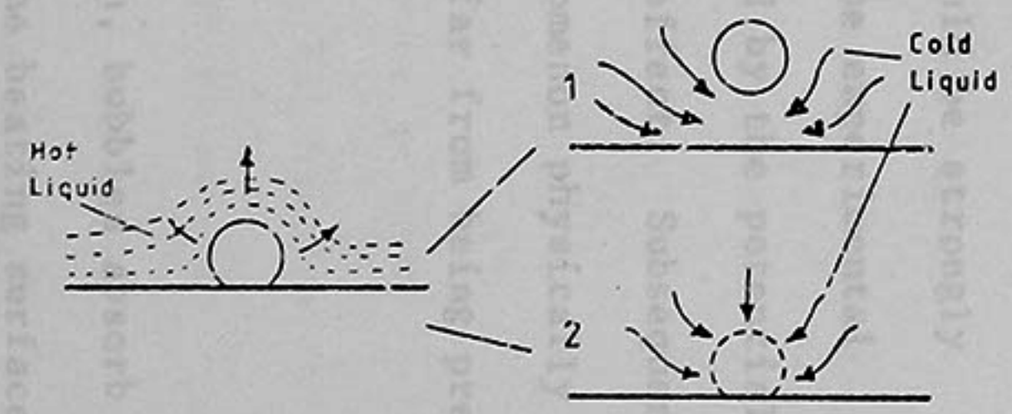
where the first term, accounting for the quenching of dry spots formed after bubbles collapse on the heating surface, contains a function involving bubble growth rate,



(a) Bubble agitation model

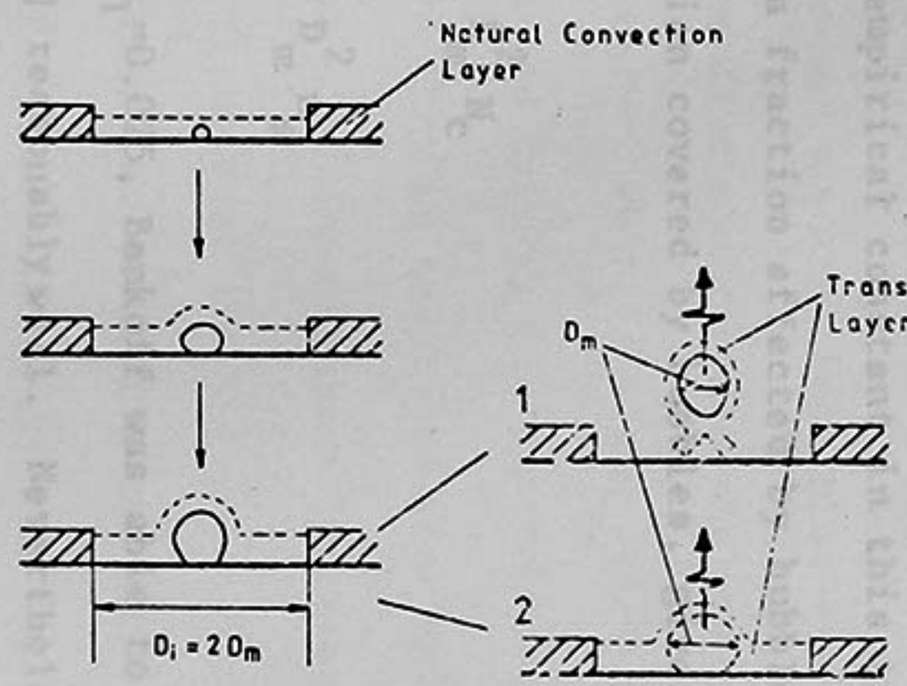


(b) Latent heat transport model

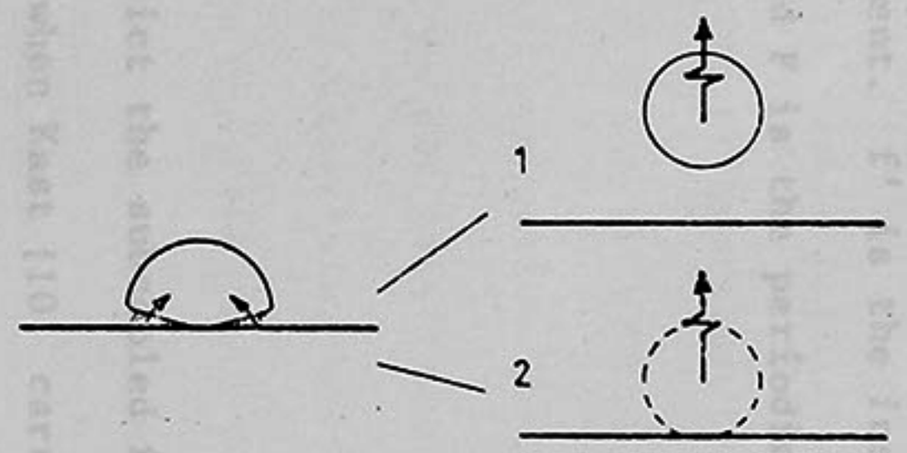


(c) Vapour-liquid exchange model

1 : DEPARTURE
2 : COLLAPSE



(d) Surface quenching model



(e) Microlayer evaporation model

Figure 2 Nucleate boiling heat transfer models.

$$f_n(\frac{t_c}{t_L}) = \int_{\frac{1}{2}}^{1} (\frac{D}{D_m}) \frac{d}{d(t/t_L)} (\frac{D}{D_m}) \sqrt{(1+\frac{t_c}{t_L}) - (\frac{t}{t_L})} \quad d(\frac{t}{t_L})$$

The second term represents the stirring heat flux contribution and it includes the only empirical constant in this treatment. f' is the instantaneous surface area fraction affected by bubbles and F is the periodically surface area fraction covered by bubbles, given by

$$f' = \frac{\pi}{4} D_m^2 N_c \tag{1-2}$$

$$F = \frac{\pi}{4} D_m^2 n_s \tag{1-3}$$

By setting β_1=0.025, Bankoff was able to predict the subcooled flow boiling data of Gunther [9] reasonably well. Nevertheless, when Kast [10] carried out measurements of heat transfer coefficients in a bubble tower where boiling was simulated by injecting gas bubbles through a porous wall, he found that the magnitude of the enhancement in heat transfer due to the agitation effect could not be compared to that observed in nucleate boiling. Forster and Greif [11] pointed out that if agitation effects were responsible for such improvement, the boiling heat flux would be strongly dependent on the temperature difference $T_w - T_b$, whereas the experimental evidence showed that boiling heat transfer was determined by the potential $T_w - T_{sat}$, where the convective velocity had a negligible effect. Subsequently it was pointed out [12] that although the agitation phenomenon physically occurs in boiling, its contribution to heat transfer is far from being predominant.

B. Latent heat transport

This mechanism postulates that during bubble growth, bubbles absorb latent heat of vaporization which is carried away from the heating surface by the liquid bulk when bubbles leave the heater surface or collapse on it.

The nucleate boiling heat flux due to latent heat transport is expressed as

$$\phi_{NB} = \rho_v \lambda V_B n_s f \qquad (1\text{-}4)$$

Bankoff [13] pointed out that the latent heat transport contribution might be quite important at high heat fluxes where the bubble populations are so high that the main contribution to heat transfer arises from the bubbles themselves rather than from the fraction of surface area not occupied by bubbles. Rallis and Jawurek [14] corroborated that suggestion experimentally, and showed that in saturated pool boiling, latent heat transport was very significant, its contribution increasing with increasing heat flux and appearing to account for the total heat flux near the CHF. At all heat fluxes in their experiments, the sum of latent heat transport and natural convection fluxes acounted for the total heat flux.

However, earlier estimates by Rohsenow and Clark [6] and Forster and Grief [11] on subcooled flow boiling data proved that the contribution of this mechanism to the high heat-transfer rates observed was negligible. Despite the fact that Bankoff [13] showed that such estimates of about 2% of the total heat flux were incorrectly computed as simultaneous condensation at the bubble tip was not taken into account, the reported correct order of magnitude of 10 times greater, is still insufficient to consider the latent heat transport mechanism as the most important heat flux contributor in subcooled nucleate flow boiling.

C. Vapour-liquid exchange model

Forster and Grief [11] formulated a vapour-liquid exchange model for nucleate boiling heat transfer where it is postulated that bubbles during growth transfer heat by pushing an equivalent bubble volume of hot liquid into the liquid bulk and replacing it by cold liquid after bubble collapse or departure. From their estimates, Forster and Greif claimed that this vapour-liquid exchange process alone could account for the observed heat fluxes in nucleate boiling.

The heat flux attributed to this mechanism is given by

$$\emptyset_{NB} = \emptyset_T^{'} = (C_p\rho)_l V_B f n_s (T_w - T_b) \qquad (1\text{-}5)$$

The main shortcoming of this model, pointed out by Bankoff [8] is the assumption that the hot liquid being pumped away from the heating surface is at the mean temperature between the wall and the bulk, which would signify a thermal boundary layer thickness of the order of the maximum bubble radius, while the experimental evidence confirms that bubble dimensions in subcooled flow boiling are much greater than such thickness [12].

D. Enthalpy transport model (or surface quenching)

Han and Griffith [15] postulated a nucleateboiling heat transfer mechanism for the isolated bubble regime, similar to that of Forster and Grief, but allowing for the fact that the cold liquid which flows to the heating surface is not all brought up to the wall temperature, but heated by a transient heat conduction process. In detail: when cold liquid flows to the heating surface after bubble collapse or departure, a thermal layer builds up and the new bubble which originates, when departing, takes with it a portion of the superheated thermal layer which is brought into the liquid bulk. Simultaneously after departure, cold liquid flows again and the process is repeated. By this cycle of events, heat is efficiently transferred from the heating surface to the liquid bulk.

In the solution, formulated as a one-dimensional transient conduction process to a semi-infinite solid (the liquid), it was assumed that the area from which the superheated layer is carried away by a bubble, nominated the area of influence, is the maximum bubble projected area multiplied by an empirical factor,

$$A_i = K(\frac{\pi}{4} D_m^2) \qquad (1\text{-}6)$$

The diameter of influence was assumed to be twice the maximum bubble diameter, $D_i = 2D_m$; so K takes the value of 4.

The nucleateboiling heat flux due to this mechanism is given by Han and Griffith as

$$\phi_{NB} = 2(\rho C_p)_l \, (T_w - T_b) \, n_s f \, [\tfrac{1}{4} D_i^2 \ell - \tfrac{1}{12} D_m^2 (\ell - \ell')] \qquad (1\text{-}7)$$

where

$$\ell = \sqrt{\pi \alpha (t_g + t_w)}$$

and

$$\ell' = \sqrt{\pi \alpha_l t_w}$$

Subsequently, Mikic and Rohsenow [16], using Han and Griffith's concepts and keeping K=4, arrived at the expression

$$\phi_{NB} = 2\sqrt{(k\rho C_p)_l} \, \sqrt{\pi f} \, n_s D_m^2 (T_w - T_b) \qquad (1\text{-}8)$$

which elminates the necessity of knowing the growth and waiting times.

Equation (1-7) can be rearranged to give

$$\phi_{NB} = 2\sqrt{(k\rho C_p)_l} \, \sqrt{\pi f} \, n_s D_m^2 \, (T_w - T_b) \left\{ 1 - \frac{1}{12} \, (1 - \sqrt{f t_w}) \right\}$$

where

$$\left\{ 1 - \frac{1}{12} \, (1 - \sqrt{f t_w}) \right\}$$

approximates to unity in most practical cases. Therefore, equation (1-8) is recommended as being the simpler to use with little or no loss of accuracy.

Han and Griffith showed that the addition of the nucleate boiling heat flux given by equation (1-17) and a natural convection component accounted for the total heat flux in nucleate pool boiling. The same was found in [16]. This surface quenching model is strictly valid only when there is no overlap in the areas of influence.

E. Evaporative model

Apart from the process of evaporation into the bubbles implied in the latent heat transport model, an evaporative model for nucleate boiling heat transfer appeared when Snyder and Edward, quoted in [17], suggested that evaporation into bubbles could occur from the bubble base or from a very thin liquid film left on the heating surface after bubble departure. Moore and Mesler [18] measured with a special thermocouple the temperature transients during nucleate pool boiling of water at atmospheric pressure

and found that the surface temperature dropped sometimes 11 to 17°C in 2 milliseconds. This fact led them to postulate that the surface was cooled during bubble growth by evaporation of a microlayer into the bubble. Subsequently, Cooper and Lloyd [19] developed a fast-response resistance thermometer which was capable of measuring local transient surface temperatures under toluene bubbles in nucleate pool boiling and observed a similar behaviour to that formerly described. Heat-transfer rates estimates in both studies [18, 19] showed that microlayer evaporation fluxes were highly significant and could account sometimes for as much as 90% of the total heat flux. Evidence on the existence of the microlayer has been given by various experimenters [20, 21, 22] and comprehensive work on microlayer theory can be found in [23, 24, 25].

The heat flux attributed to the microlayer evaporation phenomenon can be calculated from:

$$\emptyset_m = \rho_1 \lambda n_s f V_M \qquad (1\text{-}9)$$

where the volume of microlayer evaporated V_M is a time-surface area dependent function, which can be determined either by measurement involving sophisticated techniques such as those described in [26] or by the theoretical analyses implying the integration of an assumed bubble growth rate function, which in turn incorporates initial microlayer thickness considerations. Cooper [23] formulated the latter method for hemispherical bubbles and assuming a bubble-growth rate function of the form $R = C_1 t^m$, arrived at the following expression for V_M

$$V_M = \frac{\rho_1}{\rho_v}\left\{\int_o^{r_r} \delta' 2\pi r dr + \int_{r_r}^{R} (\delta'_o - \delta') 2\pi r dr\right\} \qquad (1\text{-}10)$$

where δ'_o is the initial microlayer thickness at any time (or bubble radius), given by

$$\delta'_o = C_2\sqrt{\nu_1 t_1} \qquad (1\text{-}11)$$

and δ' is the thickness of the microlayer which remains after the time interval t_2-t_1, the process being illustrated in Figure 3, reproduced from [23].

In equation (1-11) t_1 is the time for the bubble to grow to the radius considered and C_2 is a constant which was taken to be 0.8. In a recent paper by Cooper et al. [27] it has been shown that C_2 is a parameter dependent on surface tension.

Graham and Hendricks [12], proposed a 3-component additive model for nucleate pool boiling heat transfer and found that the evaporation contribution was very significant, becoming the major contributor at heat fluxes greater than 20% of the CHF. Subsequently, Judd and Hwang [28] in an experimental pool boiling study with dichloromethane as test-fluid, found that the microlayer evaporation contribution increased with increasing heat flux, accounting for 30% of the total heat flux at the highest heat flux level they investigated ($\sim 6\times10^4$ w/m^2).

3. Composite nucleate boiling heat transfer models

From the preceding discussion, it can be concluded that none of the proposed models for the nucleate boiling heat transfer mechanism, can alone be responsible for the observed enhancement in heat transfer in boiling. This apparent failure, which does not imply that none of them can actually take place in boiling under certain circumstances, has led to the proposal of composite mechanisms which invariably incorporate a single-phase convective contribution and one or more of the above models assumed to act independently but simultaneously, over different locations of the heating surface area. The early suggestion of additive contributions [29], can be fully justified by physically based intuitive reasoning: the heat flow path from fractions of a solid surface where boiling does not take place, will necessarily differ from that of those surface locations bearing bubble formation. Taking this statement as a basic principle,

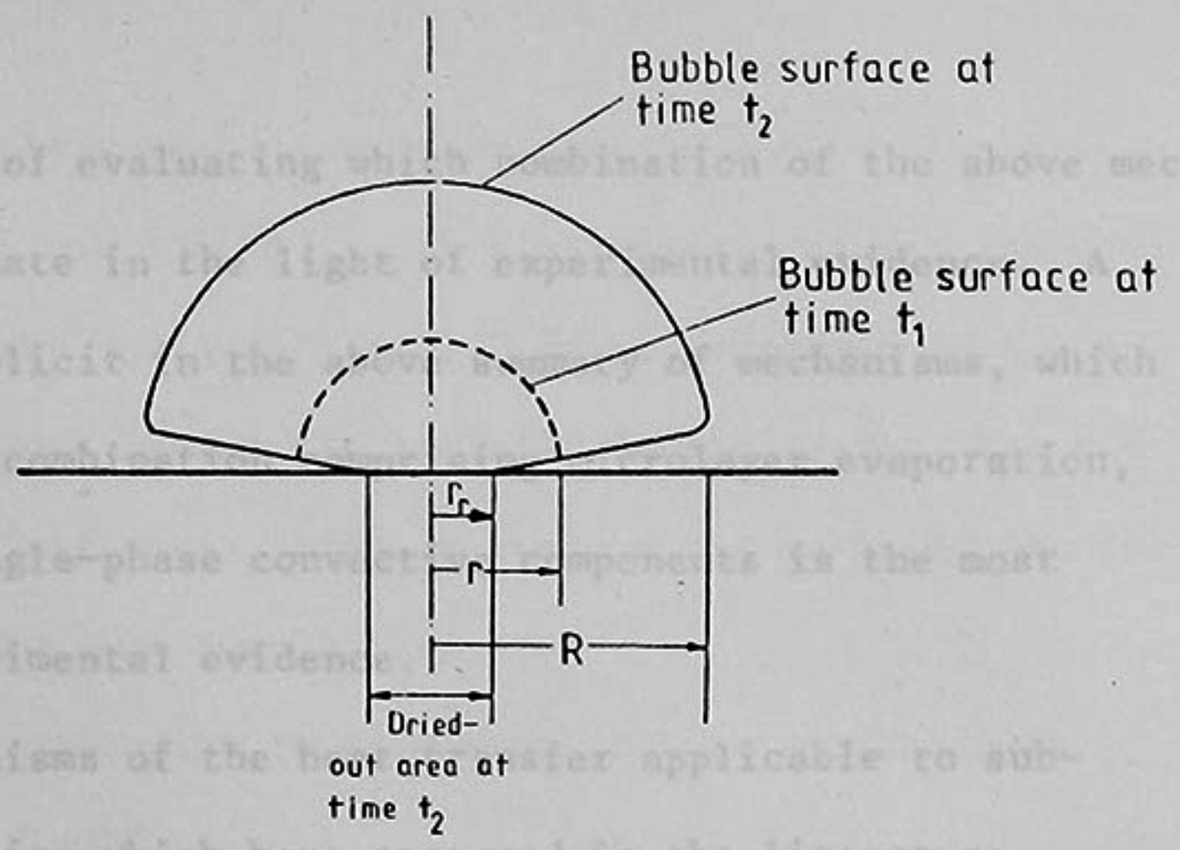


Figure 3 The microlayer in hemispherical bubbles (reproduced from reference [23]).

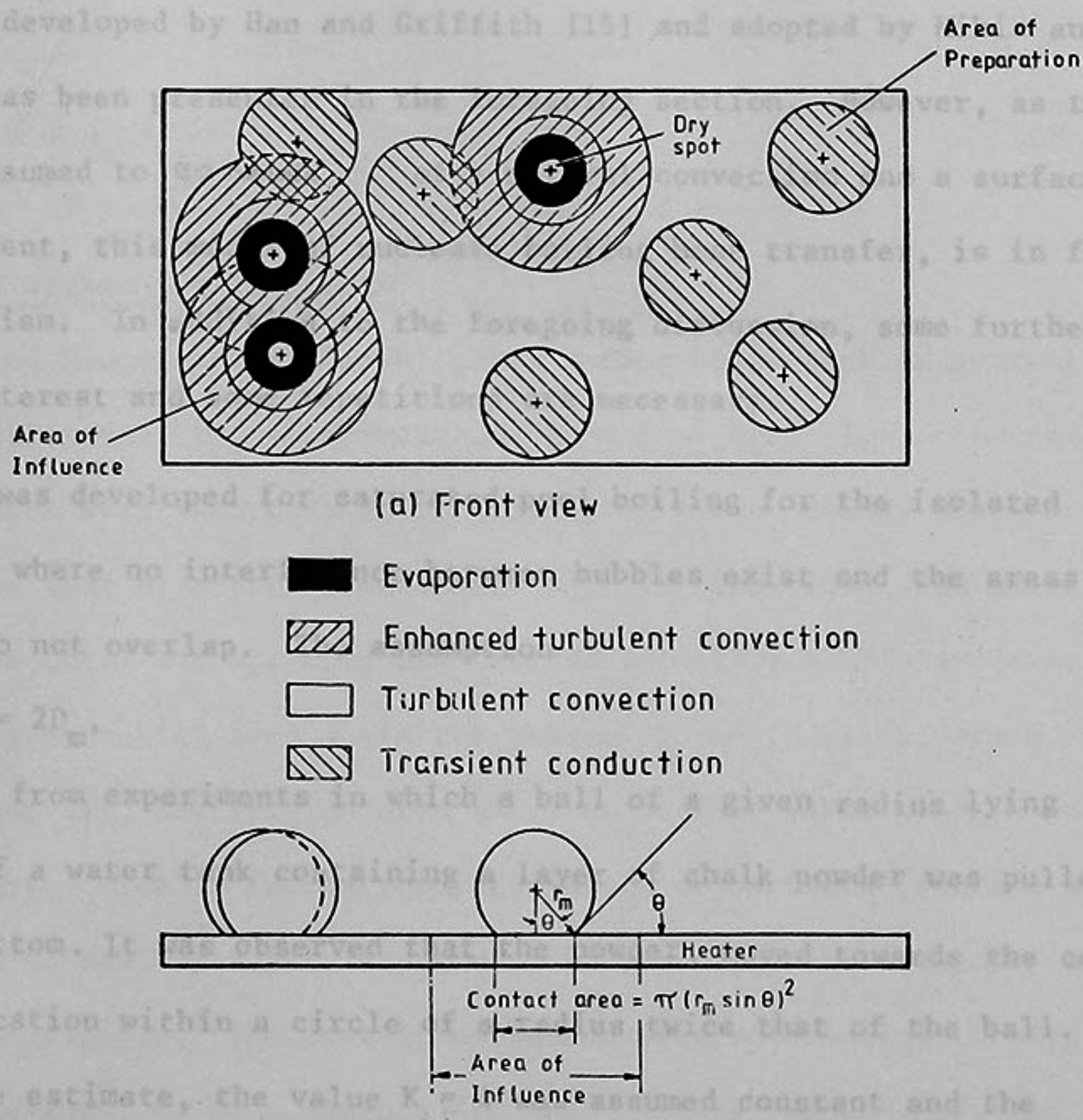


Figure 4 Model of Graham and Hendricks for nucleate boiling heat transfer [12].

then the question arises of evaluating which combination of the above mechanisms appears to be adequate in the light of experimental evidence. A most likely answer is implicit in the above summary of mechanisms, which strongly suggests that a combination comprising microlayer evaporation, surface quenching and single-phase convective components is the most consistent with the experimental evidence.

The additive mechanisms of the heat transfer applicable to subcooled nucleate flow boiling which have appeared in the literature can be grouped into two categories: one group which involves the contribution of single-phase convection and surface quenching; and another which considers the above two components and adds the microlayer evaporation contribution. They are the subject of the following three sections.

A. Han-Griffith and Mikic-Rohsenow models

The model developed by Han and Griffith [15] and adopted by Mikic and Rohsenow [16], has been presented in the foregoing section. However, as the total heat flux was assumed to consist of a natural convection and a surface quenching component, this model of nucleate boiling heat transfer, is in fact a composite mechanism. In addition to the foregoing discussion, some further points are of interest and some repetitions are necessary.

The model was developed for saturated pool boiling for the isolated bubble regime, where no interference between bubbles exist and the areas of influence do not overlap. The assumption

$$D_i = 2D_m,$$

was drawn [15] from experiments in which a ball of a given radius lying on the floor of a water tank containing a layer of chalk powder was pulled up from the bottom. It was observed that the powder, moved towards the centre of the ball location within a circle of a radius twice that of the ball. With this crude estimate, the value K = 4 was assumed constant and the model correctly predicted the experimental data of the above two studies. In addition, Mikic and Rohsenow used this model to develop a correlation

which includes surface characteristics to predict from data at a given pressure, the relationship $\emptyset$ vs ΔT_{sat} at other pressures for the same liquid boiling on the same surface. In [30] it was observed that the extrapolation of this model beyond the isolated bubble region, successfully predicted the boiling curve, perhaps because the enhanced natural convection compensated for the overlapping area.

The total heat flux according to this model can be expressed as

$$\emptyset_T = \emptyset_{NB} + (1-\beta)\emptyset_{NC} \tag{1-12}$$

where β is the fraction of the total surface area involved in boiling; and $\emptyset_{NC}$ is the natural convection contribution

The nucleate boiling heat flux, given by either equation (1-7) or equation (1-8), can alternatively be expressed as

$$\emptyset_{NB} = 2\sqrt{(k\rho C_p)_l \; f/\pi}\,(T_w - T_b)\,\beta \tag{1-13}$$

where

$$\beta = n_s K A_b = n_s K \left(\frac{\pi D_m^2}{4}\right) \tag{1-14}$$

B. Model of Graham and Hendricks

Graham and Hendricks [12] developed a rather sophisticated overall nucleate boiling heat transfer mechanism in which convection, conduction and evaporation were incorporated for the first time. Bubble shape was assumed to be that of a truncated sphere both for individual and multiple bubbles. The total surface area was divided into i) a bubble projected area, ii) a preparation area where the thermal layer is being formed to sustain boiling, and iii) an area where no boiling takes place. The bubble projected area is further divided into a dry surface fraction whose contribution to heat transfer, assumed to be convection to a vapour, is considered negligible. The contact or wetted area surrounding the dry fraction is assumed to be a microlayer which is the vapour-supplying surface. Outside this area, when the contact angle Θ is less than 90°, there will be an annulus underneath the bubble. This surface fraction and a ring

extended from the nucleation site location up to a distance of a bubble diameter, were considered areas of enhanced convection. The heat transfer for the surface fraction not involved in the above areas is calculated as free-convection. Figure 4 shows the areas where the different heat transfer mechanisms are assumed to operate.

The heat transfer rate attributed to each of these surface areas was as follows:

For the contact area, kinetic theory developed for an evaporative surface is used to evaluate the heat transfer due to microlayer evaporation. For the enhanced convection areas, turbulent free convection for horizontal surfaces is applied, multiplied by an enhancement factor K_e, taken to be constant and equal to $K_e = 1.5$. For the areas of preparation, the heat transfer is calculated as transient conduction to a semi-infinite slab, and the time involved is taken to be the waiting time. For the remaining surface, not involved in the boiling process, the heat transfer is calculated from turbulent free-convection. The total heat flux is calculated as the sum of the above contributions and given by

$$\begin{aligned}\phi_T &= [N_c A_b (1-D_r)\sin^2\theta][a_o \lambda (p_l - p_r)(\frac{g_{cM}}{2\pi R_o T_{sat}})^{\frac{1}{2}}] \\ &+ [N_c A_b (4-\sin^2\theta)]K_e[C(\frac{\beta_o g \rho_l^2}{\mu_l} Cp_l k_l^2)^{1/3}](T_w - T_b)^{4/3} \\ &+ (N_c A_b \frac{t_w}{t_g})[\frac{2k_l}{\sqrt{\pi \alpha_l t_w}}(T_w - T_b)] \\ &+ [1-N_c A_b (4+\frac{t_w}{t_g})][C(\frac{\beta_o g \rho_l^2}{\mu_l} Cp_l k_l^2)^{1/3}][T_w - T_b]^{4/3} \qquad (1\text{-}15)\end{aligned}$$

where

D_r = fraction of dry surface under a bubble = $\frac{d_r^2}{D_m^2}$

θ = bubble contact angle,

a_o = coefficient of evaporation,

p_l = liquid pressure,

p_r = receiver pressure,

g_c = conversion factor from force to mass,

M = molecular weight,

R_o = universal gas constant,

C = empirical coefficient for free convection,

β_o = coefficient of volumetric expansion,

g = acceleration due to the force of gravity.

The first, second, third and last terms of equation (1-15) are the evaporation, enhanced turbulent free convection, transient conduction and turbulent free convection contributions, respectively.

Apart from the fact that this model involves a number of empirical constants, the experimental information required in equation (1-15) is very extensive and in most cases not available. In addition, uncertainties may arise from: i) the validity of the application of the Kinetic theory to evaluate the microlayer evaporation contribution (details of the microlayer geometry are not given); ii) the assumed constant value of D_r over a large range of percentages of the CHF, which was drawn from an extrapolation of very limited experimental information at low heat flux levels (see Figure 5); iii) the parameters Θ and K_e, assumed to be the same for both single and multiple bubbles.

Graham and Hendricks applied equation (1-15) to water and methanol data and from their estimates it is observed that the calculated total heat flux over-predicted the experimental values by 4-43%.

C. Model of Judd and Hwang.

Judd and Hwang (28) formulated a composite nucleate boiling heat transfer mechanism similar to that of Graham and Hendricks [12] as far as the inclusion of evaporation, conduction and convection is concerned, but with the difference that it elminates the Kinetic theory approximation to evaluate the microlayer evaporation contribution and any enhanced natural convection contribution. The model incorporates the contribution of

natural convection, a microlayer evaporation component introduced in accordance with the geometry formulated by Cooper [23], and a nucleate boiling component. The heat transfer associated with these components is assumed to proceed independently over the different surface fractions shown in Figure 6.

The microlayer evaporation heat flux was calculated according to equation (1-9) and the value for V_M used was the average of a series of individual experimental determinations for different bubbles. For each bubble, the volume of microlayer evaporated was evaluated according to

$$V_M = 2\pi \int_o^{R_m} [\delta'_o(r) - \delta'(r,t_g)] r dr \qquad (1\text{-}16)$$

where $\delta'_o(r)$ is the initial microlayer thickness. The instantaneous microlayer thickness profile at departure $\delta'(r,t_g)$, was deduced from interferometric techniques [26].

The natural convection heat flux was computed assuming turbulent free convection multiplied by the fraction of surface area not involved in boiling. The nucleate boiling heat flux was evaluated according to the transient-conduction model of Mikic and Rohsenow [16], given by Equation (1-13).

The sum of the above components yielded the expression for the total heat flux

$$\phi_T = \rho_1 \lambda n_s f V_M + 0.18 \left[\frac{\beta_o g \rho_1^2}{\mu_1} (Cpk^2)_1\right]^{\frac{1}{3}} (T_w - T_b)^{4/3} [1-\beta]$$

$$+ 2\sqrt{(k\rho C_p)_1 \, f/\pi} \, (T_w - T_b)\beta \qquad (1\text{-}17)$$

Judd and Hwang conducted pool boiling experiments at one-half atmosphere using dichloromethane as test liquid, boiling on a glass surface coated with stannic oxide. Three different levels of heat flux each at three different levels of subcoolings were investigated; and at each

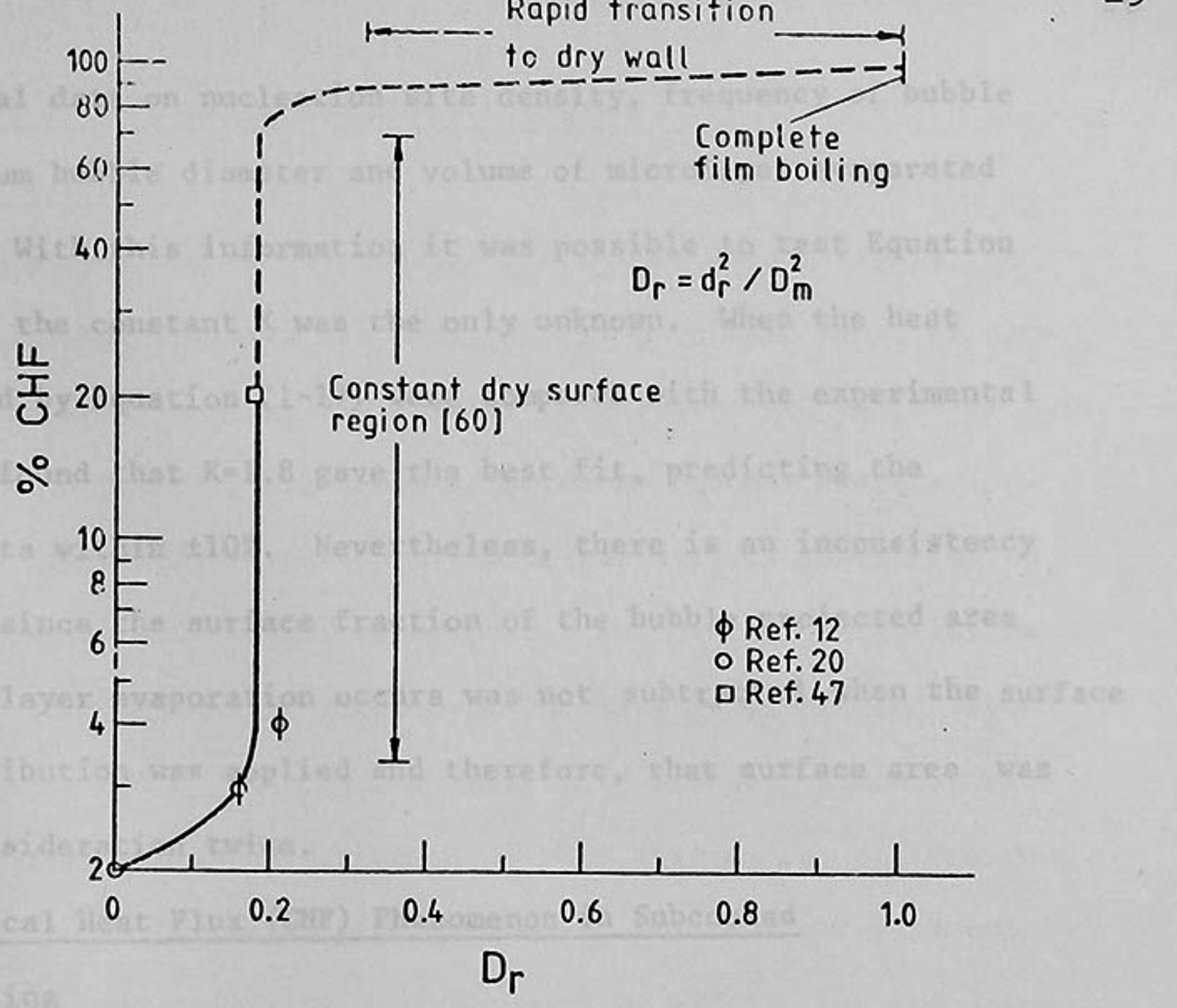


Figure 5 Fraction of dry surface area under a bubble as a function of percentage of CHF (taken from reference [12]).

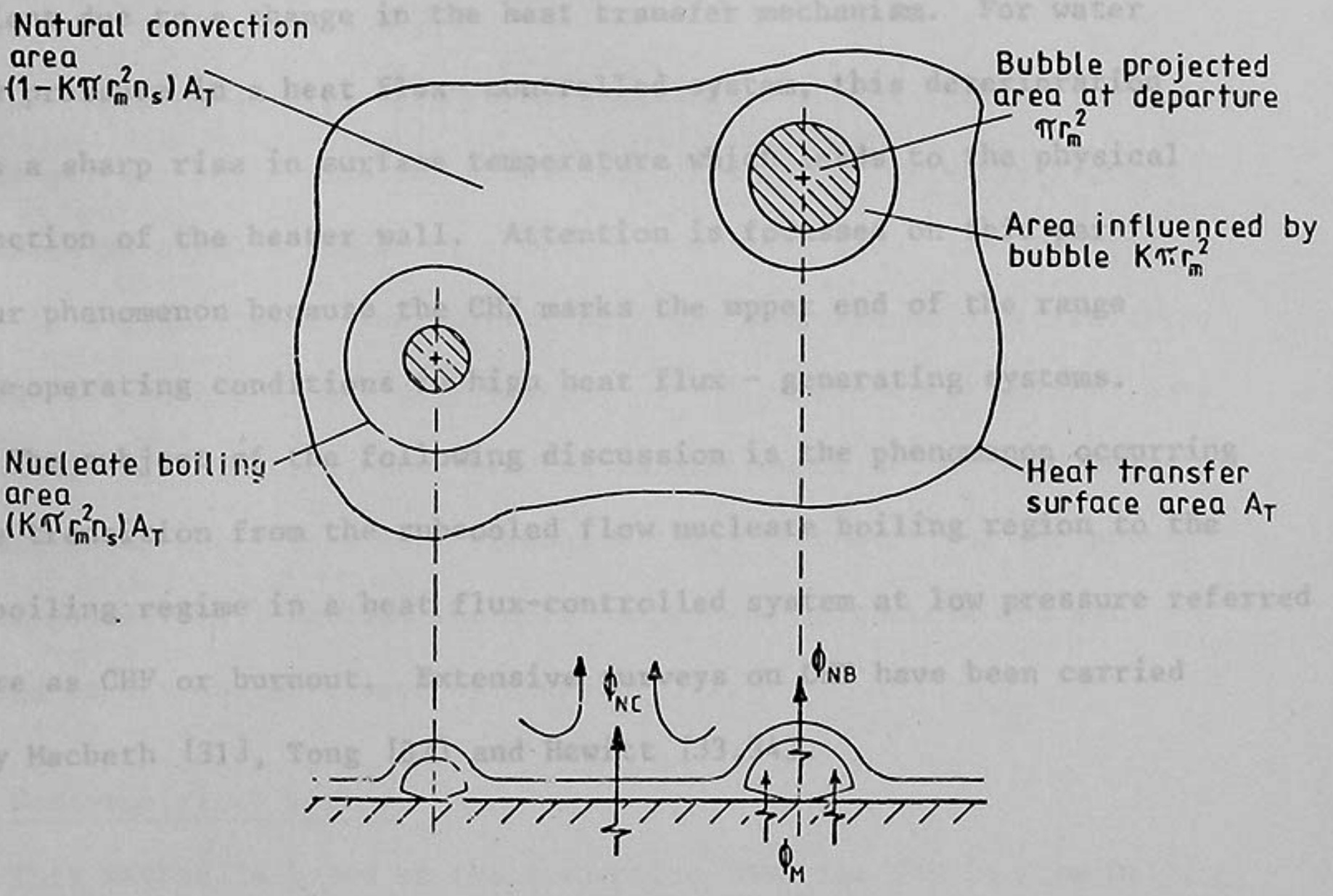


Figure 6 Model of Judd and Hwang for nucleate pool boiling heat transfer [28].

one, experimental data on nucleation site density, frequency of bubble emission, maximum bubble diameter and volume of microlayer evaporated were obtained. With this information it was possible to test Equation (1-17) in which the constant K was the only unknown. When the heat fluxes predicted by Equation (1-17) were compared with the experimental values, it was found that K=1.8 gave the best fit, predicting the experimental data within ±10%. Nevertheless, there is an inconsistency in this model, since the surface fraction of the bubble projected area where the microlayer evaporation occurs was not subtracted when the surface quenching contribution was applied and therefore, that surface area was taken into consideration twice.

II. The Critical Heat Flux (CHF) Phenomenon in Subcooled Flow Boiling

The Critical Heat Flux (CHF) condition, point C in Figure 1, which represents perhaps the most important phenomenon occurring in the boiling process, is manifested as a sudden reduction in the heat transfer coefficient due to a change in the heat transfer mechanism. For water at low pressure in a heat flux- controlled system, this deterioration causes a sharp rise in surface temperature which leads to the physical destruction of the heater wall. Attention is focussed on this particular phenomenon because the CHF marks the upper end of the range of safe-operating conditions in high heat flux - generating systems.

The subject of the following discussion is the phenomenon occurring in the transition from the subcooled flow nucleate boiling region to the film boiling regime in a heat flux-controlled system at low pressure referred to here as CHF or burnout. Extensive surveys on CHF have been carried out by Macbeth [31], Tong [32] and Hewitt [33,34].

1. Methods of investigating the CHF phenomenon

A. Empirical method

The major proportion of CHF studies lie within this category, in which experimental burnout data are obtained for a certain range of conditions, and the CHF is empirically related to the observed variables affecting it. This practice has produced numerous burnout correlations for which it is repeatedly stressed that applicability is restricted to the range of experimental conditions adopted. But even so, predictions among different correlations applicable to the same range of conditions can differ markedly [35]. This is not surprising however, since apart from the intrinsically complex nature of the CHF phenomenon, differences may arise from: i) the use of heater elements of the same material but with different surface conditions (microgeometry), ii) the burnout detection method and its accuracy when tests are not taken to destruction and iii) involuntary inclusion/exclusion of the so-called "secondary" factors affecting the CHF whose influence has not yet been systematically studied (see section II.4.B.).

Correlating burnout data perhaps date back to the late 40's when McAdams et. al. [36] produced a burnout correlation for water flowing upwards in an annulus formed by a heated stainless steel tube centrally placed in a glass tube. Ever since, with the improvement of correlating techniques, the appearance of a vast amount of experimental burnout data, and the aid of computers, more general burnout correlations have been proposed which apply to a more extensive range of conditions and several channel geometries. Perhaps the more comprehensive correlation yet produced is the one developed by Macbeth [37].

B. Semi-empirical method.

This method is based on the assumption that the CHF in flow boiling is comprised of several independent components whose contributions are additive. Individual solutions for each component are formulated and

their addition yields a semi-analytical solution of the overall CHF process. Nevertheless, apart from the fact that in some cases the expressions derived for each individual component are also empirical correlations, this method of superposition does not allow for interference among the individual contributions. A typical example using this approach is that of Levy [38] who obtained, for water, the CHF in subcooled flow boiling as the sum of 3 components; namely, the CHF in pool boiling, a heat conduction term to account for the periodic contact of subcooled liquid with the heating surface and, a single-phase forced convection contribution.

C. Theoretical method.

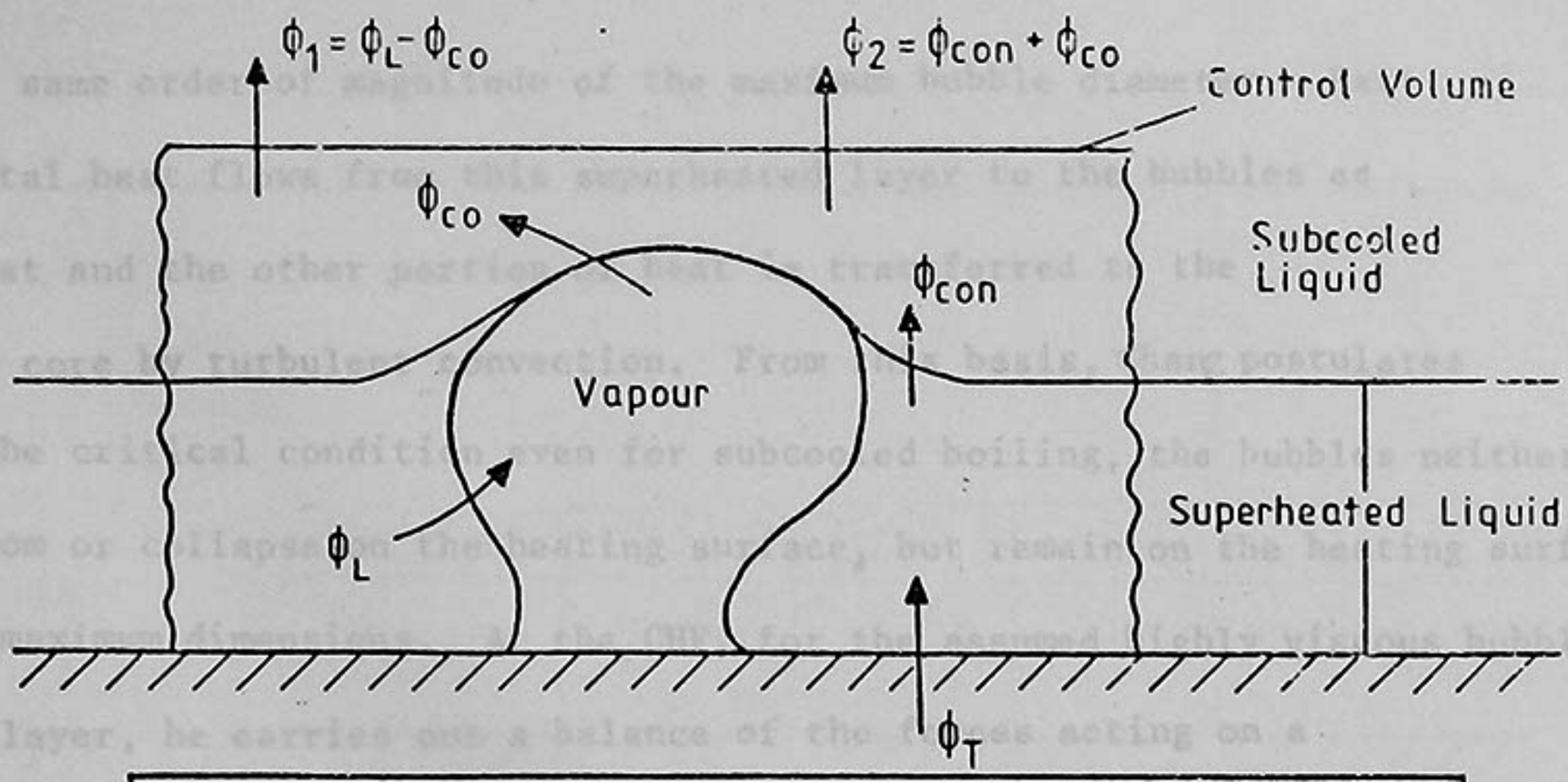
This, the best method of approach, involves the study of the mechanism of the CHF phenomenon. Starting from an idealized model, a series of assumptions, sometimes justifiable in terms of physical concepts or observed trends, are established and the difficult task of obtaining the theoretical solution of the problem is then carried out. In the ideal case, factors of an empirical nature should not be introduced or at least kept to a minimum, and both their origin and method of derivation should be clearly specified. Compared with the numerous empirical studies on CHF that have been reported, few models for the mechanism of the CHF have appeared in the literature and up to date, no general solution has been achieved.

In the following section, well known models proposed for the CHF mechanism in subcooled flow boiling (where nucleation is present), are briefly reviewed.

2. Models proposed for the mechanism of the CHF in subcooled flow boiling.

A. Chang's model

Chang [39] formulated a CHF model, illustrated in Figure 7(a), in which the total heat applied to the heating surface is transferred to a superheated liquid layer adjacent to the wall, whose thickness



$\phi_c = \phi_1 + \phi_2$

$\phi_c = C_1 \rho_V \lambda v_V^* + C_1 C_2 \rho_L \Delta H_{sub} v_L^*$

C_1, C_2 : constants

v_L^*, v_V^* : critical velocities of liquid and vapour, respectively.

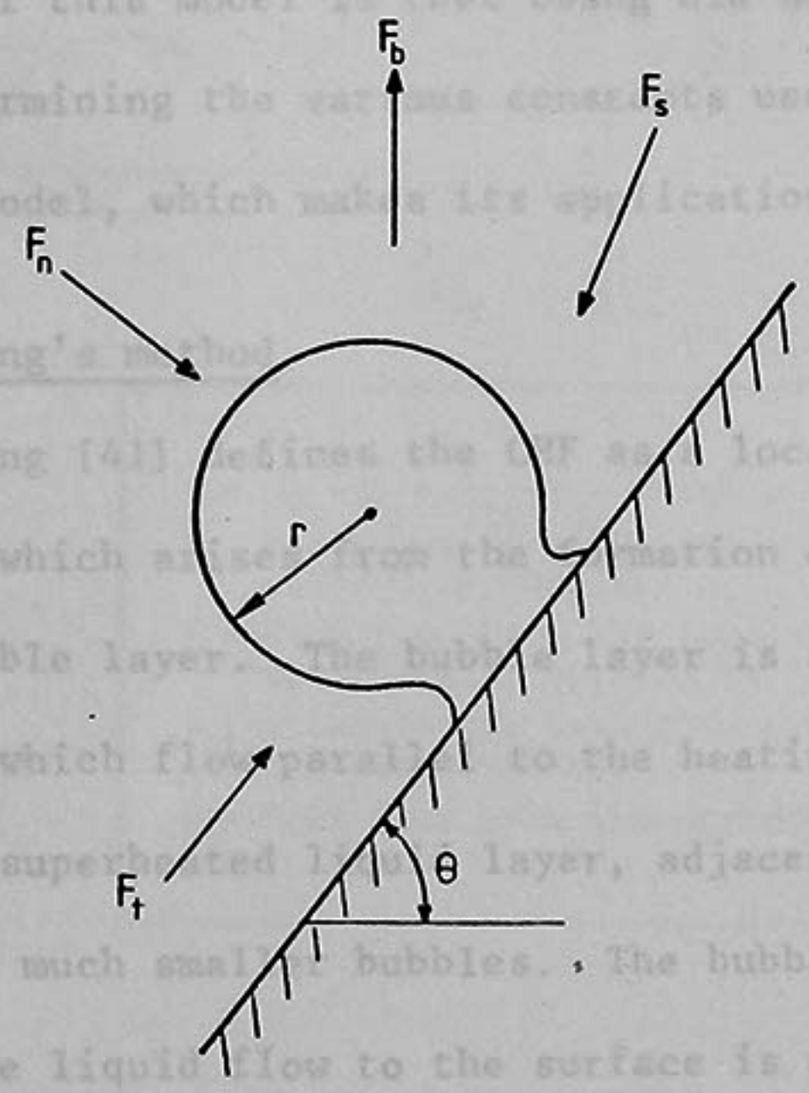
ϕ_T = total heat flux tranferred from the wall to the superheated liquid.

ϕ_L = heat flux transferred from the superheated liquid to the bubble by latent heat.

ϕ_{co} = heat flux transferred from the bubble to the subcooled liquid by condensation.

$\phi_{con} = \phi_T - \phi_L$ = heat tranferred from the superheated liquid to the subcooled liquid by convection.

(a) Heat flow from the heating surface to the liquid bulk.



$F_b = C_b r g (\rho_L - \rho_V)$

$F_s = C_s r \sigma$

$F_t = C_t r^2 \rho_L U^2$

$F_n = C_n r^2 \rho_L U^2$

U : relative velocity between the liquid and the bubble near the heating surface.

C_b, C_s, C_t, and C_n : constants.

F_b : buoyant force.

F_s : surface tension force.

F_t, F_n : components of the dynamic force.

(b) Equilibrium condition of a bubble.

Figure 7 Chang's model for CHF [39].

is of the same order of magnitude of the maximum bubble diameter. Part of the total heat flows from this superheated layer to the latent heat and the other portion of heat is transferred to the subcooled core by turbulent convection. From this basis, Chang postulates that at the critical condition even for subcooled boiling, the bubbles neither detach from or collapse on the heating surface, but remain on the heating surface at their maximum dimensions. At the CHF, for the assumed highly viscous bubble boundary layer, he carries out a balance of the forces acting on a bubble attached to the wall, Figure 7(b), and obtains a critical bubble velocity normal to the wall. This velocity is the most important variable appearing in the final expression for the CHF, which is assumed to be the sum of the latent heat transport contribution and the turbulent convective component.

Although Chang achieved an explicit mathematical expression for the CHF, it contains the vapour and liquid critical velocities and two major empirical constants whose origin is not clear. Several investigators [2, 4, 40] have correctly made the point that the main shortcoming of this model is that Chang did not provide a satisfactory method for determining the various constants used throughtout the development of his model, which makes its application impossible.

B. Tong's method

Tong [41] defines the CHF as a local overheating of the heating surface which arises from the formation of a hot patch under a bubble or a bubble layer. The bubble layer is assumed to be crowded with bubbles which flow parallel to the heating surface but separated from it by a superheated liquid layer, adjacent to the heating surface, which contains much smaller bubbles. The bubble layer develops to an extent where the liquid flow to the surface is prevented, giving rise to the critical condition. For this physical picture, depicted in Figure 8, Tong carried out an energy balance of the superheated liquid layer and

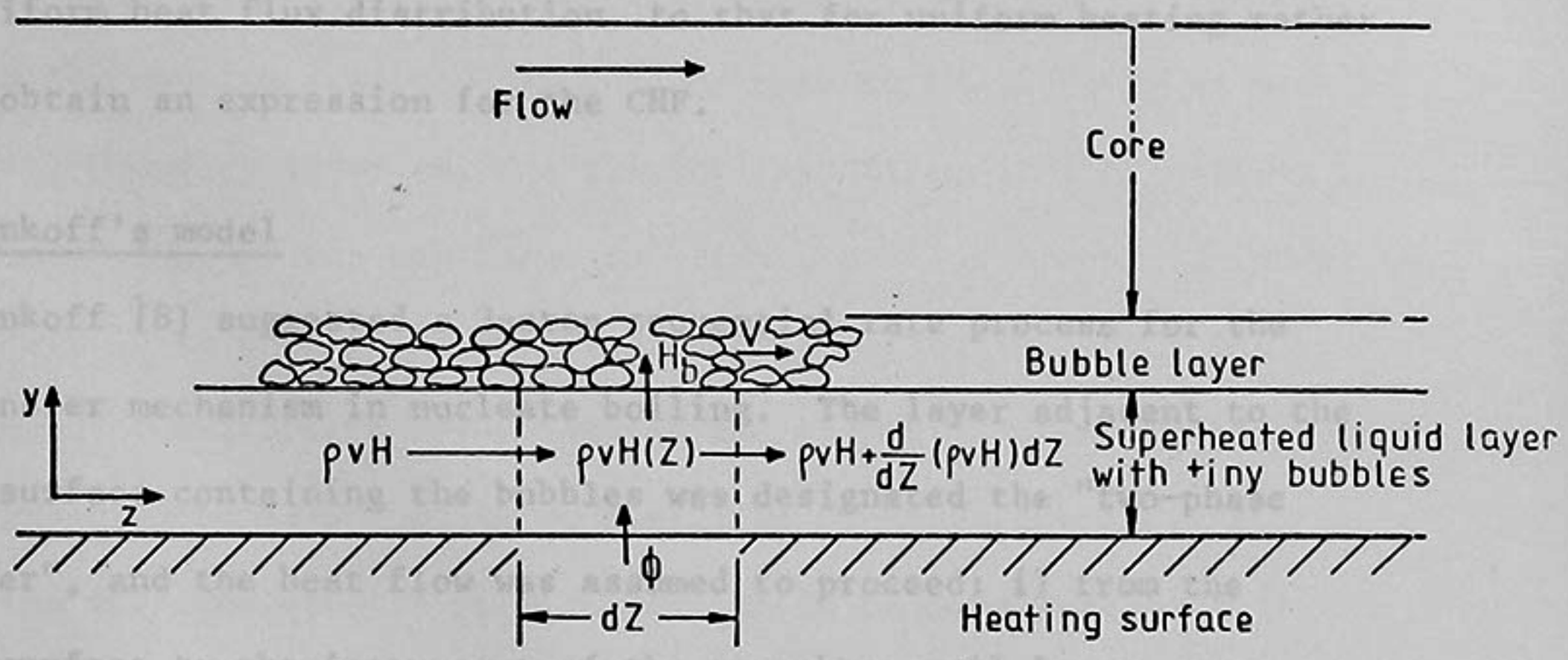
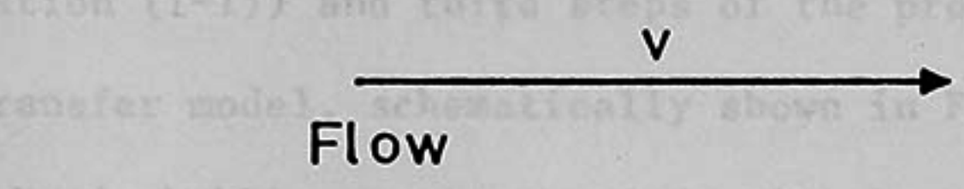
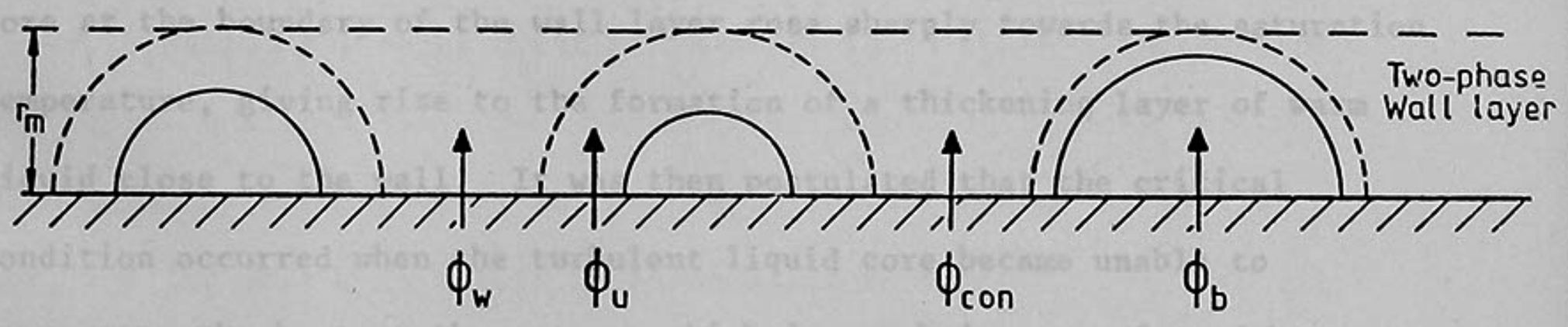


Figure 8 Tong's model for CHF [41].





$\phi_T = \phi_U + \phi_W = \phi_{CON} + \phi_b$ = Total heat flux.

ϕ_U = Heat flux from the fraction of surface periodically covered by bubbles.

ϕ_W = Heat flux from the portion of surface which is not periodically covered by bubbles.

ϕ_{CON} = Convective heat flux from the surface between bubbles at any instant.

ϕ_b = Heat flux from the surface beneath bubbles.

Figure 9 Bankoff's model for CHF [8].

then the analysis was directed to relate the CHF for the case of a non-uniform heat flux distribution to that for uniform heating rather than to obtain an expression for the CHF.

C. Bankoff's model

Bankoff [8] suggested a 3-step sequential rate process for the heat transfer mechanism in nucleate boiling. The layer adjacent to the heating surface containing the bubbles was designated the "two-phase wall layer", and the heat flow was assumed to proceed: i) from the heating surface to the inner part of the two-phase wall layer, ii) from the inner to the outer part of the two-phase wall layer, and iii) from the outer part of the wall layer to the singe-phase liquid core. Bankoff was able to obtain mathematical expressions for the first (Equation (1-1)) and third steps of the proposed nucleate boiling heat transfer model, schematically shown in Figure 9.

From Gunther's bubble parameters data [9], Bankoff observed that as the critical condition was approached, the temperature of the liquid core at the boundary of the wall layer rose sharply towards the saturation temperature, giving rise to the formation of a thickening layer of warm liquid close to the wall. It was then postulated that the critical condition occurred when the turbulent liquid core became unable to carry away the heat at the rate at which it was being transferred by the wall layer, causing an increase in bubble dimensions and population density, which in turn led to bubble coalescence. Nevertheless, an expression for the CHF was not proposed, and therefore this model still remains as purely hypothetical.

D. Kutateladze's model

Kutateladze and Leont'ev [42] carried out experiments in which boiling was simulated by injecting gas through a porous flat surface over which a liquid was forced to flow at high velocities. Visual observations led them to measure the velocity distribution across the

boundary layer and to obtain a critical gas injection rate, at which the "break away" of the forced-convection boundary layer was observed. From a rather complex analysis, an analogy between the break away process of the boundary layer and the critical condition in flow boiling was assumed. The CHF was considered to arise from flow stagnation under the boundary layer when it separates from the heating surface. The thickening of the boundary layer implies the isolation of a liquid layer which evaporates rapidly leading to a wall surface overheating. A correlation was developed to predict the CHF in flow boiling as the sum of the boundary layer separation heat flux and the CHF for pool boiling. The proposed correlation, containing a constant derived from the gas-injection experiments, was compared with a rather limited amount of data for alcohol and a reasonable agreement was observed.

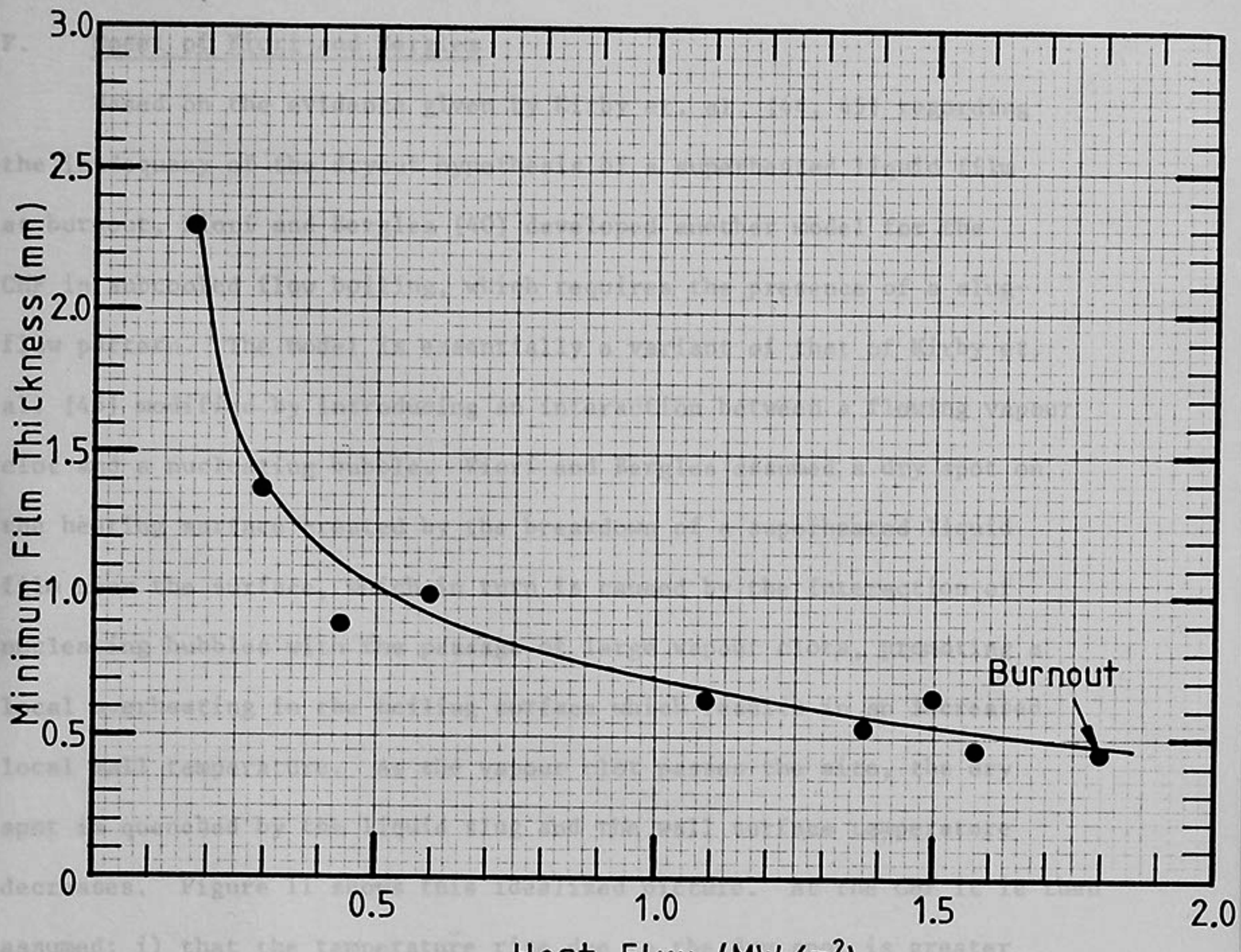
Subsequently, Tong [43] pointing out the inconsistency between the turbulent boundary layer and pool boiling concepts, re-formulated the hydrodynamic theory of the CHF employing only the boundary layer separation concept. A semi-empirical correlation for the CHF was developed, containing a major constant that was found to be a function of the vapour quality. The predicted critical heat fluxes were compared with data for water flowing in tubes at a pressure range of 69-138 bar, and for most data points a reasonable agreement was obtained (±25%). However, for subcooled orthoterphenyl, the correlation over-predicted the experimental data by up to 60%.

E. Kirby's (et. al.) model

The above four models for the CHF assume the presence of a bubble layer close to the heating surface and a turbulent liquid core. It is further postulated that at the critical condition, bubble crowding is such that the bubble layer prevents the inflow of liquid to the heating surface and burnout occurs as the result of the dryout of a superheated liquid film under the bubble blanket.

Based on earlier burnout tests for water at 1.72 bar conducted in the U.K. Atomic Energy Establishment at Winfrith, which had shown the existence of thin liquid films under large bubbles, Kirby et. al. [44] were able to test the liquid film dryout hypothesis by devising an experimental method for measuring the thickness of such film. They performed flow boiling experiments up to burnout for water at that particular pressure in a transparent channel of square cross-section where stainless steel tubes, used as test surface, were centrally placed. An electrical conductivity method was developed which enabled them by measuring the electrical conductance of the liquid film, to deduce its thickness. Their results for the liquid film thickness as a function of heat flux, reproduced in Figure 10, showed that at burnout the liquid film still existed, invalidating therefore, the proposed liquid film dryout hypothesis for the burnout mechanism. These results led them [45] to suggest a different mechanism for burnout, which postulates the formation of a dry patch underneath a growing bubble which arises from the evaporation of a very thin liquid film under the bubble (the microlayer). The heater temperature in the dry area rises sharply, being rewetted after bubble departure or collapse. At burnout, the dry patch rapidly stabilizes reaching the Leidenfrost temperature at which rewetting is prevented causing the dry patch to spread radially resulting in the physical destruction of the test surface.

Despite the fact that an explicit expression for the CHF using this model has not yet been achieved and that evidence of the existence of a dry patch under a nucleating bubble has been given only for boiling experiments conducted on glass surfaces coated with thin electrically conductive substances [20,46,47] but not for commonly used metallic surfaces, this model stands as a most promising candidate for the mechanism of the CHF.



Water / Stainless Steel

Geometry: Tubular heaters centrally placed in a channel of square cross section (25.4 mm x 25.4 mm)

Vertical upflow

Tube dimensions:

D_{in} = 7.37 mm

δ = 0.53 mm

L_H = 142 mm

P = 1.72 bar

G = 1356 Kg / m^2 sec

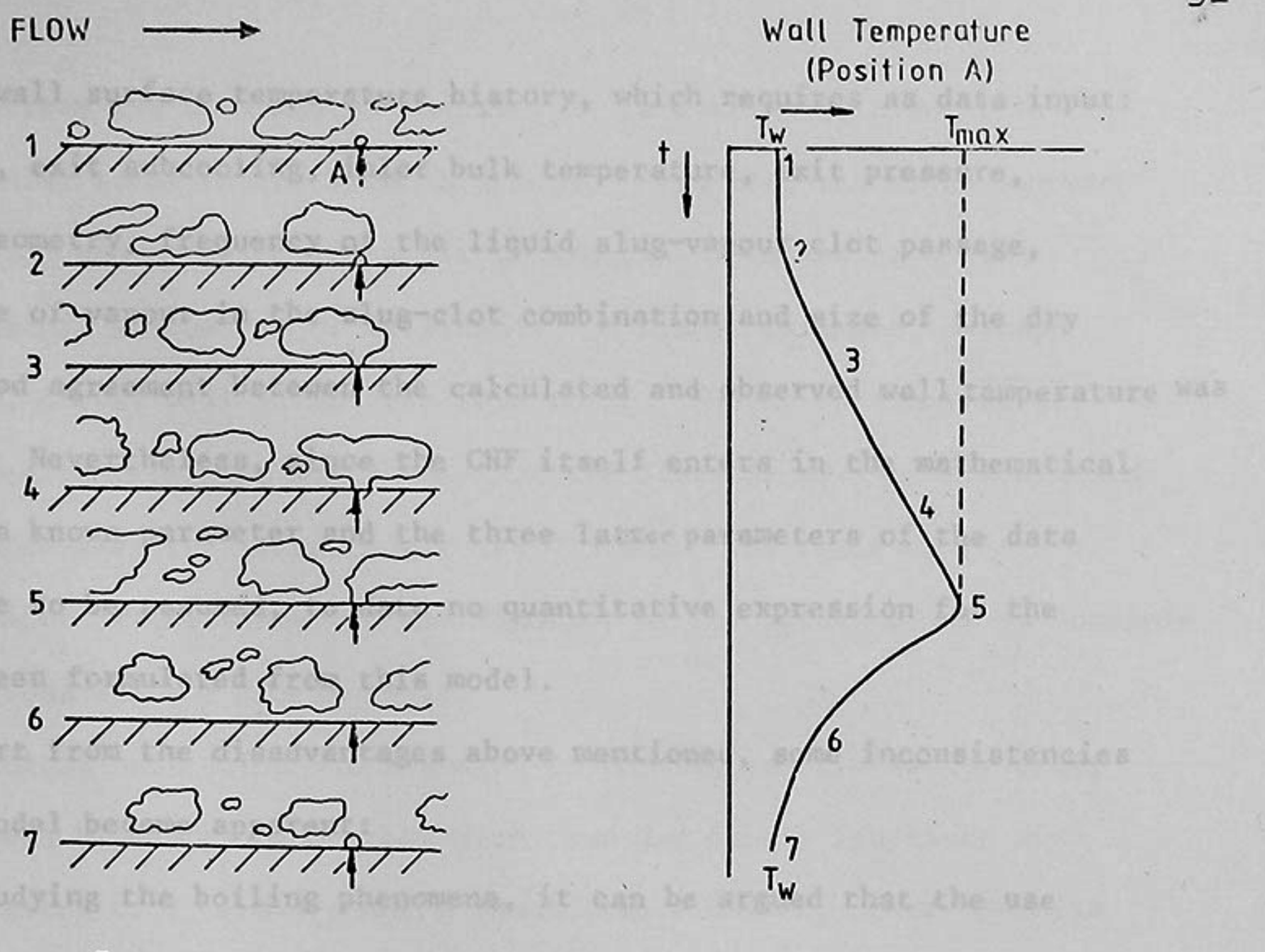
$\Delta T_{sub_{in}}$ = 6.11 °K

Figure 10 Liquid film thickness under a bubble layer as a function of heat flux [44].

F. Model of Fiori and Bergles

Based on the evidence given by Kirby et. al. [44, 45] regarding the inadequacy of the dryout hypothesis of a superheated liquid film at burnout, Fiori and Bergles [40] developed another model for the CHF in subcooled flow boiling, which requires the presence of a slug-flow pattern. The model is essentially a variant of that of Kirby et. al. [45] modified by introducing an interaction between a flowing vapour clot and a nucleating bubble. Fiori and Bergles assumed a dry spot on the heating surface created by the breakdown of a superheated liquid film near the surface, which in turn is caused by the interaction of nucleating bubbles with the passage of large vapour clots, promoting a local overheating in the boiling surface which results in an increased local wall temperature. As the vapour clot passes the site, the dry spot is quenched by the liquid slug and the wall surface temperature decreases. Figure 11 shows this idealized picture. At the CHF it is then assumed: i) that the temperature rise due to the dry spot is greater than the temperature drop during quenching, and ii) that this sequence of events is repeated until the band of Leidenfrost temperatures is reached, the point at which the quenching is prevented and the physical destruction of the heating surface occurs.

Simultaneous measurement of surface wall temperature and cine-photographic films at burnout, showed both the flow pattern corresponding to slug-flow and the proposed type of surface temperature increase, as illustrated in Figure 12 (redrawn from reference [40]). In these experiments an annular channel, consisted of a glass outer tube with a heated stainless steel central tube, was used. In order to measure the surface temperature a hole was drilled near the downstream end of the stainless steel tube to accommodate a thermocouple which lay flush with the boiling surface. The appearance of "small" pinholes (no size was given) in the destroyed test sections was taken as further evidence to support the highly localized burnouts implied in the model. A computer program was developed to pre-



$T_{max} - T_w = \Delta T_{rise} = \Delta T_{quench}$ (Below Burnout)

$\Delta T_{rise} > \Delta T_{quench}$ at Burnout

Figure 11 Model of Fiori and Bergles for CHF [40].

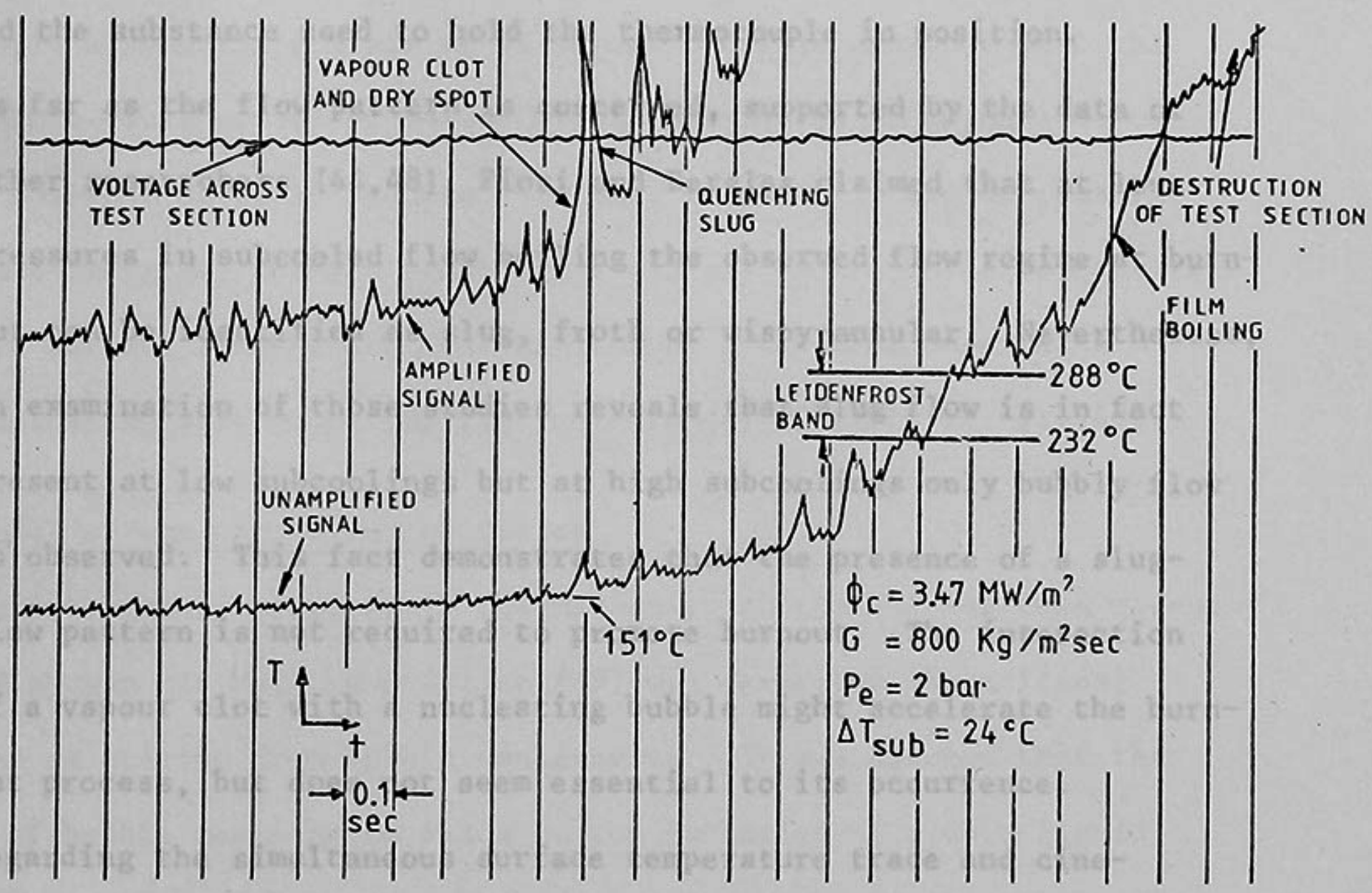


Figure 12 Surface temperature trace at CHF in slug flow [40].

dict the wall surface temperature history, which requires as data input: heat flux, exit subcooling, inlet bulk temperature, exit pressure, channel geometry, frequency of the liquid slug-vapour clot passage, percentage of vapour in the slug-clot combination and size of the dry spot. Good agreement betewen the calculated and observed wall temperature was obtained. Nevertheless, since the CHF itself enters in the mathematical model as a known parameter and the three latter parameters of the data input have to be assumed, to date no quantitative expression for the CHF has been formulated from this model.

Apart from the disadvantages above mentioned, some inconsistencies in this model become apparent:

i) In studying the boiling phenomena, it can be argued that the use of thermocouples lying flush with the boiling surface (perhaps requiring some polishing), can alter the surface characteristics and peturb the flow of heat in the vicinity due to the different thermo-properties of the heating surface material and both the thermocouple and the substance used to hold the thermocouple in position.

ii) As far as the flow pattern is concerned, supported by the data of other researchers [44,48], Fiori and Bergles claimed that at low pressures in subcooled flow boiling the observed flow regime at burn-out can be identified as slug, froth or wispy-annular. Nevertheless, an examination of those studies reveals that slug flow is in fact present at low subcoolings but at high subcoolings only bubbly flow is observed. This fact demonstrates that the presence of a slug-flow pattern is not required to promote burnout. The interaction of a vapour clot with a nucleating bubble might accelerate the burn-out process, but does not seem essential to its occurrence.

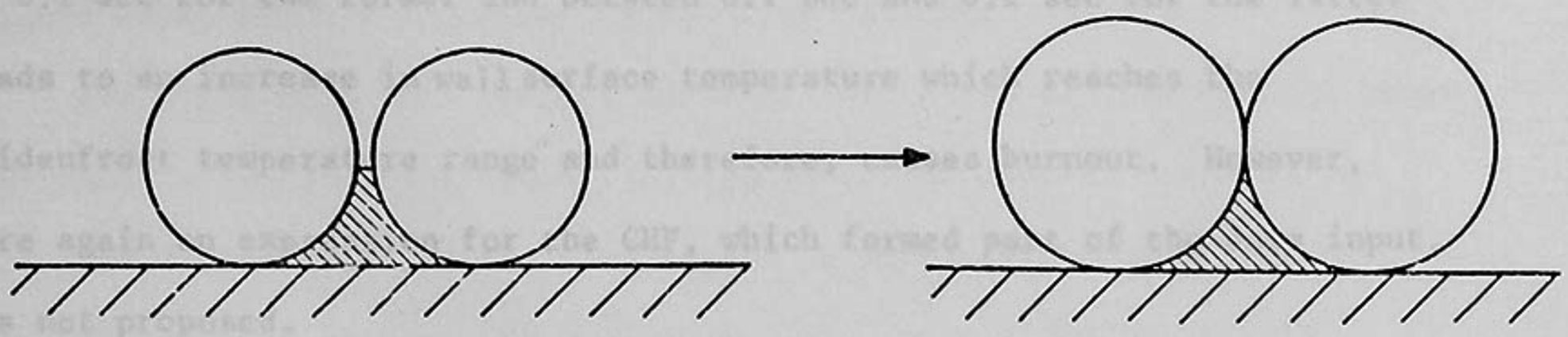
iii) Regarding the simultaneous surface temperature trace and cine-photographic film at burnout, it can be pointed out that it was extremely fortunate that burnout occurred in the precise location under observation. Although burnout generally occurs along the

downstream end of a heated surface, it is difficult to see how the axial location was known a priori. Even with the axial burnout location known, selecting a circumferential location of a tube represents another major difficulty. A simple estimate, perhaps the simplest, will illustrate this point. The outer diameter of the heated tube used was 7.04mm and the diameter of the hole drilled to accommodate the thermocouple was 0.343mm. The ratio of the perimeter of the former to the diameter of the latter gives 64 possible locations for the thermocouple.

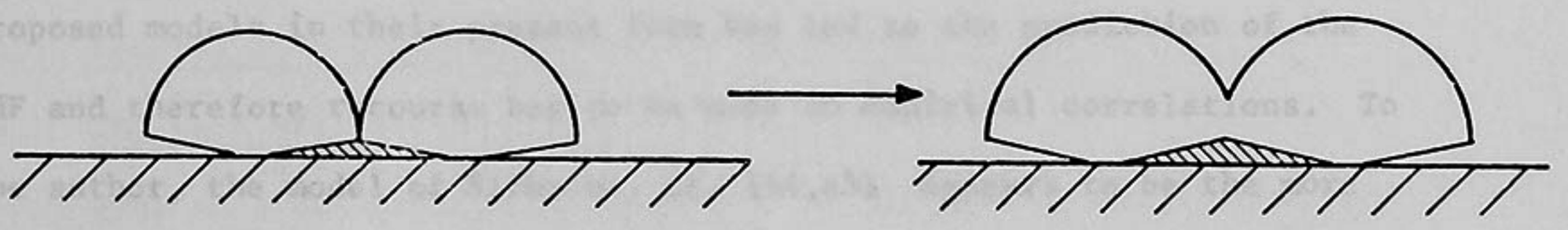
iv) As violent nucleation was reported to persist under a vapour clot, it seems highly probable that more than one bubble interacts with the vapour clot, and perhaps a considerable number, since the size of the clots was much greater than that of individual bubbles. As it is observed that the cyclic overheating occurs over the same surface location, for burnout to occur a sequence of vapour clots interacting with the same bubble would be required. This would imply a synchronized series of vapour clots in sequence with the bubble cycle period of an individual bubble, which appears to be a somewhat unlikely process. In this respect, it may be possible that the given surface temperature history corresponded in fact to the surface temperature fluctuations of a dry area underneath a nucleating bubble, as implied in the model of Kirby et. al.[45].

G. Model of van der Molen and Galjee

An interesting approach to the mechanism of the CHF has been recently proposed by van der Molen and Galjee [49] who described the critical condition as arising from bubble coalescence. It was assumed that the process of bubble coalescence leads to the isolation of a thin liquid layer, Figure 13, which at the CHF evaporates rapidly giving rise to a dry area, and a sharp increase in wall surface temperature. A heat conduction equation was solved for both the case of a vapour clot passage



(a) Spherical bubbles



(b) Hemispherical bubbles

Figure 13 Isolation of liquid by bubble coalescence [49].

(slug flow assumed) and a bubble layer (bubbly flow) isolating the surface from the liquid bulk. The results showed that a residence time of 0.1 sec for the former and between 0.1 sec and 0.2 sec for the latter leads to an increase in wall surface temperature which reaches the Leidenfrost temperature range and therefore, causes burnout. However, here again an expression for the CHF, which formed part of the data input, was not proposed.

H. Concluding remarks on the proposed models for the CHF mechanism

Despite the fact that important advances have been made in understanding the basic nature of the CHF in subcooled flow boiling and several ways of promoting dramatic changes in surface temperature leading to burnout have been theoretically formulated, the physical mechanism originating burnout still remains unknown. To date, none of the proposed models in their present form has led to the prediction of the CHF and therefore recourse has to be made to empirical correlations. To the author, the model of Kirby et. al. [44,45] appears to be the more consistent with available information. Nevertheless, its verifications will be only possible when new and more appropriate experimental techniques are devised for the microscopic study of the processes taking place during boiling in the proximity of the heating surface.

3. Flow regimes and their relationship with the CHF

Most theoretical approaches to the definition of the mechanism of subcooled CHF describe the burnout process in terms of a specific flow regime. Nevertheless, there is no evidence to suggest such a relationship and the assumption of one has proved fruitless. While it seems reasonable to assume firstly, that the flow of heat proceeds differently for different portions of a heating surface, depending on whether there is bubble formation or not, and secondly that the heat transfer path from the wall to the flowing liquid may vary according to the flow pattern, burnout is a phenomenon occurring on the heating surface and

therefore, it must be described in terms of conditions prevailing close to the heating surface and not in terms of conditions operating in the liquid bulk, which are defined by the flow pattern.

The hypothesis that the mechanism of initiation of flow boiling burnout under subcooled conditions (perhaps up to low quality regions) is the same irrespective of the flow regime is supported by the fact that the relationship between CHF and subcooling, (or alternatively exit quality) does not show any abrupt change, and burnout data lie well over a single line (see Figure 14), although the flow pattern from high to low subcooling can vary considerably. As nucleation has been observed to persist underneath large vapour masses in slug slow pattern [40], a Kirby-type of model for the mechanism of the CHF would be applicable to the entire subcooled region.

4. General trends in the parameters affecting the CHF.

A. The main parameters effect

From numerous experimental studies, it has been generally observed that for a liquid flowing under stable conditions in a uniformly heated section, the CHF is a function of five primary parameters:

$$\emptyset_c = f_n(\Delta T_{sub_{in}}, G, P, D, L_H) \qquad (1\text{-}18)$$

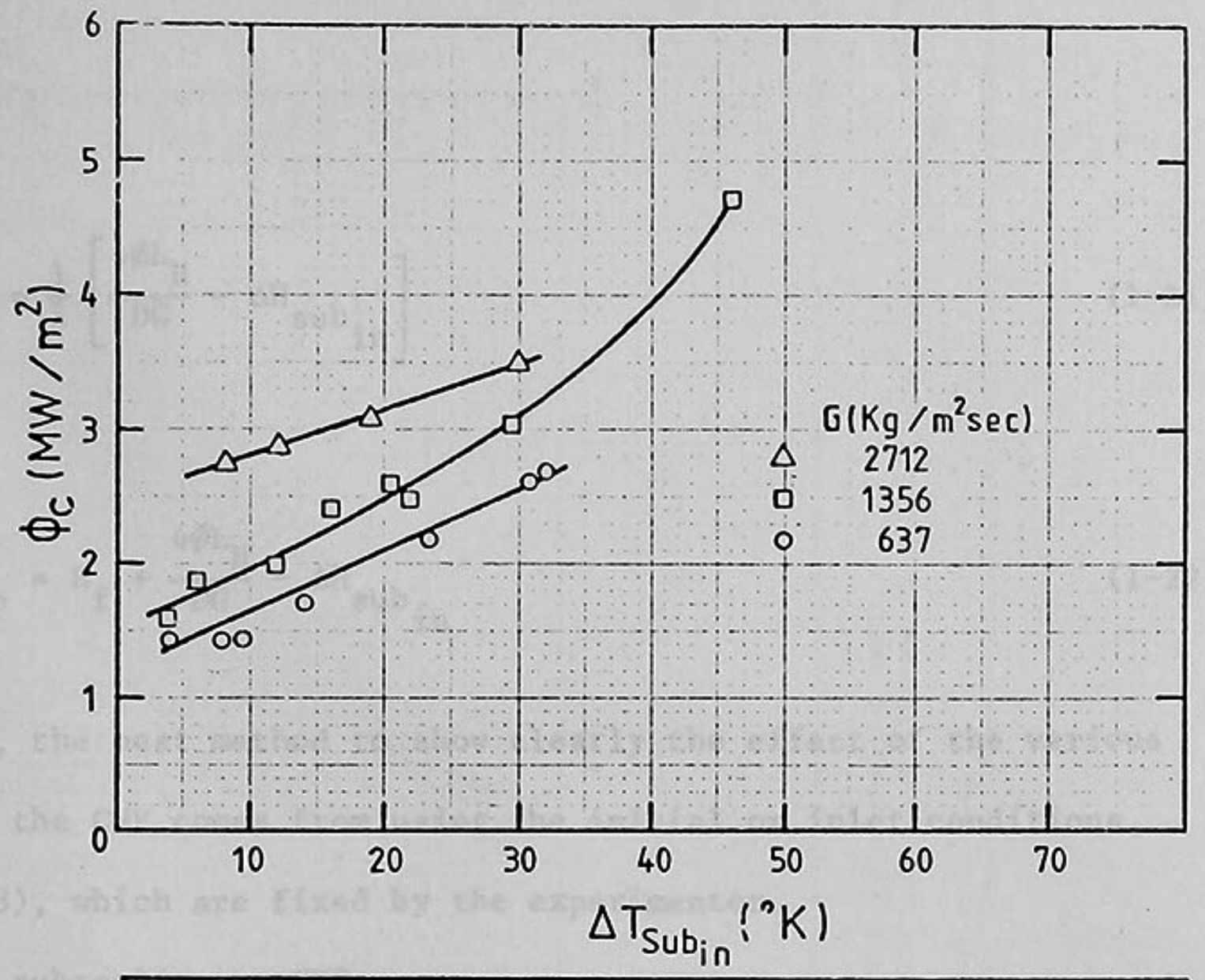
Possible alternatives to equation (1-18) have arisen from the practice of correlating the CHF in terms of parameters characterizing conditions at the burnout location or at the channel exit. For example Equation (1-18) can be written as

$$\emptyset_c = f_n(x_e, G, P, D, L_H) \qquad (1\text{-}19)$$

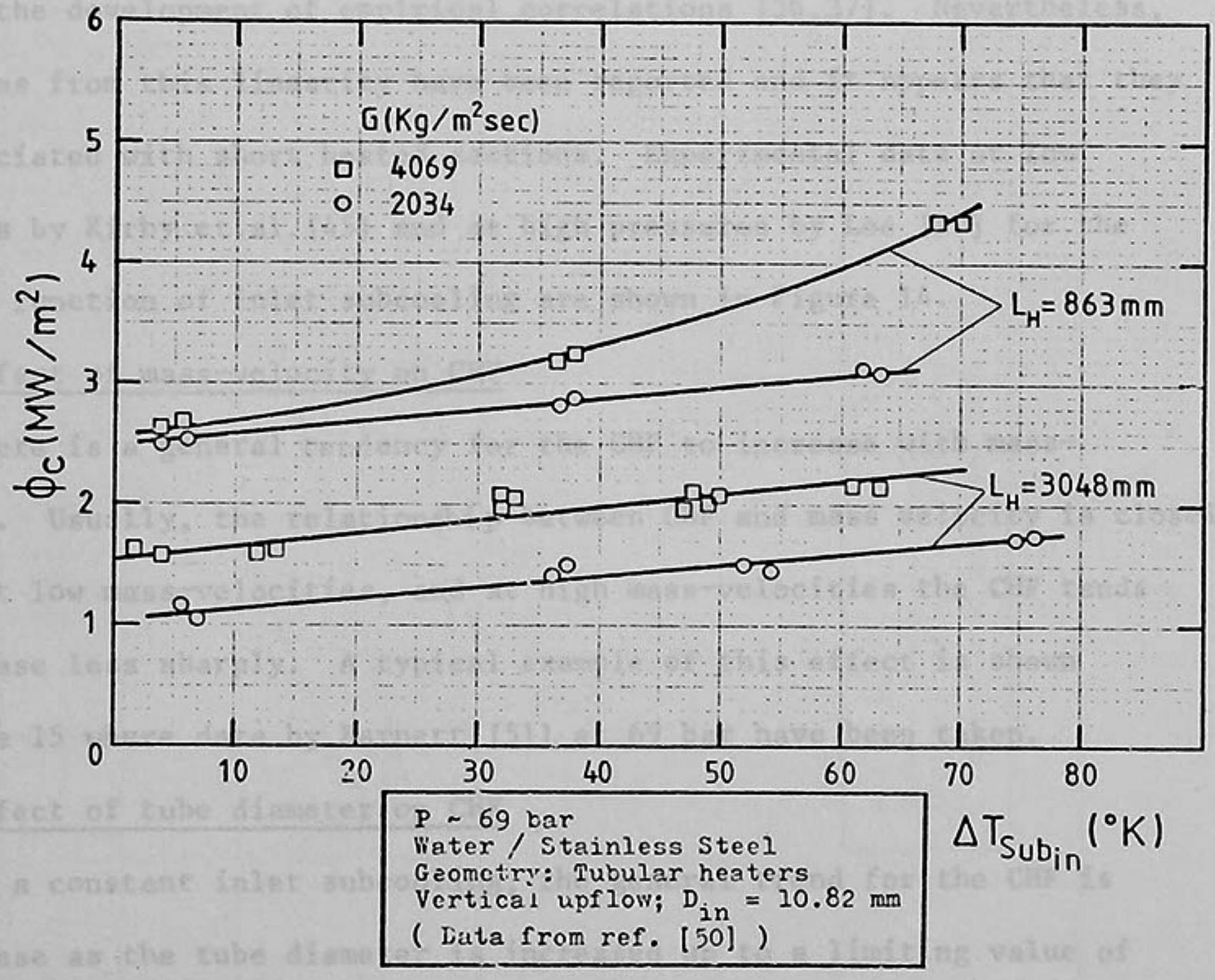
or

$$\emptyset_c = f_n(H_e, G, P, D, L_H) \qquad (1\text{-}20)$$

where both the thermodynamic mass-quality and the fluid enthalpy at the exit of a heated tube can be computed by using the heat balance expression.



(a) Low pressure



(b) High pressure

Figure 14 The effect of inlet subcooling on CHF.

Hence,

$$X_e = \frac{1}{\lambda}\left[\frac{4\emptyset L_H}{DG} - \Delta H_{sub_{in}}\right] \qquad (1\text{-}21)$$

and

$$H_e = H_f + \frac{4\emptyset L_H}{DG} - \Delta H_{sub_{in}} \qquad (1\text{-}22)$$

However, the best method to show clearly the effect of the various parameters on the CHF comes from using the initial or inlet conditions, Equation (1-18), which are fixed by the experimenter.

a) Effect of subcooling on CHF

A plot of CHF against inlet subcooling, keeping the other parameters constant, has proved to be the best representation of CHF data [31]. It has been generally agreed that the CHF increases with increasing subcooling. The usual linear relationship has been repeatedly used in the development of empirical correlations [36,37]. Nevertheless, deviations from this linearity have been reported and it appears that they are associated with short heated sections. Experimental data at low pressures by Kirby et.al.[45] and at high pressures by Lee [50] for the CHF as a function of inlet subcooling are shown in Figure 14.

b) Effect of mass-velocity on CHF

There is a general tendency for the CHF to increase with mass-velocity. Usually, the relationship between CHF and mass velocity is closely linear at low mass-velocities, and at high mass-velocities the CHF tends to increase less sharply. A typical example of this effect is shown in Figure 15 where data by Barnett [51] at 69 bar have been taken.

c) Effect of tube diameter on CHF

At a constant inlet subcooling, the general trend for the CHF is to increase as the tube diameter is increased up to a limiting value of diameter beyond which such effect becomes insignificant. This effect is shown

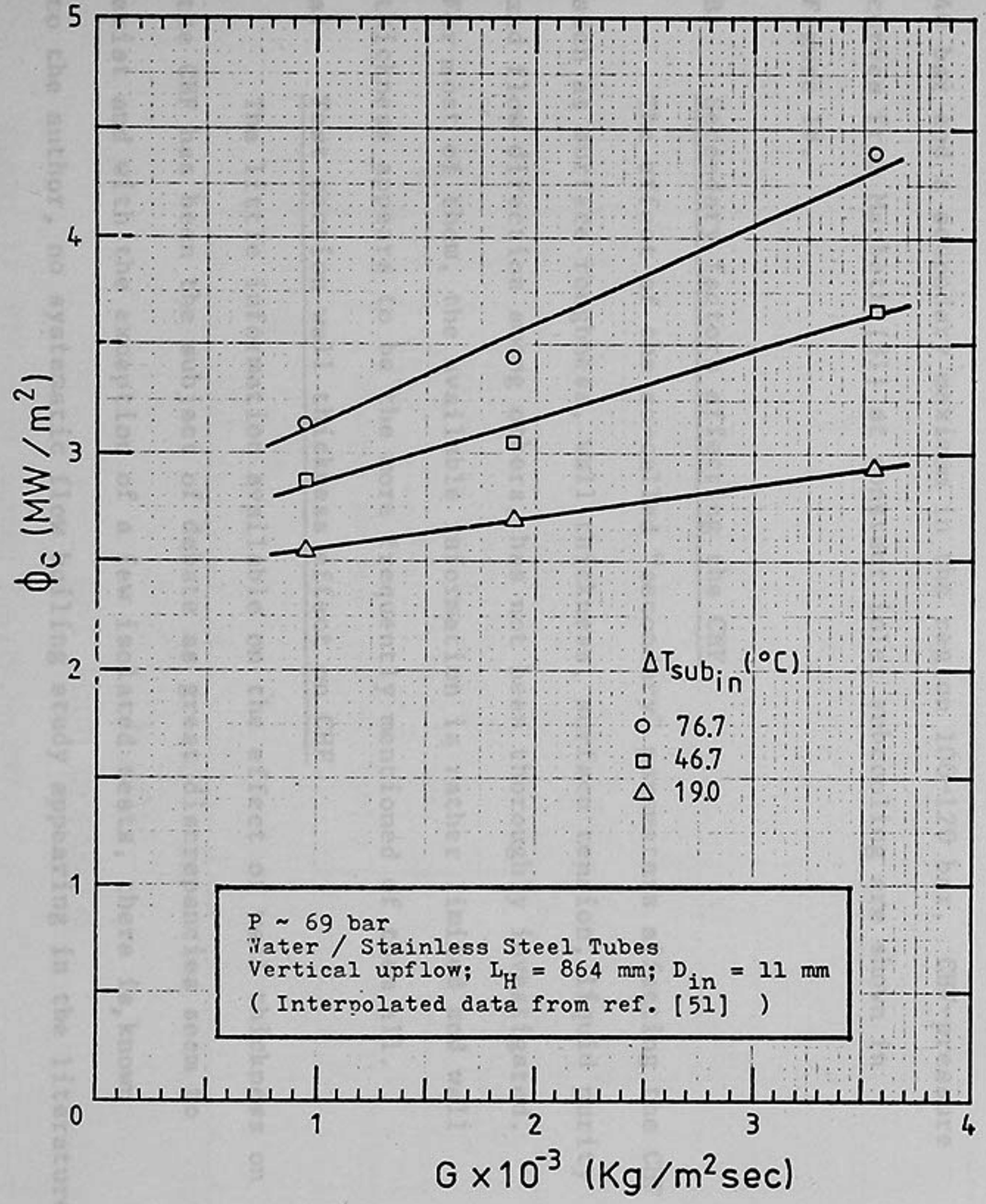
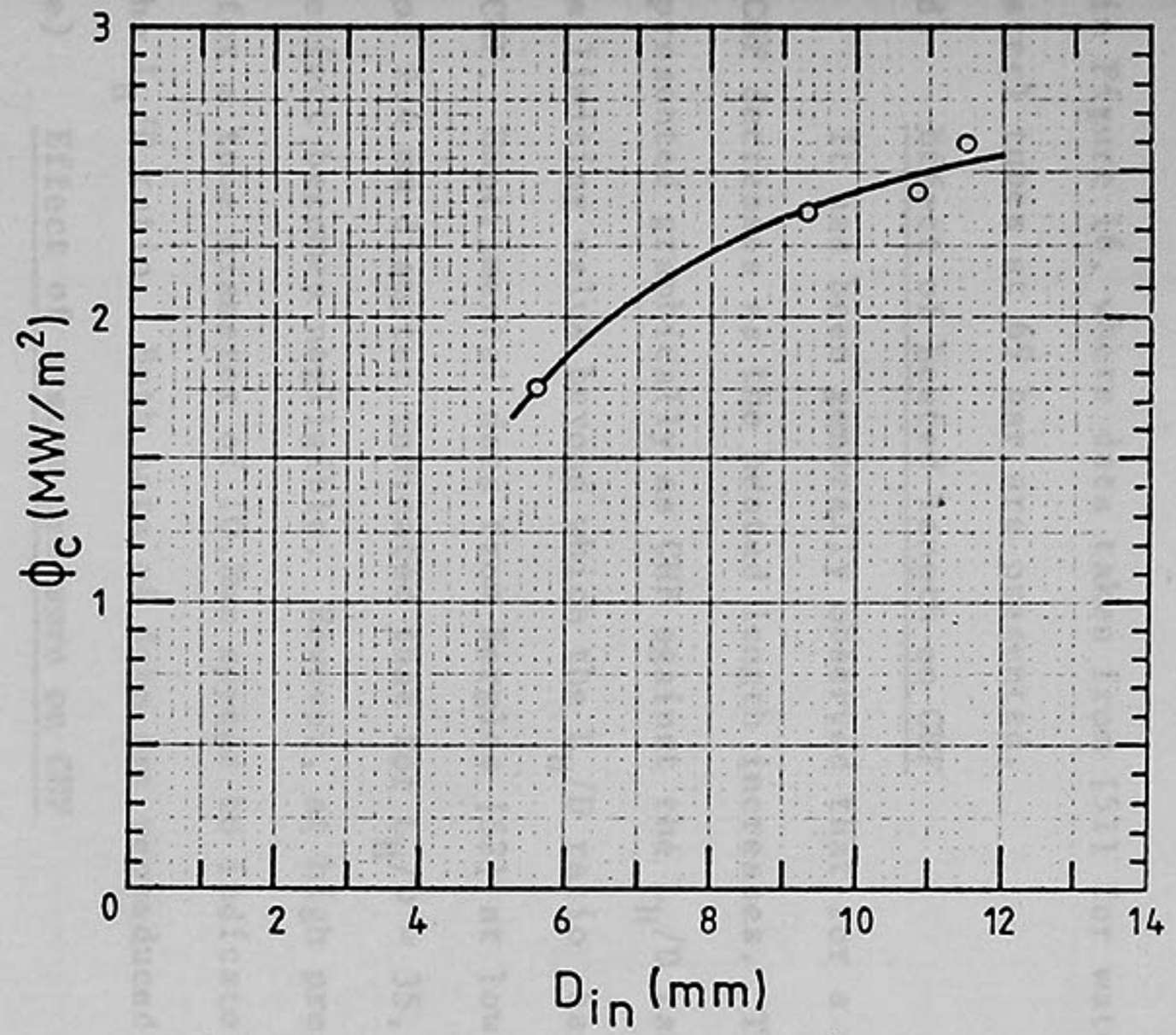


Figure 15 Effect of mass-velocity on CHF.



P ~ 69 bar
Water / Stainless Steel Tubes
Vertical upflow; I_H = 1359 mm; G = 1017 Kg/m^2 sec; $\Delta T_{sub_{in}}$ = 76.7 °K
(Data from ref. [51])

Figure 16 Effect of tube diameter on CHF.

in Figure 16, where data taken from [51] for water flowing in stainless steel tubes at 69 bar are presented.

d) Effect of heated length on CHF

It has been generally observed that for a given tube diameter, the CHF decreases as the heated length increases. This effect is usually presented graphically as CHF against the L_H/D ratio. There appears to be a limiting value beyond which the L_H/D ratio has little or no effect on CHF. Experimental data from Bergles [52] at low pressures with a tube of 2.4 mm diameter indicated that for $L_H/D = 35$, the heated length effect becomes negligible. However, at high pressures, the data from Lee [50] for a tube diameter of 10.8mm appear to indicate a much greater limiting value of the L_H/D ratio. Both sets of data are reproduced in Figure 17.

e) Effect of system pressure on CHF

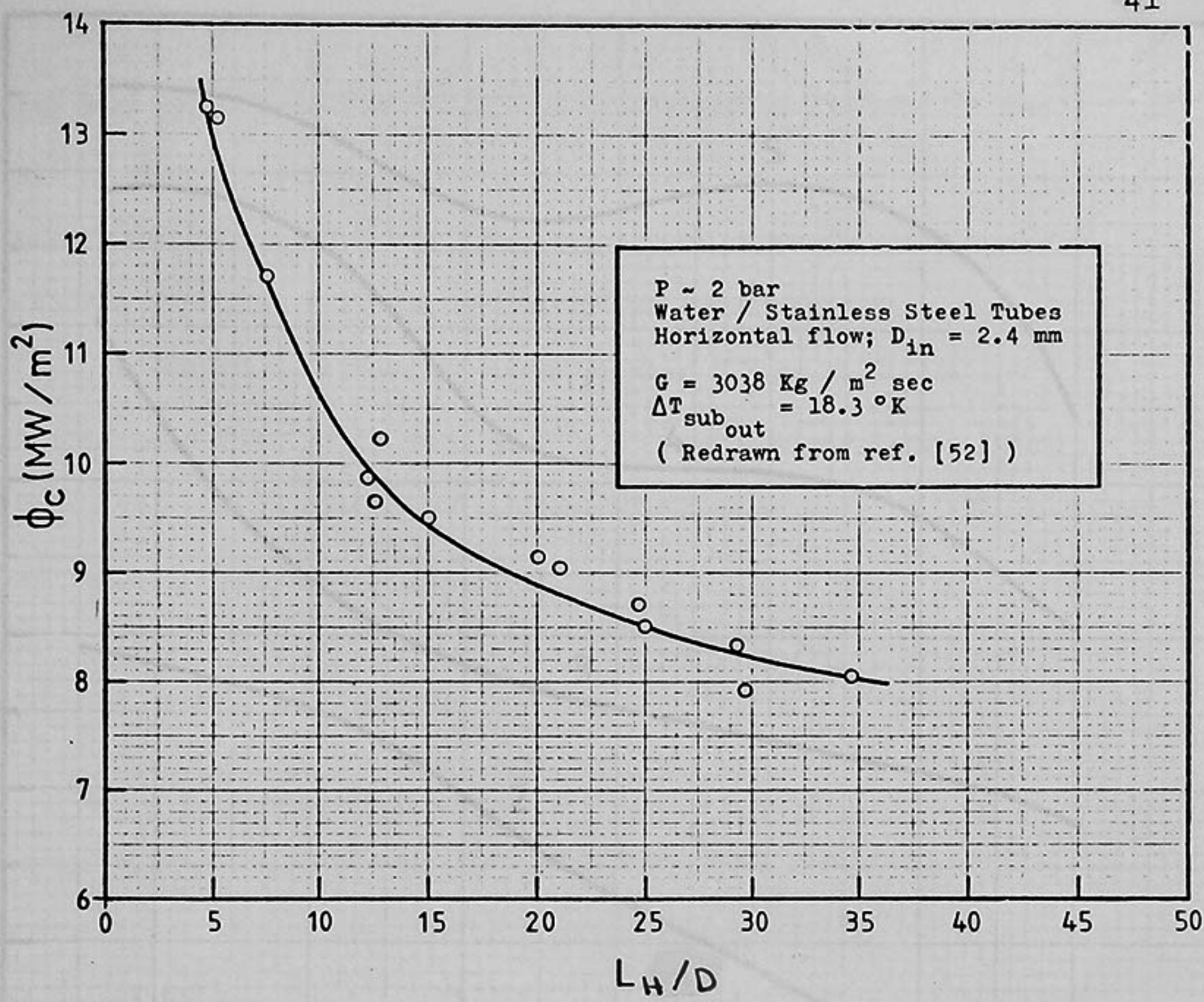
The effect of pressure on the CHF is much more complex. Most experimental observations seem to indicate an increase in CHF as the system pressure increases at low pressure, reaching a first maximum around 40 bar and a secondary maximum in the region 100-120 bar. CHF-pressure curves from Macbeth [31] at constant inlet subcooling are shown in Figure 18.

B. Secondary factors affecting the CHF

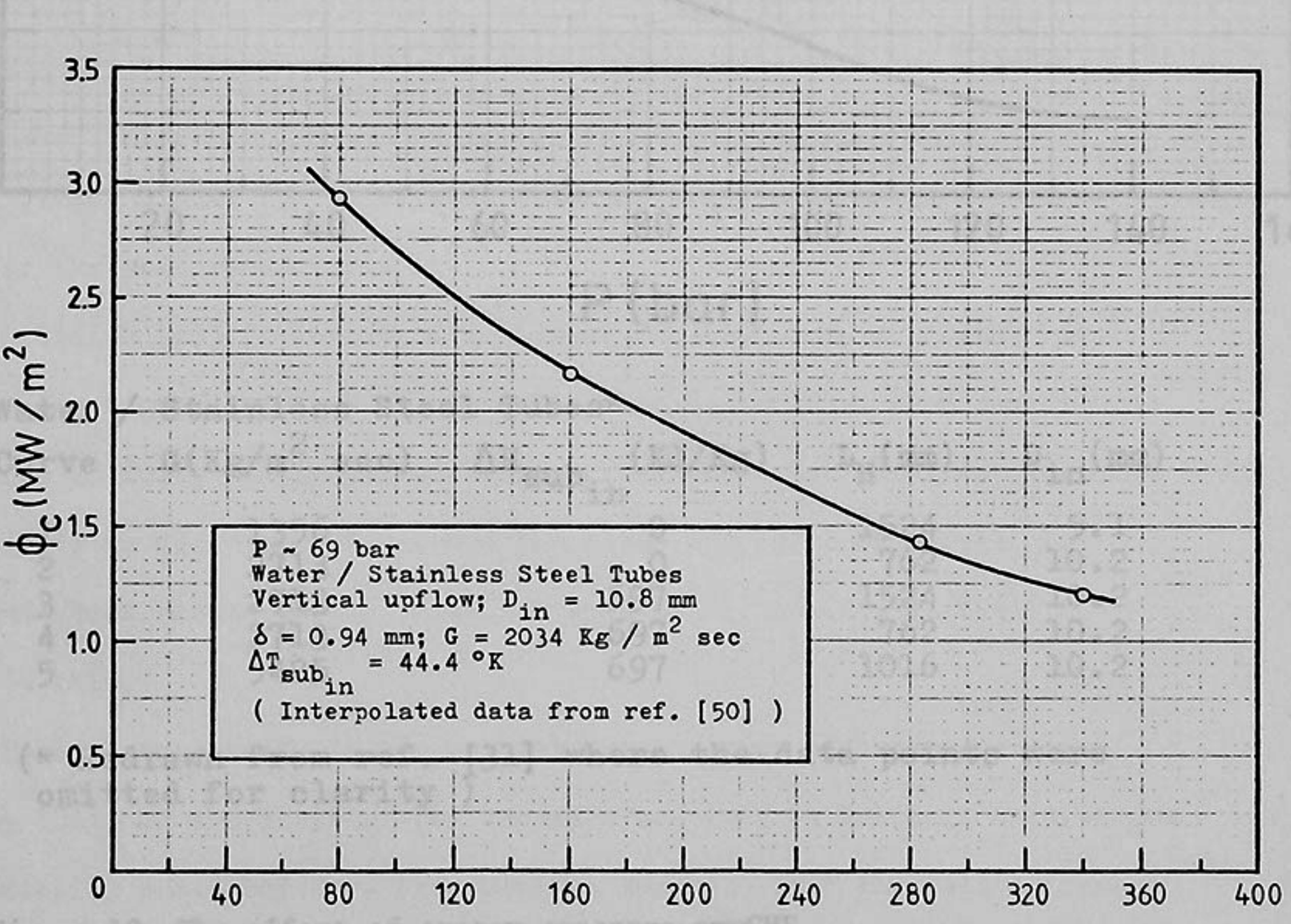
The effect of the so-called "secondary" parameters affecting the CHF such as surface roughness, wall thickness, surface tension, liquid purity and flow direction among others, has not been thoroughly investigated. For most of them, the available information is rather limited and wall thickness appears to be the more frequently mentioned of them all.

a) Test section wall thickness effect on CHF

The little information available on the effect of wall thickness on the CHF has been the subject of debate as great discrepancies seem to exist and with the exception of a few isolated tests, there is, known to the author, no systematic flow boiling study appearing in the literature

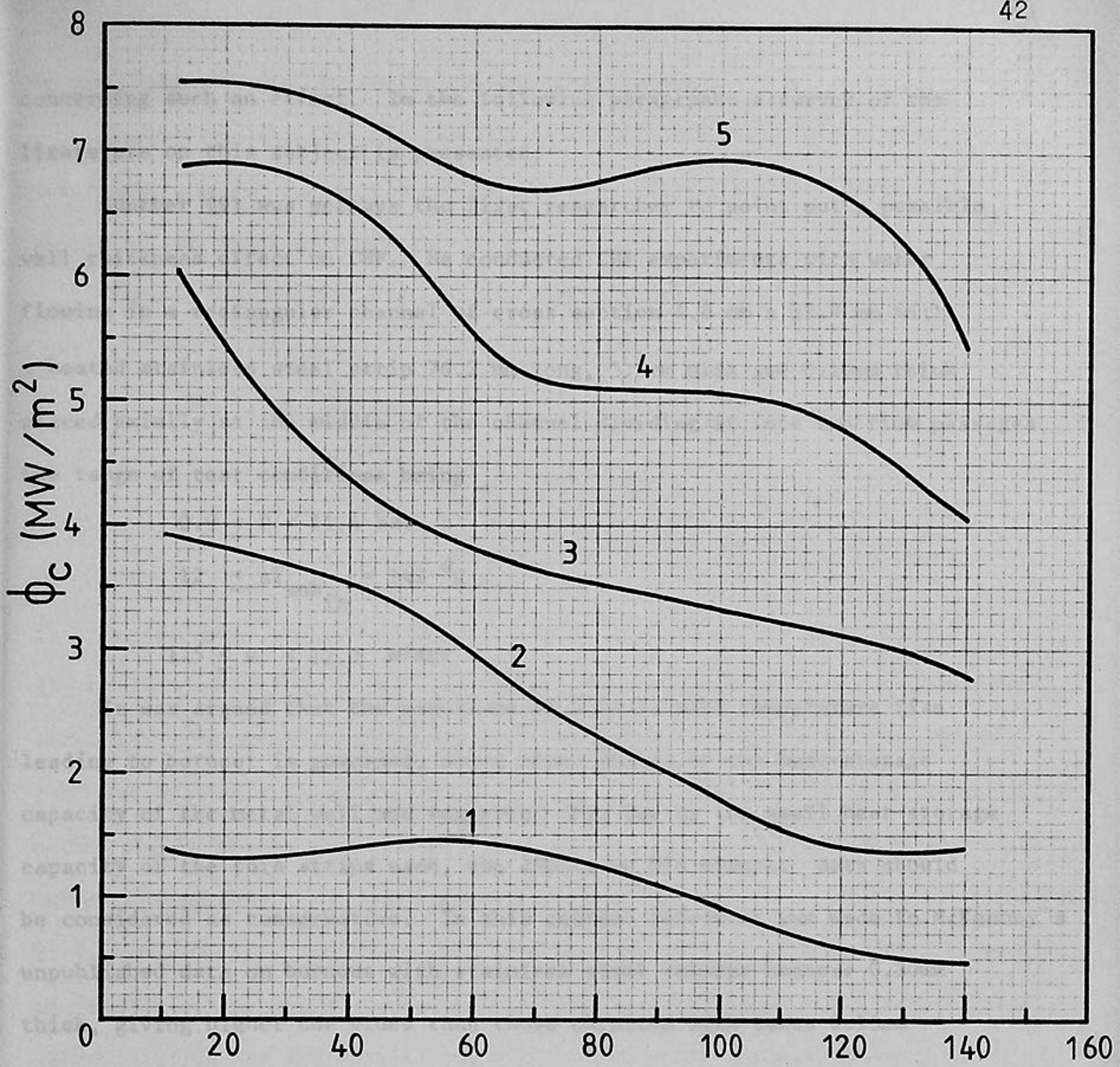


(a) Low pressure



(b) High pressure

Figure 17 Effect of heated length on CHF.



Water / Stainless Steel Tubes*

Curve	G(Kg/m^2 sec)	$\Delta H_{sub_{in}}$ (KJ/Kg)	L_H(mm)	D_{in}(mm)
1	1356	0	1524	5.1
2	2713	0	762	10.2
3	2713	697	1524	10.2
4	2713	697	762	10.2
5	5425	697	1016	10.2

(* Redrawn from ref. [31] where the data points were omitted for clarity)

Figure 18 The effect of system pressure on CHF.

concerning such an effect. In the following paragrpahs a survey of the literature on this subject is presented.

Gunther [9] was perhaps the first researcher to point out a possible wall thickness effect on CHF. He conducted CHF experiments with water flowing in a rectangular channel of cross section 4.8 mm x 12.7 mm with a heated stainless steel strip 76.2 mm long, 3.2mm wide and 0.10mm thick placed axially at the middle of the channel dividing it into two flow passages, the range of test conditions being

$$0.9 \leq P \leq 11.4 \text{ bar}$$

$$12 \leq \Delta T_{sub_{in}} \leq 142 \ ^{o}K$$

$$1.5 \leq v \leq 12.2 \text{ m/sec}$$

It was argued that the magnitude of a local wall temperature rise leading to burnout is governed, among other things,by the heat-storage capacity of the metal wall and suggested that due to the small heat-storage capacity of the thin strips used, the limits on his burnout data should be considered as conservative. In this context reference was made to McKenney's unpublished data on burnout with stainless steel tubular heaters 0.30mm thick, giving higher CHF vlues than those obtained with tubes 0.13mm thick at the same conditions.

Griffith [53] in correlating burnout data for both pool and flow boiling for a great variety of geometries and conditions, when assessing the range validity of his correlation, pointed out that thin test surfaces were likely to decrease CHF because the capability of a metal wall to dissipate heat excess when a local hot spot is formed is limited if the strip is thin.

Macbeth concluded, in his comprehensive review of burnout in flow boiling [31], on the basis of the accuracy achieved by burnout correlations in predicting published data from various sources, that the wall thickness effect (excluded from all correlations) must be small.

Experimental determinations regarding wall thickness effect on

CHF have been reported by the following investigators:

Aladyev et. al. [54], tested two tubes with different wall thickness, 0.4mm and 2mm and report having found no effect on CHF. However, details of the tests were not given.

Tippets [55] carried out CHF tests with water at 69 bar flowing in a vertical heated rectangular channel within the range of conditions:

$146 \leq G \leq 1950$ Kg/m^{2}sec

L_H = 940mm

Channel width = 53mm

Channel spacing = 6.35mm or 12.7mm, and stainless steel strips of thickness 0.15mm and 0.25mm

An average decrease of 20% for the thinner strip was reported and the observed differences in CHF values between the two different thicknesses under the same operational conditions were attributed to "local thin spots" produced by silver-soldering, by the 60 cycles/sec alternating current heating method and by damage to the strips produced by overheating during previous CHF determinations, all these causes affecting the thicker heater to lesser extent. It was subsequently suggested that a certain portion of data with little scatter ascribable to the above causes were to be considered as more reliable representative of CHF values, but such arbitrary selective exclusion of experimental data is highly questionable. Although Tippets was not able to give a substantiated explanation close examination of his data reveals that even if the given average decrease of 20% in CHF for the thinner strip is correct, increases in CHF as between the 0.15mm and the 0.25mm thick strip ranged in fact, from 8% to 43%. The consistently higher CHF's obtained when using the 0.25mm thickness-walled strip can hardly be attributed to the causes given.

Vliet and Leppert [56] carried out CHF determinations for water near saturation, under atmospheric pressure, flowing normal to stainless steel heated tubes and wires, whose heated lengths varied from 50mm to 150mm and flow velocities in the range 0.37m/sec to 2.9m/sec. Although they observed slight increments in CHF when using thicker walled tubes, they

concluded that the CHF was independent of wall thickness. However, from estimates made from their plotted data, it was found that the increase in CHF for a tube with a 1.52mm wall thickness compared to one with 0.25mm wall thickness is about 8%. Complete independence of CHF from wall thickness is observed beyond a wall thickness of about 1mm.

Lee [50] conducted CHF experiments with water at 69 bar flowing in a stainless steel tube of 9.25mm internal diameter at mass-velocities of 2034 and 4068Kg/m^2sec. The range of inlet subcoolings was 23 to 372KJ/Kg and tested wall thicknesses of 0.86 and 2.08mm at heated lengths of 864 and 1730mm. At a heated length of 864mm, the thicker tube gave 8% higher CHF, whereas no difference was observed when the heated length was 1730mm.

Hewitt et. al. [57] studying liquid film flow in annular flow, carried out CHF determinations forwater in stainless steel tubes of 9.3 mm diameter and wall thicknesses of 0.91 and 2.03mm. On estimates from their data within a range of 10 to 80^{o}K of inlet subcooling at mass-velocities of 119, 163 and 298Kg/m^2sec and outlet pressures of 1.24, 1.38 and 1.93 bar respectively, consistently higher critical heat fluxes for the thicker tube are observed, the range of increase in CHF varying from 6 to 15% for the thicker tube . The explanation given for this effect was that the rate of temperature rise under a dry patch is higher for a thin-walled tube.

Fiori and Bergles [40] conducted 12 burnout tests with subcooled water flowing in a stainless steel tube at 2.4mm diameter and tested 0.30 and 1.98mm wall thickness. Analysing their data, it is observed that at a pressure of about 2 bar, inlet subcooling of about 115KJ/Kg and mass-velocities of 2034, 4070 and 6100 Kg/m^2sec, increases in CHF with the thicker tube ranged from 21% at the highest mass-velocity to 56% for the lowest mass-velocity. At a pressure of about 6 bar, inlet subcooling of about 125 KJ/Kg and mass-velocities of 4070 and 6100 Kg/m^2sec, the increase in CHF for both mass-velocities is of 5% for the thicker tube.

The other two tests, one carried out at a pressure of 2.62 bar, mass-velocity of 4476 Kg/m^2sec and inlet subcooling of 110 KJ/Kg for the 1.98mm thick tube, and the other at a pressure of 6.34 bar, mass-velocity of 2034 Kg/m^2sec, inlet subcooling of 114 KJ/Kg for the 0.30mm thick tube, lack significance since these conditions are not comparable to those of any other test.

To summarize the above discussion, with the exception of two sets of data at high pressures [50,54], an effect of wall thickness on CHF for the system water-stainless steel at low pressures (1-2 bar) in flow boiling has been observed. The forementioned studies give evidence to support the fact that there exists at least a range of wall thickness where the CHF is affected. It is believed that the success claimed in correlating CHF data [31] does not contradict this experimental fact, and although a review of the world data on CHF is beyond the scope of the present study, well known CHF correlations [37,58,59] , predict the CHF within 20 to 30%. It would follow then that first, variations in CHF due to wall thickness effect can to a major extent be absorbed within the accuracy range of the correlation and secondly, the data from which a given correlation was derived, may be beyond the possible range of wall thickness affecting the CHF.

b) The effect of other parameters on CHF

In the comprehensive reviews by Collier [1] and Macbeth [31] of the little available information on the effect of secondary factors on the CHF it is indicated that:

i) the CHF is not significantly affected by surface roughness, surface tension and liquid purity, and

ii) in vertical flow, the CHF appears to be lower for downflow than that for upflow under the same conditions, the effect being higher at low mass-velocities. Kirby [45] reported reductions in CHF ranging from 10% to 30%.

III Purpose of the present study

The primary objectives of the present experimental study of the subcooled flow boiling of water at atmospheric pressure are fivefold:

1) To carry out a high-speed cine photographic study (10,000 frames/sec) of the flow structure near the CHF (up to 95% of the CHF);

2) to determine the test section wall thickness effect on CHF in flow boiling, which seems not to have been systematically investigated previously;

3) to carry out a complete quantitative study of the bubble parameters near the CHF for the bubbly flow regime;

4) to propose a nucleate boiling heat transfer model which eliminates the inconsistencies shown by previous models and allows for the overlapping areas of bubble influence and,

5) to test the proposed models for the mechanism of subcooled CHF in flow boiling against the detailed experimental observations obtained in this study at large subcoolings.

In the pursuit of the above basic objectives a considerable amount of experimental data was obtained, which made it possible: (i) to develop an empirical correlation for the CHF which includes wall thickness as a parameter, (ii) to assess the adequacy of the proposed nucleate boiling heat transfer model and, (iii) to formulate a possible alternative for the mechanism of subcooled CHF.

In addition, from the bubble parameters study carried out for the same heating surface under the same conditions of flow and subcooling with varying levels of heat flux, from 70% to 95% of the average measured CHF, it was found that a deactivation/reactivation process of nucleation sites took place, i.e. some active sites at a low heat flux were deactivated at a higher heat flux and re-activated at further higher fluxes. Special attention was given to this process and a simple site deactivation theory was developed.

CHAPTER TWO

EXPERIMENTAL EQUIPMENT AND TEST PROCEDURE

Experimental tests from single-phase forced convection up to burnout were conducted for water flowing upwards through a vertically positioned channel of rectangular cross-section electrically heated on one wall, with a glass window forming the front wall so that high speed cine photographic films could be taken. The ranges of parameters investigatedin the present study are as follows:

System pressure: atmospheric (1.013 bar)

Test section geometry: a rectangular channel with one side uniformly heated.

Test surface: Material - stainless steel

Heated length - 150 ± 1 mm

Width - 10 ± 0.1 mm

Wall thickness - 0.08 to 0.20 mm

Water flow velocity: 0.8 to 2.0 m/sec

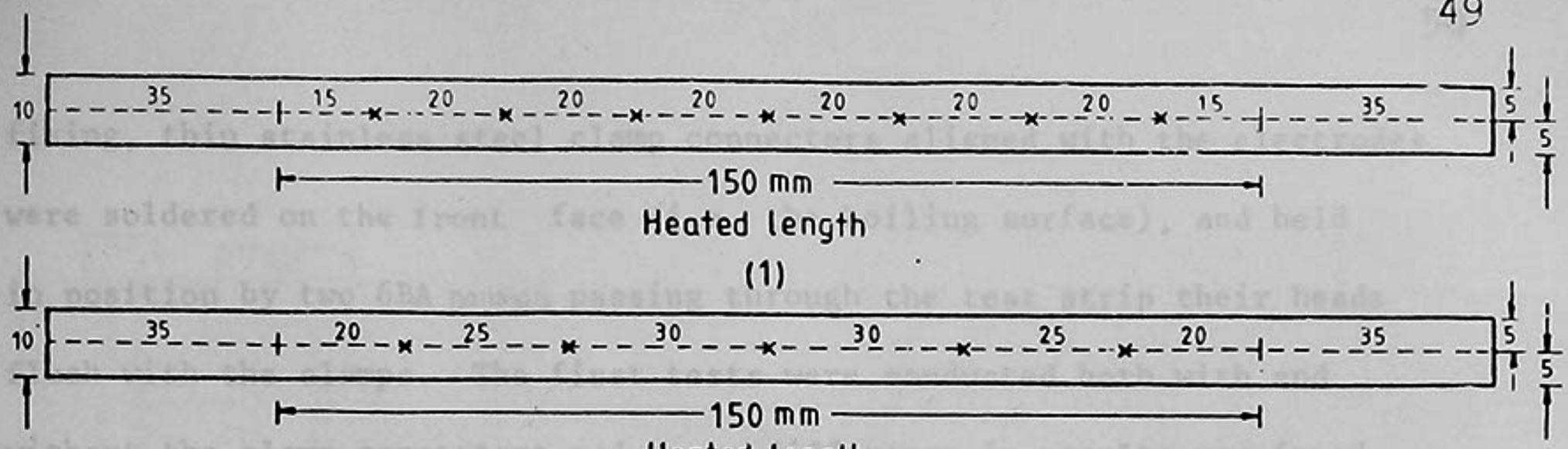
Inlet subcooling: 20 to 80 ^{o}K

I. Experimental Apparatus

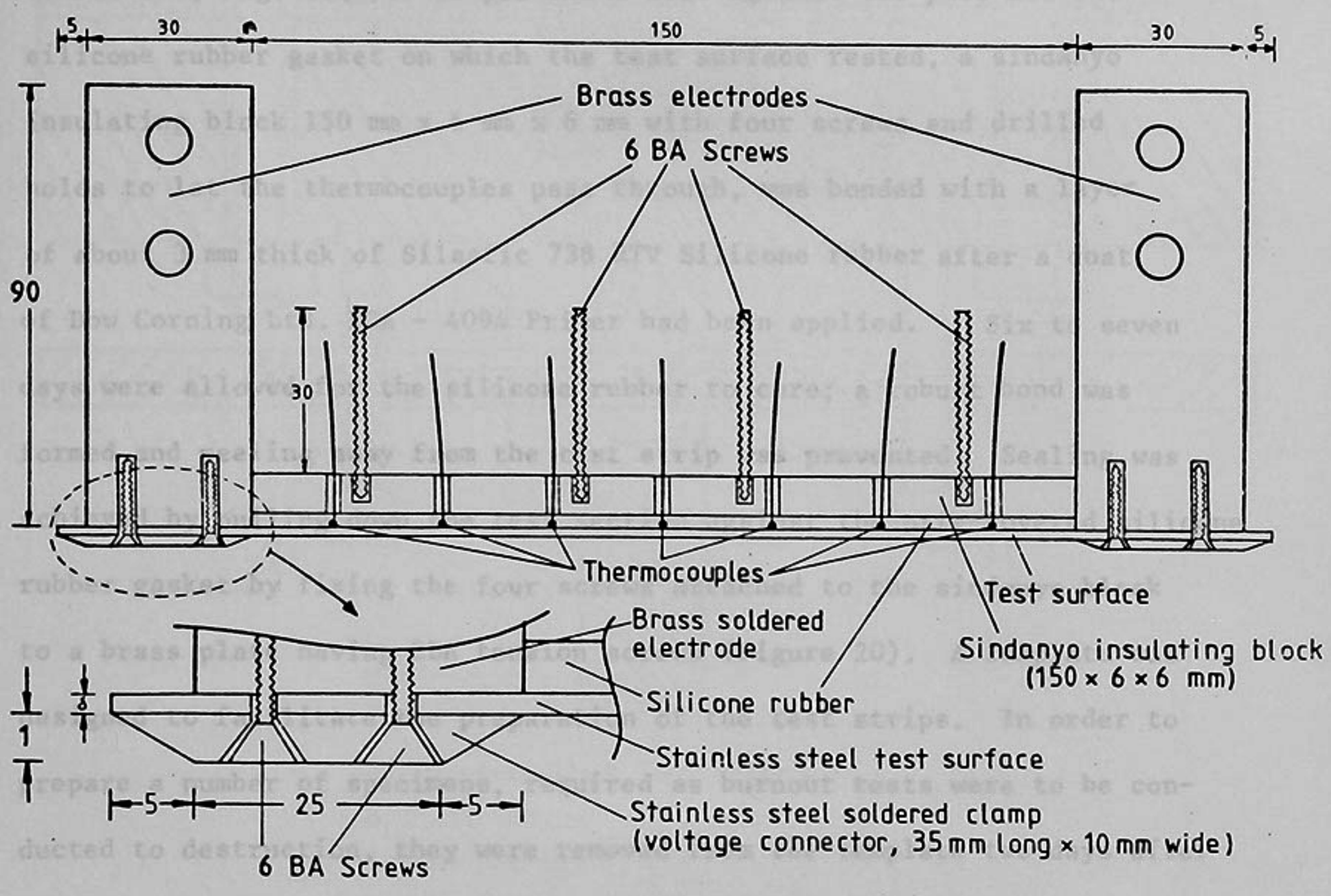
1. The test section

The test section, Figure 19, consisted of stainless steel strips 220 mm long by 10 mm wide cut from hard rolled stainless steel sheets British standard 1449 EN58A of three different thicknesses: 0.08, 0.13 and 0.20 mm. The hot junction of arc-welded copper-constantan thermocouples previously calibrated were attached to but electrically insulated from the back of the test strips by a thin layer of epoxy "Rapid Araldite" cement. Two different thermocouple position arrangements were used, Figure 19(a), to provide the temperature profile along the heated length of the test surfaces.

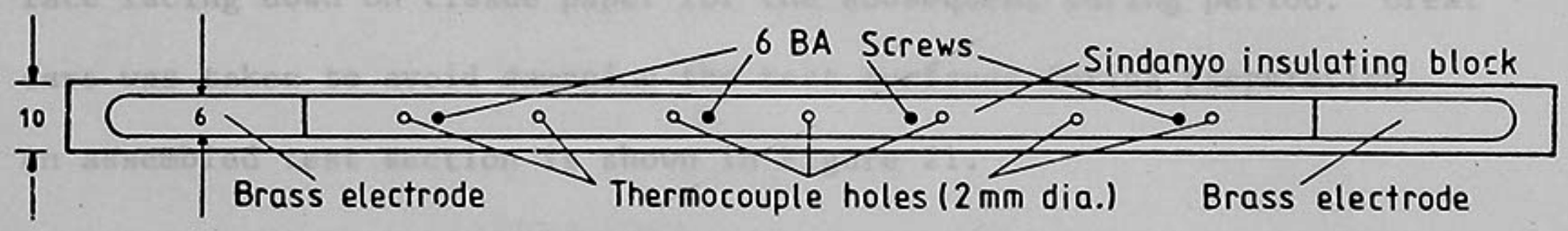
Brass electrodes were soldered to the rear face of the test specimens 150 mm apart. In order to provide more mechanical strength and facilitate



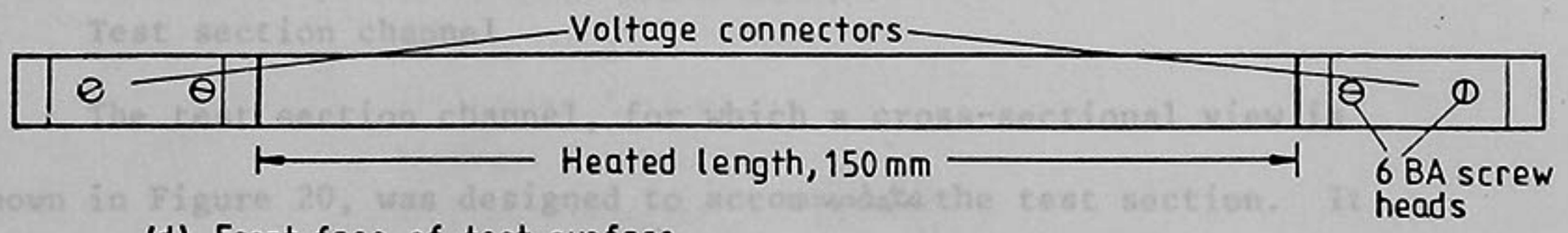
(a) Thermocouple position arrangements along the rear face of the test surfaces.



(b) Side view of an assembled test section.



(c) Back of assembled test section.



(d) Front face of test surface.

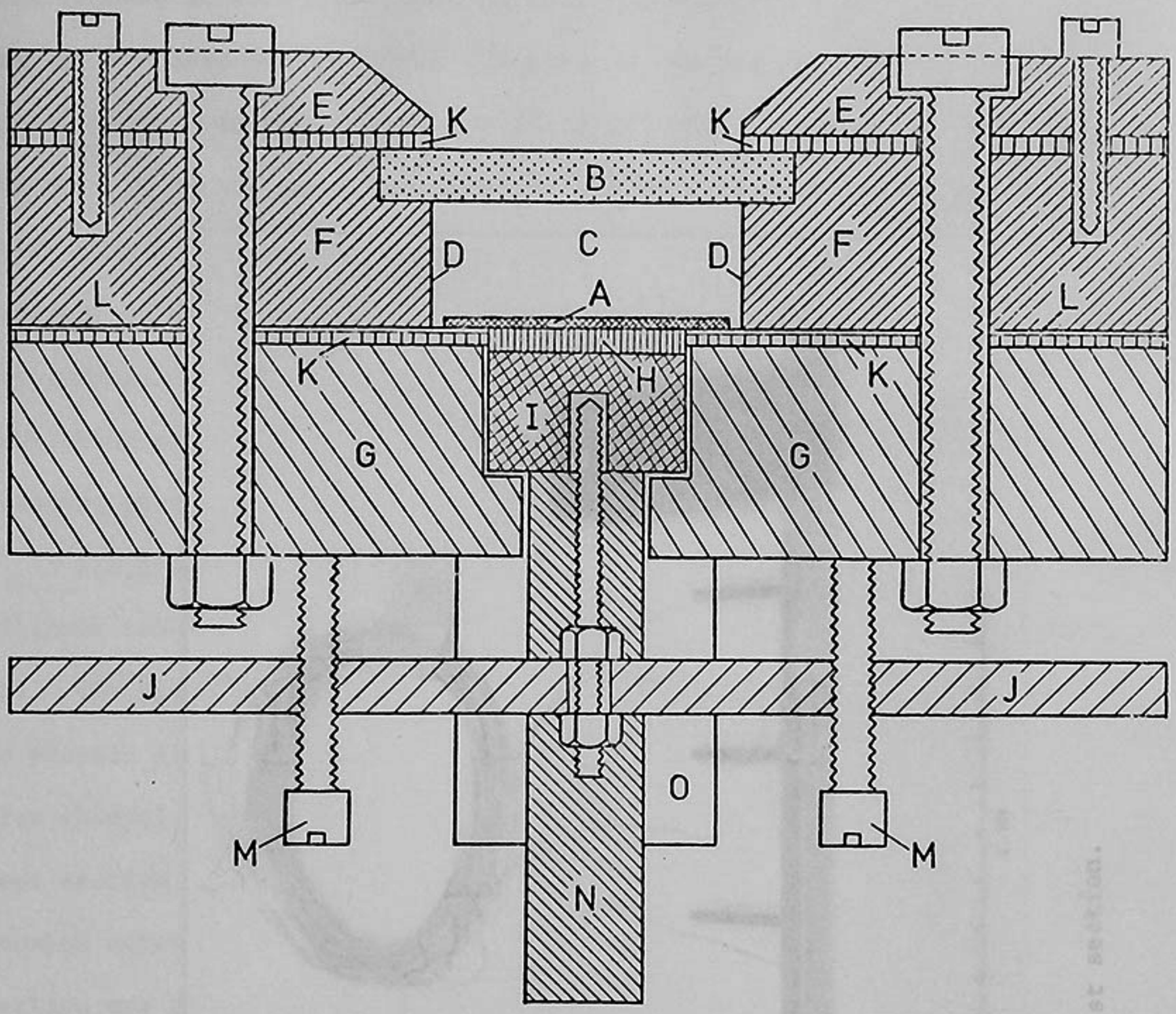
◆ [DIMENSIONS IN MILLIMETRES]

Figure 19 Views of the test section.

fixing, thin stainless steel clamp connectors aligned with the electrodes were soldered on the front face (i.e. the boiling surface), and held in position by two 6BA screws passing through the test strip their heads flush with the clamps. The first tests were conducted both with and without the clamp connectors and as no difference in results was found the great majority of tests was carried out with specimens having clamp connectors, Fig. 19(b). To provide a seal against the ptfe and the silicone rubber gasket on which the test surface rested, a sindanyo insulating block 150 mm x 6 mm x 6 mm with four screws and drilled holes to let the thermocouples pass through, was bonded with a layer of about 3 mm thick of Silastic 738 RTV Silicone rubber after a coat of Dow Corning Ltd. DCA - 4094 Primer had been applied. Six to seven days were allowed for the silicone rubber to cure; a robust bond was formed and peeling away from the test strip was prevented. Sealing was achieved by pulling down the test section against the ptfe-covered silicone rubber gasket by fixing the four screws attached to the sindanyo block to a brass plate having 2BA tension screws (Figure 20). A template was designed to facilitate the preparation of the test strips. In order to prepare a number of specimens, required as burnout tests were to be conducted to destruction, they were removed from the template two days after preparation and left to cure open to the atmosphere with the boiling surface facing down on tissue paper for the subsequent curing period. Great care was taken to avoid damaging the test surfaces during preparation. An assembled test section is shown in Figure 21.

2. Test section channel

The test section channel, for which a cross-sectional view is shown in Figure 20, was designed to accommodate the test section. It consisted of a sindanyo insulating plate, a stainless steel top plate and a stainless steel clamping plate. The test section was bolted onto the ptfe-covered silicone rubber gasket placed on the top of the



A-Stainless Steel Test Surface
B-Glass Window
C-Flow Channel
D-ptfe Adhesive Tape
E-Stainless Steel Clamping Plate
F-Stainless Steel Plate
G-Sindanyo Insulating Plate
H-Silicone Rubber
I-Sindanyo Backing Block
J-Brass Plate
K-Silicone Rubber Gasket
L-ptfe Tape
M-Tension Screws
N-Brass Electrode
O-Flow Connector

Figure 20 Cross-sectional view of the test section channel. (Not at scale).

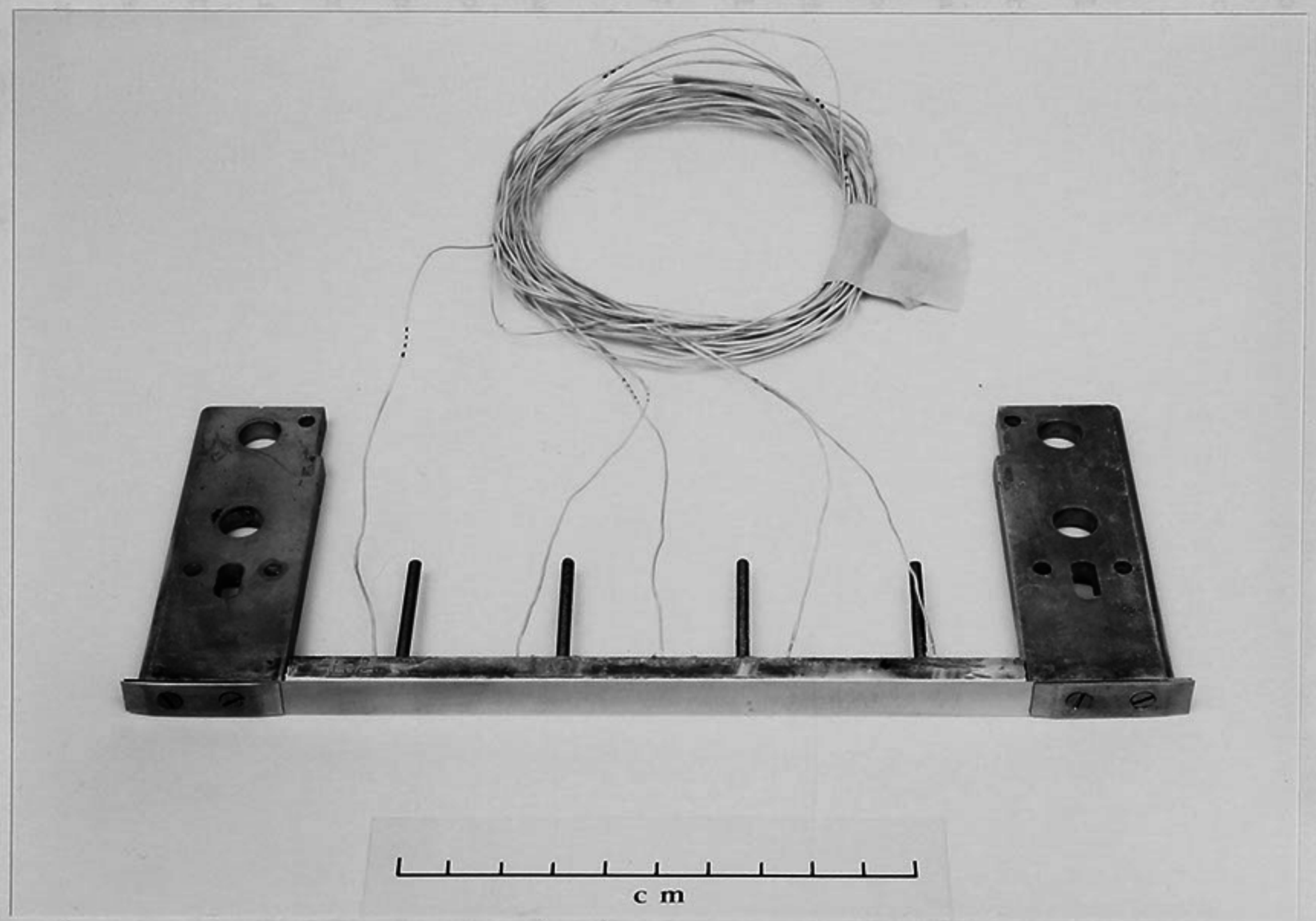


Figure 21 An assembled test section.

sindanyo insulating plate, (G) Figure 20, and provided with a central slot rounded at both ends which permitted access to the electrodes, and the sindanyo backing block (I) attached to the back of the test section. The stainless steel top plate (F) with a central slot of 368 mm x 12 mm x 5 mm on one side and 356 mm x 28 mm x 5mm on the other side to accommodate a glass window, was placed on top of the sindanyo plate and a rectangular cross-sectional channel of 12 mm x 5 mm was formed. Figure 22 shows the test section bolted onto the sindanyo insulating plate, the stainless steel plate and the stainless steel clamping plate.

The glass window, (B) Figure 20, was sealed with ptfe tape and a silicone rubber gasket and bolted onto the stainlees steel clamping plate (E). The side walls of the channel were covered with ptfe adhesive tape to provide electrical insulation between the test section and the flow channel. The screws attached to the sindanyo backing block of the test section were fixed to the brass plate (J) and by tightening the tension screws (M) against the sindanyo insulating plate (G), the test section was pulled down against the silicone rubber gasket, hence providing the sealing. The flow connectors (0) 300 mm apart were placed normal to the heating surface. In order to prevent heat losses, 60Ω resistance guard heaters were attached to the back of the test section channel. A thermocouple was attached to the bottom of the sindanyo plate under the guard heater to monitor the temperature at that location. Views of the whole assembly as vertically positioned in the forced convection rig are shown in Figure 23.

3. The forced-convection boiling rig

The flow diagram of the flow boiling rig is shown in Figure 24. To prevent water contamination all the piping in the loop was made of stainless steel. Degassed and distilled water at atmospheric pressure was circulated by a centrifugal pump through variable-area flow meters,

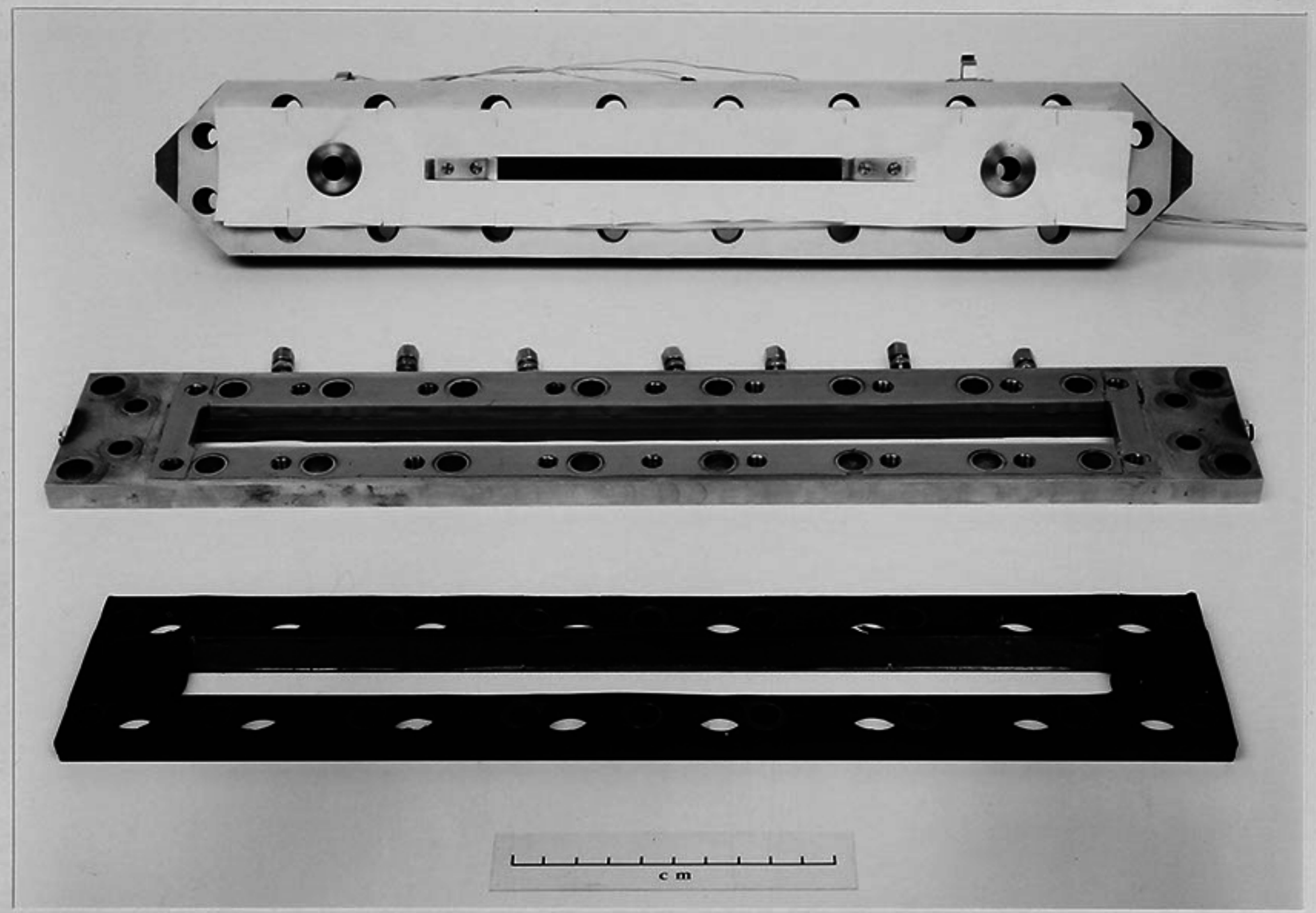


Figure 22 Test section bolted onto the sindanyo plate; stainless steel plate and stainless steel clamping plate.

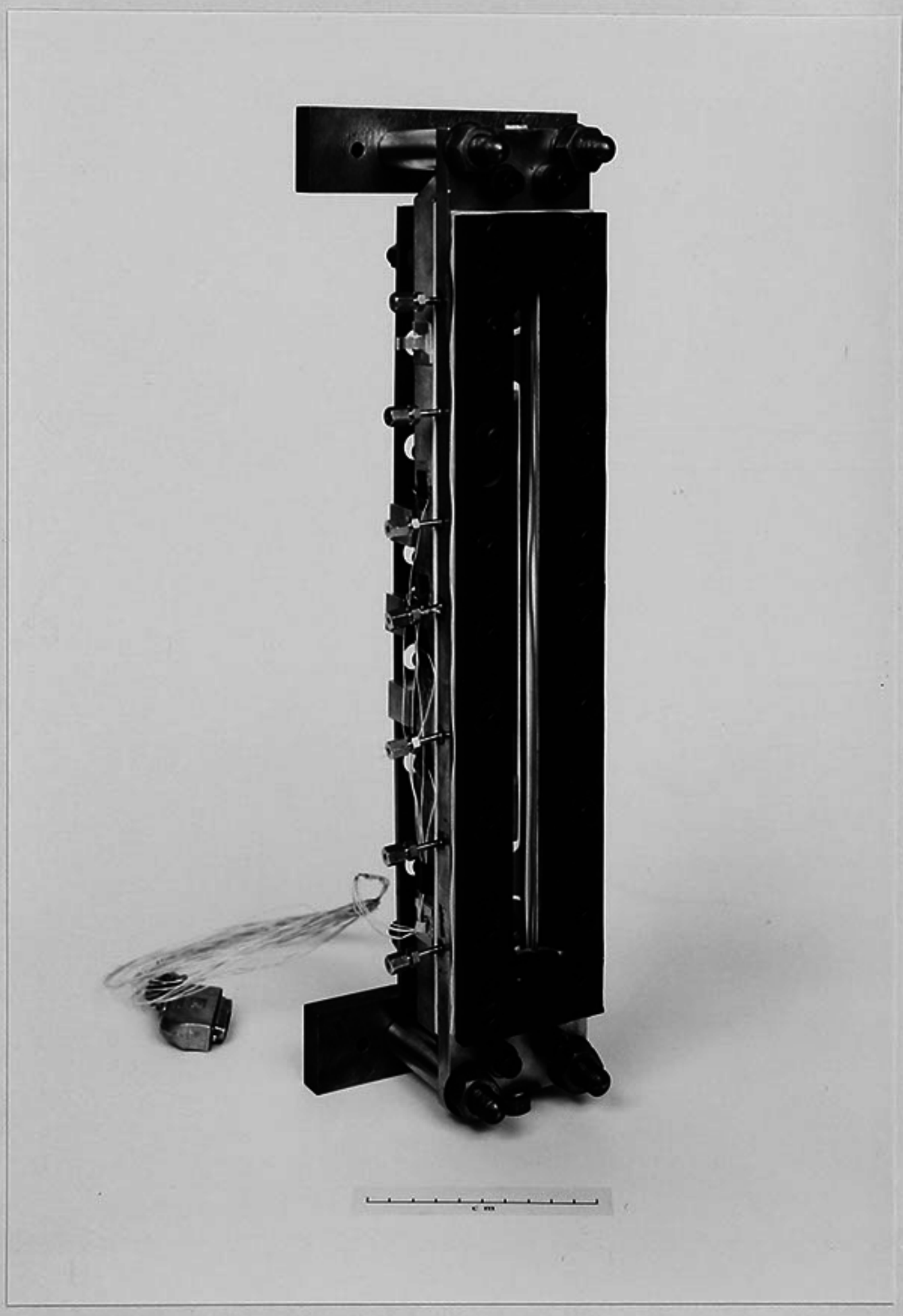


Figure 23(a) Front view of the test section channel.

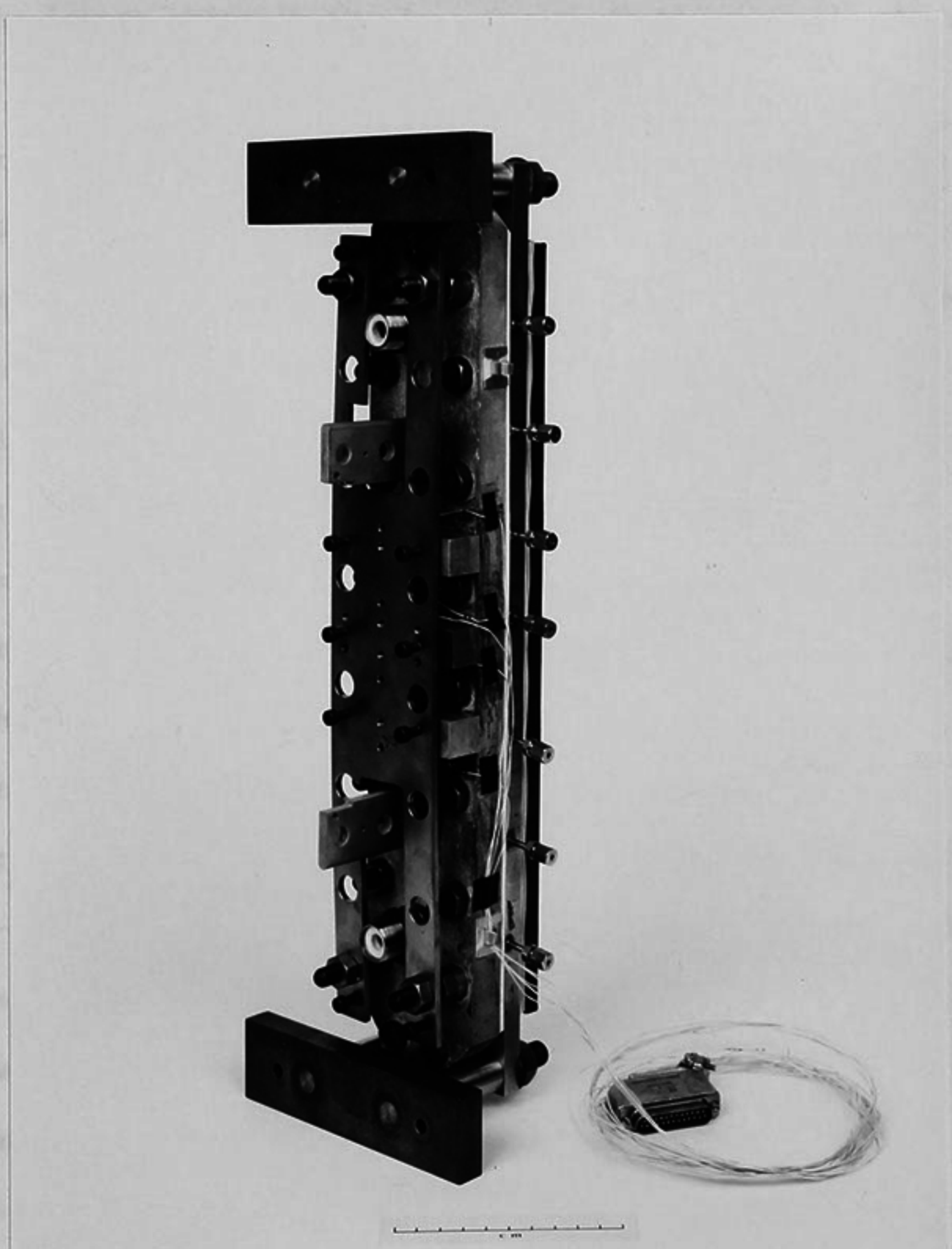


Figure 23(b) Rear view of the test section channel.

a pre-heating section, the test section channel, a by-pass to a degassing /pressurizing tank and water-cooled tubular heat exchangers. The pressurizing tank at the upper point of the loop contained an electric tubular immersion heater and was also used as a storage tank. Water was injected into the system by a make-up reciprocating pump. A line connected to the lowest point in the loop was available to drain the water of the system.

Power for the test section was supplied by a direct current rectifier rated at 500 Amp maximum. The rectifier permitted coarse control of the power supply and finer control of power to the test section was achieved by means of a variable water-cooled resistor in series with the test section. Insulated copper cables were attached to the electrodes at the back of the test section. The electrical current passed through the test section was determined by measuring the voltage drop across a precision shunt. Alternating current was available to supply power to the immersion heater, preheaters, guard heaters and both pump motors.

The inlet and outlet bulk water temperatures were measured by copper-constantan thermocouples located in wells constructed from small diameter, thin-walled stainless steel tubes. Small holes were drilled throught the main pipe close to the flow connectors of the test channel and the wells were soldered and inserted with sealed ends, one upstream and one downstream, at about the centre of the flow pipe.

All the temperatures were measured by copper-constantan thermocouples calibrated to $\pm 0.1^{\circ}C$ against a Control and Readout Ltd. platinum resistance thermometer in an oil bath. The cold junctions of the thermocouples were immersed in an electrically stirred distilled water ice bath. The voltage drop across the test section, the voltage drop across the shunt resistance for current determination and the thermocouples emf were measured using a Fenlow 501 digital voltmeter accurate to 1μvolt up to an ambient temperature of $37^{\circ}C$, adapted with selector switches for the scanning of the various voltages measured.

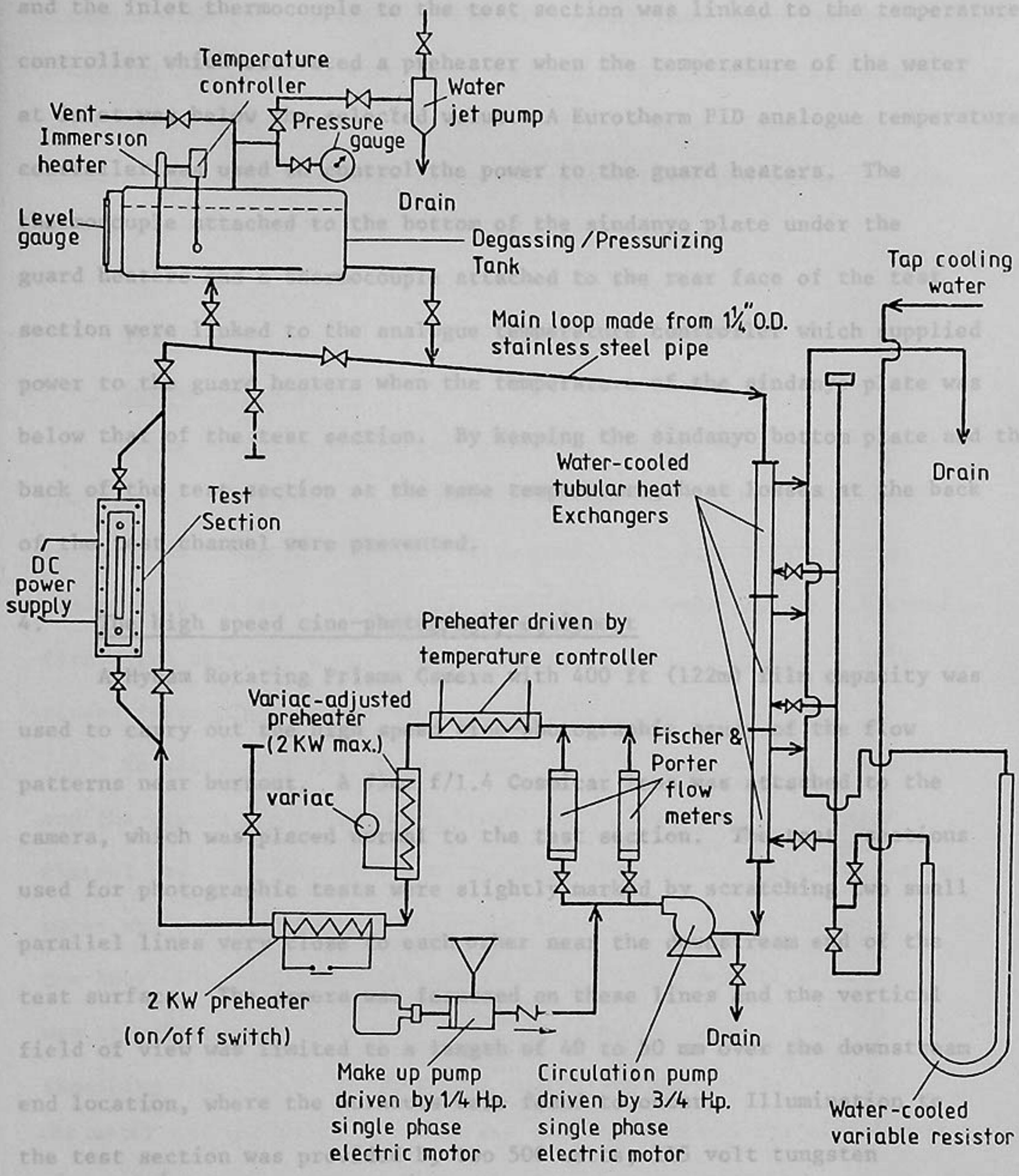


Figure 24 Schematic diagram of the forced-convection boiling rig.

A Eurotherm DHS digital temperature controller was used to maintain the water inlet temperature at a desired value (± 0.5°C), and the inlet thermocouple to the test section was linked to the temperature controller which activated a preheater when the temperature of the water at inlet was below the selected value. A Eurotherm PID analogue temperature controller was used to control the power to the guard heaters. The thermocouple attached to the bottom of the sindanyo plate under the guard heaters and a thermocouple attached to the rear face of the test section were linked to the analogue temperature controller which supplied power to the guard heaters when the temperature of the sindanyo plate was below that of the test section. By keeping the sindanyo bottom plate and the back of the test section at the same temperature, heat losses at the back of the test channel were prevented.

4. The high speed cine-photography equipment

A Hycam Rotating Prisma Camera with 400 ft (122m) film capacity was used to carry out the high speed cine-photographic study of the flow patterns near burnout. A 75mm f/1.4 Cosmicar lens was attached to the camera, which was placed normal to the test section. The test sections used for photographic tests were slightly marked by scratching two small parallel lines very close to each other near the downstream end of the test surface. The camera was focussed on these lines and the vertical field of view was limited to a length of 40 to 50 mm over the downstream end location, where the burnouts were found to occur. Illumination to the test section was provided by two 500 watts, 115 volt tungsten semi-silvered lamps connected to a transformer having brigth and dim lighting levels. Bright lighting level was used for all the films taken. Ilford Mark V 16mm films of 100ft (∿ 30m) length were used. The camera was operated at a speed of 10,000 frames per second and about 50 ft of film were required before the motor of the camera reached the selected speed, which was checked by means of the timing light facility available in the camera. The light pulse was provided by a stroboscope

rated at 1000 cycles per second. Figure 25 shows the set up of the high-speed cine photographic equipment. After several unsuccessful attempts with the operation of the high speed cine camera, where focussing and lighting were found to be difficult parameters to set, the detailed schematic set up shown in Figure 26 was found to be adequate for obtaining well contrasted and defined photographic films during flow boiling.

II Test procedure

1. System preparation

During cleaning of the test sections, nothing was done to alter the surface characteristics of the test specimens, which were used in the conditions in which they were received. Just before being placed into the test channel, the test sections were carefully cleaned first with acetone, then with a detergent solution, and thoroughly rinsed first with hot and then with distilled water.

To start a series of test runs, the rig water was drained off and the system was filled with freshly distilled water. The test channel was then installed into the rig. Before each run, the system water was degassed by allowing it to boil under vacuum for about one hour. The degassing/storage tank was filled and the water was circulated in the loop at low flow rate, the test channel remaining isolated. The immersion heater was used to boil the water and the water jet pump was used to draw out the air content. This recommended procedure [36] was adopted to avoid a high concentration of dissolved gasses and air trapped in the system.

During experimental tests, to reduce heat losses the whole test section channel with exception of the glass window was covered with glass fibre insulation (see Figure 25).

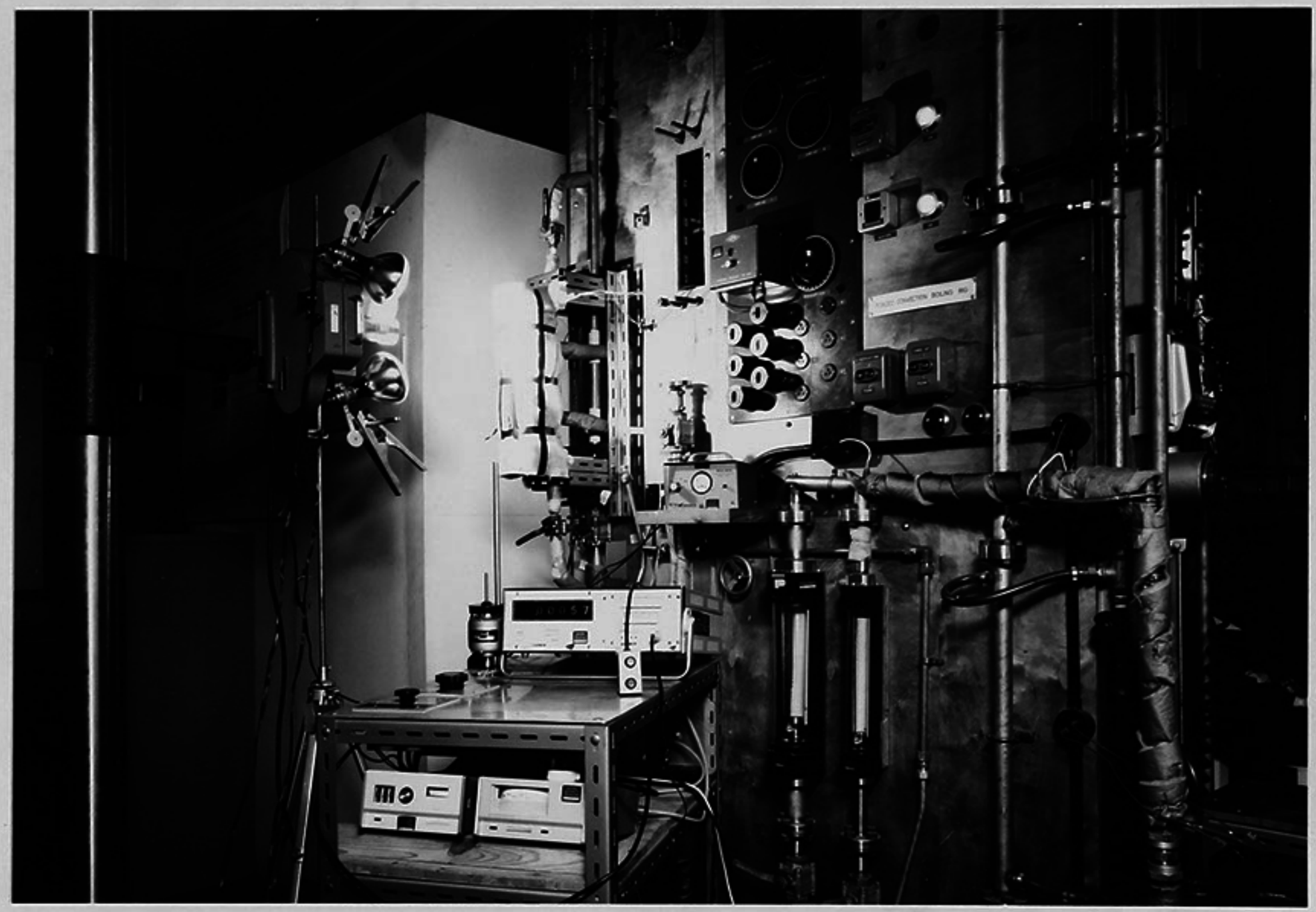


Figure 25 High-speed cine-photography equipment.

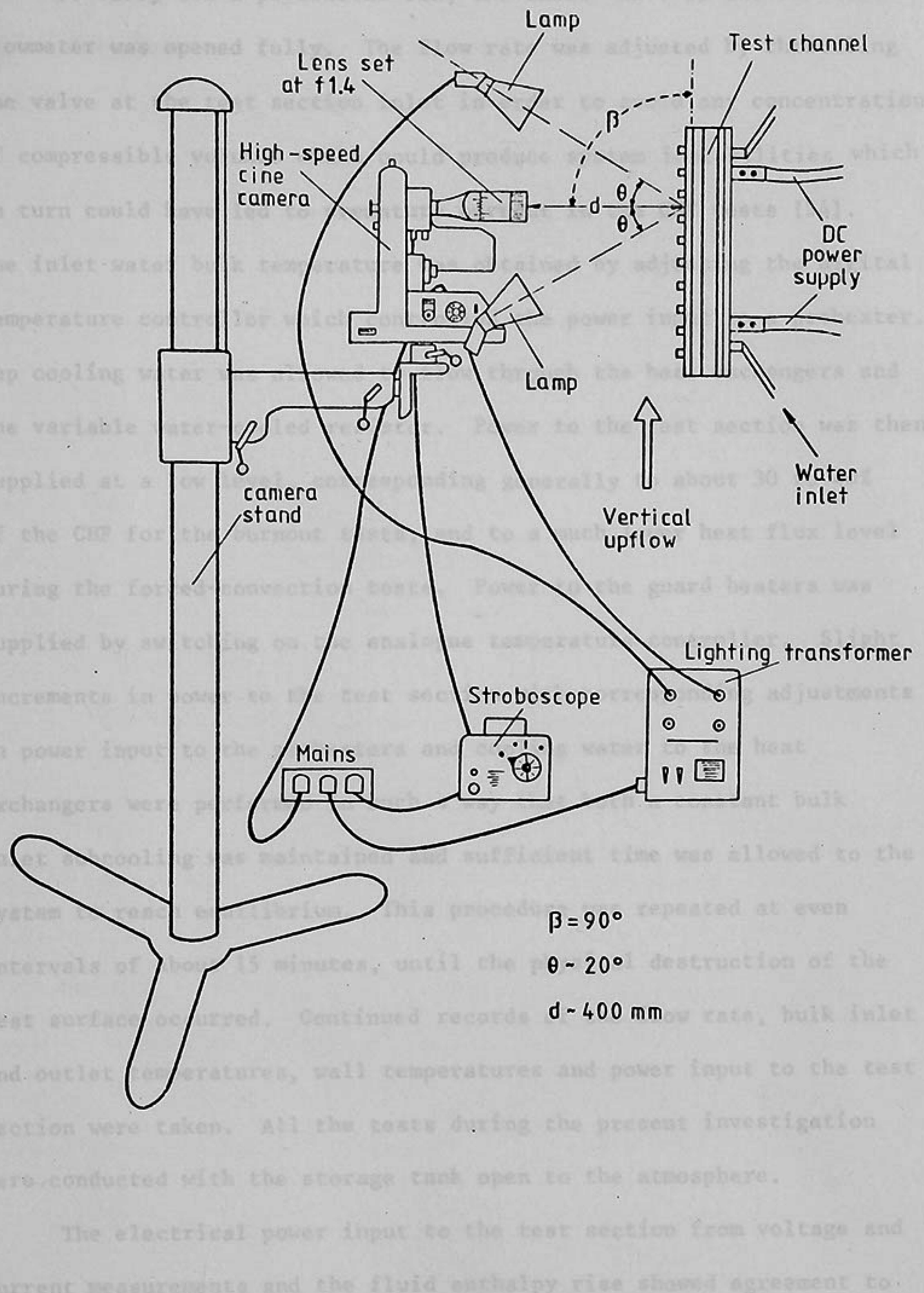


Figure 26 Set-up of the high speed cine-photography equipment.

2. Test procedure

To carry out a particular run, the inlet valve to the selected flowmeter was opened fully. The flow rate was adjusted by throttling the valve at the test section inlet in order to avoid any concentration of compressible volumes which could produce system instabilities which in turn could have led to premature burnout in the CHF tests [54]. The inlet water bulk temperature was obtained by adjusting the digital temperature controller which controlled the power input to a preheater. Tap cooling water was allowed to flow through the heat exchangers and the variable water-cooled resistor. Power to the test section was then supplied at a low level, corresponding generally to about 30 to 40% of the CHF for the burnout tests, and to a much lower heat flux level during the forced-convection tests. Power to the guard heaters was supplied by switching on the analogue temperature controller. Slight increments in power to the test section with corresponding adjustments in power input to the preheaters and cooling water to the heat exchangers were performed in such a way that both a constant bulk inlet subcooling was maintained and sufficient time was allowed to the system to reach equilibrium. This procedure was repeated at even intervals of about 15 minutes, until the physical destruction of the test surface occurred. Continued records of the flow rate, bulk inlet and outlet temperatures, wall temperatures and power input to the test section were taken. All the tests during the present investigation were conducted with the storage tank open to the atmosphere.

The electrical power input to the test section from voltage and current measurements and the fluid enthalpy rise showed agreement to within 5%. As the wall temperatures were measured at the back of the test sections, a correction for the temperature drop across the wall was applied in order to obtain the required wall surface temperature, which was calculated by means of the steady-state one-dimensional

heat conduction equation for systems with internal heat generation (see Appendix A). Experimental error estimates for the present investigation are presented in Appendix B.

CHAPTER THREE

EXPERIMENTAL RESULTS. PART I: SINGLE PHASE FORCED-CONVECTION AND NUCLEATE FLOW BOILING

I. Single phase forced-convection experiments

The experimental tests were performed at Reynolds numbers based on the mean hydraulic diameter of the channel (D_H = 7.06 x 10^{-3} m) in the range of 10^4 - 6 x 10^4. The steady-state heat transfer coefficients were determined by measuring the wall temperature on the rear face of the heated strips and correcting for the temperature drop across its thickness (see Appendix A) at several axial locations along the heated length. The temperature readings of the thermocouple placed 20 mm away from the downstream end of the test section, Figure 19, were used to compute the heat transfer coefficients, since the temperature profile, Figure 27, showed the flow to be fully developed at that particular location (approximately 30 hydraulic diameters of heated length).

Several tests at different conditions were conducted over the single phase forced-convection region and the results, compared with some relevant correlations, are shown in Figure 28. It was found that the measured heat transfer coefficients were in close agreement, to within 7% with the empirical correlation of James et al. [63] developed for ducts of rectangular cross-section heated on one wall only for fully-developed turbulent flow and expressed as

$$Nu = \frac{[0.104\ Re^{0.0016Pr+0.75}]Pr^{0.4}\ \mu_r (213Re^{-0.9})}{e^{0.0134Pr}\ (2.05 + 1.62e^{-A})} \qquad (3\text{-}1)$$

where

μ_r is the ratio of the fluid viscosity evaluated at the average bulk temperature $\overline{T}_b$ to the fluid viscosity evaluated at the wall temperature T_w, and A is the aspect channel parameter, defined as the ratio of width of the channel normal to the heating surface to breadth

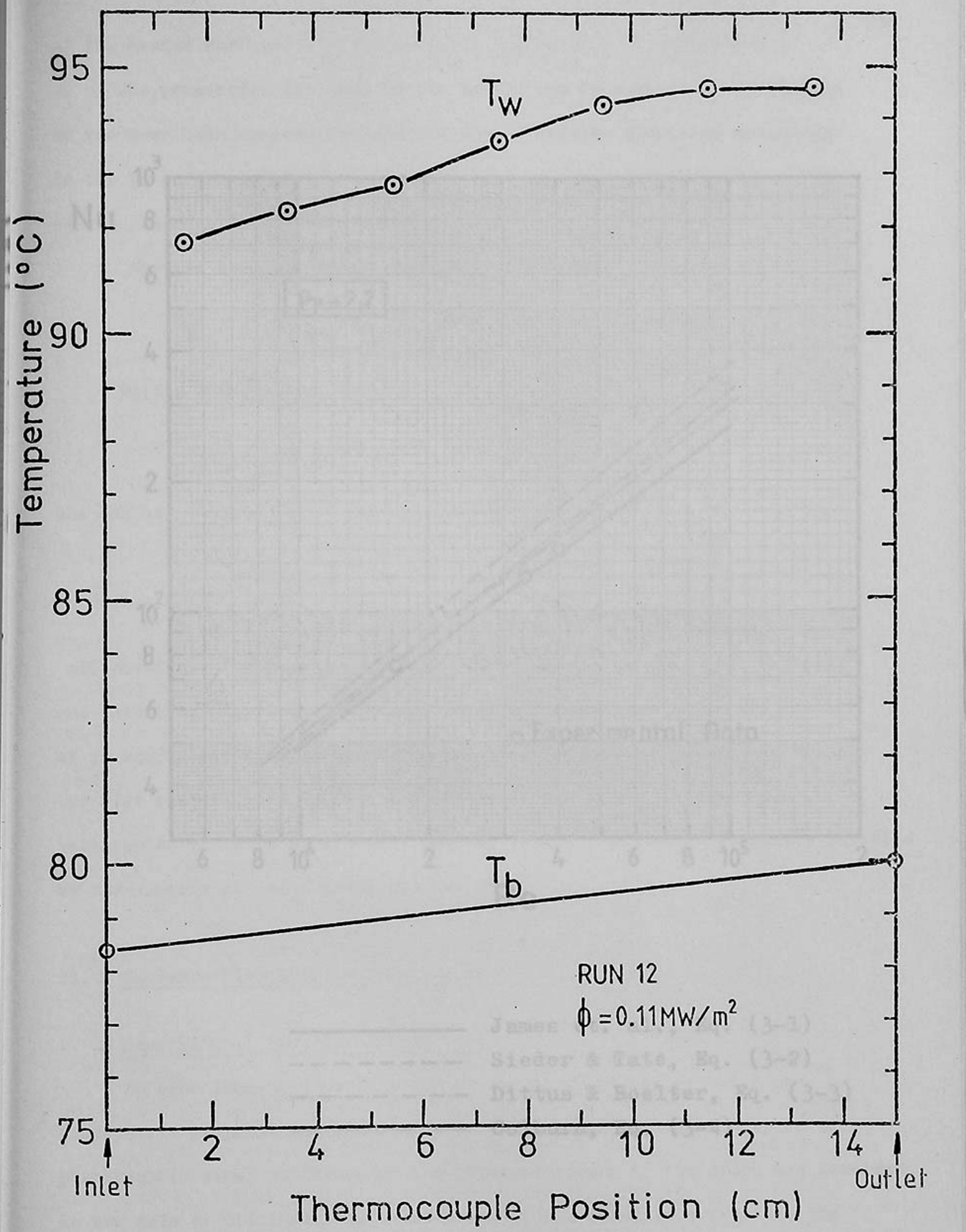
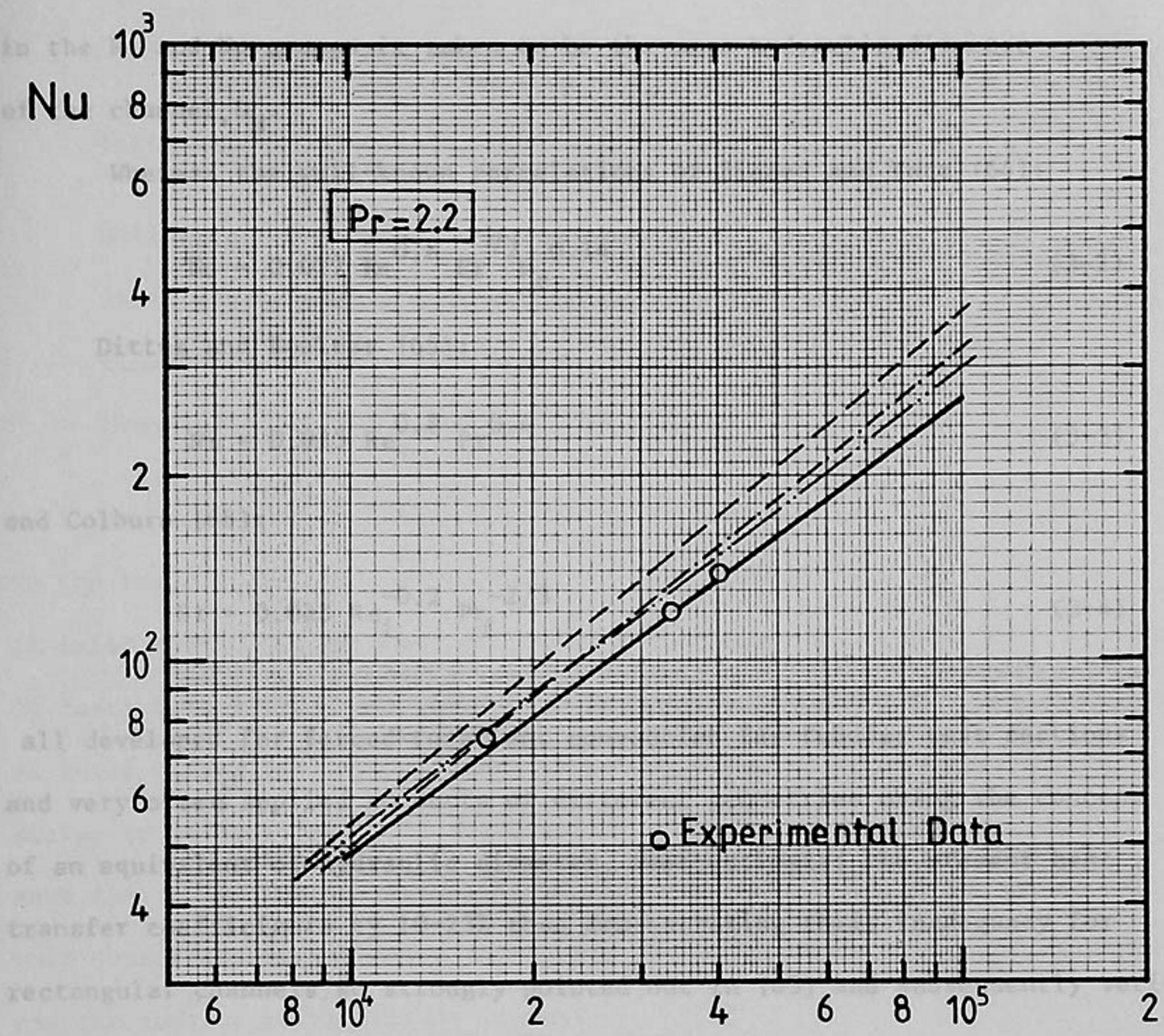


Figure 27. Temperature profile along the heated surface.



——————— James et. al., Eq. (3-1)
– – – – – – – – – Sieder & Tate, Eq. (3-2)
—·—·—·—·—·— Dittus & Boelter, Eq. (3-3)
——··——··—— Colburn, Eq. (3-4)

Figure 28 Single-phase forced convection heat transfer data.

of the heated surface.

The properties involved in the Re, Nu and Pr numbers are evaluated at the mean bulk temperature and the characteristic dimension appearing in the Re and Nu groups is taken to be the mean hydraulic diameter of the channel, D_H.

Whereas the well-known correlations of Sieder and Tate [64]:

$$Nu = 0.027\ Re^{0.8}\ Pr^{1/3}\ \mu_r^{0.14} \tag{3-2}$$

Dittus and Boelter [65]:

$$Nu = 0.023\ Re^{0.8}\ Pr^{0.4} \tag{3-3}$$

and Colburn [66]:

$$St = 0.023\ Re_f^{-0.2}\ Pr_f^{-2/3} \tag{3-4}$$

all developed for forced-turbulent convection for tubular test sections and very often applied to ducts of different geometries using the concept of an equivalent or hydraulic diameter, over-estimated the present heat transfer coefficients by 10-23% thus demonstrating their inadequacy for rectangular channels so strongly pointed out in [63] and subsequently verified by the experiments of Kenning and Kao [67].

II. Nucleate Flow Boiling Experiments

1. Experimental flow boiling curves

An experimental investigation of the flow boiling of water at atmospheric pressure was undertaken in conjunction with a high-speed cine photographic study to determine the physical nature of the processes involved in the rate at which heat is transferred from a metallic surface to the flowing liquid.

The range of variables covered by the present investigation is as follows:

System pressure: atmospheric

Test section geometry: a channel of rectangular cross-section with one side electrically heated.

Test surface: stainless steel strips, 150±1 mm heated length x 10±0.1 mm wide.

Wall thickness: 0.08, 0.13 and 0.20 mm.

Inlet subcooling: 20, 50 and 80^{o}K.

Flow direction: vertical upflow.

Mass-velocity: 800, 1700 and 2000 Kg/m^{2}sec.

The number of different experimental runs was 27, corresponding to the three different wall thicknesses each submitted to three levels of inlet subcooling at three different mass-velocities. However, altogether 70 tests were carried out since each of the 27 different runs was conducted at least twice, Table 1, to test reproducibility. As each test was conducted to burnout (physical destruction), a new test specimen was used each time. The resulting boiling curves, plotted as heat flux against wall superheat are presented in Figures 29 to 31, where the upper data points are the corresponding burnout values.

Over the fully-developed boiling region, where the heat flux - wall superheat relationship is generally expressed dimensionally as

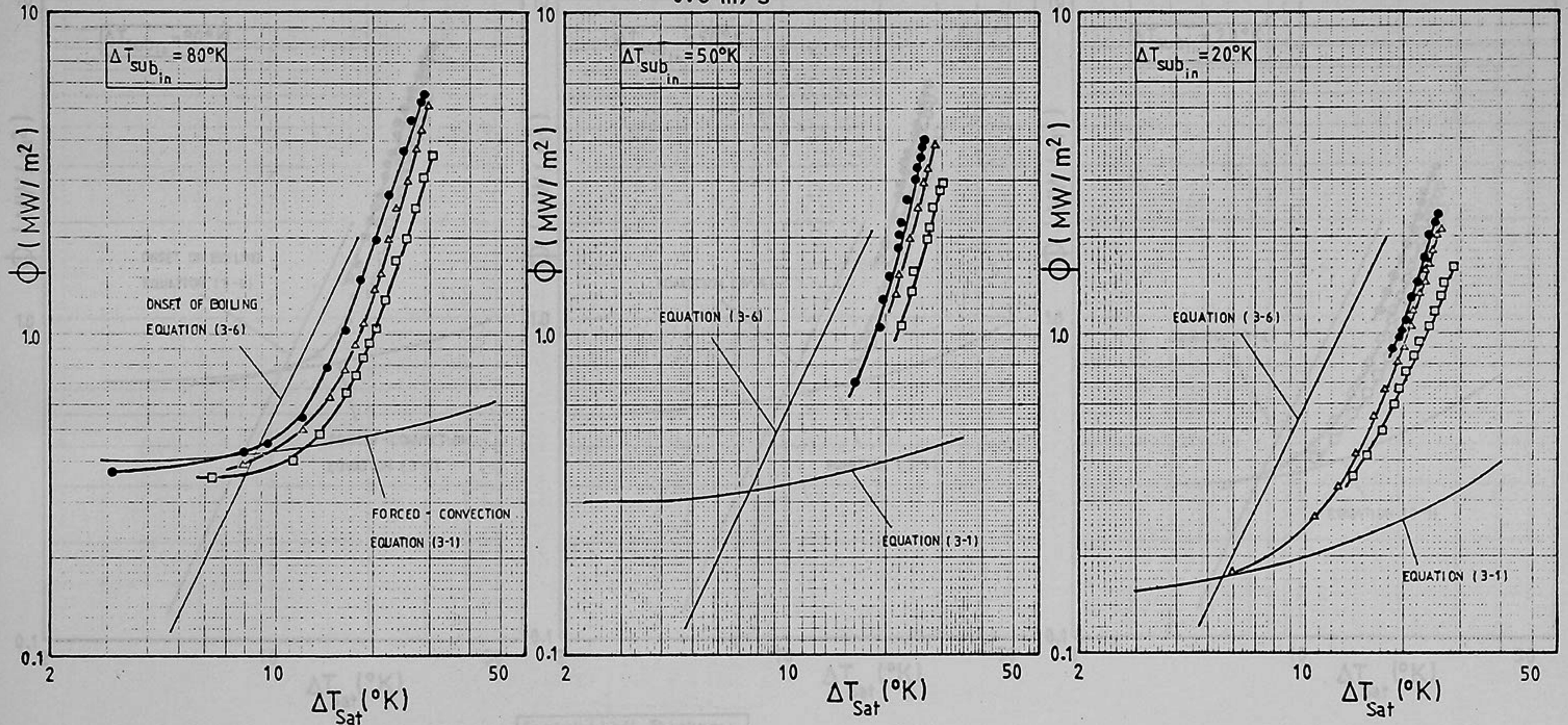
$$\Delta T_{sat} = \psi \emptyset^{n} \qquad (3\text{-}5)$$

where ΔT_{sat} is in ^{o}K and $\emptyset$ is in w/m^{2}, the exponent n for the present data, listed in Table 1, ranged from 0.25 to 0.44, which lies within the range of values reported elsewhere as stated by Collier [1]. However, no systematic relationship was found between the value of the exponent and the three variables considered here, i.e. wall thickness, inlet subcooling and mass velocity.

Table 1. Range of experimental data. Identification run numbers, number of times that each test was conducted and values of the exponent n for the fully-developed boiling region (equation (3-5)) derived from Figures 29 to 31.

System pressure: atmospheric. Water/stainless steel strips (150 mm long x 10 mm wide). Geometry: a channel of rectangular cross-section with one side electrically heated. D_H = 7 mm; L_H = 150 mm. Flow direction: vertical upflow.

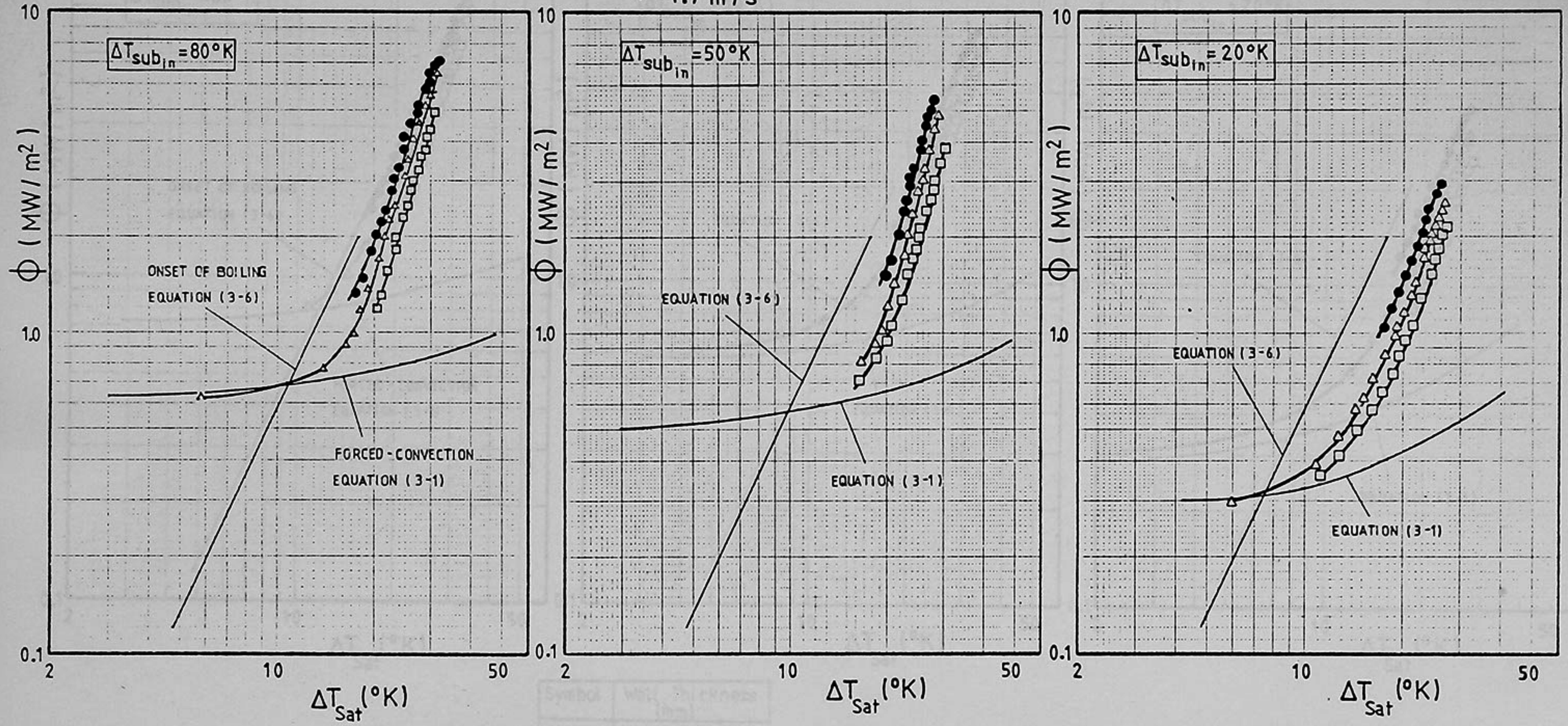
FLOW VELOCITY v(m/sec)	INLET SUBCOOLING $\Delta T_{sub_{in}}$ (^oK)	TEST SECTION WALL THICKNESS								
		δ = 0.08 mm			δ = 0.13 mm			δ = 0.20 mm		
		RUN NUMBER	TIMES CONDUCTED	EXPONENT n	RUN NUMBER	TIMES CONDUCTED	EXPONENT n	RUN NUMBER	TIMES CONDUCTED	EXPONENT n
0.8	80	1	3	0.33	10	2	0.30	19	3	0.33
	50	2	3	0.30	11	2	0.27	20	2	0.25
	20	3	3	0.42	12	2	0.31	21	2	0.32
1.7	80	4	2	0.30	13	3	0.31	22	3	0.35
	50	5	3	0.30	14	2	0.26	23	2	0.28
	20	6	2	0.35	15	2	0.39	24	2	0.40
2.0	80	7	3	0.32	16	4	0.40	25	2	0.44
	50	8	3	0.35	17	2	0.43	26	4	0.41
	20	9	3	0.34	18	3	0.39	27	3	0.44



Symbol	Wall Thickness (mm)
□	0.08
△	0.13
●	0.20

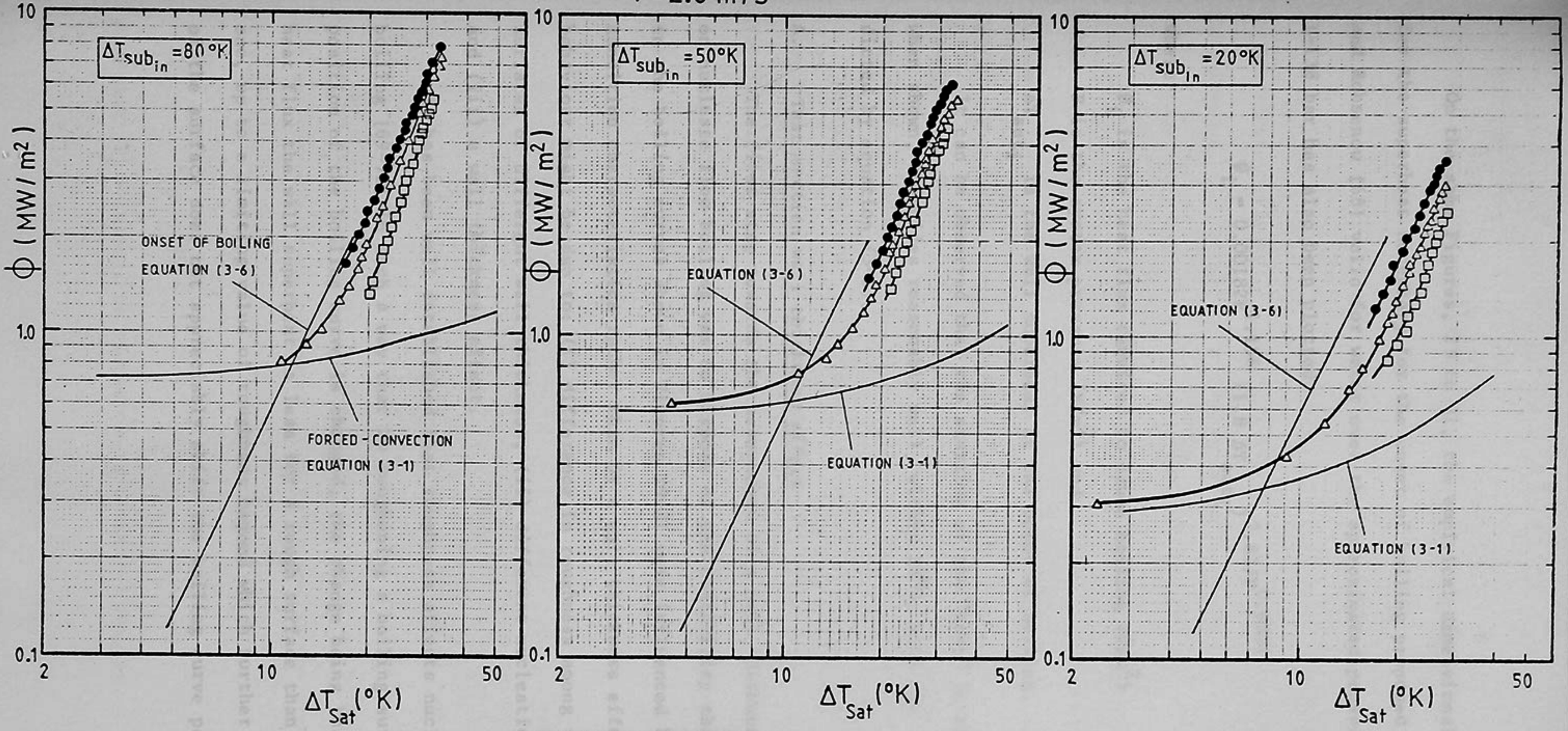
Figure 29 Experimental flow boiling curves; v= 0.8 m/sec.

Water / Stainless Steel
P = 1.013 bar
v = 1.7 m/s



Symbol	Wall Thickness (mm)
□	0.08
△	0.13
●	0.20

Figure 30 Experimental flow boiling curves;
v= 1.7 m/sec.



Symbol	Wall Thickness (mm)
□	0.08
△	0.13
●	0.20

Figure 31 Experimental flow boiling curves; v= 2.0 m/sec.

On the same Figures, 29 to 31, the empirical dimensional expression for the superheat necessary for the onset of boiling proposed by Bergles and Rohsenow [68] valid for water over the approximated pressure range 1-138 bar has also been plotted,

$$\emptyset_i = 0.00182P^{1.156} \ (1.8 \ \Delta T_{sat_i})^{2.83/P^{0.0234}} \qquad (3\text{-}6)$$

where

$\emptyset_i$ is the heat flux required to cause boiling (W/m^2)

P is the system pressure (N/m^2) and

ΔT_{sat_i} is the wall superheat at the onset of boiling.

It can be observed that the starting of the "knee" in the curves, when shown, coincides reasonably well, within $\pm 2^oK$, with the values predicted by equation (3-6).

A. Test section wall thickness effect

The first step towards the assessment of a wall thickness effect on nucleate flow boiling was to dispose of the possibility that the shifts in the boiling curves shown in Figures 29-31 were influenced by surface condition characteristics rather than by a wall thickness effect. Such behaviour might be due to: (i) difference in roughness among the three surfaces of different wall thickness, (ii) different nucleation characteristics and (iii) a wall thickness effect.

It has been well established that roughness affects nucleate boiling [69-72] in such a way that by roughening a boiling surface, the position of the boiling curve is changed, the change being that for a given heat flux the wall superheat is less for a rough surface than for a smoother one, up to a limiting value of roughness beyond which further roughening of the surface does not appreciably shift the boiling curve position.

(i) can be elucidated simply by measuring the relative roughness of the three surfaces. This was done taking random samples of the specimens and measuring their roughnesses lengthwise at several axial locations in a "Talysurf" surface measuring instrument. A typical result is presented in Figure 32 from which it can be observed that the Centre Line Average, CLA, roughness of the three surfaces, is indeed very similar, the average roughness being 0.139μm (±20%).

To examine (ii), specimens of the three surfaces of different thicknesses were submitted to a gas-diffusion test using a method developed to determine surface condition effects on boiling on commercial engineering surfaces by comparing the performance of a surface submitted first to a gas-bubble nucleation experiment and subsequently to a flow boiling experiment, a technique recently proposed by Eddington and Kenning [73].

Briefly the steps in the gas-diffusion procedure are (1) place the clean surface flat in a container and flood it with water saturated with nitrogen at a given initial pressure P_s, (2) wait for a settling period and then reduce the pressure in the container to a final pressure P thus supersaturating the liquid by a $\Delta P = P_s - P$, (3) photograph from above a chosen marked area in which gas bubbles grow at the active nucleation sites with effective radii

$$r_e > \frac{2\sigma}{\Delta p} \qquad (3\text{-}7)$$

By varying the final pressure, a range of activated cavity sizes can be obtained as a function of ΔP. To simulate the effect of subcooling in the gas nucleation tests an overpressure P_2 ($>P_s$) can be applied to the test surface once in the container but before reducing the pressure to P. This defines a prepressurisation level

$$\Delta P_p = P_2 - P_s \qquad (3\text{-}8)$$

such that $\Delta P_p = 0$ would be equivalent to saturated boiling.

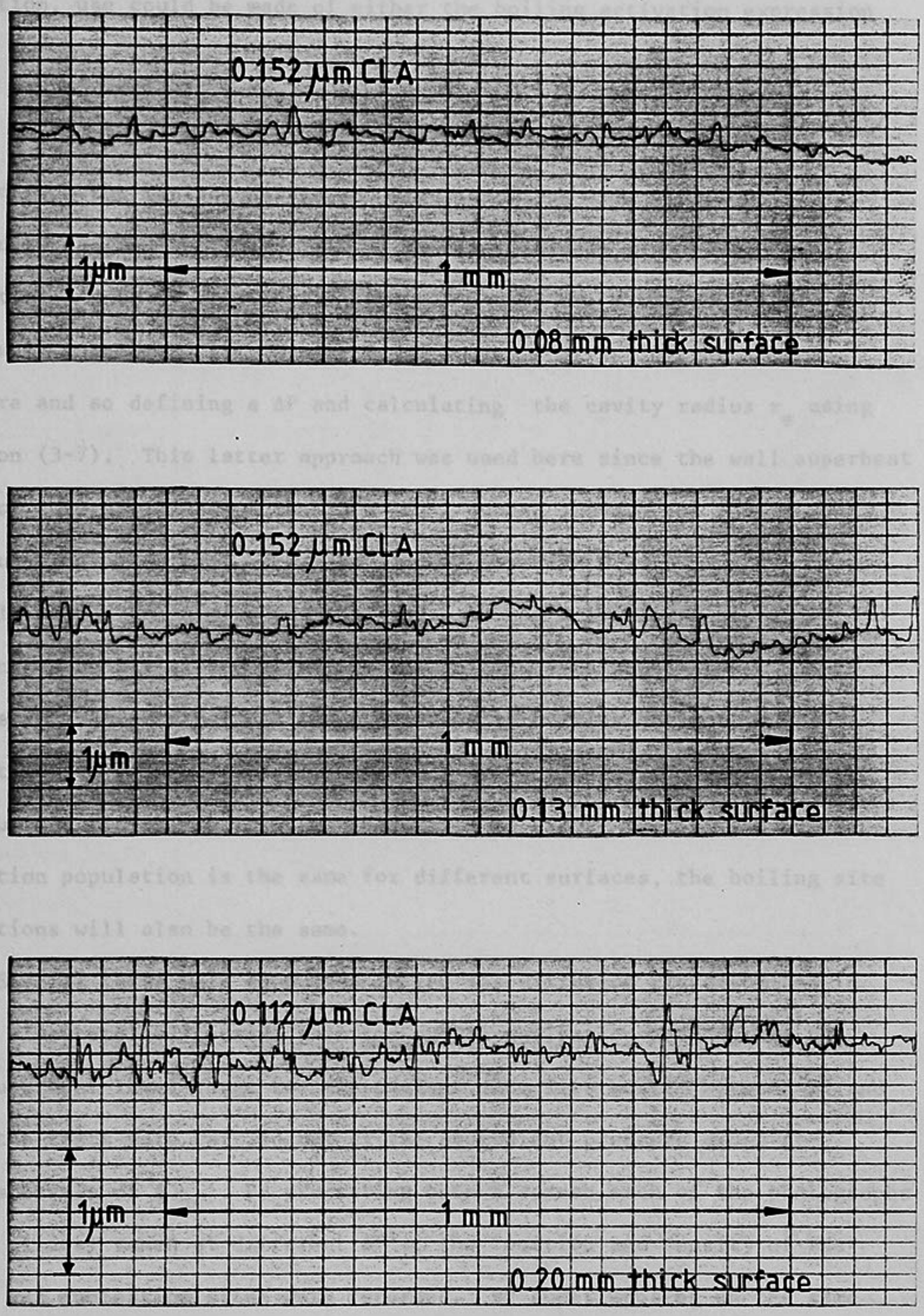


Figure 32 Typical roughness profiles of the test surfaces.

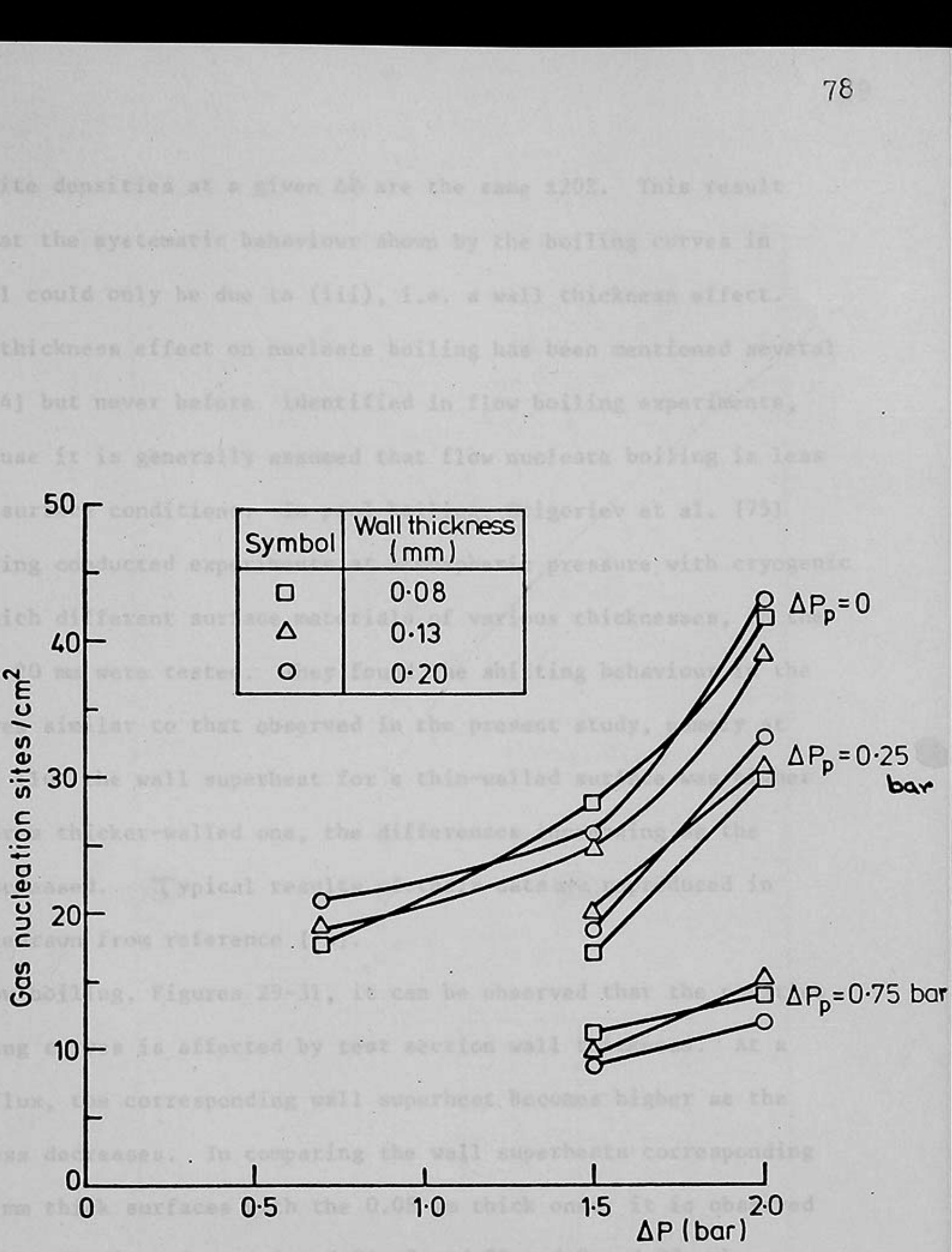
To establish the link between vapour-bubble nucleation and gas-bubble nucleation, use could be made of either the boiling activation expression

$$r_e = \frac{2\sigma T_{sat} V_{fg}}{\lambda \Delta T_{sat}} \qquad (3\text{-}9)$$

derived from the Laplace-Kelvin and Clausius-Clapeyron equations [73] valid only at low superheats ($\sim 10^{o}K$) or alternatively from conventional steam tables data by finding the saturation pressure corresponding to a given wall superheat, i.e. a wall temperature, subtracting the system pressure and so defining a ΔP and calculating the cavity radius r_e using equation (3-7). This latter approach was used here since the wall superheat range of interest exceeded the $10^{o}K$ level quoted above. The cavity radii as a function of ΔP or T_w are tabulated in Appendix C.

It should be pointed out that there is not a 1:1 correspondence between gas bubble site populations and boiling site populations, due to interference effects between sites observed in boiling but not in gas nucleation [73]. Nevertheless, materials are nominally the same with the same surface finish, so it seems reasonable to expect that if gas bubble nucleation population is the same for different surfaces, the boiling site populations will also be the same.

Several tests were conducted in the gas-diffusion rig described in detail elsewhere [62], using this gas bubble nucleation method. As the wall superheat level range for the present data lies mostly between 20 and $35^{o}K$, the tests were carried out at the equivalent pressure drops at various levels of ΔP_p. By projecting onto a screen each of the photographs (35 mm slides) taken at different ΔP's, the location and density of the active gas nucleation sites were recorded. By superimposing on the same screen subsequent photographs, the active gas nucleation site density as a function of ΔP shown in Figure 33, was obtained, hence demonstrating that the surface characteristics of the three surfaces here employed were very similar. For the three surfaces of different wall thickness the gas



Test conditions:
20 minutes settling period.
Photographs taken 10 minutes after pressure reduction

Figure 33. Gas nucleation density as a function of ΔP.

nucleation site densities at a given ΔP are the same ±20%. This result indicates that the systematic bahaviour shown by the boiling curves in Figures 29-31 could only be due to (iii), i.e. a wall thickness effect.

A wall thickness effect on nucleate boiling has been mentioned several times [17, 74] but never before identified in flow boiling experiments, perhaps because it is generally assumed that flow nucleate boiling is less affected by surface conditions. In pool boiling, Grigoriev et al. [75] reported having conducted experiments at atmospheric pressure with cryogenic fluids in which different surface materials of various thicknesses, in the range 0.2 to 20 mm were tested. They found the shifting behaviour in the boiling curves similar to that observed in the present study, namely at a given heat flux the wall superheat for a thin-walled surface was higher than that for a thicker-walled one, the differences increasing as the heat flux increased. Typical results of their data are reproduced in Figure 34, redrawn from reference [75].

In flow boiling, Figures 29-31, it can be observed that the position of the boiling curves is affected by test section wall thickness. At a given heat flux, the corresponding wall superheat becomes higher as the wall thickness decreases. In comparing the wall superheats corresponding to the 0.20 mm thick surfaces with the 0.08 mm thick ones, it is observed that with the exception of runs 6 and 24, 7 and 25 and 9 and 27, where the difference remained nearly constant over the range of heat flux considered, this difference in wall superheat increases as the heat flux is increased, as tabulated in Table 2. Alternatively, at a given wall superheat, the corresponding heat flux becomes higher as wall thickness increases. The difference between the heat flux for a thicker walled surface and that for a thinner one increases with increasing wall superheat as shown in Table 2.

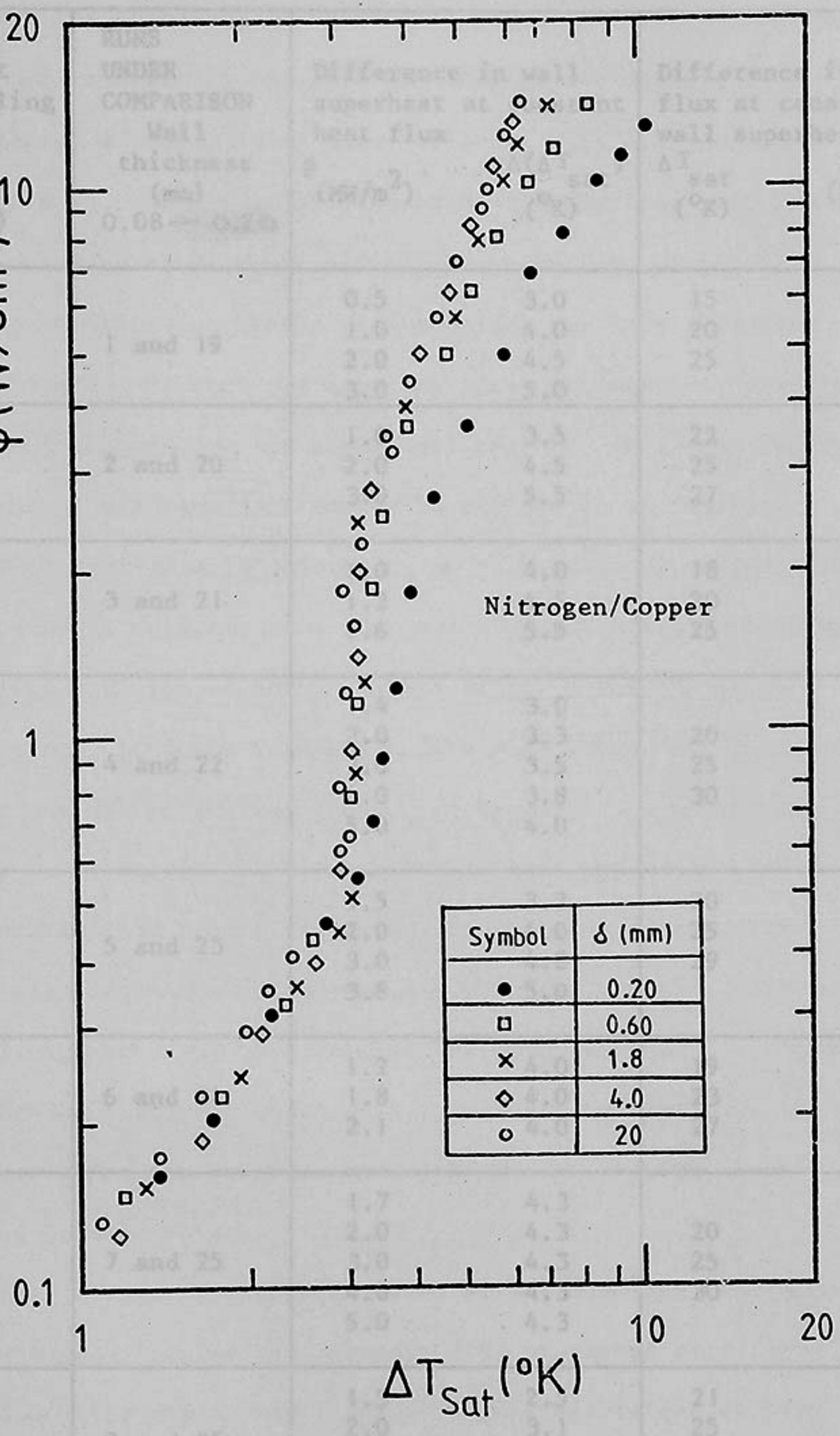


Figure 34 Effect of wall thickness on nucleate pool boiling, (redrawn from Grigoriev et. al. [75]).

Table 2. Difference in wall superheats at constant heat flux and difference in heat fluxes at constant wall superheats for two surfaces of different thickness.

Flow Velocity v (m/sec)	Inlet Subcooling $\Delta T_{sub_{in}}$ (^oK)	RUNS UNDER COMPARISON Wall thickness (mm) 0.08 — 0.20	Difference in wall superheat at constant heat flux		Difference in heat flux at constant wall superheat	
			$\emptyset$ (MW/m^2)	$\Delta(\Delta T_{sat})$ (^oK)	ΔT_{sat} (^oK)	$\Delta\emptyset$ (MW/m^2)
0.8	80	1 and 19	0.5 1.0 2.0 3.0	3.0 4.0 4.5 5.0	15 20 25	0.32 0.83 1.70
	50	2 and 20	1.0 2.0 3.0	3.5 4.5 5.5	22 25 27	0.94 1.40 2.00
	20	3 and 21	1.0 1.2 1.6	4.0 4.5 5.5	18 20 25	0.24 0.40 1.05
1.7	80	4 and 22	1.4 2.0 3.0 4.0 5.0	3.0 3.3 3.5 3.8 4.0	20 25 30	0.60 1.50 1.60
	50	5 and 23	1.5 2.0 3.0 3.8	3.7 4.0 4.8 5.0	20 25 29	0.54 1.70 2.50
	20	6 and 24	1.2 1.8 2.1	4.0 4.0 4.0	19 23 27	0.50 0.77 1.00
2.0	80	7 and 25	1.7 2.0 3.0 4.0 5.0	4.3 4.3 4.3 4.3 4.3	20 25 30	1.05 1.55 2.10
	50	8 and 26	1.5 2.0 3.0 4.0	2.5 3.1 4.1 4.2	21 25 30	0.80 1.25 1.60
	20	9 and 27	1.2 1.8 2.5	5.0 5.0 5.0	18 23 27	0.55 1.10 1.20

B. Inlet Subcooling Effect.

To characterize the effect of subcooling on nucleate boiling, experimental data are often plotted as heat flux against the temperature difference $T_w - \overline{T}_b$. A typical representation of the present data following this procedure is presented in Figure 35. This form of presenting flow boiling data has the advantage of showing up clearly the effect of subcooling, since the curves corresponding to different levels of subcooling are well separated from one another. However, it does not give any clear information regarding its effect on the wall temperature (or superheat) over the fully-developed boiling region and hence the same data should be plotted in the customary manner, i.e. heat flux against wall superheat, as it has been long recognised [36] that this temperature difference is the governing potential in boiling.

Since subcooling and flow velocity notably affect bubble dynamics parameters (f, D_m, etc.), it seems reasonable to expect these variables to exert some influence on the boiling curve. Nevertheless, ever since the excellent early investigation of McAdams et. al [36] who found that in the fully-developed boiling region the relationship between heat flux and wall superheat was independent of subcooling and flow velocity, arguments for and against this independence have arisen, but no author has elucidated this problem by defining precisely under what particular combinations of the forementioned variables the position and slope of the boiling curve will be affected and to what extent.

In pool boiling, two quite opposite trends with subcooling have been reported. On the one hand Bergles and Rohsenow [68] presented data for the fully-developed boiling region and found, for constant values of heat flux, higher values of wall superheat as subcooling was increased. They explained this shifting behaviour by arguing that higher superheats would be required to activate nuclei when the fluid bulk was subcooled. On the other hand, Judd and Merte [76], observed that for a given heat flux the

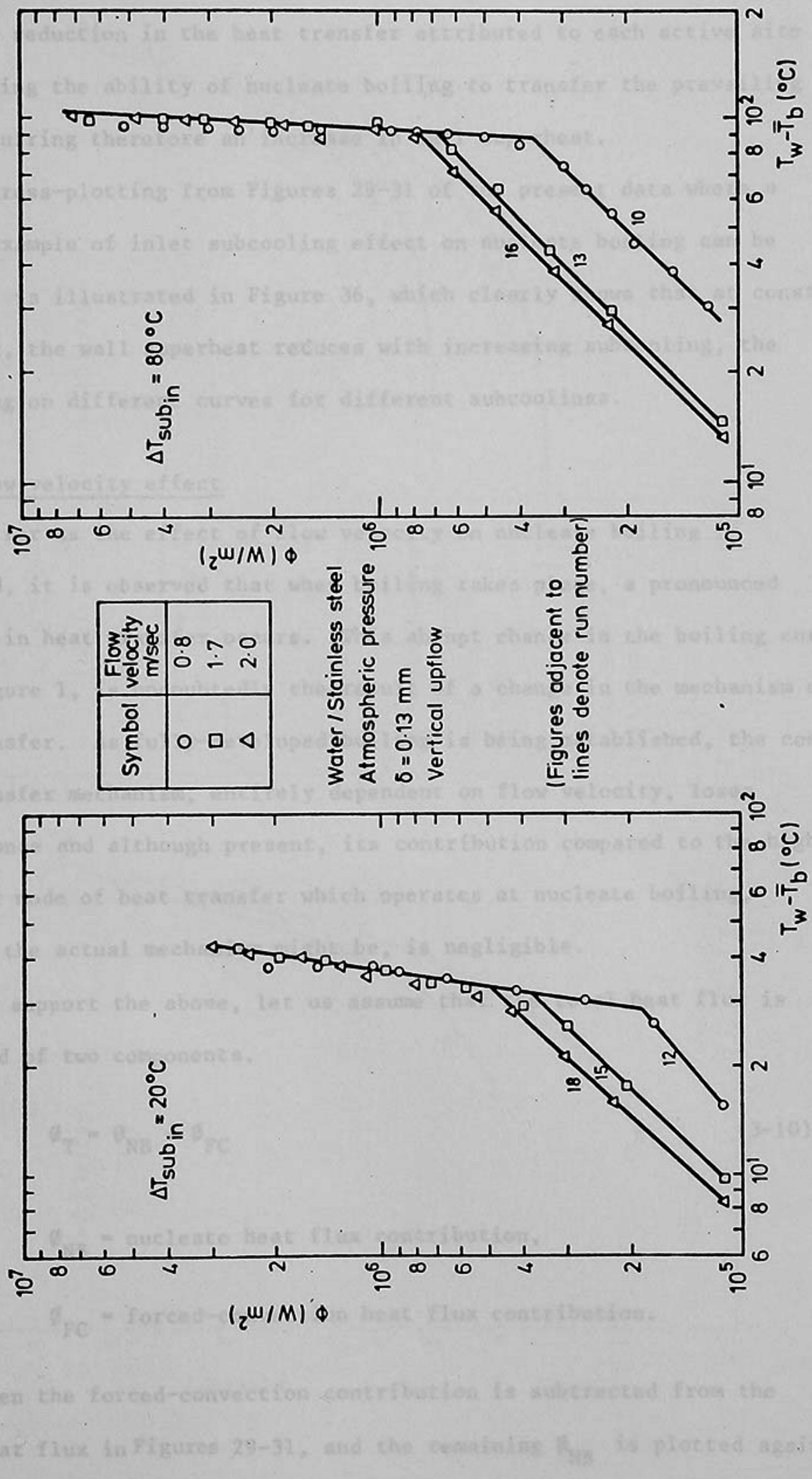


Figure 35. Heat flux against temperature difference $T_w - \bar{T}_b$.

wall superheat first rises slightly and then decreases sharply as subcooling is increased. The explanation given was that as subcooling was increased, maximum bubble diameter and the frequency of bubble emission diminished, causing a reduction in the heat transfer attributed to each active site and limiting the ability of nucleate boiling to transfer the prevailing heat, requiring therefore an increase in wall superheat.

A cross-plotting from Figures 29-31 of the present data where a typical example of inlet subcooling effect on nucleate boiling can be observed, is illustrated in Figure 36, which clearly shows that at constant heat flux, the wall superheat reduces with increasing subcooling, the data lying on different curves for different subcoolings.

C. Flow velocity effect

As far as the effect of flow velocity on nucleate boiling is concerned, it is observed that when boiling takes place, a pronounced increase in heat transfer occurs. This abrupt change in the boiling curve path, Figure 1, is undoubtedly the result of a change in the mechanism of heat transfer. As fully-developed boiling is being established, the convective heat transfer mechanism, entirely dependent on flow velocity, loses significance and although present, its contribution compared to the highly efficient mode of heat transfer which operates at nucleate boiling, whatever the actual mechanism might be, is negligible.

To support the above, let us assume that the total heat flux is comprised of two components.

$$\emptyset_T = \emptyset_{NB} + \emptyset_{FC} \qquad (3\text{-}10)$$

where

$\emptyset_{NB}$ = nucleate heat flux contribution,

$\emptyset_{FC}$ = forced-convection heat flux contribution.

when the forced-convection contribution is subtracted from the total heat flux in Figures 29-31, and the remaining $\emptyset_{NB}$ is plotted against

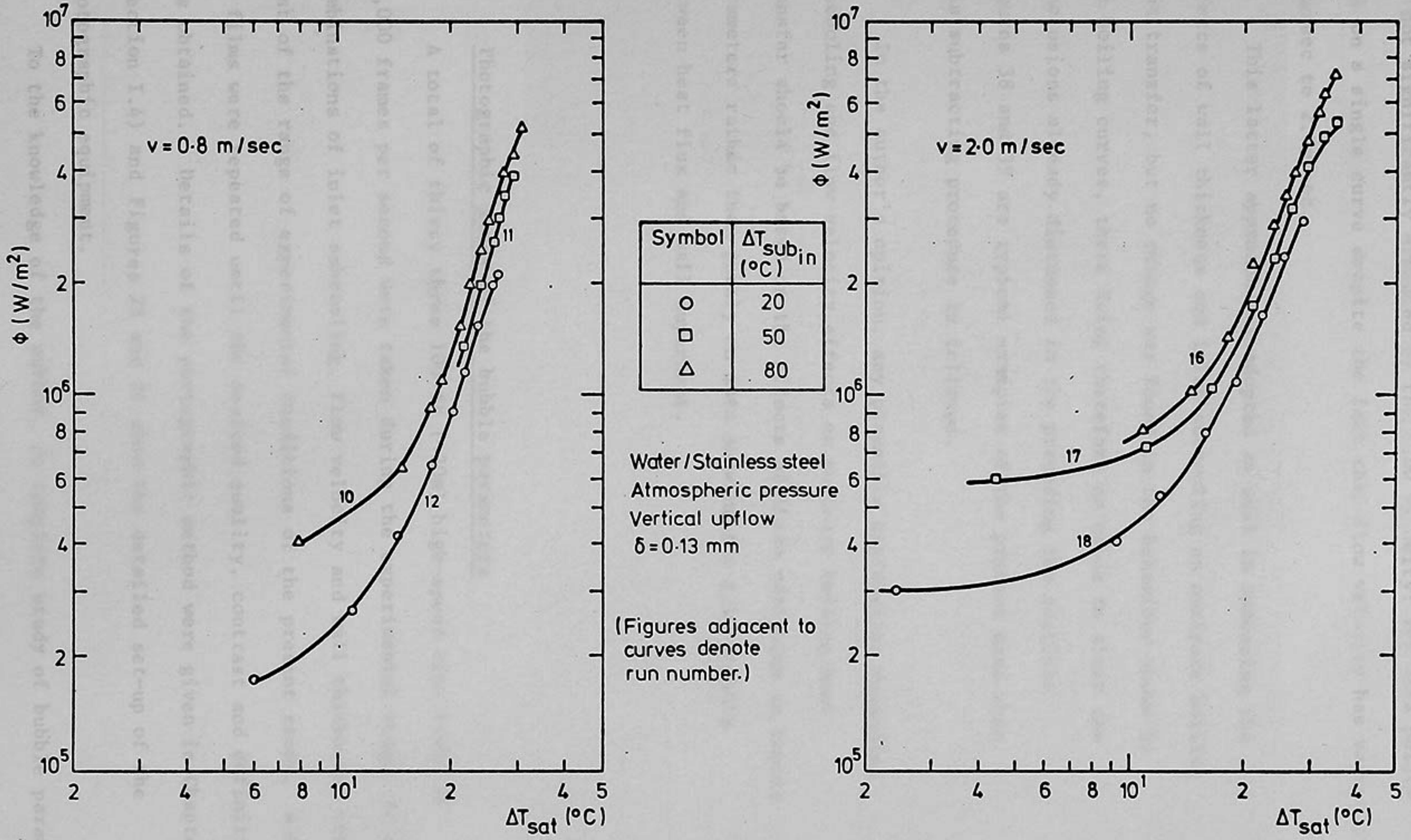


Figure 36. The effect of inlet subcooling on nucleate boiling heat transfer.

superheat as shown in Figure 37, it is observed that the present data are not significantly affected by the flow velocity: the data points lie well on a single curve despite the fact that flow velocity has varied from 0.8m/sec to 2.0m/sec.

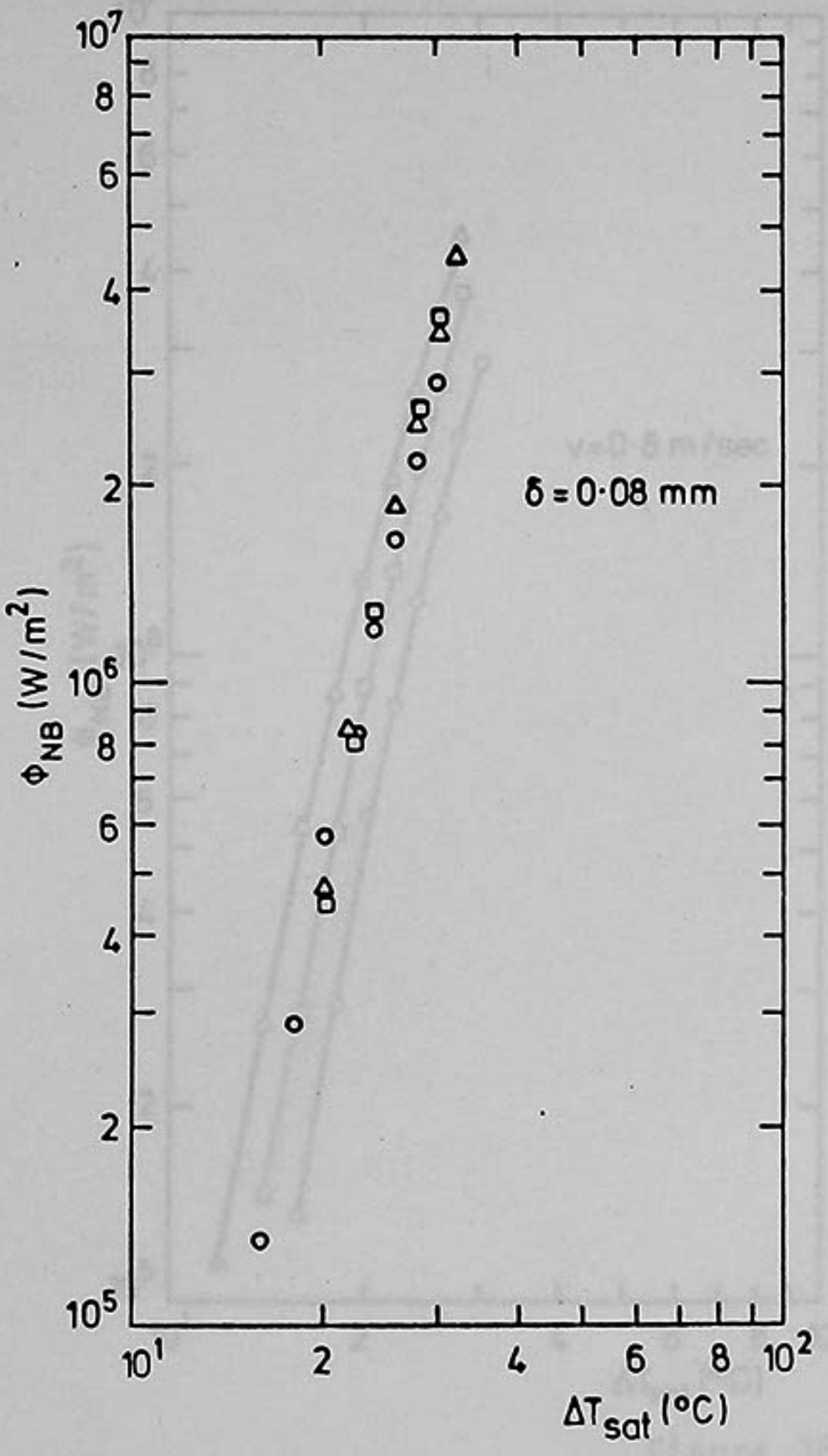
This latter approach was adopted as well in assessing the effects of wall thickness and inlet subcooling on nucleate boiling heat transfer, but no change was found in the behaviour shown by the boiling curves, there being therefore no cause to alter the conclusions already discussed in the preceding two sections. Figures 38 and 39 are typical examples of the present data when this subtracting procedure is followed.

In the author's opinion, any plausible explanation regarding subcooling and flow velocity effects on nucleate boiling heat transfer should be based on the effects of these variables on bubble parameters rather than purely on data showing the relationship between heat flux and wall superheat.

2. Photographic study of the bubble parameters

A total of thirty three 100 ft (∿30m) high-speed cine films at 10,000 frames per second were taken during the experimental stage, at several combinations of inlet subcooling, flow velocity and wall thickness, covering most of the range of experimental conditions of the present study. A number of films were repeated until the desired quality, contrast and definition was obtained. Details of the photographic method were given in Chapter Two (section I.4) and Figures 25 and 26 show the detailed set-up of the photographic equipment.

To the knowledge of the author, no complete study of bubble parameters at heat fluxes as high as 95% of the CHF has been undertaken. This is not



Symbol	v m/sec
○	0·8
□	1·7
△	2·0

Water / Stainless steel
Atmospheric pressure
Vertical upflow
$\Delta T_{sub_{in}} = 80°C$

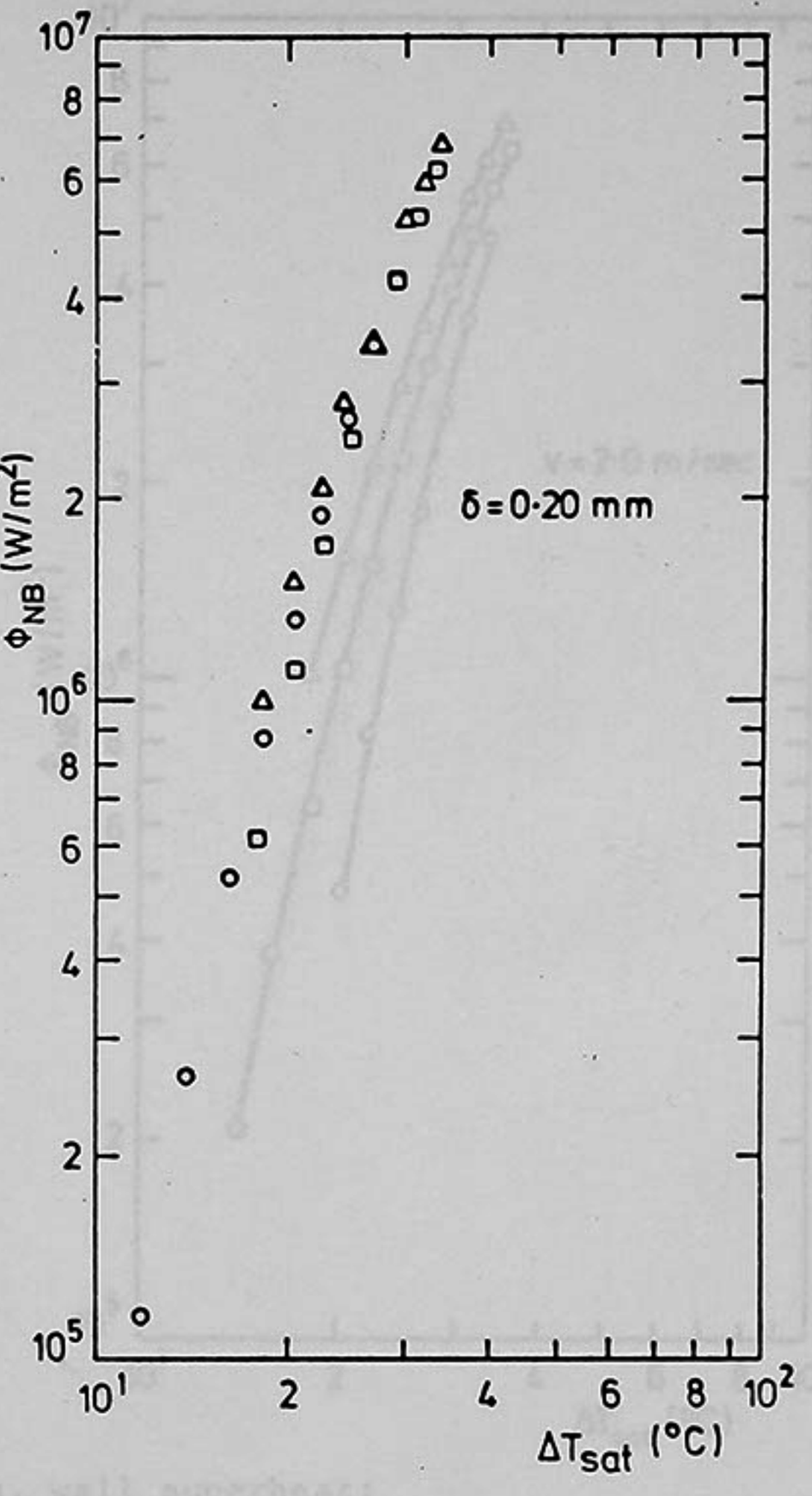


Figure 37. Nulceate boiling heat flux vs. wall superheat: typical flow velocity effect.

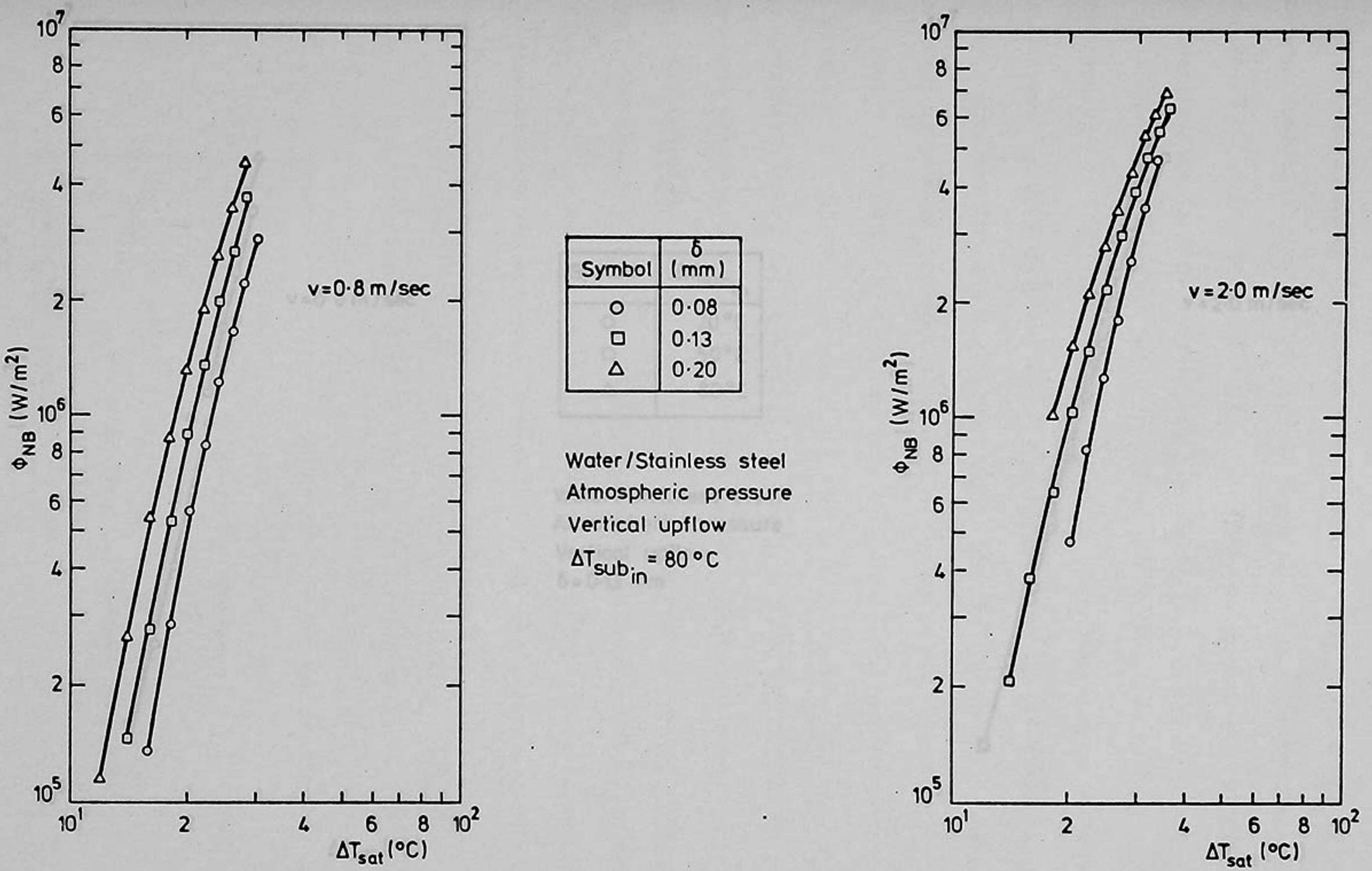
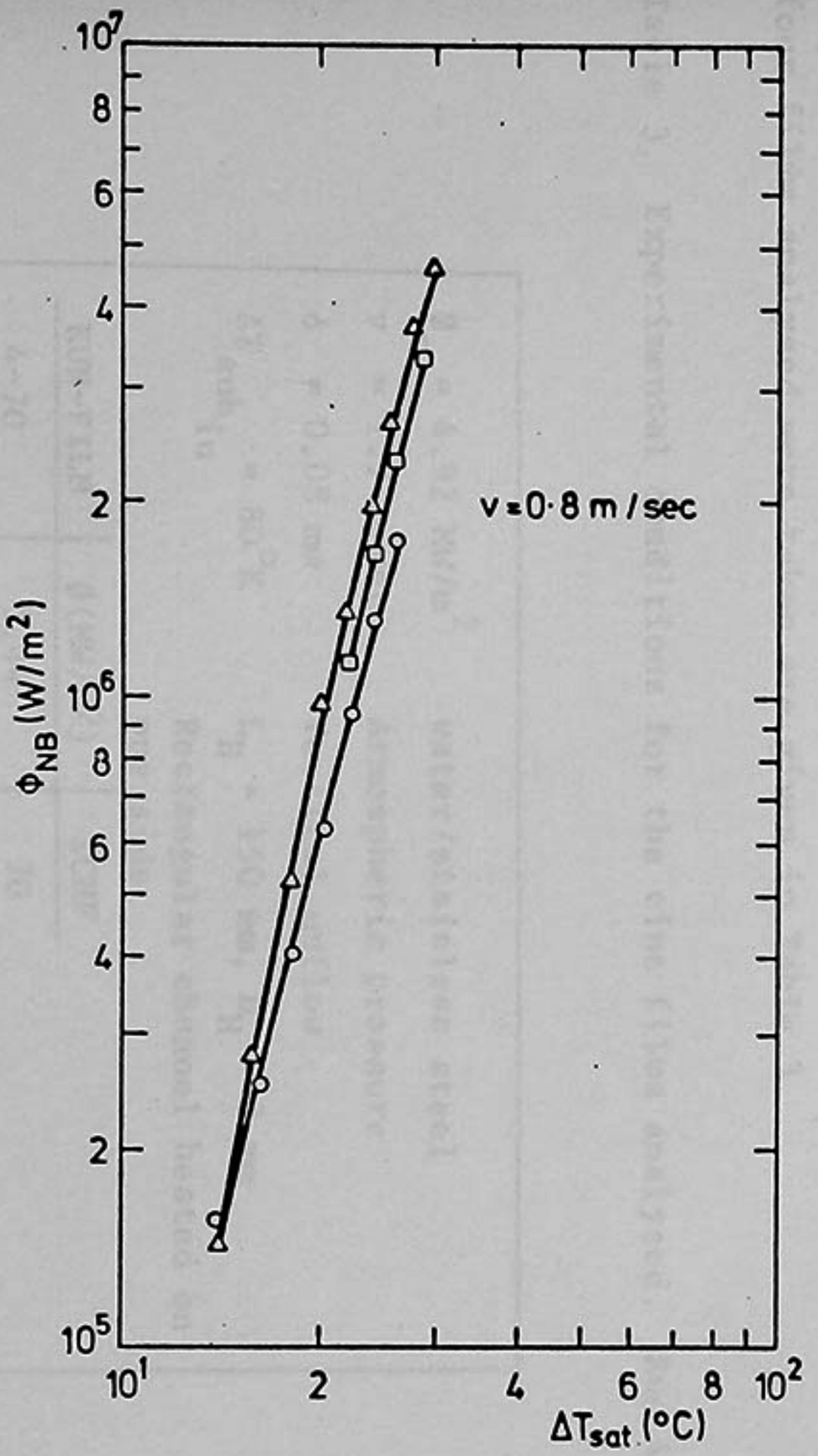


Figure 38. Nucleate boiling heat flux vs. wall superheat: typical wall thickness effect.



Symbol	$\Delta T_{sub_{in}}$
○	20°C
□	50°C
△	80°C

Water / Stainless steel
Atmospheric pressure
Vertical upflow
δ = 0·13 mm

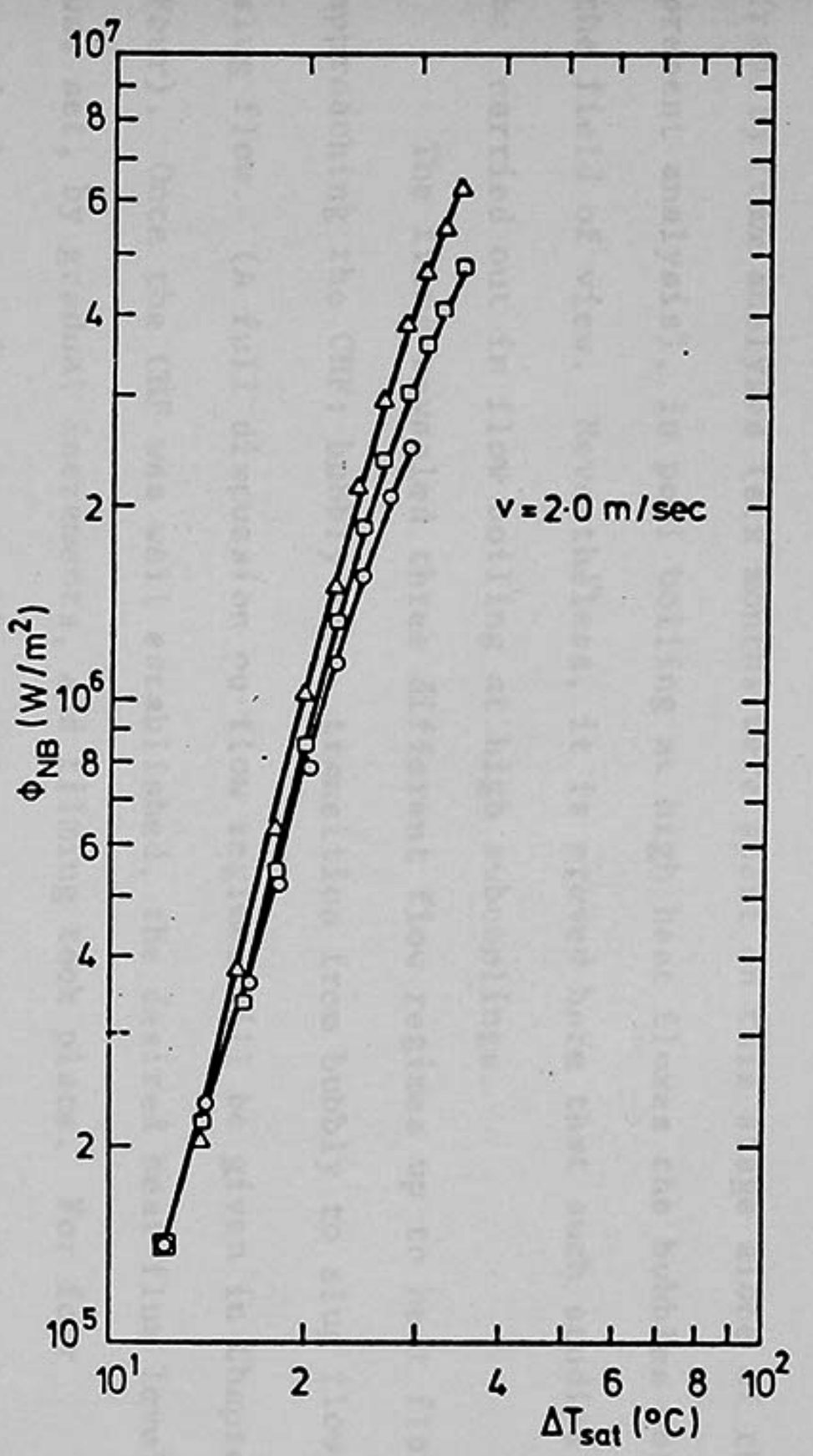


Figure 39. Nucleate boiling heat flux vs. wall superheat: typical subcooling effect.

surprising, since apart from the difficulties which arise from the high-speed cine photography itself, and the highly time-consuming but unavoidable frame by frame analyses (six months were spent on this stage alone of the present analysis), in pool boiling at high heat fluxes the bubbles obscure the field of view. Nevertheless, it is proved here that such studies can be carried out in flow boiling at high subcoolings.

The films revealed three different flow regimes up to heat fluxes approaching the CHF: bubbly flow, transition from bubbly to slug flow and slug flow. (A full discussion on flow regimes will be given in Chapter Four). Once the CHF was well established, the desired heat flux level was set, by gradual increments, and filming took place. For four particular runs (runs 4, 6, 13 and 15, see Table 1 for conditions), a series of four films were taken for the same surface on the same area at constant operational conditions, as the heat flux applied to the test sections was varied from 70 to 95% of the CHF. For the present analysis, in order to obtain a clear view of the boiling surface, experimental run 4 was chosen to determine the bubble parameters since the flow pattern for this particular run was bubbly flow up to the 95% of the CHF value. The conditions which were kept constant, and the heat fluxes at which the four films analysed were taken are given in Table 3.

Table 3. Experimental conditions for the cine films analysed. Run 4.

$\emptyset_c$ = 4.92 MW/m^2	water/stainless steel
v = 1.7 m/sec	Atmospheric pressure
δ = 0.08 mm	Vertical upflow
$\Delta T_{sub_{in}}$ = 80^{o}K	L_H = 150 mm, D_H = 7 mm
	Rectangular channel heated on one side

RUN-FILM	$\emptyset$(MW/m^2)	%CHF
4-70	3.44	70
4-80	3.94	80
4-90	4.43	90
4-95	4.67	95

At each different heat flux, a sample of forty consecutive frames located toward the end of the films, where the cine camera reached full speed, was used to carry out the photographic analysis. This analysis was confined to an area of one square centimetre, being the second square centimetre from the downstream end of the heated section, where burnout normally occurred. Photographic prints from the films enlarged tenfold were used, and the area of interest was marked on the prints, using the voltage clamp connector, Figure 19, as a reference line and the width of the test strip as a dimension reference. One hundred and sixty individual frames were used in this analysis.

A. Method of analysis

Before the prints were used, a first attempt to measure the bubble parameters was made by projecting each frame from the films directly onto graph paper in an attempt to obtain high magnification. However, with this technique it was difficult to distinguish the actual bubble boundaries from the grain grade of the film itself, and after some period of time projecting the same frame, normally 30 to 40 minutes, the film overheated causing some distortion of the bubble images. This method was abandoned and the following technique was found to be satisfactory.

Transparent sheets were laid over the prints and the centre locations of the individual bubbles present on each of the forty frames were marked with small dots using a fine-point marker. This first "bubble locations map" was copied onto tracing paper using another colour marker. The squares on both sheets were numbered in chronological order 1 to 40. By superimposing square (i.e. frame) 1 on top of square 2, then square 2 on top of square 3, and so on, the locations of possible new-born bubbles and their corresponding frames of "birth" were found. This second map of 39 squares corresponding to the bubbles born in frames 2 to 40 (it being impossible to tell which bubbles if any were "born" in the first frame), was subsequently copied onto tracing paper. To eliminate 'sliding' bubbles from the data, single

frames from this sheet of apparent new-born bubbles were checked against the subsequent frame from the original bubble locations map, and bubbles not appearing over at least two consecutive frames were not taken into account, as the average bubble lifetime was found to be 3 to 5 frames.

With its location and frame of birth known, each individual bubble was readily identified and followed in the prints from appearance to collapse. At each heat flux level, 30 bubbles were chosen at random from the prints. The films were then directly projected onto graph paper in order to obtain higher magnification and the selected bubbles were drawn taking great care in following their actual boundaries to obtain shape and size as accurately as possible. These 30 selected bubble pictures for each film were used to determine maximum bubble diameter, diameter as a function time; waiting, growth and life times and frequency of vapour bubble emission, while the new-born bubble maps were used to obtain bubble population density, nucleation site density, spatial distribution of nucleation sites and separation distance between pairs of nearest neighbour nucleation sites.

It was found that most of the bubbles were circular in shape (only two dimensions were considered since the films were taken normal to the boiling surface), growing and collapsing at the same location, from which it was deduced that they remained attached to the surface as in Gunther's study [9]. When the whole films were running in projection, it was observed that a few bubbles generated upstream (out of the field of view) did in fact slide along the surface, mostly close to the edges of the heated strip.

B. The measured bubble parameters

The arithmetical mean values obtained in the present investigation for all the measured bubble parameters are tabulated in Table 4 and plotted against heat flux in Figure 40.

Table 4. Average bubble parameters as a function of heat flux (Run 4).
System pressure: atmospheric. Water/Stainless steel. Vertical upflow.
Geometry: a channel of rectangular cross-section with one side electrically heated.
D_H = 7mm; L_H = 150 mm

Experimental conditions for run 4: $\Delta T_{sub_{in}} = 80^oK$; $v = 1.7$ m/sec; $\delta = 0.08$ mm; $\phi_c = 4.92$ Mw/m^2

RUN/ FILM	% CHF	HEAT FLUX ϕ (MW/m^2)	LIFE TIME t_L (msec)	GROWTH TIME t_g (msec)	WAITING TIME t_w (msec)	BUBBLE CYCLE PERIOD t_c (msec)	FREQUENCY OF BUBBLE EMISSION f (sec^{-1})	MAXIMUM BUBBLE DIAMETER D_m (mm)	BUBBLE POPULATION DENSITY $NX10^{-8}$ ($\frac{bubbles}{m^2 sec}$)	NUCLEATION SITE DENSITY $n_s x10^{-4}$ ($\frac{sites}{m^2}$)	WALL SUPERHEAT ΔT_{sat} (^oK)	SEPARATION DISTANCE BETWEEN TWO NEAREST SITES S (mm)	FRACTION OF SURFACE AFFECTED BY BUBBLES F $= \frac{\pi}{4} D_m^2 n_s$
4-70	70	3.44	0.39	0.195	1.95	2.34	430	0.40	3.92	99	27.6	0.66	0.124
4-80	80	3.94	0.37	0.185	1.80	2.17	460	0.40	5.58	118	28.5	0.61	0.148
4-90	90	4.43	0.34	0.170	1.62	1.96	510	0.40	7.50	141	29.8	0.56	0.177
4-95	95	4.67	0.32	0.160	1.33	1.65	610	0.40	9.95	152	30.1	0.53	0.191

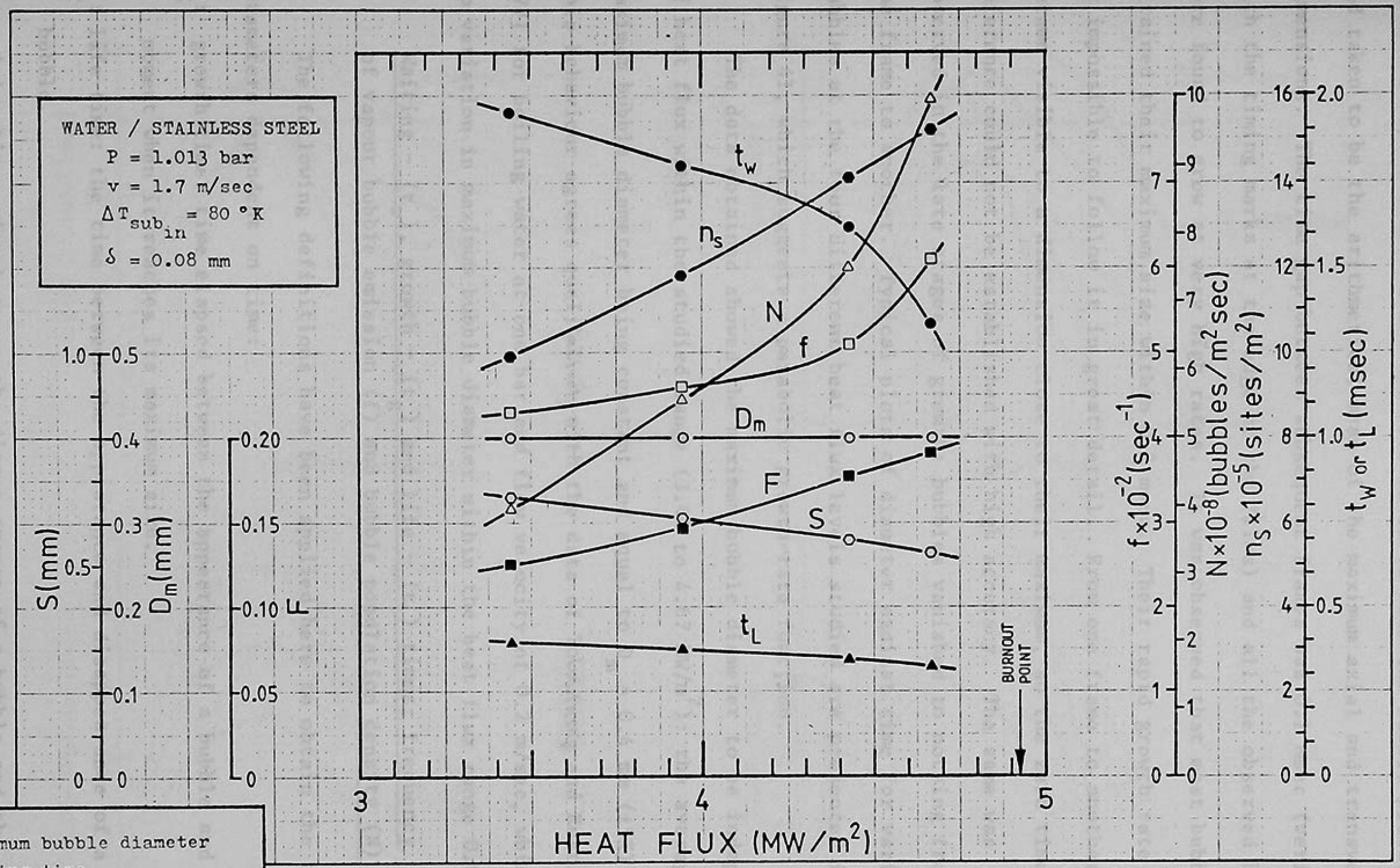


Figure 40. The effect of heat flux on bubble parameters.

a) Maximum bubble diameter, D_m

The vapour bubble diameters were measured from the bubble pictures and taken to be the arithmetical mean of the maximum axial and transverse dimensions. The time gap between subsequent frames was 0.1 msec (verified with the timing marks at the edge of the films) and all the observed bubbles were found to grow at very high rates. It was observed that most bubbles attained their maximum size within 0.2 msec. Their rapid growth rate made it impossible to follow it in great detail. From one frame to another bubbles became visible to a dimension close to their maximum, so the zero time reference could not be established with high accuracy. The same was observed in the late stages of growth: bubbles vanished to nothing from one frame to another. Typical plots of diameter against time for various bubbles at the four different heat flux levels studied are presented in Figure 41, which suggests a parabolic growth-rate function.

The data obtained showed the maximum bubble diameter to be independent of heat flux within the studied range (3.44 to 4.67 MW/m^2): the average maximum bubble diameter being constant and equal to D_m = 0.4 mm (±5%). This behaviour agrees qualitatively with the data of Tolubinsky and Kostanchuk [77] for boiling water at one bar and flow velocity of 0.2 m/sec, which show no variation in maximum bubble diameter within the heat flux range 0.05 to 1.0MW/m^2.

b) Waiting - (t_w), growth - (t_g) and life - (t_L) times; frequency of vapour bubble emission (f) and bubble population density (N)

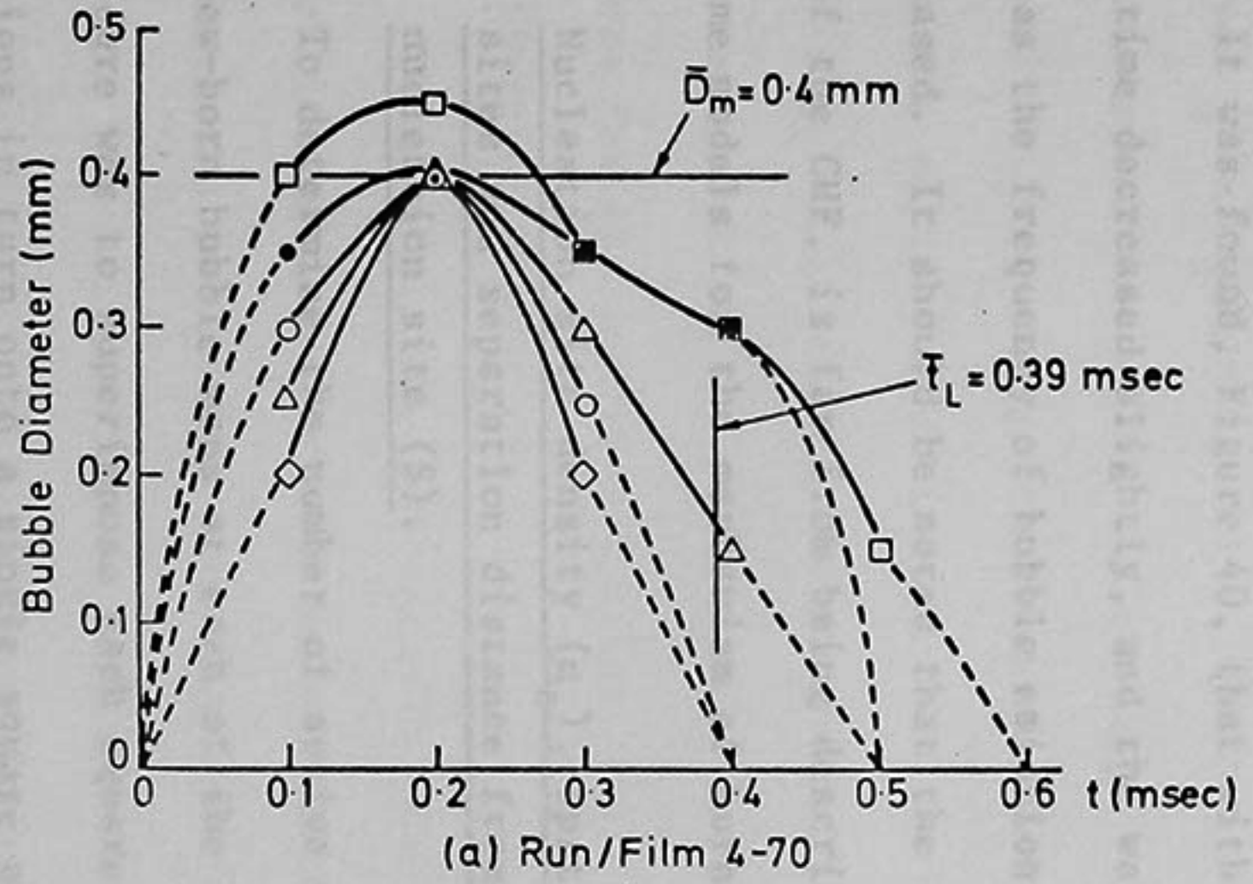
The following definitions have been applied here to obtain the bubble parameters dependent on time:

t_g: growth time: time elapsed between the appearance of a bubble and the moment when it reaches its maximum size.

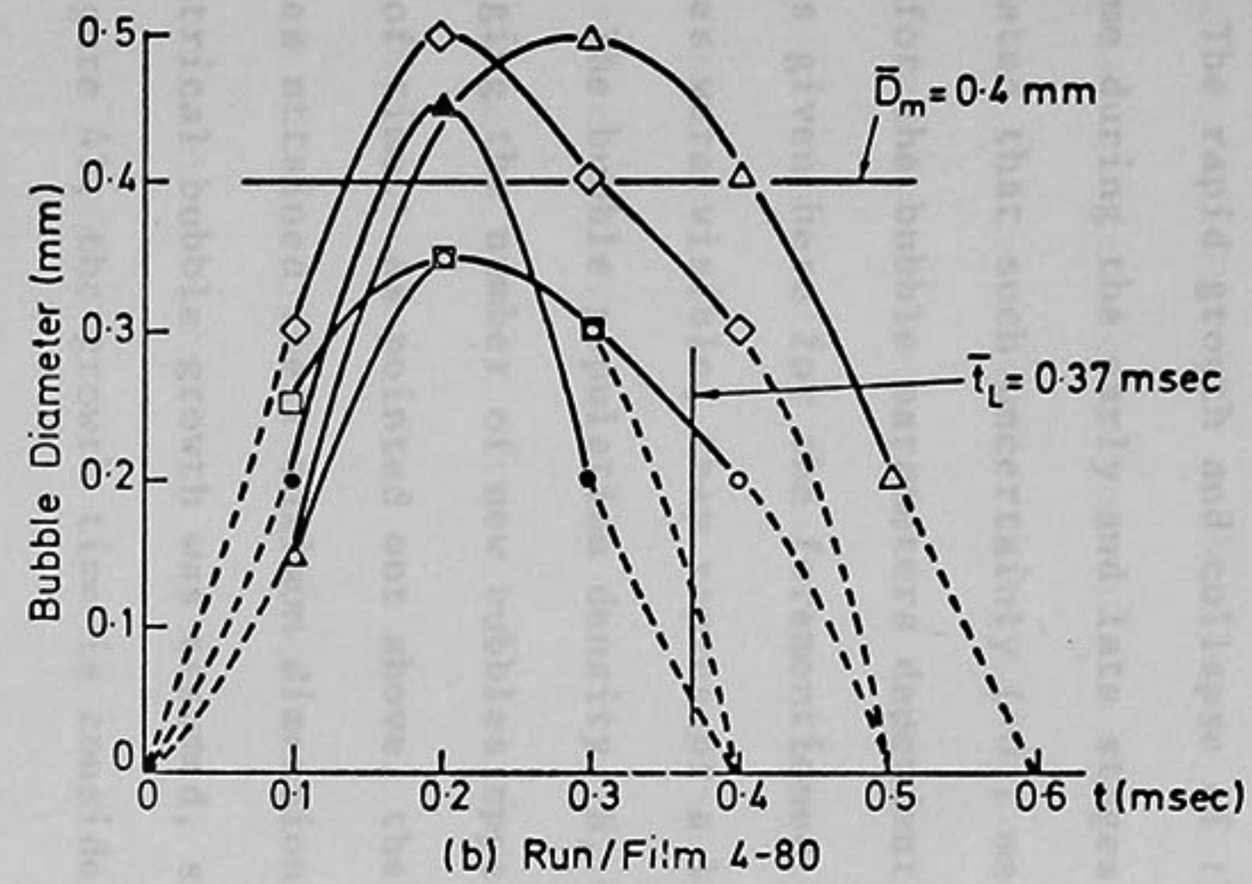
t_L: life time: the time between the appearance and disappearance of a single bubble.

t_W: waiting time: time between the disappearance of a bubble and the appearance of another on the same location.

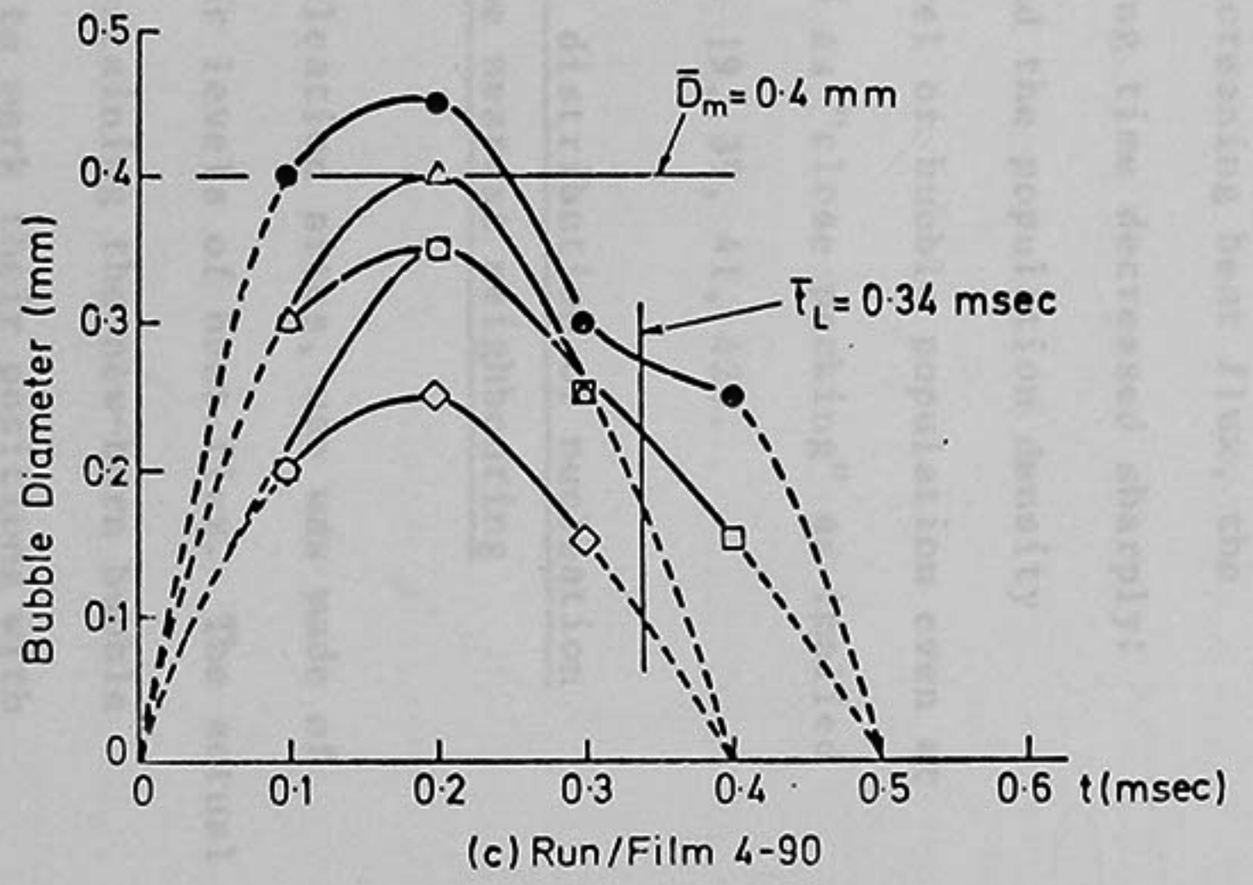
t_c: bubble cycle period = $t_W + t_L$: the time between the appearance of one



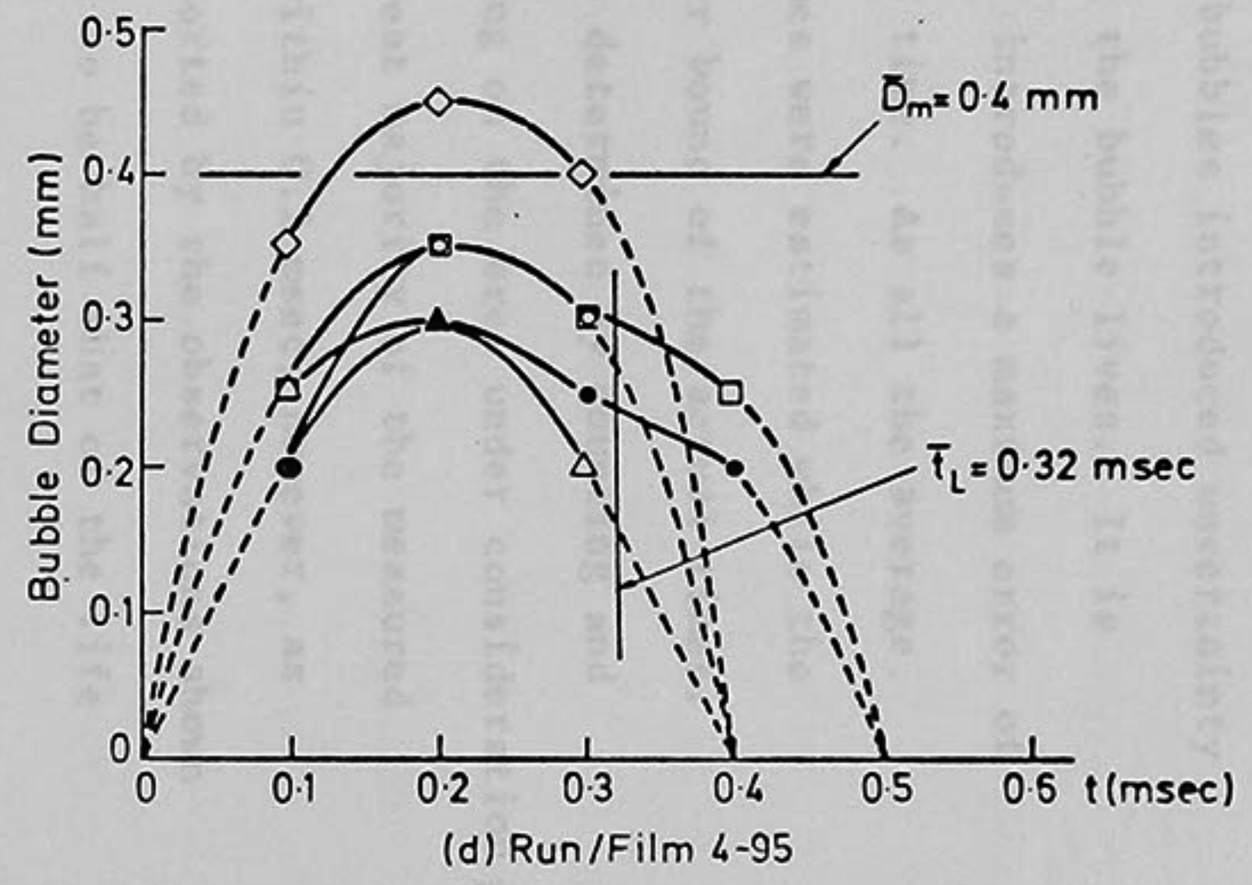
(a) Run/Film 4-70



(b) Run/Film 4-80



(c) Run/Film 4-90



(d) Run/Film 4-95

Figure 41 Bubble diameter as a function of time.

bubble and the appearance of a second one on the same surface location.

f: vapour bubble frequency of emission = $1/t_c$.

The rapid growth and collapse of the bubbles introduced uncertainty in time during the early and late stages of the bubble lives. It is estimated that such uncertainty (+0.1 msec) introduces a maximum error of -20% for the bubble parameters dependent on time. As all the average values given here for the forementioned times were estimated while the bubbles were visible, they represent a lower bound of the actual times.

The bubble population density, N, was determined by counting and averaging the number of new bubbles appearing on the area under consideration per unit of time. As pointed out above, the great majority of the measured bubbles attained their maximum dimensions within 0.2 msec; however, as symmetrical bubble growth was assumed, supported by the observations shown in Figure 41, the growth time is considered to be half that of the life time.

It was found, Figure 40, that with increasing heat flux, the life time decreased slightly, and the waiting time decreased sharply; whereas the frequency of bubble emission and the population density increased. It should be noted that the level of bubble population even at 95% of the CHF, is far from being described as "close packing" as implied in some models for the mechanism of burnout [9, 39, 41, 42].

c) Nucleation site density (n_s), spatial distribution of nucleation sites and separation distance from the nearest neighbouring nucleation site (S).

To determine the number of active nucleation sites, use was made of the new-born bubble maps at each of the four levels of heat flux. The actual procedure was to superimpose each square containing the new-born bubble locations in turn onto a single square and to mark their positions with a small dot. On most of the surface locations considered as active nucleation sites two new born bubbles originated over the 40 frames of film analysed. The corresponding percentage of sites on which just one bubble was originated

(since the analysis was limited to these 40 frames) were 21%, 16%, 10% and 4% for run-film 4-70, 4-80, 4-90 and 4-95 respectively. It was found that the number of active nucleation sites increased with increasing heat flux, but unlike reported data by Gaertner and Westwater [78] and Sultan and Judd [79] who in pool boiling observed that increasing heat flux bubbles continued to originate from nucleation sites already active at lower heat fluxes, in the present study not all the sites activated at a lower heat flux remained active at all higher heat fluxes, but a deactivation and reactivation process took place, which will be discussed in detail later (see secion II.3).

When the heat flux was plotted as a function of the active nucleation site density, Figure 42, it was found that the relationship between these two variables, generally reported as

$$\emptyset \alpha n_s^b \qquad (3\text{-}11)$$

was observed in the present data. The exponent b generally lies between $\frac{1}{3}$ and $\frac{2}{3}$ for metallic surfaces, according to Hsu and Graham [2]. The numerical value for the exponent b in the present study was found to be 0.62 which is in good agreement with the range quoted above.

The spatial distributions of the active nucleation sites for each level of heat flux are presented in Figures 43 and 44, where the dots represent their location and the figures by the dots are identification numbers for the individual sites, used to establish their activation/deactivation histories.

To complete the photographic analysis of the bubble parameters, the separation distance between a nucleation site and its nearest neighbour was measured for each active site at the four different levels of heat flux and the arithmetic mean values are presented in Table 4. As expected, increasing the heat flux, nucleation site density increases, resulting in a decrease in the mean separation distance.

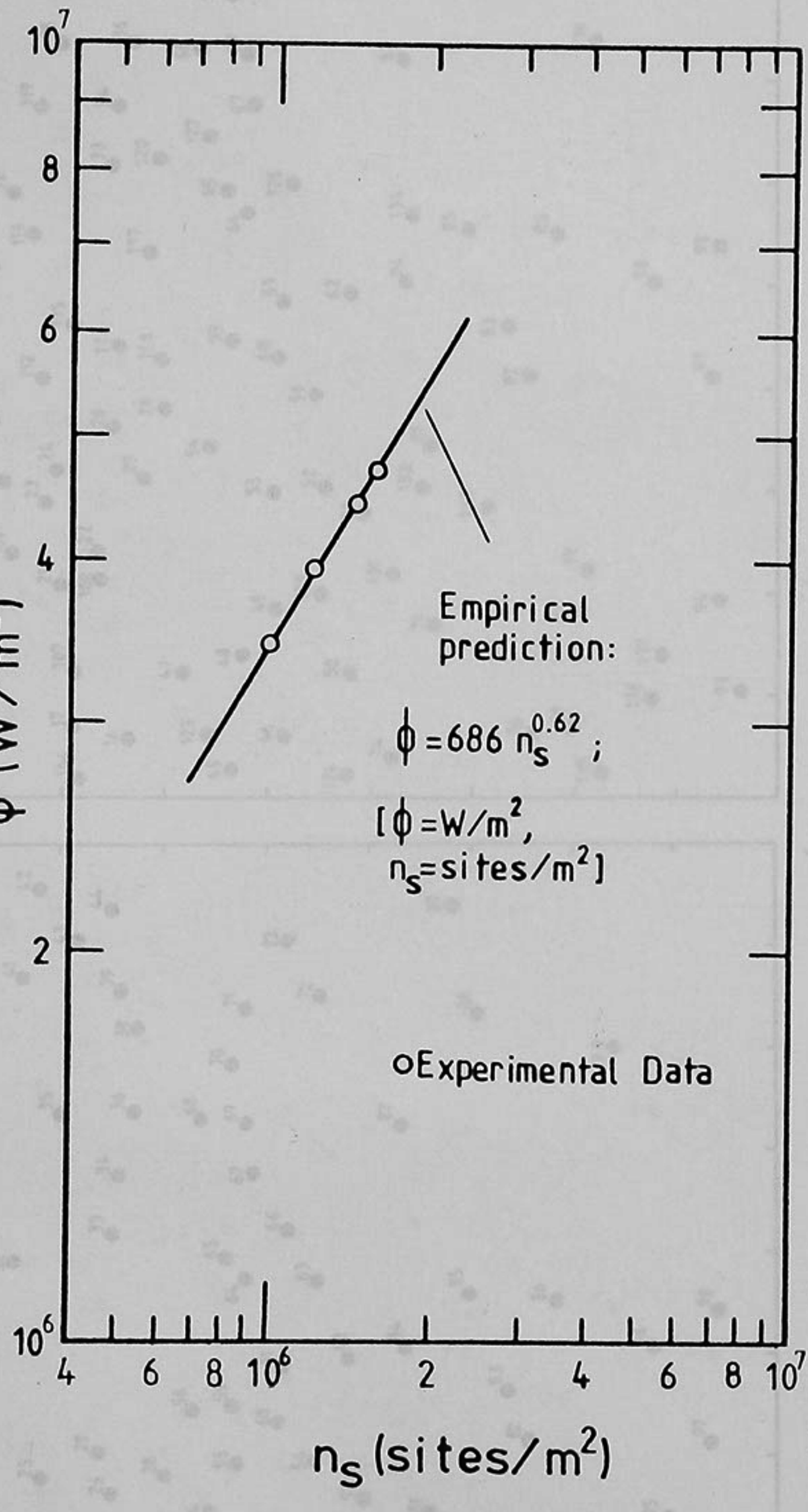


Figure 42. Heat flux as a function of active nucleation site density.

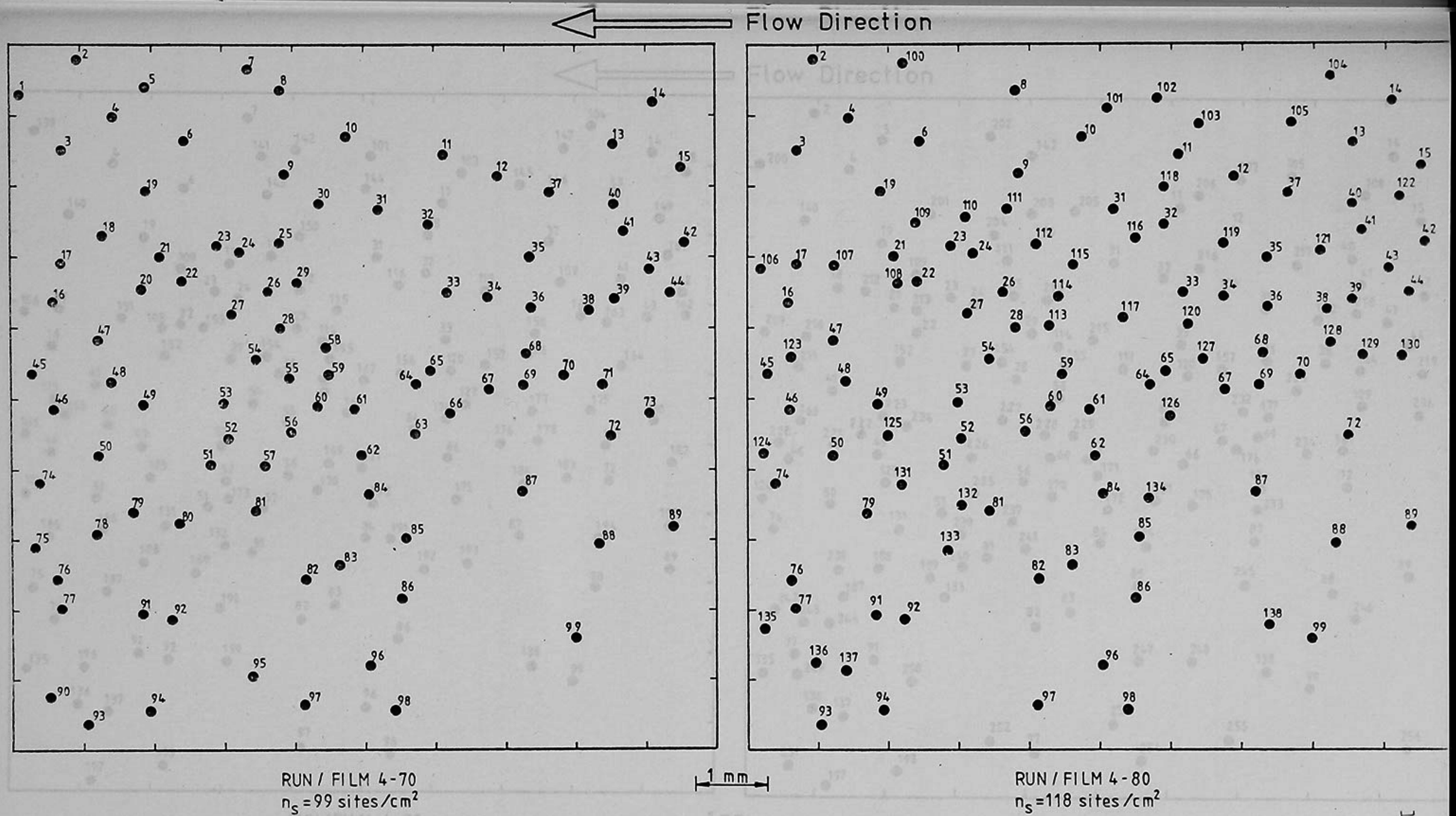


Figure 43 Spatial distribution of nucleation sites, run 4, 70% and 80% of the CHF.

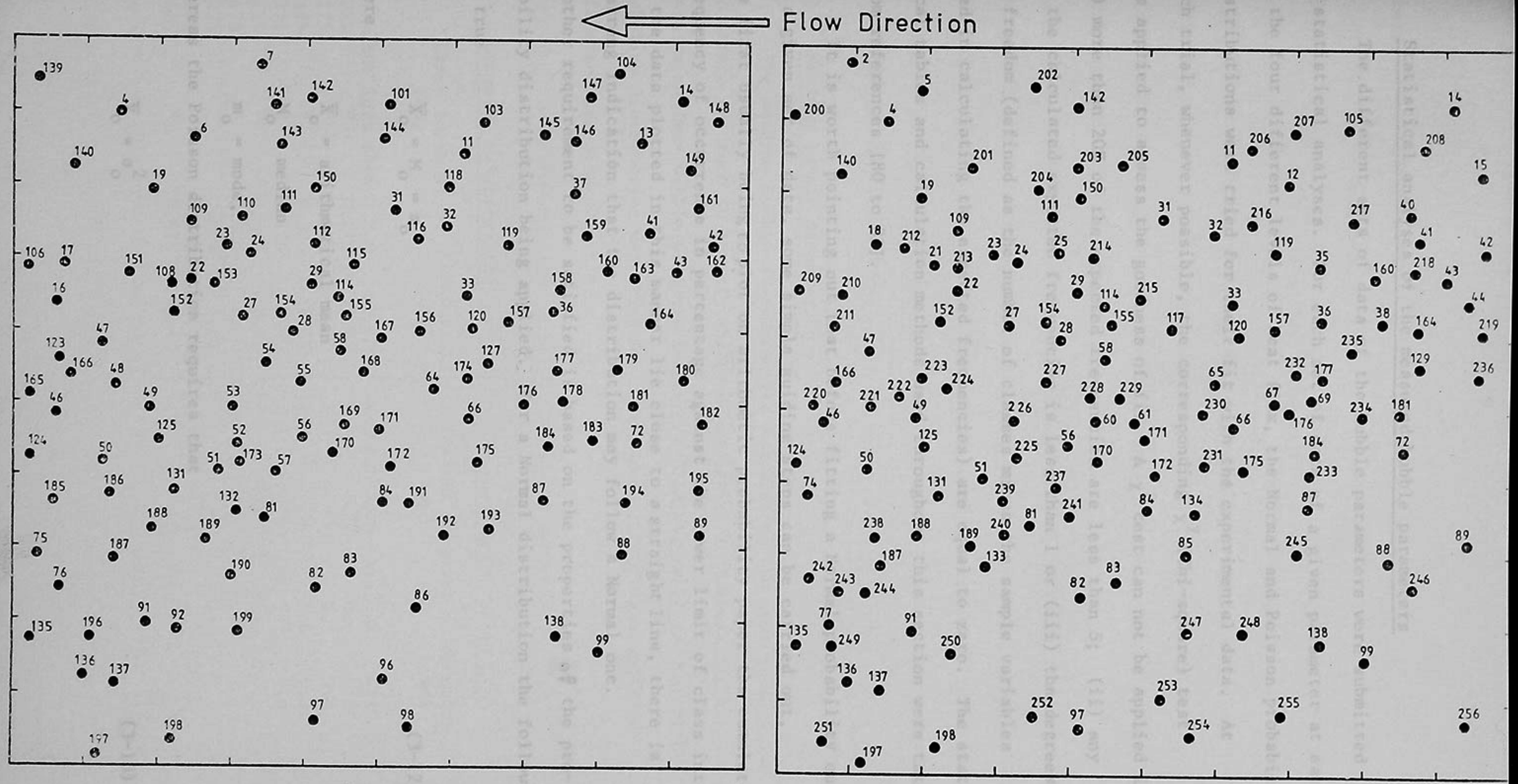


Figure 44 Spatial distribution of nucleation sites, run 4, 90% and 95% of the CHF.

C. Statistical analyses of the measured bubble parameters

The different sets of data of the bubble parameters were submitted to statistical analyses. For each set of data of a given parameter at each of the four different levels of heat flux, the Normal and Poisson probability distributions were tried for their fit with the experimental data. At each trial, whenever possible, the corresponding χ^2 (Chi-square) test was applied to assess the goodness of fit. A χ^2 test can not be applied if: (i) more than 20% of the expected frequencies are less than 5; (ii) any of the calculated expected frequencies is less than 1 or (iii) the degrees of freedom (defined as the number of classes minus the sample variables used in calculating the expected frequencies) are equal to zero. The statistical tables and calculation methods used throughout this section were taken from references [80 to 82].

It is worth pointing out that before fitting a Normal probability curve to a given set of data, some simple guiding steps can be carried out, the first usually being to plot on arithmetic probability paper the cumulative frequency of occurrence in percentage against the lower limit of class interval. If the data plotted in this manner lie close to a straight line, there is a strong indication that the distribution may follow a Normal one. Another requirement to be satisfied is based on the properties of the probability distribution being applied. For a Normal distribution the following is true

$$\bar{X}_o = M_o = m_o \qquad (3\text{-}12)$$

where

$\bar{X}_o$ = arithmetical mean

M_o = median

m_o = mode,

whereas the Poisson distribution requires that

$$\bar{X}_o = \sigma_o^2 \qquad (3\text{-}13)$$

where

σ_o^2 = variance

($\sigma_o = \sqrt{\sigma_o^2}$ = standard deviation)

If the conditions established by equations (3-12) or (3-13) are not satisfied within certain margins (usually ±20%), the given sample distribution could not have been drawn from a population having a Normal or Poisson distribution respectively.

When a statistical analysis is being applied, it is very important to specify the criteria adopted during the testing procedure. Surprisingly, very often this is neglected and the final results frequently lack detailed information, which may lead to inadequate interpretations. This point is considered further below.

a) Maximum bubble diameter.

The maximum bubble diameters were measured to the nearest 0.05 mm. To stress the need to specify criteria precisely, an example for the data on maximum bubble diameter is presented below, where the Normal probability distribution was tried to fit the same set of data under two different grouping criteria.

Grouping criterion (1)				Grouping criterion (2)			
Class interval (mm)			Midpoint (mm)	Class interval (mm)			Midpoint (mm)
0.175	but less than	0.225	0.20	0.2	but less than	0.3	0.25
0.225	"	0.275	0.25	0.3	"	0.4	0.35
0.275	"	0.325	0.30	0.4	"	0.5	0.45
0.325	"	0.375	0.35	0.5	"	0.6	0.55
0.375	"	0.425	0.40	0.6	"	0.7	0.65
0.425	"	0.475	0.45				
0.475	"	0.525	0.50				
0.525	"	0.575	0.55				
0.575	"	0.625	0.60				
0.625	"	0.675	0.65				

Under these grouping criteria, the maximum bubble diameter data are presented in Figure 45, plotted as frequency of occurrence against midpoint, and the difference can easily be appreciated: under the grouping criterion (1) the data bear no resemblance to a Normal distribution. Figure 46 shows the same sets of data plotted on arithmetic probability paper and Table 5 gives the mean, median and mode values calculated for these two grouping criteria. It is observed that using scheme (2) the data tend to lie closer to straight lines and the measures of central tendencies are less scattered as is indicated by the ratio of the highest to lowest measure of central tendency used as an index proportional to the degree of scatter. It is worth recalling that when grouping takes place, the calculation of the arithmetic mean proceeds differently than without grouping. This latter method was used to obtain the average values of the bubble parameters of the present data shown in Figure 40, with the exception of the frequency of bubble emission data for which the average values given were calculated using the harmonic mean. The arithmetical mean without grouping is calculated.

$$\overline{X}_{o_i} = \frac{\sum_{i=1}^{n_o}}{n_o} \tag{3-14}$$

whereas when grouping takes place it is expressed as

$$\overline{X}_o = \frac{\sum_{i=1}^{n_o} X_{o_i} f_{o_i}}{\sum_{i=1}^{n_o} f_{o_i}} = \frac{\sum_{i=1}^{n_o} X_{o_i} f_{o_i}}{n_o} \tag{3-15}$$

The Normal probability distribution was tried for fit with the data of run-film 4-90 under the two forementioned grouping criteria and the resulting curves are presented in Figure 47, where the difference stands out at a glance: when grouping criterion (1) is applied, the experimental data are far from behaving in a Normal manner, while when using criterion (2), the data closely follow a Normal distribution. The

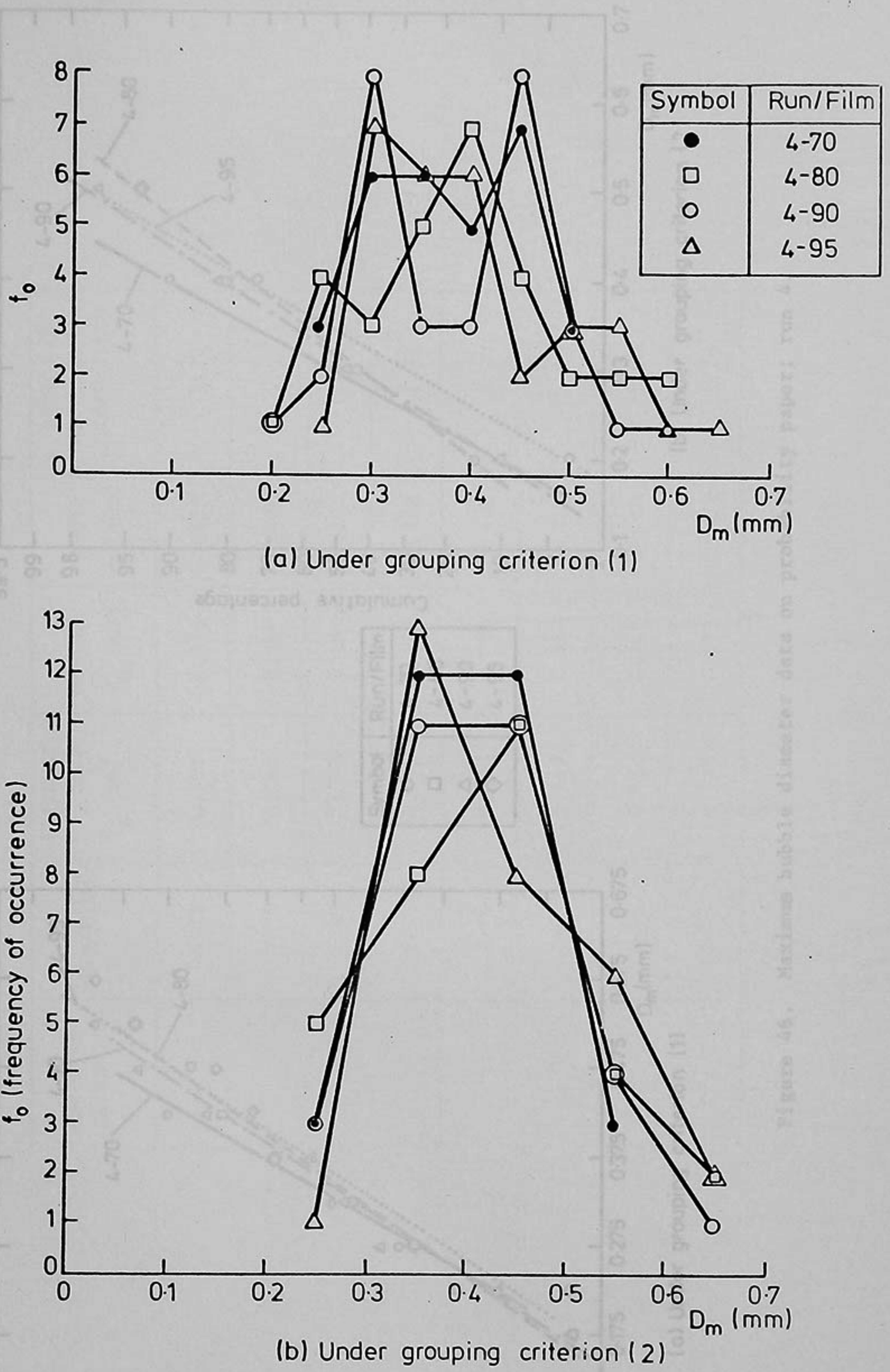
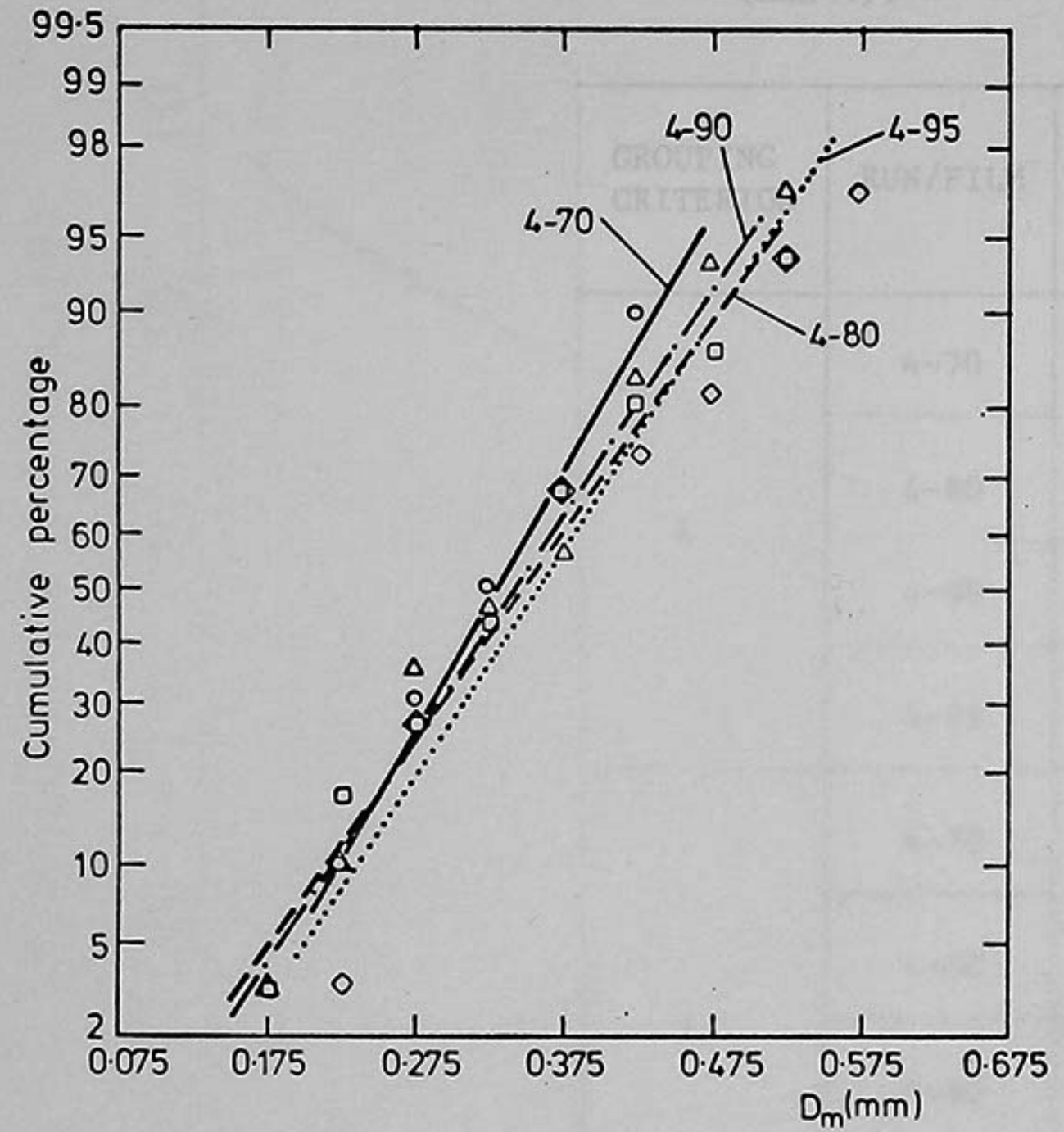
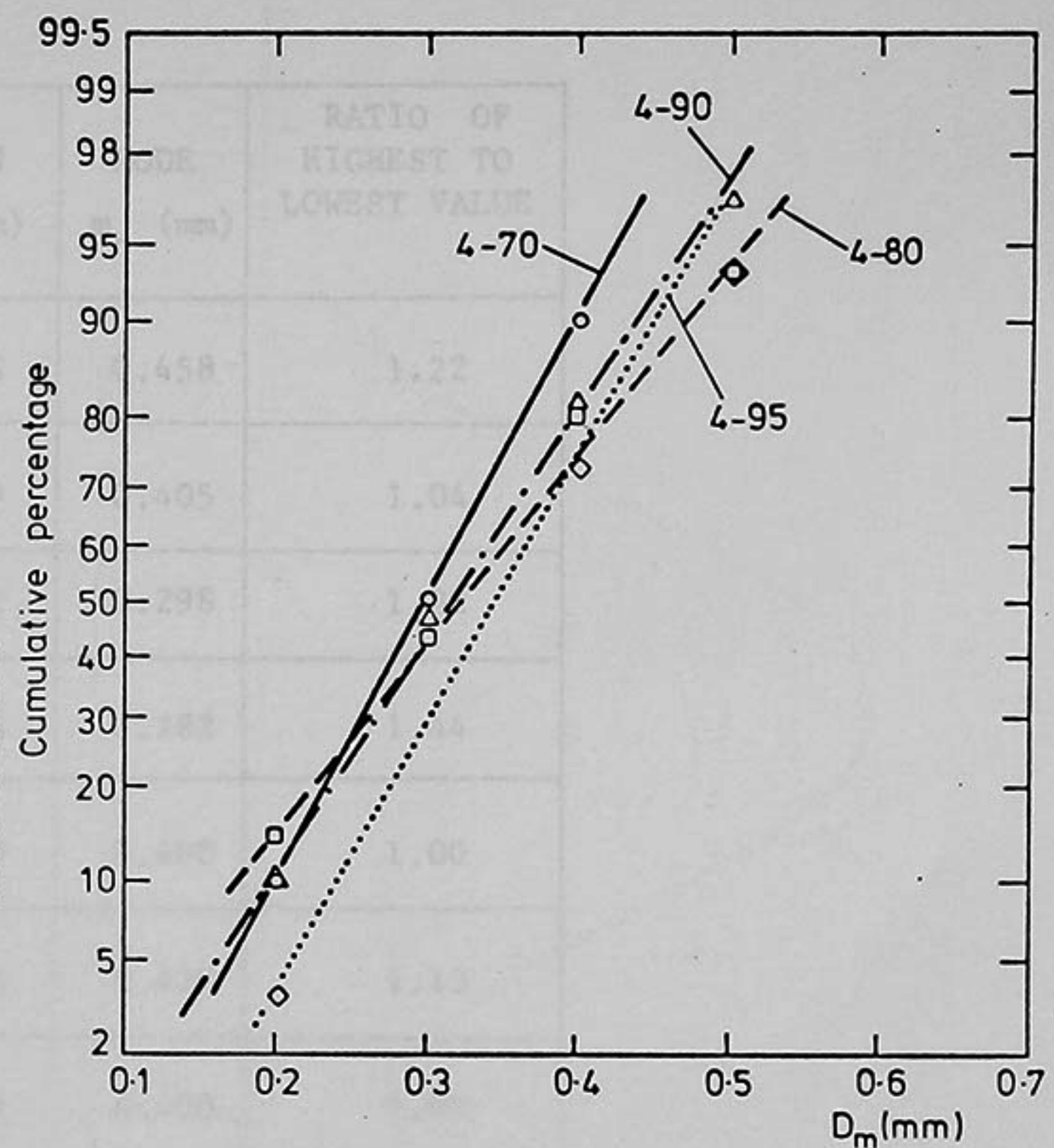


Figure 45. Maximum bubble diameter data under two different grouping criteria; run 4.



(a) Under grouping criterion (1)

Symbol	Run/Film
○	4-70
□	4-80
△	4-90
◇	4-95

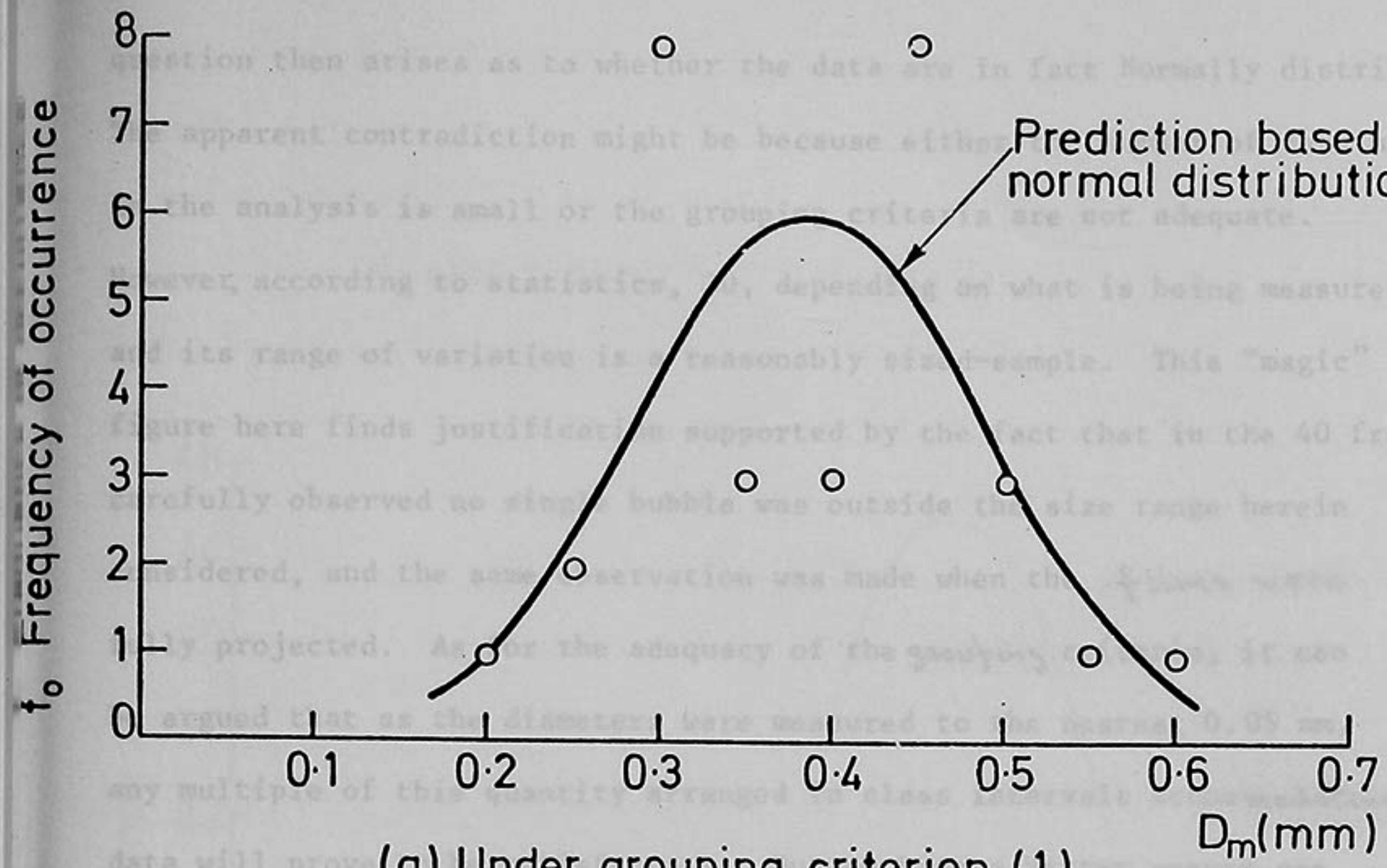


(b) Under grouping criterion (2)

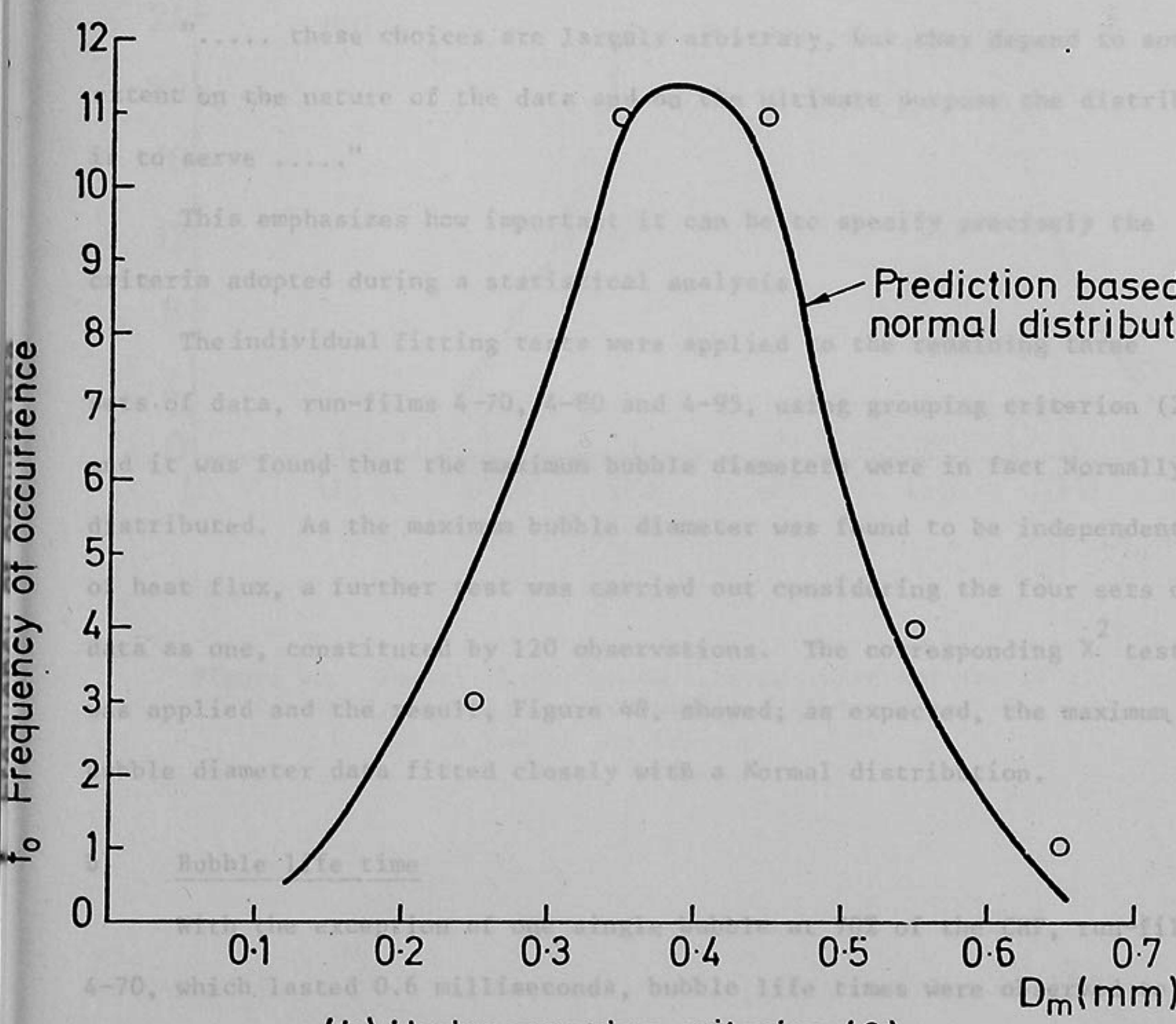
Figure 46. Maximum bubble diameter data on probability paper; run 4.

Table 5. Statistical measures of central tendencies for maximum bubble diameter data under two different grouping criteria (Run 4).

GROUPING CRITERION	RUN/FILM	ARITHMETIC MEAN $\overline{D}_m$ (mm)	MEDIAN M_o (mm)	MODE m_o (mm)	RATIO OF HIGHEST TO LOWEST VALUE
1	4-70	0.377	0.375	0.458	1.22
	4-80	0.392	0.389	0.405	1.04
	4-90	0.387	0.392	0.298	1.32
	4-95	0.405	0.383	0.282	1.44
2	4-70	0.400	0.400	0.400	1.00
	4-80	0.417	0.418	0.470	1.13
	4-90	0.413	0.409	0.400	1.03
	4-95	0.432	0.413	0.334	1.29



(a) Under grouping criterion (1)



(b) Under grouping criterion (2)

Figure 47. Normal distribution fitting curves for maximum bubble diameter data; run-film 4-90.

question then arises as to whether the data are in fact Normally distributed. The apparent contradiction might be because either the number of data used in the analysis is small or the grouping criteria are not adequate. However, according to statistics, 30, depending on what is being measured and its range of variation is a reasonably sized-sample. This "magic" figure here finds justification supported by the fact that in the 40 frames carefully observed no single bubble was outside the size range herein considered, and the same observation was made when the films were fully projected. As for the adequacy of the grouping criteria, it can be argued that as the diameters were measured to the nearest 0.05 mm, any multiple of this quantity arranged in class intervals accommodating all data will prove to be satisfactory. But perhaps a better answer can be found in Freund [80] who stated:

"..... these choices are largely arbitrary, but they depend to some extent on the nature of the data and on the ultimate purpose the distribution is to serve ....."

This emphasizes how important it can be to specify precisely the criteria adopted during a statistical analysis.

The individual fitting tests were applied to the remaining three sets of data, run-films 4-70, 4-80 and 4-95, using grouping criterion (2) and it was found that the maximum bubble diameters were in fact Normally distributed. As the maximum bubble diameter was found to be independent of heat flux, a further test was carried out considering the four sets of data as one, constituted by 120 observations. The corresponding χ^2 test was applied and the result, Figure 48, showed, as expected, the maximum bubble diameter data fitted closely with a Normal distribution.

b) Bubble life time

With the exception of one single bubble at 70% of the CHF, run-film 4-70, which lasted 0.6 milliseconds, bubble life times were observed to lie within 0.3 to 0.5 milliseconds, and it was this rather small range,

Under grouping criterion (2)

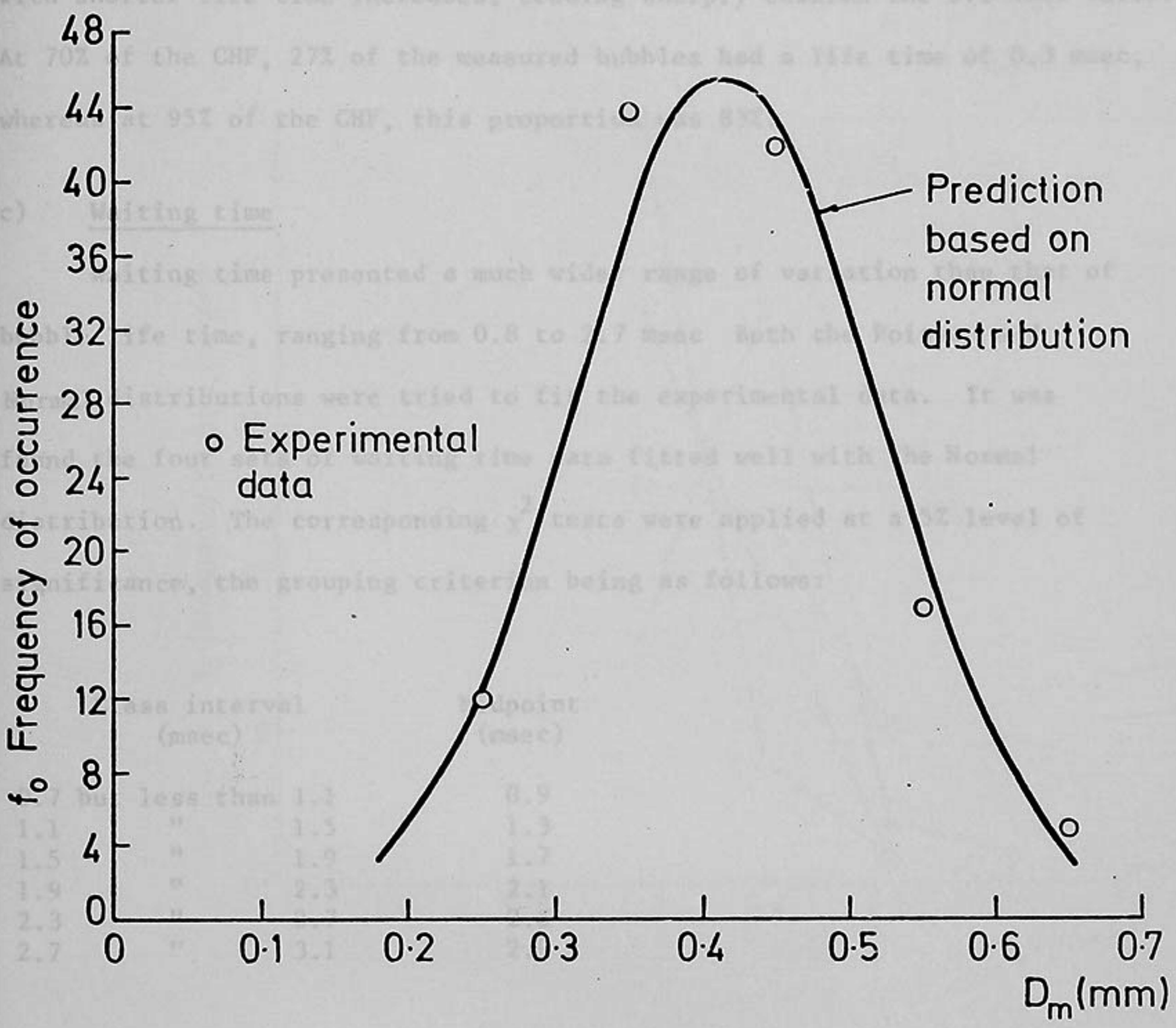


Figure 48. Normal distribution fitting curve for the total number of maximum bubble diameter data. Run 4, 70% to 95% of the CHF.

giving only 3 class intervals, which made it impossible to test any fitting procedure (see section II.2.C.). As the heat flux was increased the values of 0.3 and 0.4 msec predominated. The frequency of occurence polygons of the bubble life time data as obtained are presented in Figure 49, where it can be observed that as the heat flux increases, the number of bubbles with shorter life time increases, tending sharply towards the 0.3 msec value. At 70% of the CHF, 27% of the measured bubbles had a life time of 0.3 msec, whereas at 95% of the CHF, this proportion was 83%.

c) Waiting time

Waiting time presented a much wider range of variation than that of bubble life time, ranging from 0.8 to 2.7 msec Both the Poisson and Normal distributions were tried to fit the experimental data. It was found the four sets of waiting time data fitted well with the Normal distribution. The corresponding χ^2 tests were applied at a 5% level of significance, the grouping criterion being as follows:

Class interval (msec)	Midpoint (msec)
0.7 but less than 1.1	0.9
1.1 " 1.5	1.3
1.5 " 1.9	1.7
1.9 " 2.3	2.1
2.3 " 2.7	2.5
2.7 " 3.1	2.9

Figure 50 shows the Normal distribution fitting curves for the four sets of data. It can be observed that as the heat flux is increased the mean waiting time decreases sharply and the range of variation becomes narrower.

d) Frequency of bubble emission

It has been suggested [83] that for calculating the average value of frequency of bubble emission use should be made of the harmonic mean

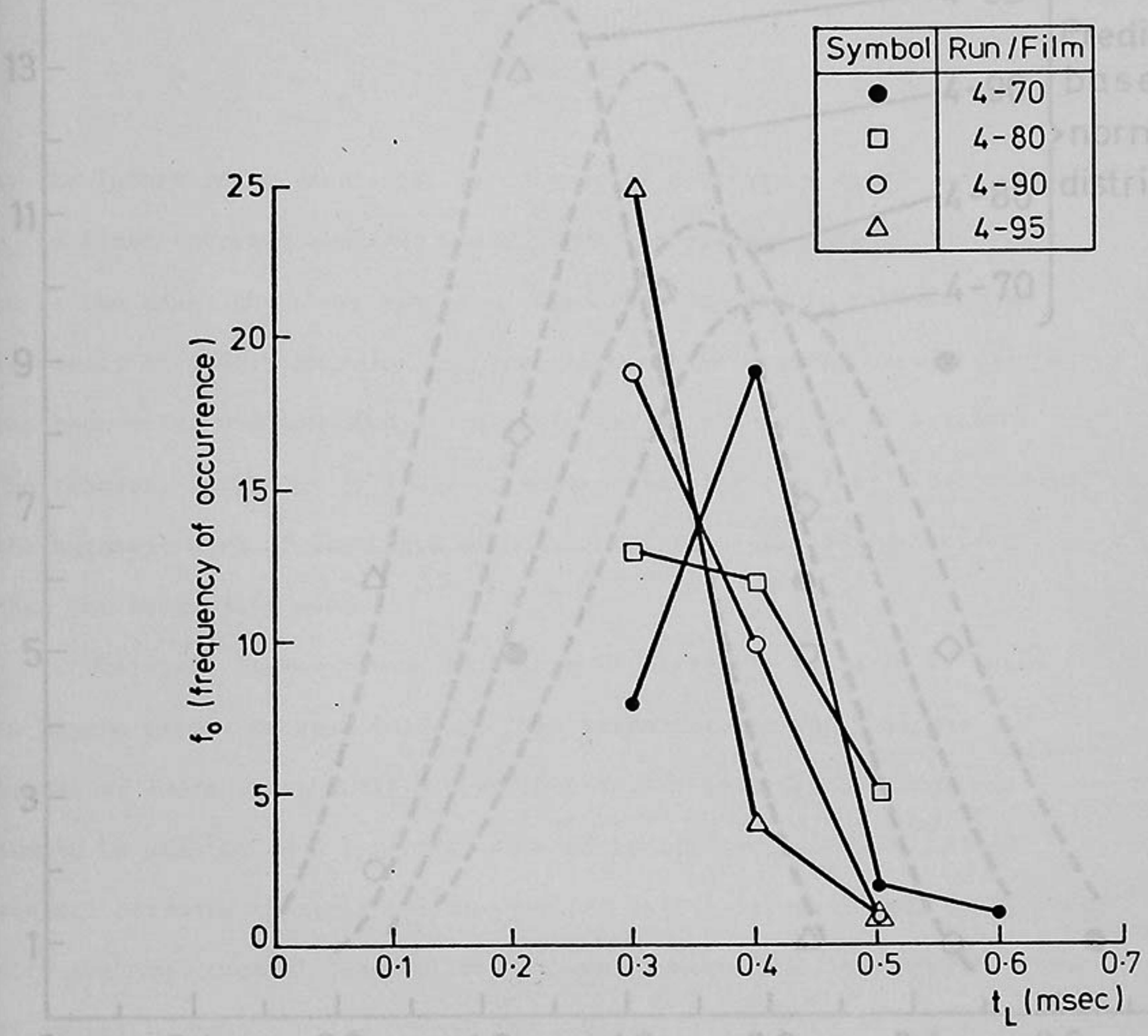


Figure 49. Frequency distribution polygons for bubble life time data; run 4.

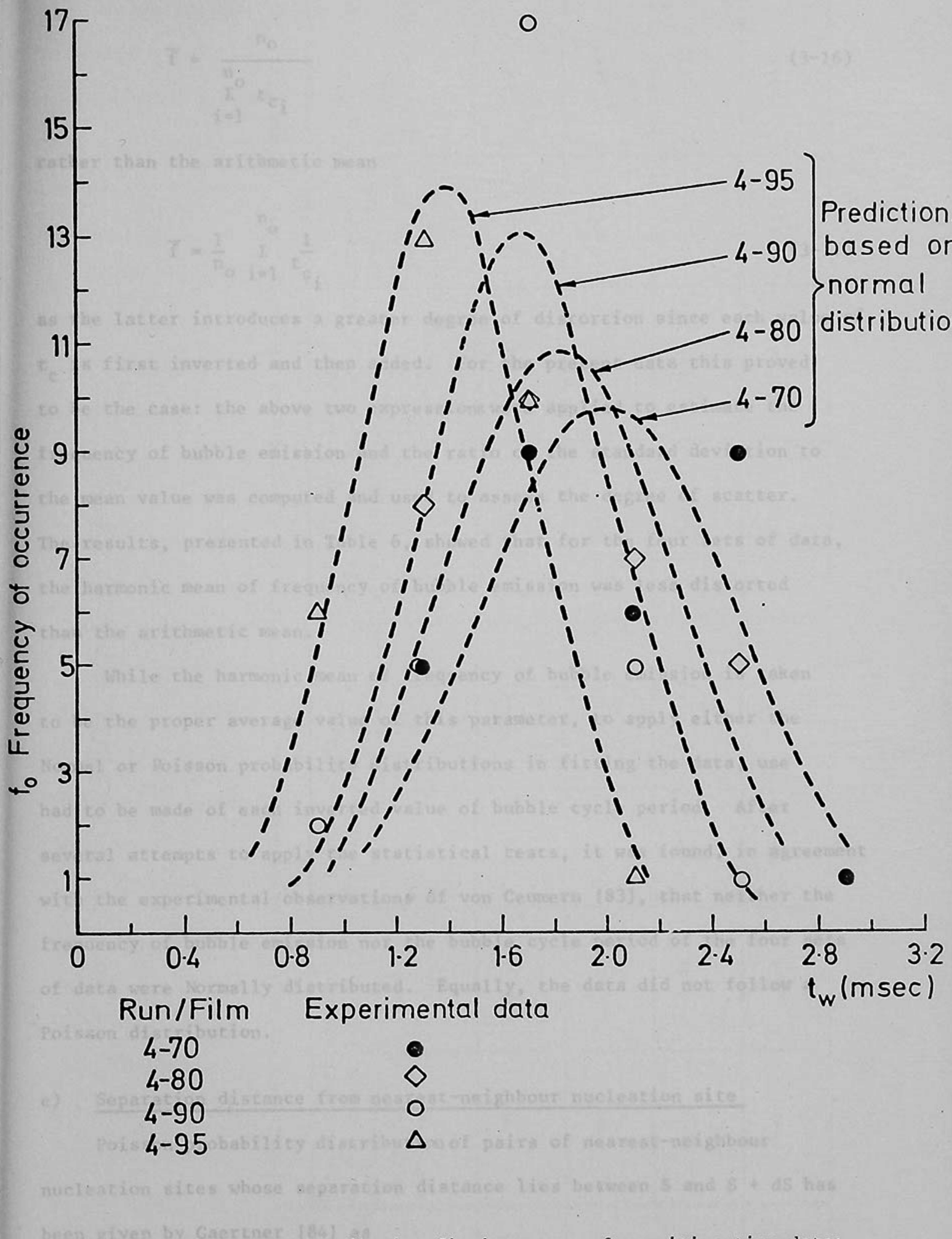


Figure 50. Normal distribution fitting curves for waiting time data; run 4.

$$\overline{f} = \frac{n_o}{\sum_{i=1}^{n_o} t_{c_i}} \qquad (3\text{-}16)$$

rather than the arithmetic mean

$$\overline{f} = \frac{1}{n_o} \sum_{i=1}^{n_o} \frac{1}{t_{c_i}} \qquad (3\text{-}17)$$

as the latter introduces a greater degree of distortion since each value of t_c is first inverted and then added. For the present data this proved to be the case: the above two expressions were applied to estimate the frequency of bubble emission and the ratio of the standard deviation to the mean value was computed and used to assess the degree of scatter. The results, presented in Table 6, showed that for the four sets of data, the harmonic mean of frequency of bubble emission was less distorted than the arithmetic mean.

While the harmonic mean of frequency of bubble emission is taken to be the proper average value of this parameter, to apply either the Normal or Poisson probability distributions in fitting the data, use had to be made of each inverted value of bubble cycle period. After several attempts to apply the statistical tests, it was found, in agreement with the experimental observations of von Ceumern [83], that neither the frequency of bubble emission nor the bubble cycle period of the four sets of data were Normally distributed. Equally, the data did not follow a Poisson distribution.

e) Separation distance from nearest-neighbour nucleation site

Poisson probability distribution of pairs of nearest-neighbour nucleation sites whose separation distance lies between S and S + dS has been given by Gaertner [84] as

$$P(S) = 2\pi n_s S e^{-n_s \pi S^2} \, dS \qquad (3\text{-}18)$$

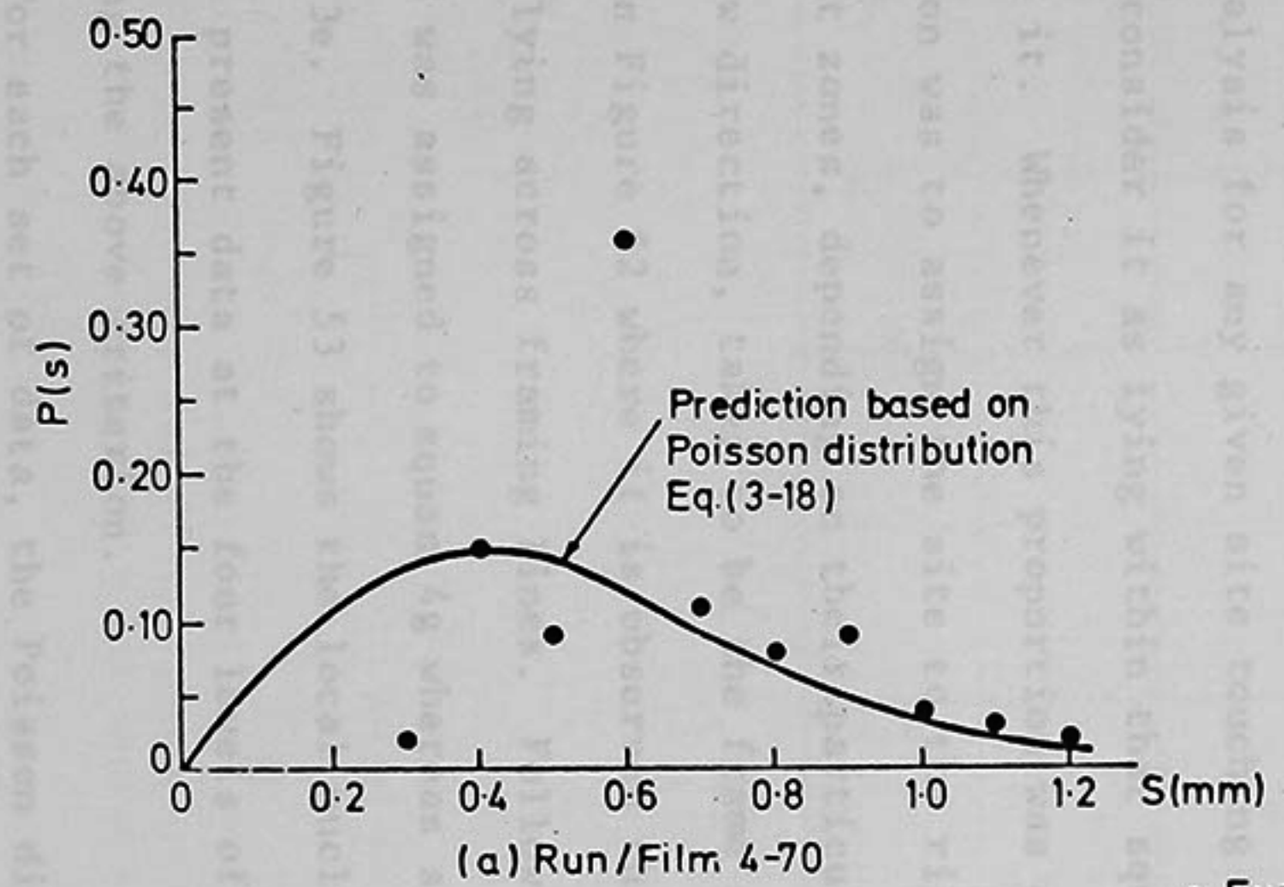
Table 6. Harmonic and arithmetical means and degree of distortion for the frequency of bubble emission data (Run 4).

RUN/FILM	Harmonic mean of frequency of bubble emission $f(sec^{-1})$	Average bubble cycle period $\overline{t_c}$(msec)	Standard deviation σ_o(msec)	$\sigma_o / \overline{t_c}$ (α degree of distortion)	Arithmetic mean of frequency of bubble emission $f(sec^{-1})$	Average reciprocal of bubble cycle period $(\overline{\frac{1}{t_c}})$(msec)	Standard deviation σ_o $(msec^{-1})$	$\sigma_o / (\overline{1/t_c})$ (α degree of distortion)
4-70	428	2.34	0.446	0.191	445	0.445	0.091	0.204
4-80	460	2.17	0.403	0.186	476	0.476	0.101	0.212
4-90	510	1.96	0.307	0.157	524	0.524	0.093	0.178
4-95	608	1.65	0.300	0.182	628	0.628	0.123	0.196

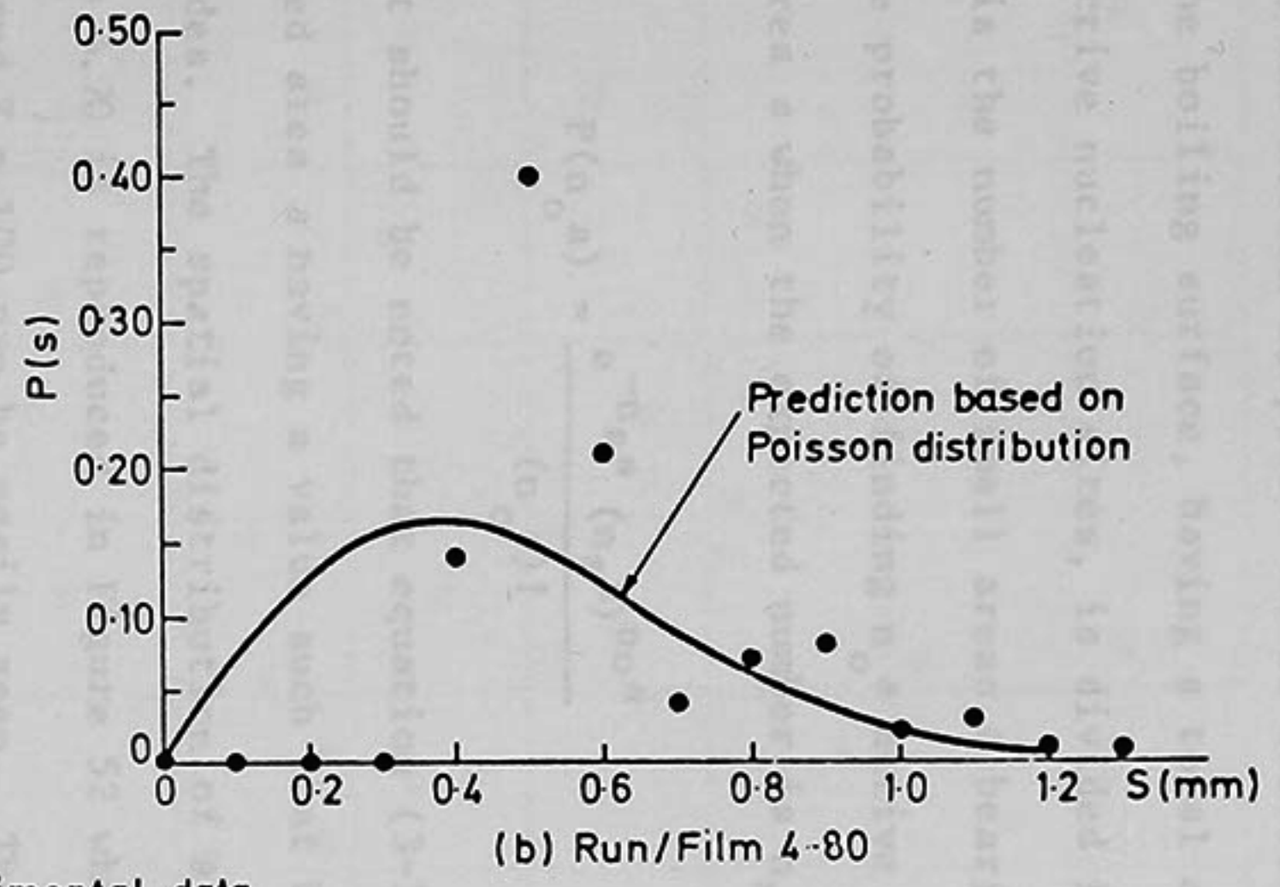
In the present investigation, the separation distances were estimated to the nearest 0.1 millimetre and each set of data at the corresponding four levels of heat flux was submitted to both Poisson (equation (3-18)) and Normal distribution fitting tests. The result , corroborated by the χ^2 tests applied, is presented in Figure 51: the distributions of the separation distance between nearest-neighbour sites for the present data followed neither Poisson nor Normal distributions, but were found to be irregular. This behaviour, as far as the Poisson distribution is concerned, is in accordance with the experimental flow boiling study of Eddington and Kenning [73] with water at atmospheric pressure and low subcoolings. Figure 51 shows a very interesting feature: it suggests no nucleation close to an existing active site. This may well be the cause of discrepancy between the theoretical prediction and the actual behaviour. (This point is considered further in section II.3.).

f) Spatial distribution of local active nucleation sites.

To the knowledge of the author, the first statistical study of boiling in which the Poisson distribution, which implies random scattering, was applied to the spatial distribution of active nucleation sites was comprehensively described by Gaertner [84], who, when conducting pool boiling experiments with water containing dissolved salts of nickel at atmospheric pressure for three levels of heat flux ranging from 0.63×10^6 to 1.0×10^6 W/m^2 on a copper surface, found that the local active nucleation site densities followed Poisson distributions quite well. Basing their work on this analysis, Sultan and Judd [79] recently investigated the spatial distributions of active nucleation sites in pool boiling for water at atmospheric pressure on a copper surface at various levels of heat flux, 0.064×10^6 to 0.333×10^6 W/m^2, and subcoolings ranging from 0 to about 50^oK. Their results substantiated Gaertner's hypothesis concerning the spatial randomness distribution concept, since their data of local site densities also followed the Poisson distribution.

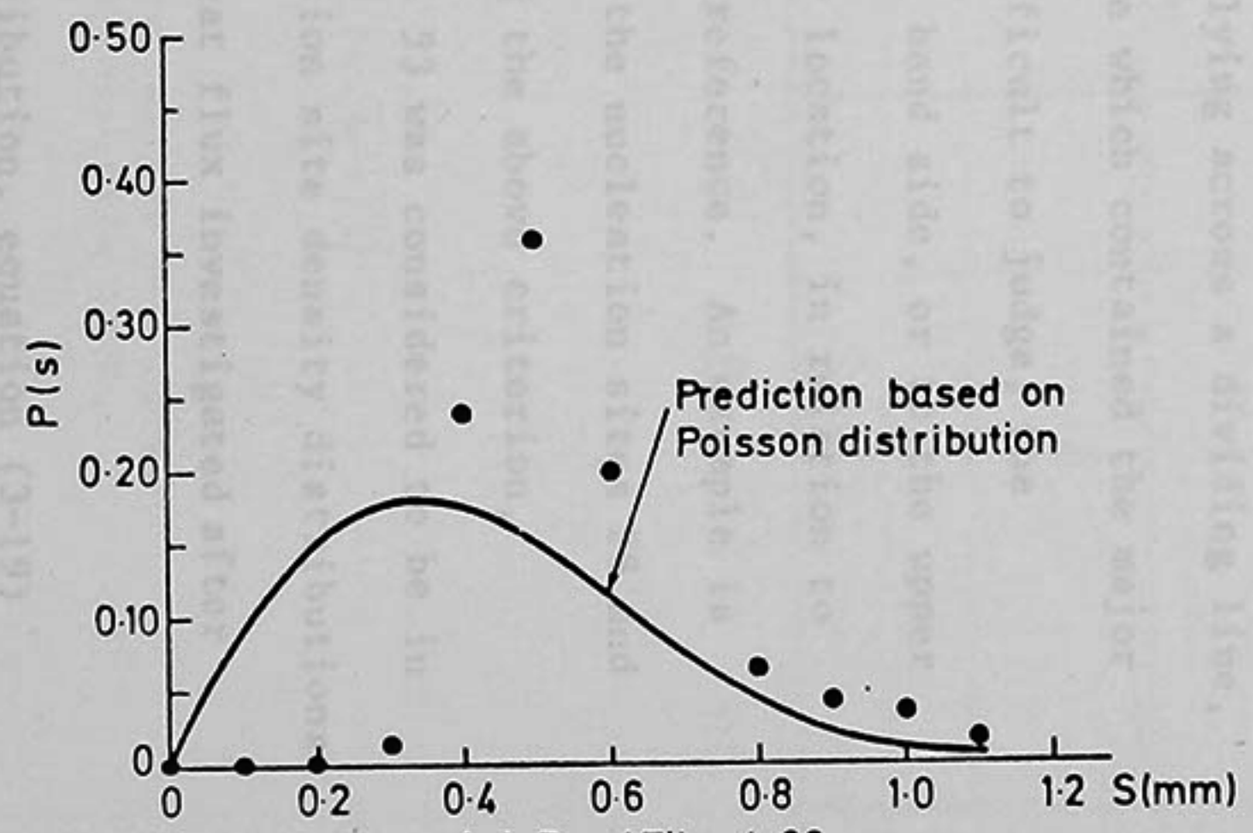


(a) Run/Film 4-70

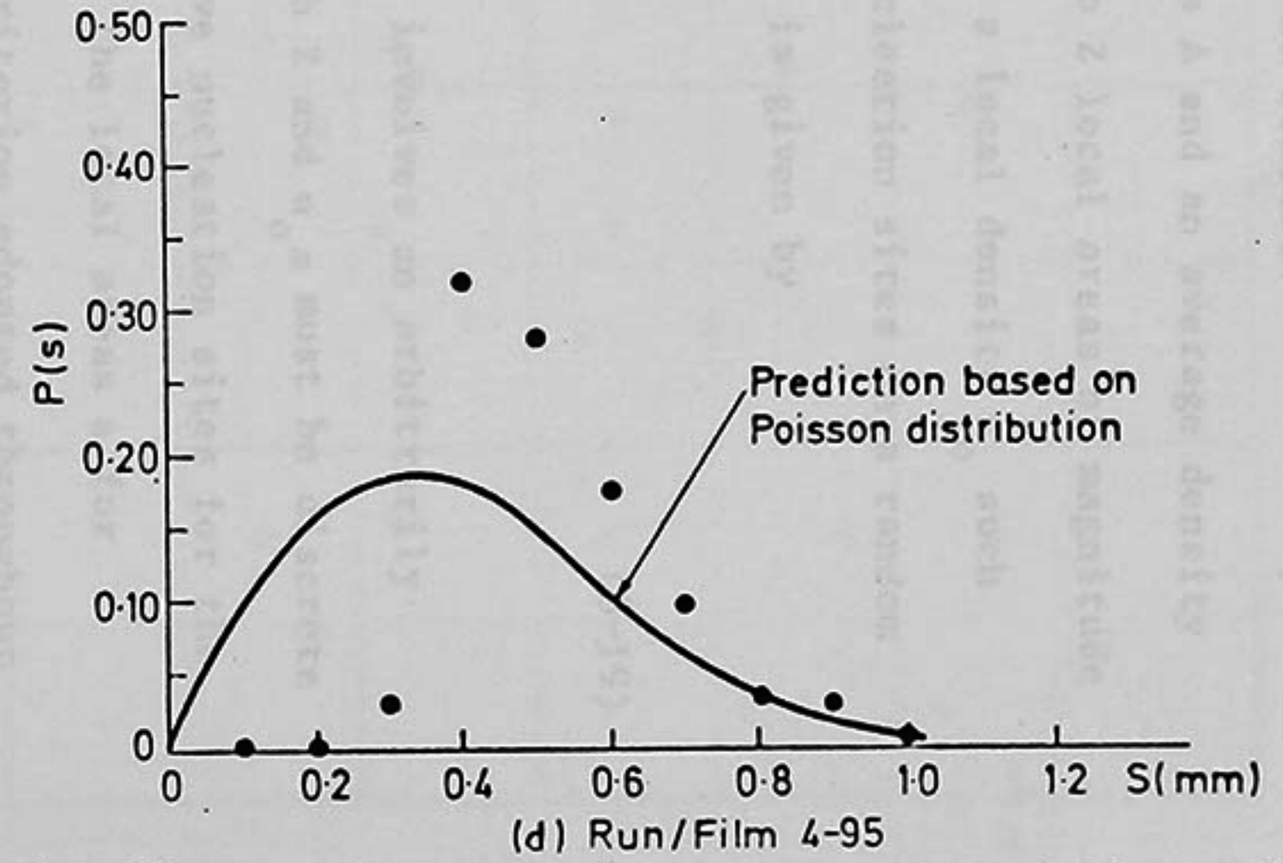


(b) Run/Film 4-80

● Experimental data



(c) Run/Film 4-90



(d) Run/Film 4-95

Figure 51 Distributions of separation distance between pairs of nearest neighbour sites.

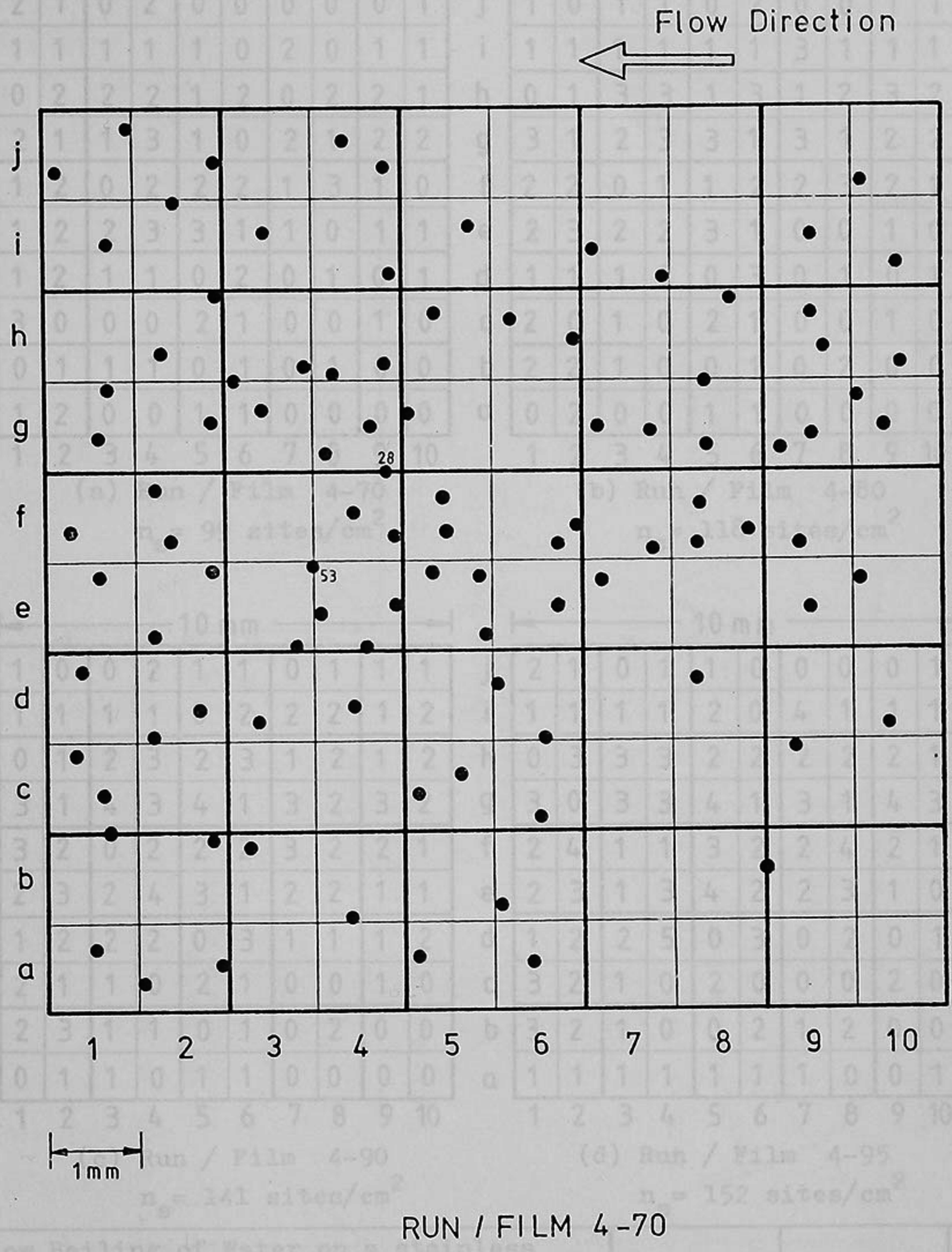
Gaertner's treatment of the distribution of local active sites densities on a boiling surface regarding the Poisson probability equation was herein adopted. It is described as follows:

The boiling surface, having a total area A and an average density of n_s active nucleation sites, is divided into Z local areas of magnitude a. Z_n is the number of small areas a bearing a local density n_o such that the probability of finding $n_o a$ active nucleation sites on a random local area a when the expected number is $n_s a$, is given by

$$P(n_o a) = \frac{e^{-n_s a} (n_s a)^{n_o a}}{(n_o a)!} \qquad (3\text{-}19)$$

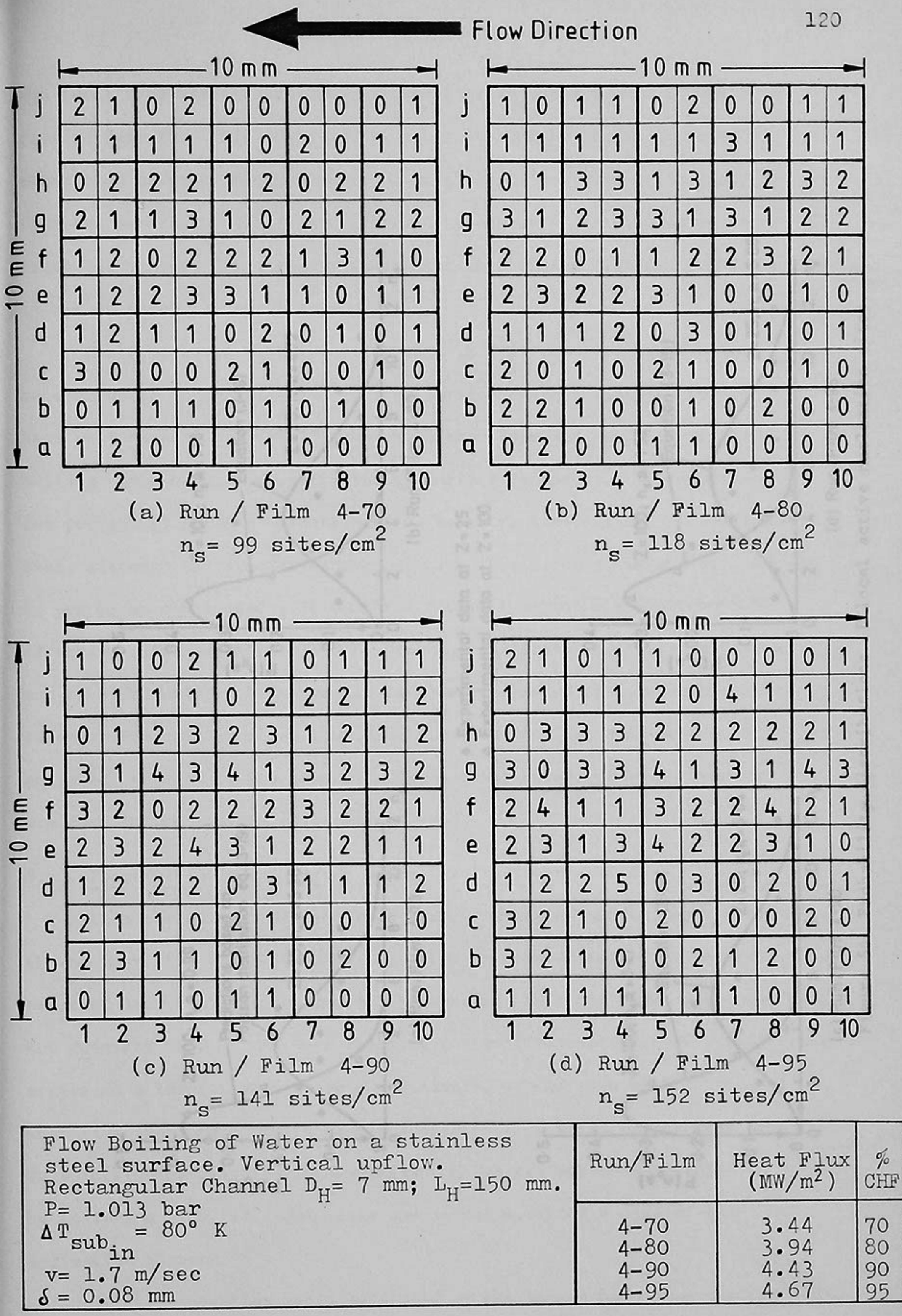
It should be noted that equation (3-19) involves an arbitrarily specified area a having a value such that both Z and $n_o a$ must be discrete magnitudes. The spatial distribution of active nucleation sites for the run-film 4.70 is reproduced in Figure 52 where the local areas a for Z = 25 and Z = 100 can be easily seen. The criterion adopted throughout this analysis for any given site touching or lying across a dividing line, was to consider it as lying within that square which contained the major part of it. Whenever this proportion was difficult to judge, the criterion was to assign the site to the right hand side, or to the upper adjacent zones, depending on their particular location, in relation to the flow direction, taken to be the frame of reference. An example is shown in Figure 52 where it is observed that the nucleation sites 28 and 53 are lying across framing lines. Following the above criterion, site 28 was assigned to square 4g whereas site 53 was considered to be in square 3e. Figure 53 shows the local nucleation site density distributions for the present data at the four levels of heat flux investigated after applying the above criterion.

For each set of data, the Poisson distribution, equation (3-19) at Z = 25 and Z = 100 was applied and the results are shown in Figure 54. The χ^2 tests confirmed that the data were fitted by the Poisson law when



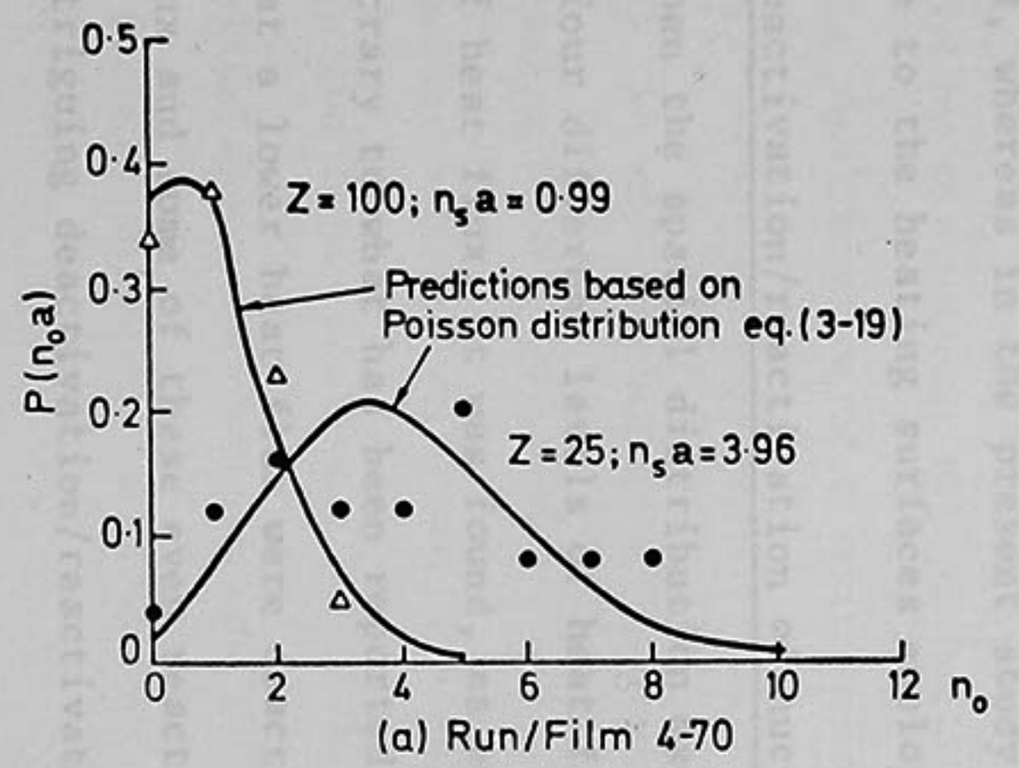
RUN / FILM 4-70

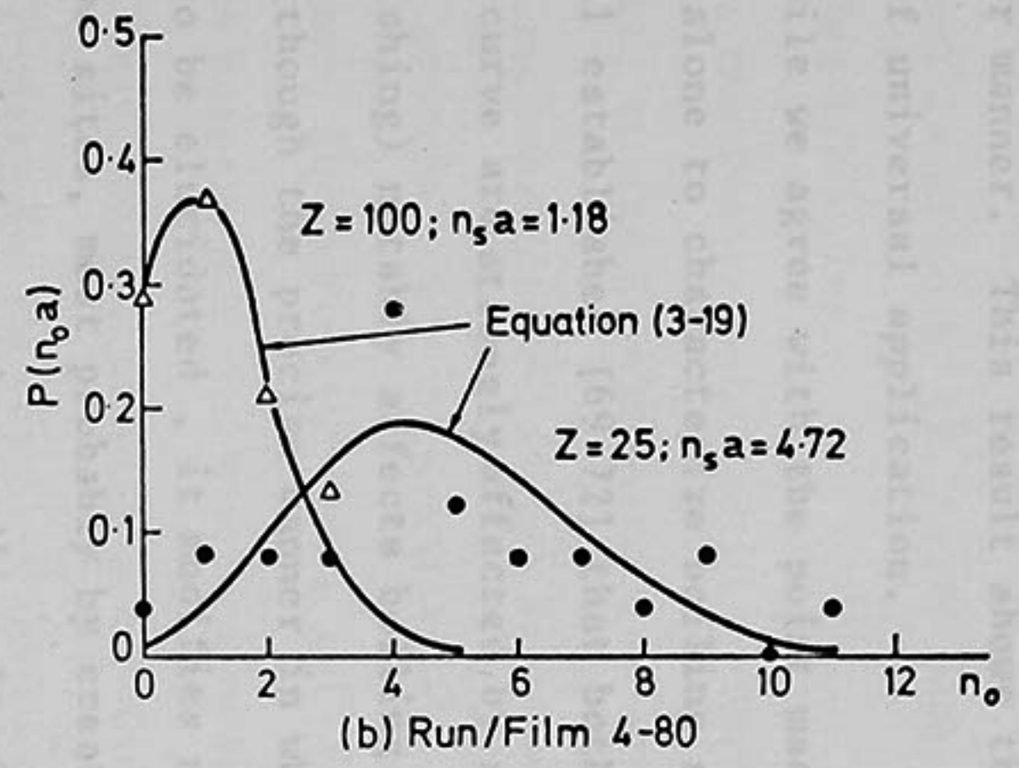
Figure 52. Spatial distribution of local active nucleation sites at Z = 100 and Z = 25; run-film 4-70.



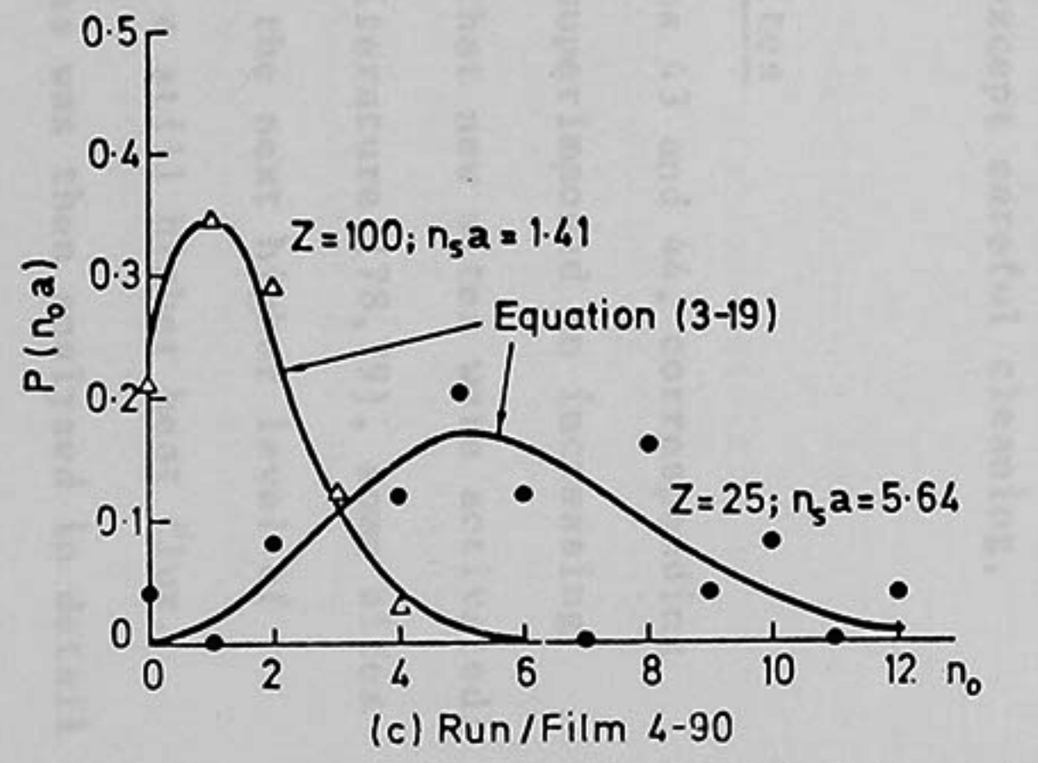
Flow Boiling of Water on a stainless steel surface. Vertical upflow. Rectangular Channel D_H= 7 mm; L_H=150 mm. P= 1.013 bar $\Delta T_{sub_{in}}$ = 80° K v= 1.7 m/sec δ = 0.08 mm	Run/Film	Heat Flux (MW/m^2)	% CHF
	4-70	3.44	70
	4-80	3.94	80
	4-90	4.43	90
	4-95	4.67	95

Figure 53. Local active nucleation site densities; run 4, 70% to 95% of the CHF.





• Experimental data at Z = 25
△ Experimental data at Z = 100



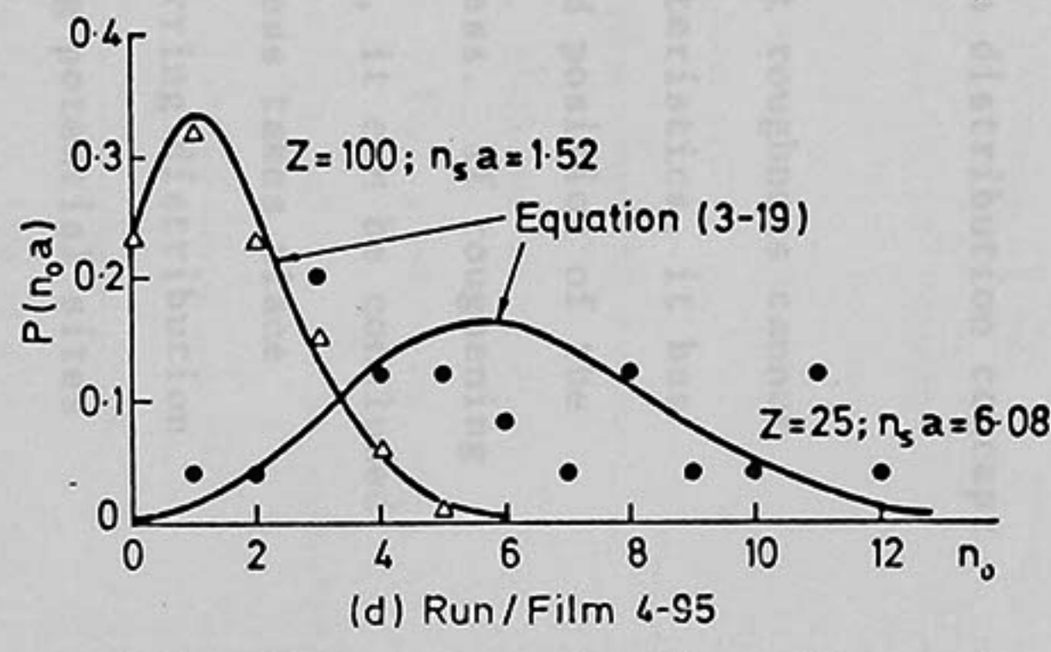


Figure 54 Probability distributions of local active nucleation sites.

the total area was divided into 100 local areas but not when it was divided into 25. This discrepancy, substantiated by the analysis of separation distance between pairs of neighbour sites, led us to conclude that the nucleation sites in the present study were distributed in an irregular manner. This result shows that the Poisson distribution concept in not of universal application.

While we agree with the point made in [79] that roughness cannot be used alone to characterize boiling surface characteristics, it has been well established [69-72] that both the slope and position of the boiling curve are strongly affected by surface roughness. If roughening (or polishing) notably affects boiling heat transfer, it can be concluded that, although the precise manner in which this process takes place is yet to be elucidated , it modifies naturally-occurring distribution of active sites, most probably by creating/destroying potential sites and/or by altering cavity radii. It should be noted that in both forementioned pool boiling studies [79,84] the boiling specimens were polished, whereas in the present study nothing except careful cleaning, was done to the heating surfaces employed.

3. Deactivation/reactivation of nucleation sites

When the spatial distribution maps, Figures 43 and 44, corresponding to the four different levels of heat flux were superimposed in increasing order of heat flux, it was found, as expected, that new sites were activated; but contrary to what has been reported in the literature [78,79], some sites active at a lower heat flux were deactivated at the next higher level of heat flux and some of these even reactivated at a still higher heat flux. This intriguing deactivation/reactivation process was then analysed in detail by following each individual site and so establishing a site by site activation history.

If the nucleation sites activated at the lowest heat flux studied

(70% CHF for run 4) had remained active at subsequent higher fluxes, a total of 152 sites would have been found. However, as deactivation/reactivation process took place, altogether 256 different sites were observed at the combinations given in Table 7. Figure 55, derived from consecutive superimposition of the spatial distribution maps shows the actual location of the total number of sites and their individual activation histories.

As the rather peculiar behaviour of these nucleation sites has, to the knowledge of the author, never before been reported in boiling experiments, it was felt necessary to pay special attention to this process. In comparing bubble gas nucleation with vapour-boiling nucleation, Eddington and Kenning [73], drawing attention to the discrepancies observed between the two modes of nucleation, have proposed seeding and thermal interference processes involved in boiling but not present in gas nucleation as the possible explanation responsible for the differences they observed. The possible reasons for site deactivation, originally suggested by Kenning [85] when discussing the present observations, and amplified by the author, are presented below.

The deactivation of a nucleation site is likely to be due to:

1) "Self" deactivation: here the site is not very stable, possibly because:

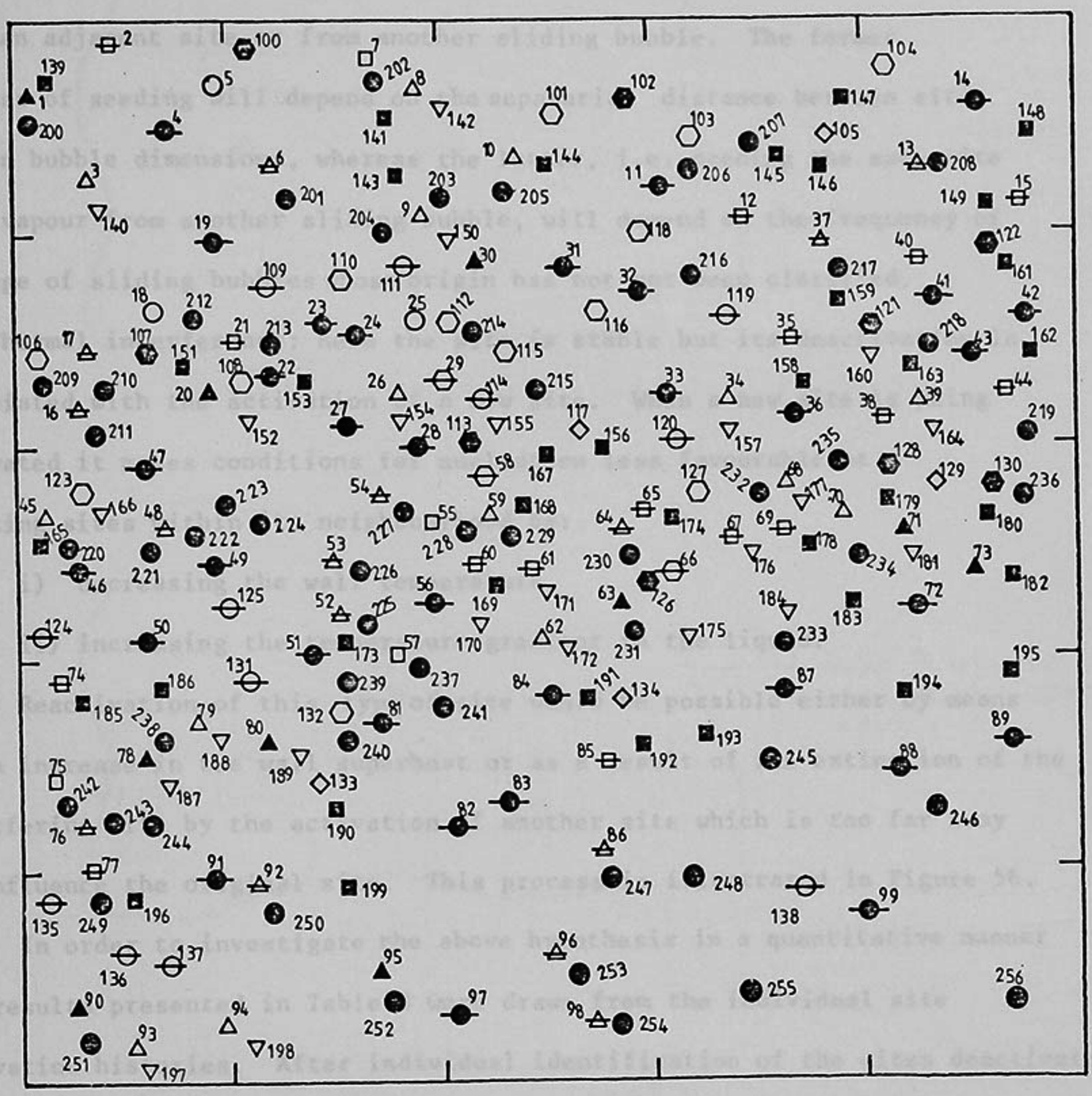
i) it was originally activated at a lower heat flux by the passage of a sliding bubble which momentarily decreased its velocity by interacting with another bubble, with vapour being trapped by the site. As a matter of fact, in the films analysed, Table 3, it was observed that some bubbles which slide along the heating surface changed their direction, and most probably their velocity, although no quantitative measurements were taken;

ii) by chance liquid penetrates further than usual after the collapse of a bubble and as a result, the site is deactivated. The site could be filled completely with liquid or the liquid drive the interface to a position where it would require higher superheat for reactivation.

Table 7. Nucleation site activation histories.
Run 4.
$\Delta T_{sub_{in}}$ = 80°K
v = 1.7 m/sec.
δ = 0.08 mm
$\emptyset_c$ = 4.92 MW/m^2

HEAT FLUX (% CHF)				ACTIVE NUCLEATION SITES/cm^2 AT THE INDICATED HEAT FLUX(ES)
70	80	90	95	
✓	✓	✓	✓	33
✓	✓	✓		15
✓	✓		✓	16
✓		✓	✓	3
	✓	✓	✓	12
✓	✓			15
✓		✓		4
✓			✓	3
	✓	✓		13
	✓		✓	5
		✓	✓	23
✓				10
	✓			9
		✓		38
			✓	57
99	118	141	152	256

(see Figure 55 for individual site locations)



Symbol	Active Sites at (% CHF)
▲	70
⬢	80
■	90
●	95
△	70 & 80
□	70 & 90
○	70 & 95
⬡	80 & 90
◇	80 & 95
▽	90 & 95
⟛	70, 80 & 90
⊟	70, 80 & 95
⊖	70, 90 & 95
⊖	80, 90 & 95
●	70, 80, 90 & 95

Figure 55. Spatial distibution and individual site activation histories; run 4, 70% to 95% of the CHF.

Reactivation of this type of nucleation site would proceed either by increasing the wall superheat (i.e. heat flux) or by "seeding" with vapour from an adjacent site or from another sliding bubble. The former process of seeding will depend on the separation distance between sites and on bubble dimensions, whereas the latter, i.e. seeding the same site with vapour from another sliding bubble, will depend on the frequency of passage of sliding bubbles whose origin has not yet been clarified.

2) Thermal interference: here the site is stable but its deactivation is associated with the activation of a new site. When a new site is being activated it makes conditions for nucleation less favourable at existing sites within its neighbourhood by:

i) decreasing the wall temperature,

ii) increasing the temperature gradient in the liquid.

Reactivation of this type of site would be possible either by means of an increase in the wall superheat or as a result of the extinction of the interfering site by the activation of another site which is too far away to influence the original site. This process is illustrated in Figure 56.

In order to investigate the above hypothesis in a quantitative manner the results presented in Table 8 were drawn from the individual site activation histories. After individual identification of the sites deactivated during the three heat flux increments, i.e. 70 to 80% CHF, 80 to 90% CHF and 90 to 95% CHF, the separation distance between each of the observed deactivated sites, column n_{s_D} in Table 8 (those sites active at $\emptyset_1$ but not at $\emptyset_2$, where $\emptyset_2 > \emptyset_1$), and the new activated sites, column n_{s_A} in Table 8 (sites active at $\emptyset_2$ but not at $\emptyset_1$), were measured and from this analysis, the information given in Table 9 was derived. The deactivated sites during each heat flux variation were classified according to the above hypothesis into two groups of site types: Type I, is of those deactivated sites lying in the area of influence of a newly activated

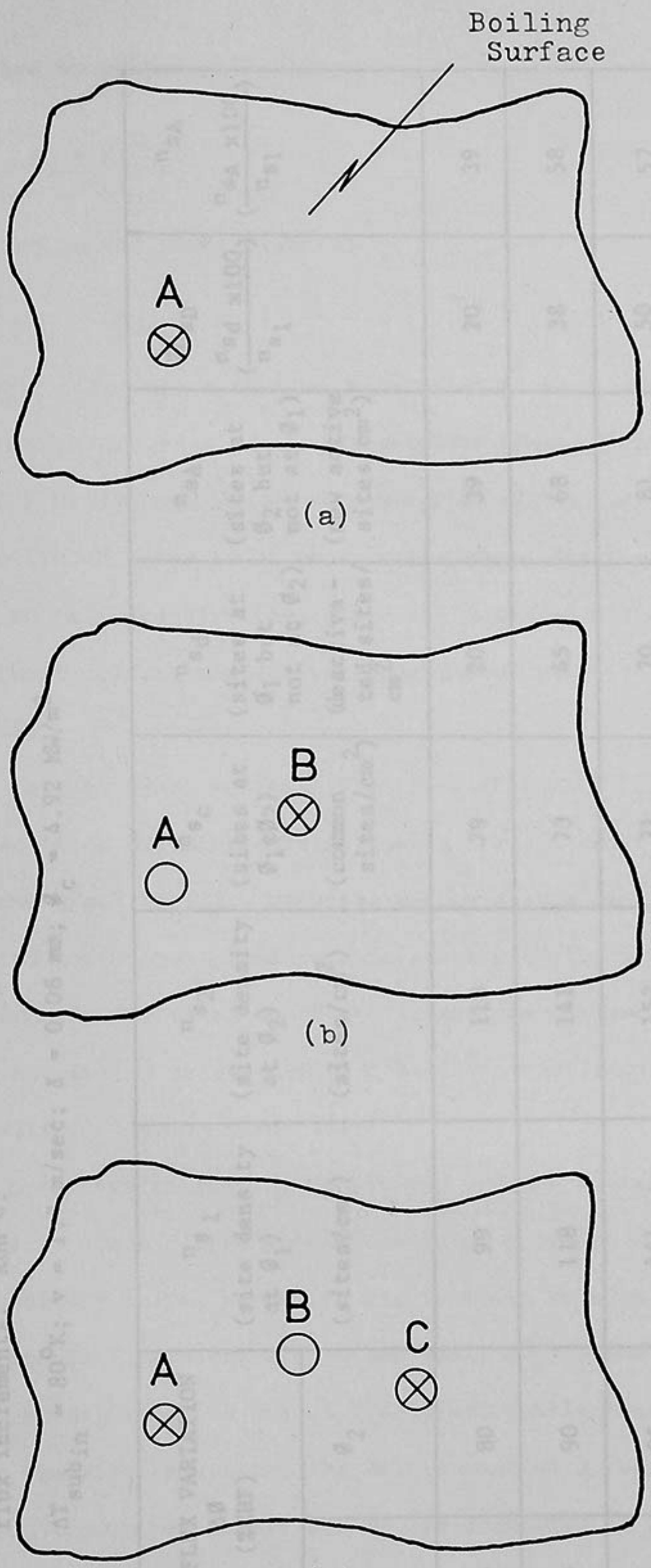


Figure 56. Deactivation/reactivation of nucleation sites by thermal interference.

Table 8. Deactivation/activation of nucleation sites during heat flux increments. Run 4.

$\Delta T_{sub_{in}} = 80^{o}K$; v = 1.7 m/sec; δ = 0.08 mm; $\emptyset_c = 4.92$ MW/m^2

HEAT FLUX VARIATION $\Delta\emptyset$ (%CHF)		n_{s_1} (site density at $\emptyset_1$)	n_{s_2} (site density at $\emptyset_2$)	n_{s_c} (sites at $\emptyset_1 \varepsilon \emptyset_2$)	n_{s_d} (sites at $\emptyset_1$ but not at $\emptyset_2$)	n_{s_A} (sites at $\emptyset_2$ but not at $\emptyset_1$)	$\%n_{s_D}$ $(\frac{n_{s_d} \times 100}{n_{s_1}})$	n_{s_A} $(\frac{n_{s_A} \times 100}{n_{s_1}})$
$\emptyset_1$	$\emptyset_2$	(sites/cm^2)	(sites/cm^2)	(common sites/cm^2)	(deactivated sites/cm^2	(new active sites/cm^2)		
70	80	99	118	79	20	39	20	39
80	90	118	141	73	45	68	38	58
90	95	141	152	71	70	81	50	57

site, defined by equation (1-6)

$$A_i = K(\frac{\Pi}{4}D_m^2) \qquad (1\text{-}6)$$

which implies an influence diameter

$$D_i = \sqrt{K}\,D_m \qquad (3\text{-}20)$$

If as a first approximation K is taken to be 4, the first type of deactivated sites is of those sites whose deactivation is associated with the activation of a new site within two bubble radii. Type II of deactivated sites is of those sites whose deactivation proceeds according to self-deactivation, since the measured distance between them and their nearest new-activated neighbour site is greater than two bubble radii.

The results given on Table 9 suggest that with the exception of the deactivated sites during the heat flux increment, $\Delta\emptyset$, from 70 to 80% of the CHF, the great majority of sites may be deactivated by thermal interference from new sites. This is consistent with the behaviour shown in Figure 51 regarding the distribution of the separation distance between nearest neighbour nucleation sites: the probability of nucleation close to an existing site is greatly diminished.

The reactivation seeding mechanism, perhaps an important contributor to reactivation in a packed-bubble condition or where the bubble dimensions are comparatively large, seemed to play a minor role in the present study where the bubble dimensions are rather small ($\overline{D}_m$= 0.4mm) and the boiling regime can be described as one of "isolated" bubble condition.

With the above evidence, the development of a simple, but realistic, deactivation theory was undertaken and is presented as follows:

It is assumed that the deactivation process is entirely dependent on the activation of new sites at a higher heat flux, over the interval $\Delta\emptyset$

Table 9. Classification of deactivated sites during heat flux variations. Run 4.

$\Delta T_{sub_{in}}$ = 80°K, v = 1.7 m/sec; δ = 0.08 mm; $\emptyset_c$ = 4.92 MW/m^2

HEAT FLUX VARIATION $\Delta\emptyset$ (% CHF)	n_{s_D} Total number of deactivated sites during $\Delta\emptyset$ per cm^2	Type Group	Number of deactivated sites/cm^2 in Type group	% deactivated sites in type group
70–80	20	I	8	40
		II	12	60
80–90	45	I	36	80
		II	9	20
90–95	70	I	47	67
		II	23	33

Table 10. Comparison between observed and predicted fraction of deactivated sites during heat flux intervals. Run 4.

HEAT FLUX VARIATION (%CHF)		$Kn_{s_2}\frac{\pi\bar{D}_m^2}{4}$	$\frac{n_{s_A}}{n_{s_1}}$	(n_{s_D}/n_{s_1}) Fraction of sites deactivated during $\Delta\emptyset$		$\frac{(n_{s_D}/n_{s_1})_{Predicted}}{(n_{s_D}/n_{s_1})_{observed}}$
$\emptyset_1$	$\emptyset_2$			Predicted Eq. (3-21)	Observed	
70	80	0.59	0.39	0.23	0.20	1.15
80	90	0.71	0.58	0.41	0.38	1.08
90	95	0.76	0.57	0.43	0.50	0.87

such that one could expect the number of sites deactivated to be proportional to the number of new activated sites. In other words, the fraction of sites deactivated with respect to $\emptyset_1$ is proportional to the probability that deactivated sites lie within the area of influence of a new site and to the fraction of new sites activated during the increment of heat flux. This can be mathematically expressed as

$$\frac{n_{s_D}}{n_{s_1}} = (n_{s_2} A_i)(n_{s_A}/n_{s_1}) \qquad (3\text{-}21)$$

where

n_{s_D} = number of sites per unit of area deactivated during $\Delta\emptyset = \emptyset_2 - \emptyset_1$; $\emptyset_2 > \emptyset_1$

n_{s_1} = nucleation site density at $\emptyset_1$

n_{s_2} = nucleation site density at $\emptyset_2$

n_{s_A} = number of new active sites per unit area (sites at $\emptyset_2$ but not at $\emptyset_1$)

A_i = area of influence (equation (1-6)).

Making use of the results given on Table 8, equation (3-21) was applied and the results obtained, presented in Table 10, show that the above derived deactivation equation predicts the present data with reasonable accuracy (±15%). However, it should be pointed out that apart from the fact that the choice for the value of K is quite arbitrary, the first product on the right hand side of equation (3-21) implies that there is no overlap in the areas of influence, although this is not always true. These points are broadly discussed in Chapter 5.

CHAPTER FOUR

EXPERIMENTAL RESULTS. PART II: CRITICAL HEAT FLUX

I. High-speed cine photographic observations

Within the range of experimental conditions, presented in Table 1, a set of 33 cine films at a speed of 10,000 frames per second was taken in order to observe the nature of the physical processes occurring during flow boiling of subcooled water at atmospheric pressure at various levels of heat flux ranging from 30% up to 95% of the measured critical heat fluxes. All the films were taken normal to the boiling surface and the field of view was restricted to a length of 4 to 5 cm located over the downstream end of the test section where the burnouts were found to occur. For each film, a sequence of 10 representative frames was chosen, and from them, photographic prints enlarged tenfold were made and used in the present analysis.

1. Flow patterns near the CHF

The physical configurations adopted by the distributions of the vapour and liquid phases while flowing through a heated channel, customarily known as flow regimes or patterns, are to a great extent subject to the observer's interpretation, since there exists no established general criterion of classification. Here therefore, the discussion is restricted to a qualitative description of the flow patterns near the CHF.

Essentially, two types of flow regimes were observed in the present study, a third one being the transition from one to the other. They are: bubbly flow and slug flow. The definitions adopted to characterize them are:

Bubbly Flow: the vapour phase is mainly constituted of individual bubbles distributed in a continuous liquid phase. Bubble coalescence may exist with occasional formation of small vapour patches or clusters (small compared to the channel's width) often localized near the downstream end of the heated surface.

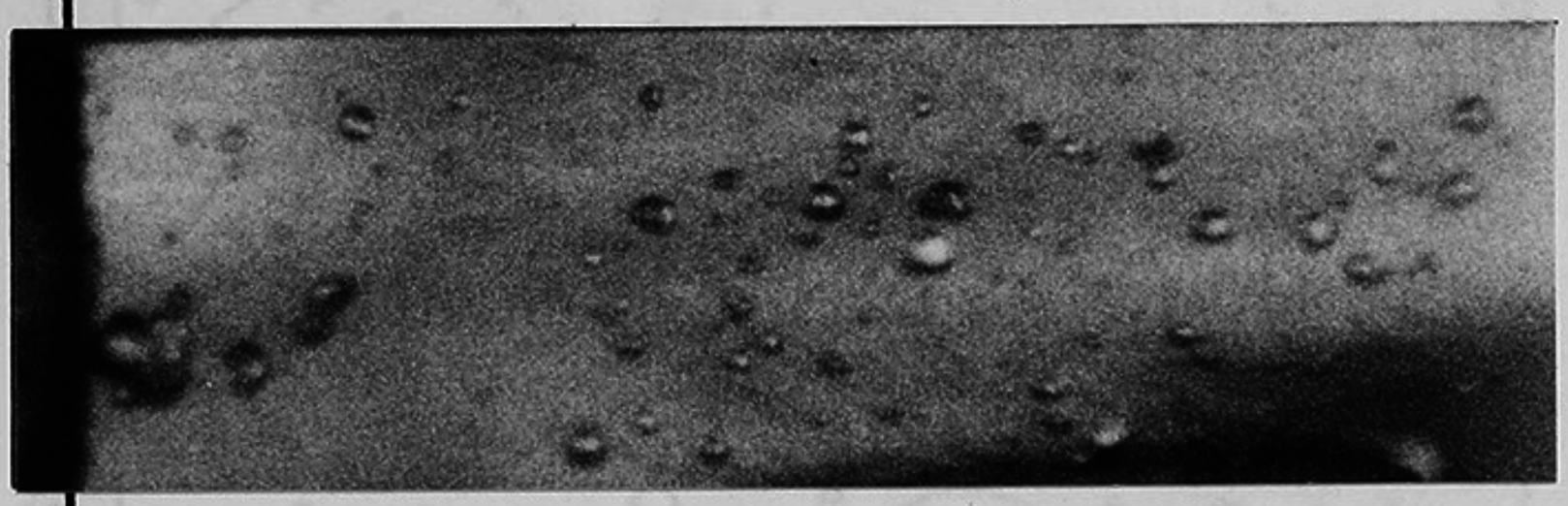
Transition from Bubbly to Slug Flow: it is characterized by frequent vapour masses of irregular form, identifiable as patches or clusters whose size is relatively large compared to the individual bubbles which are still present. The vapour phase is distributed in a continuous liquid phase.

Slug Flow: the vapour phase is characterized by large vapour masses whose width is comparable to the channel's width (or diameter) and whose length varies, but is always greater than the channel's width. These appear quite frequently and vapour clots flow alternatively with liquid slugs which contain smaller vapour masses and bubbles. Nucleation under these vapour clots is clearly observed.

It is not possible to describe even qualitatively the formation of the large vapour clots, since they all proceeded from upstream, originating out of the field of view. However, as far as the formation of the vapour clusters is concerned, it was observed that they arose when the population of bubbles present was large, but far from being close - packed as assumed in some models for the mechanism of CHF [8,39,41,42]. It is interesting to note that bubble coalescence existed even at heat fluxes as low as 30% of the CHF. It is also worth pointing out that due to the construction of the test channel (details are given in Chapter Two) it was not possible to determine either the thickness of the vapour masses (bubbles or patches) or their distance from the heating surface, although presumably they flowed closer to the heated surface than to the glass window.

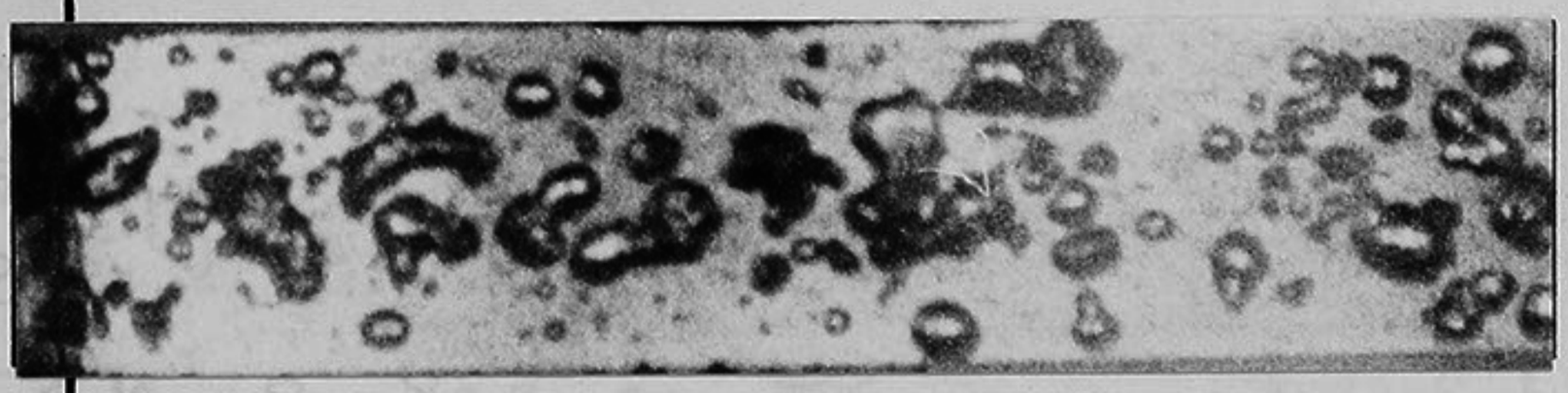
Typical photographs of the three flow regimes are presented in Figure 57. A number of possible, and more sophisticated classifications of flow patterns is shown in Figure 58; although they were sketched from actual photographic prints, they can be considered simply as intermediate transitional stages between the well-differentiated flow regimes described above. The flow regimes observed near the CHF are in qualitative agreement with the data from other experimenters for water on tubular geometries [40,45,86] and have also been observed at burnout for Freon-113 flowing

Water / Stainless steel
Atmospheric pressure
Vertical upflow



Run 6, 80% CHF

(a) Bubbly Flow



Run 21, 60% CHF

(b) Transition from bubbly to slug



Run 12, 90 % CHF

(c) Slug Flow

Figure 57. Flow patterns near the CHF. (Photographic prints from high-speed cine films taken normal to the heating surface in a channel of rectangular cross-section).

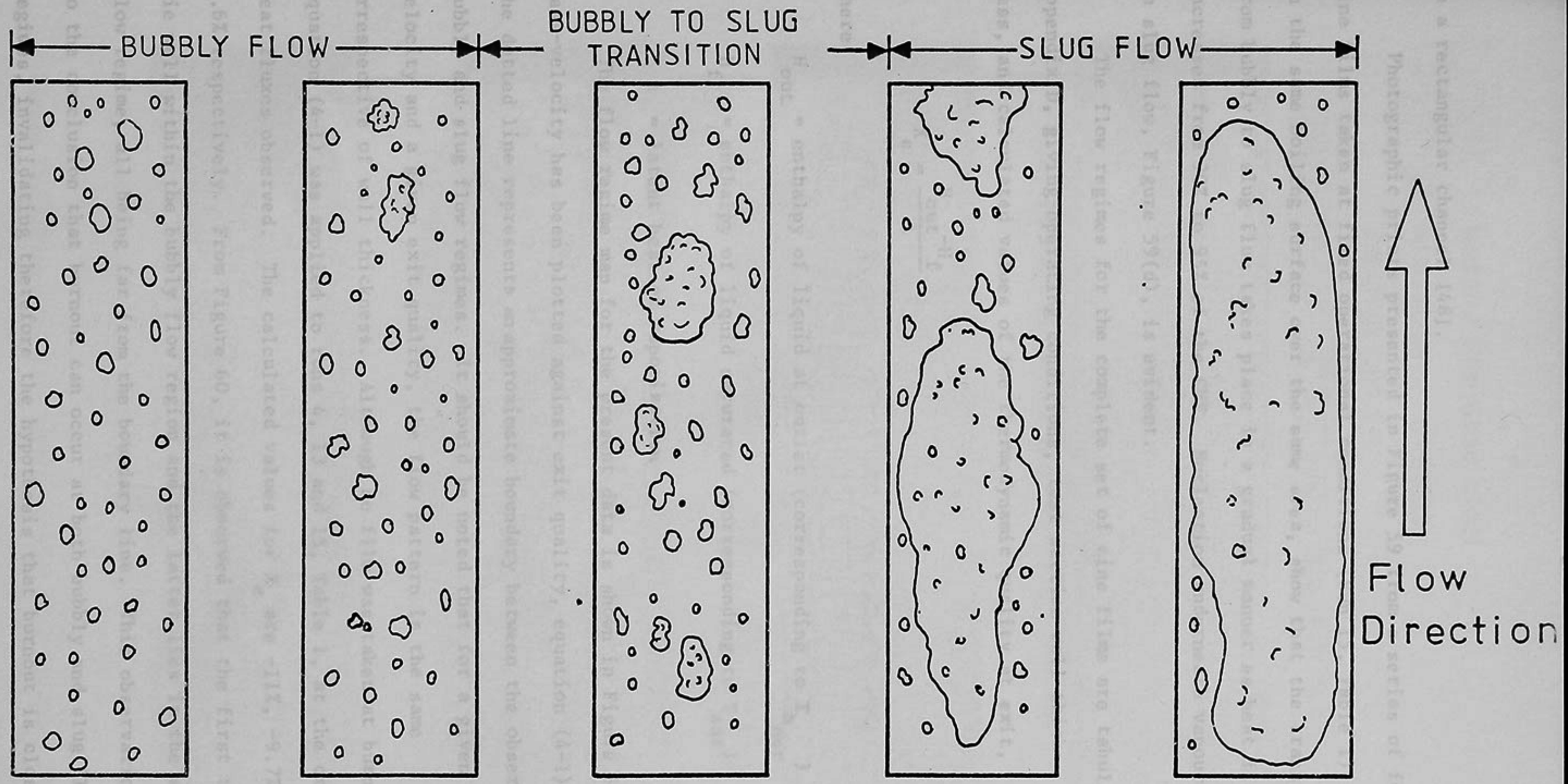


Figure 58. Idealized picture of the flow patterns near the CHF in a channel of rectangular cross-section viewed from above.

in a rectangular channel [48].

Photographic prints presented in Figure 59 from a series of four cine films taken at fixed operational conditions (Run 15, Table 1) on the same boiling surface over the same area, show that the transition from bubbly to slug flow takes place in a gradual manner as heat flux increases from 70% to 95% of the CHF. Nucleation underneath vapour clots in slug flow, Figure 59(d), is evident.

The flow regimes for the complete set of cine films are tabulated in Appendix D, giving operating conditions, test section wall thickness, and calculated values of the thermodynamic quality at exit,

$$X_e = \frac{H_{out} - H_f}{\lambda} \qquad (4\text{-}1)$$

where

H_{out} = enthalpy of liquid at outlet (corresponding to $T_{b_{out}}$)

H_f = enthalpy of liquid saturated (corresponding to T_{sat})

λ = latent heat of vaporization

The flow regime map for the present data is shown in Figure 60, where mass-velocity has been plotted against exit quality, equation (4-1), and the dotted line represents an approximate boundary between the observed bubbly and slug flow regimes. It should be noted that for a given mass-velocity and a given exit quality, the flow pattern is the same irrespective of wall thickness. Although no film was taken at burnout, equation (4-1) was applied to runs 4, 13 and 15, Table 1, at the critical heat fluxes observed. The calculated values for X_e are -11%, -9.7% and 1.6% respectively. From Figure 60, it is observed that the first two values lie well within the bubbly flow region and the latter lies in the slug flow regime, all being far from the boundary line. This observation leads to the conclusion that burnout can occur at both bubbly and slug flow regimes, invalidating therefore the hypothesis that burnout is closely

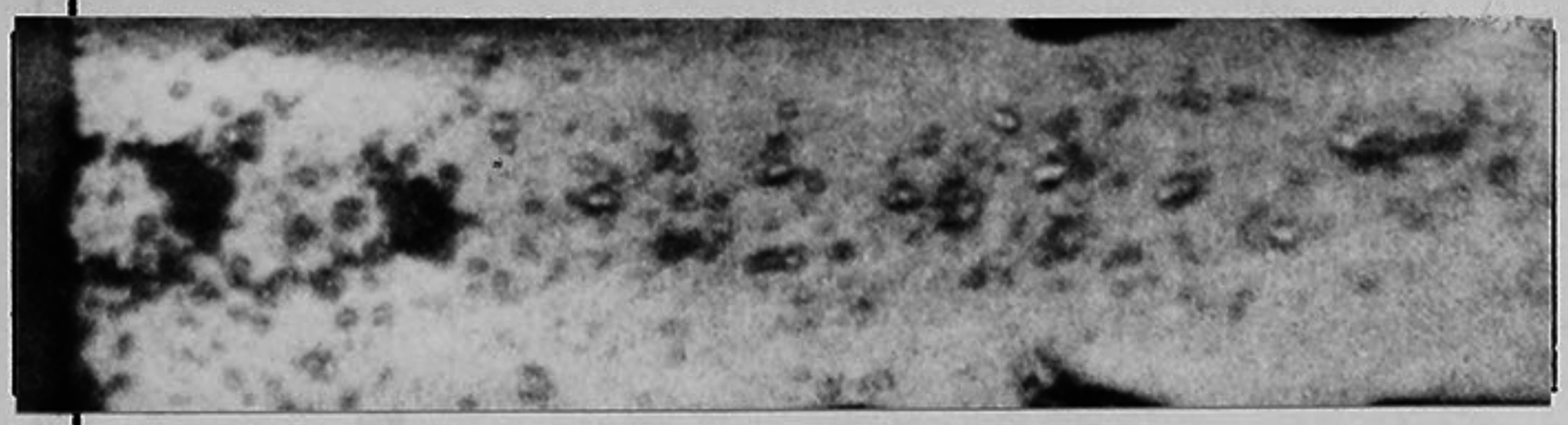
Water / Stainless steel

Atmospheric pressure

Vertical upflow

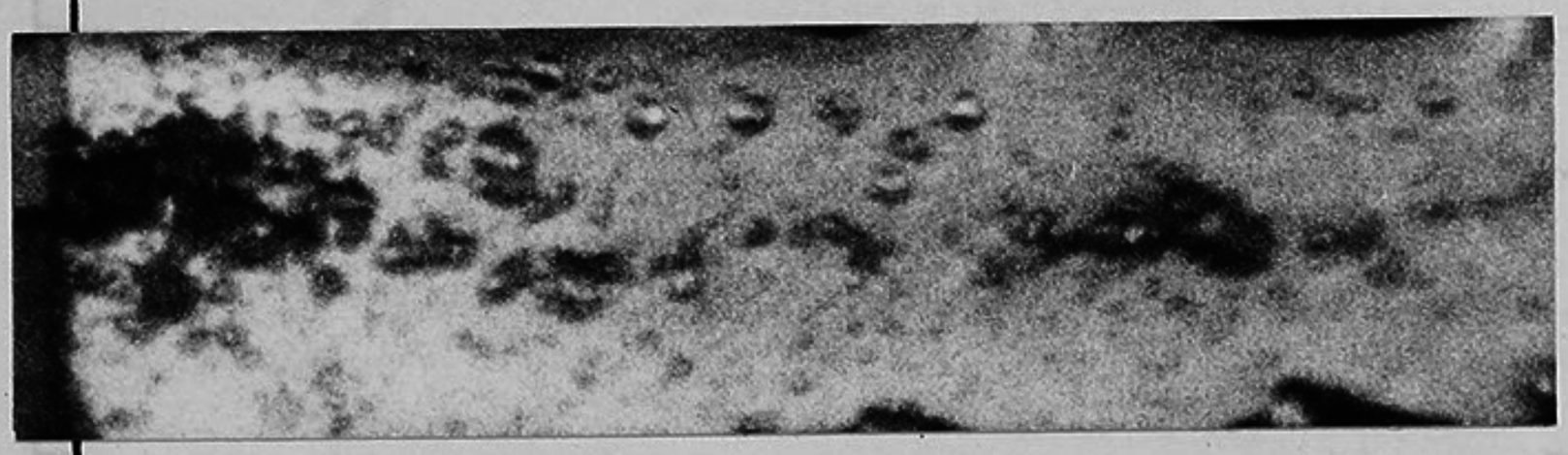
END OF THE HEATED SECTION

Flow direction



10 mm

(a) Bubbly flow; 70% CHF



10 mm

(b) Bubbly to slug transition; 80% CHF



10 mm

(c) Slug flow; 90% CHF



10 mm

(d) Slug flow; 95 % CHF

Figure 59. Transition from bubbly to slug flow regimes. Run 15. (Photographic prints from high-speed cine films taken normal to the heating surface in a channel of rectangular cross-section).

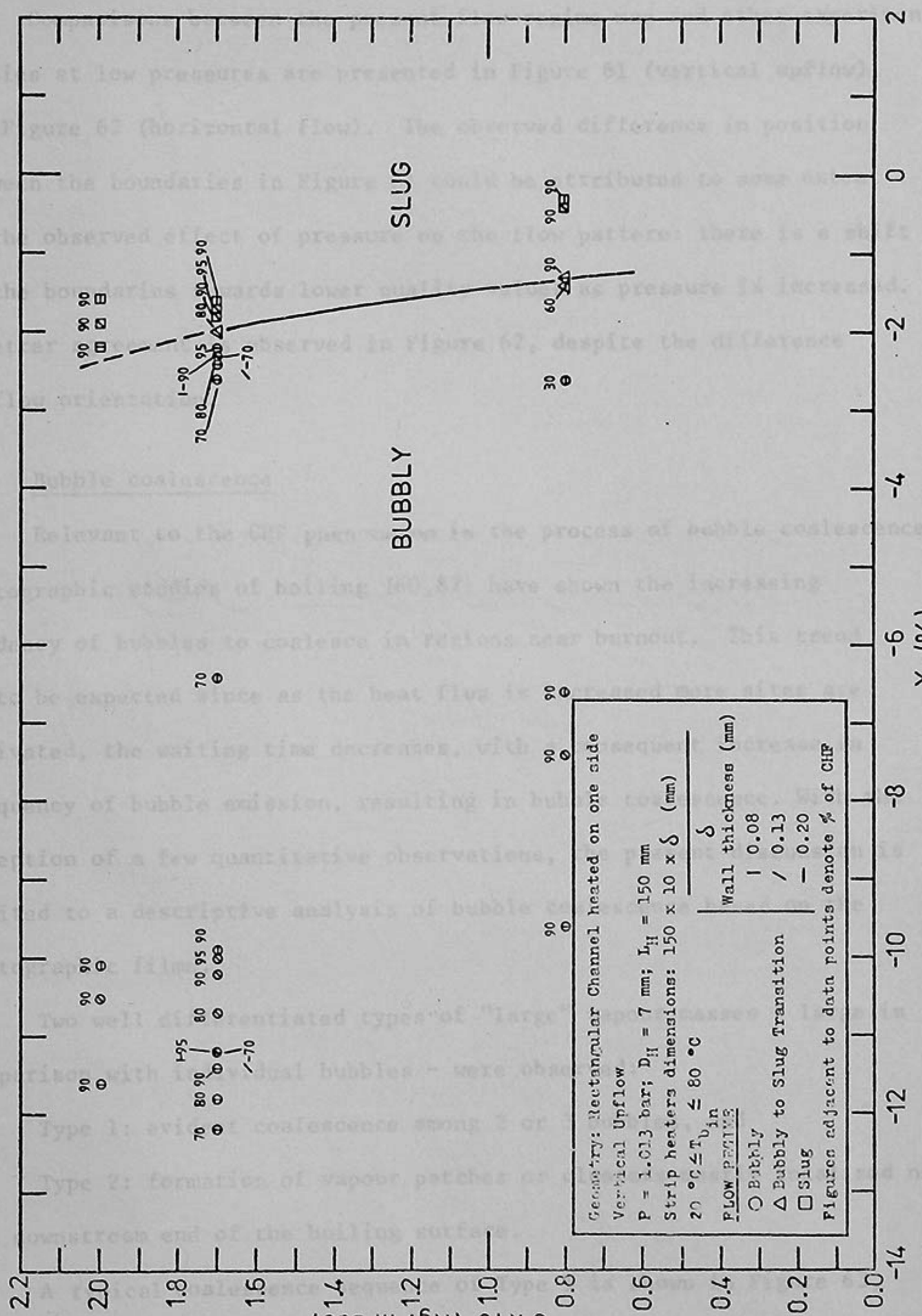


Figure 60. Present flow-regime map (water/stainless steel).

associated with slug flow as implied in a model for the mechanism of subcooled CHF at low pressures [40].

Comparisons between the present flow-regime map and other experimental studies at low pressures are presented in Figure 61 (vertical upflow) and Figure 62 (horizontal flow). The observed difference in position between the boundaries in Figure 61 could be attributed to some extent to the observed effect of pressure on the flow pattern: there is a shift in the boundaries towards lower quality values as pressure is increased. A better agreement is observed in Figure 62, despite the difference in flow orientation.

2. Bubble coalescence

Relevant to the CHF phenomenon is the process of bubble coalescence. Photographic studies of boiling [60,87] have shown the increasing tendency of bubbles to coalesce in regions near burnout. This trend is to be expected since as the heat flux is increased more sites are activated, the waiting time decreases, with a consequent increase in frequency of bubble emission, resulting in bubble coalescence. With the exception of a few quantitative observations, the present discussion is limited to a descriptive analysis of bubble coalescence based on the photographic films.

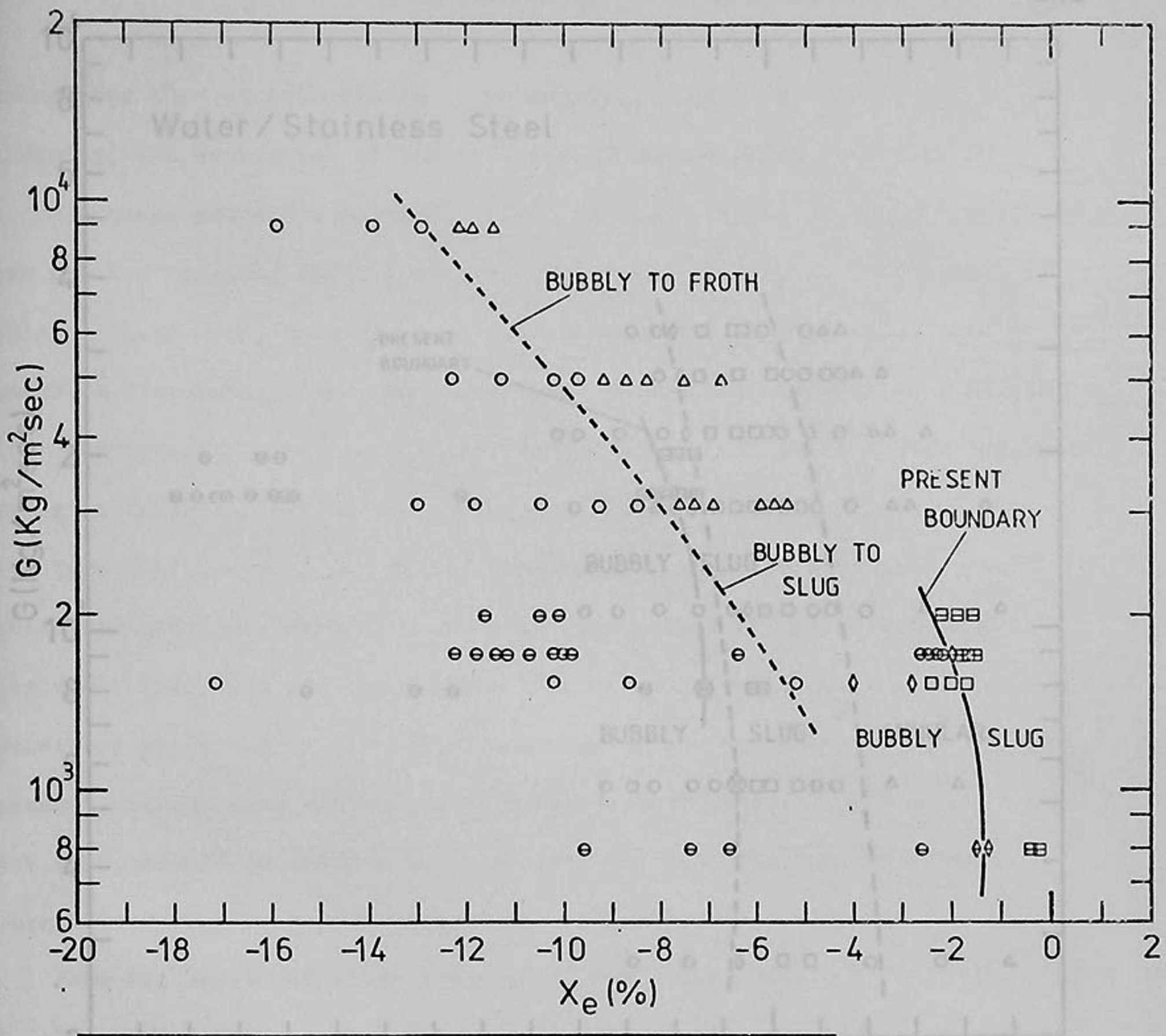
Two well differentiated types of "large" vapour masses - large in comparison with individual bubbles - were observed:

Type 1: evident coalescence among 2 or 3 bubbles, and

Type 2: formation of vapour patches or clusters mostly localized near the downstream end of the boiling surface.

A typical coalescence sequence of Type 1 is shown in Figure 63, whereas bubble clustering (patch) is shown in Figure 59(b). The first type of vapour formation was observed even at heat fluxes as low as 30% of the CHF as shown in Figure 63.

When few (2-3) bubbles coalesced, Type 1, there was an apparent



Fiori and Bergles Data [40]
Geometry: Tubular heaters
Vertical Upflow
$P_e \sim 2$ bar; D = 2.4 mm; L_H = 71.6 mm; $T_{b_{in}}$ = 21°C; L_H/D = 30

FLOW REGIME

- ○ Bubbly
- ◊ Bubbly to Slug Transition
- □ Slug
- ⬡ Bubbly to Froth
- △ Froth

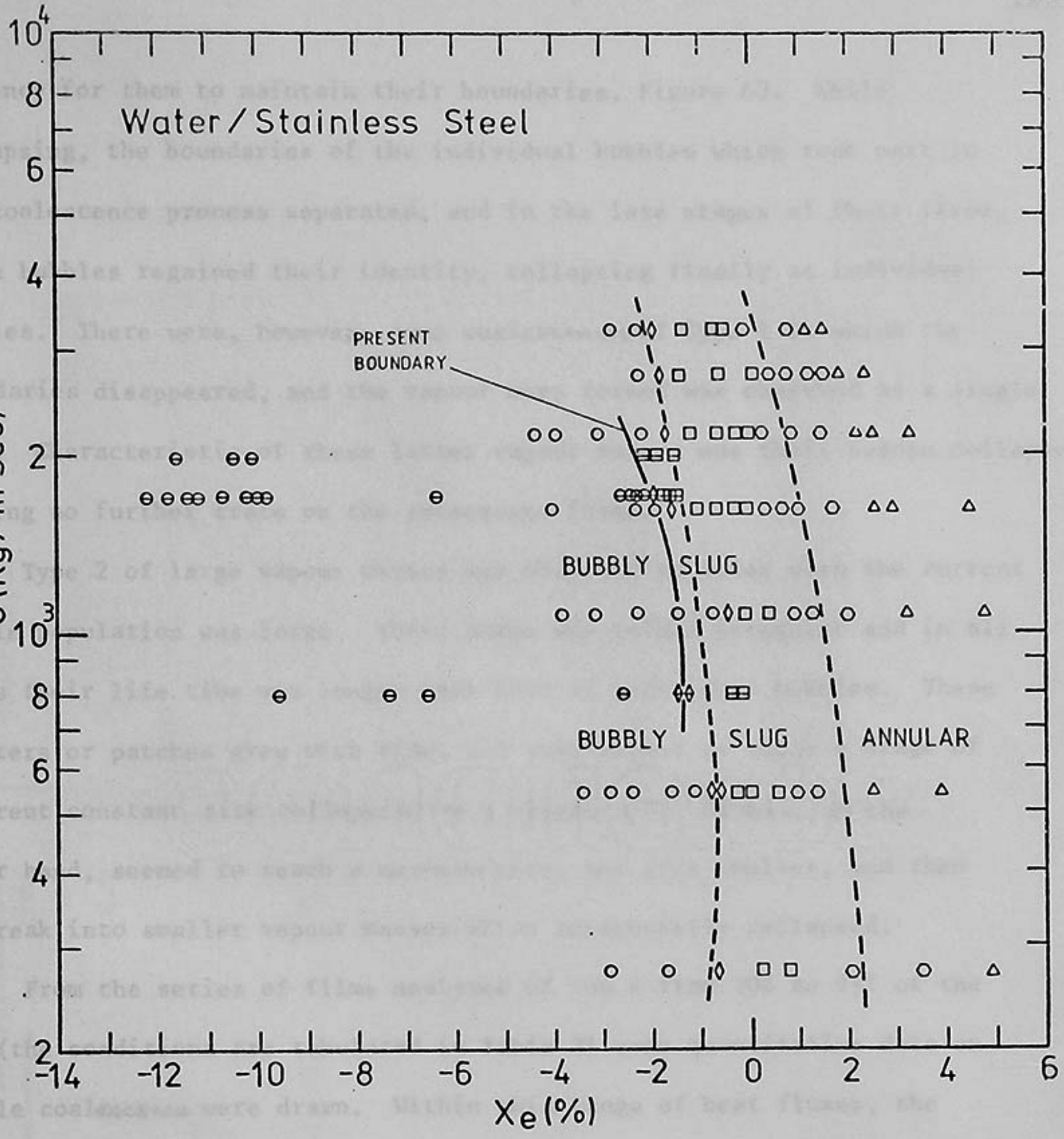
Present Data
Geometry: Rectangular Channel heated on one side
Vertical Upflow. L_H/D = 21
P = 1.013 bar; D_H = 7 mm; L_H = 150 mm
Strip heaters dimensions: 150 x 10 x δ (mm)
0.08 mm ≤ δ ≤ 0.20 mm

20 °C ≤ $T_{b_{in}}$ ≤ 80 °C

FLOW REGIMEN

- ⊖ Bubbly
- ⧫ Bubbly to Slug Transition
- ⊟ Slug

Figure 61. Comparison between flow-regime maps for water/stainless steel in vertical upflow.



Bergles, et. al. Data[86]
Geometry: Tubular heaters
Horizontal Flow. $L_H/D = 60$
$P_e \sim 2$ bar; D = 6.15 mm; L_H = 368 mm
$T_{b_{in}}$ = 65.6 °C

FLOW REGIMEN

- o Bubbly
- ◊ Bubbly to Slug Transition
- □ Slug
- ○ Slug to Annular Transition
- △ Annular

Present Data
Geometry: Rectangular Channel heated on one side
Vertical Upflow. $L_H/D = 21$
P = 1.013 bar; D_H = 7 mm; L_H = 150 mm
Strip heaters dimensions: 150 x 10 x δ (mm)
0.08 mm ≤ δ ≤ 0.20 mm

20 °C ≤ $T_{b_{in}}$ ≤ 80 °C

FLOW REGIMEN

- ⊖ Bubbly
- ◊ Bubbly to Slug Transition
- ⊟ Slug

Figure 62. Comparison between the present flow-regime map (vertical upflow) and that of Bergles et al. [86] (horizontal flow).

tendency for them to maintain their boundaries, Figure 63. While collapsing, the boundaries of the individual bubbles which took part in the coalescence process separated, and in the late stages of their lives, these bubbles regained their identity, collapsing finally as individual bubbles. There were, however, some coalescances of Type 1 in which the boundaries disappeared, and the vapour mass formed was observed as a single unit. Characteristic of these latter vapour masses was their sudden collapse leaving no further trace on the subsequent frame.

Type 2 of large vapour masses was observed to arise when the current bubble population was large. Their shape was rather irregular and in all cases their life time was longer than that of individual bubbles. These clusters or patches grew with time, and some seemed to reach a stage of apparent constant size collapsing as a single unit. Others, on the other hand, seemed to reach a maximum size, and grow smaller, and then to break into smaller vapour masses which subsequently collapsed.

From the series of films analysed of run 4 from 70% to 95% of the CHF (the conditions are tabulated in Table 3) some quantitative data on bubble coalescence were drawn. Within this range of heat fluxes, the vapour masses formed corresponded to Type 1, i.e. coalescence among few individual bubbles. An increase in the frequency of coalscence events with increasing heat flux was observed. Table 11 summarizes these quantitative observations over the 40 frames analysed at each of the four levels of heat flux.

Table 11. Bubble coalescence data for run 4.

RUN/FILM	%CHF	No. of coalescence events over the 40 frames analysed (= 4 msec time interval)	Average life time of the vapour masses formed (msec)	Average maximum (equivalent) diameter of the vapour masses formed (mm)
4-70	70	17	0.56	0.68
4-80	80	27	0.59	0.85
4-90	90	27	0.56	0.80
4-95	95	37	0.53	0.80

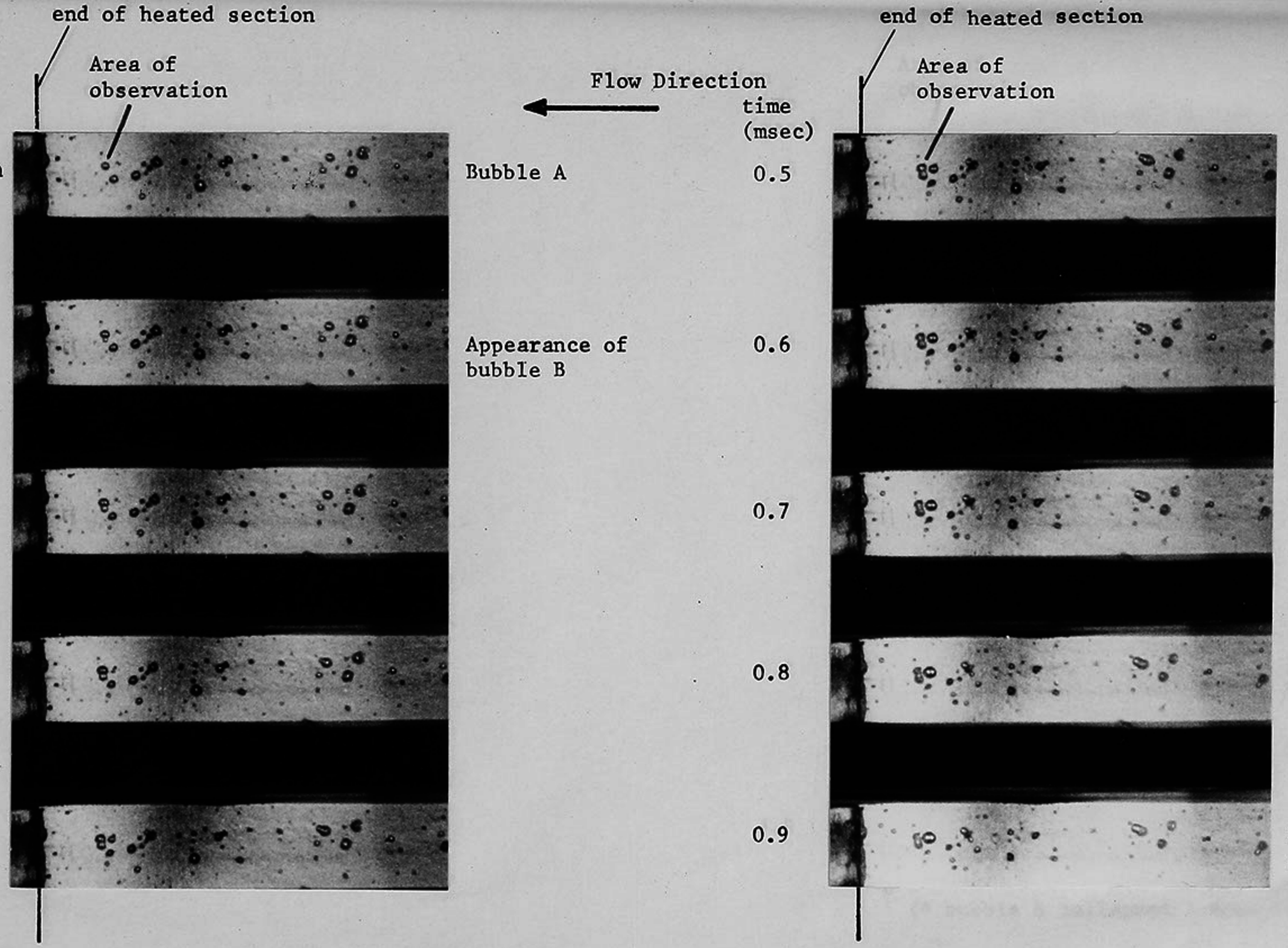


Figure 63 A bubble coalescence sequence of type 1. Run 21, 30% of CHF.
(front views).

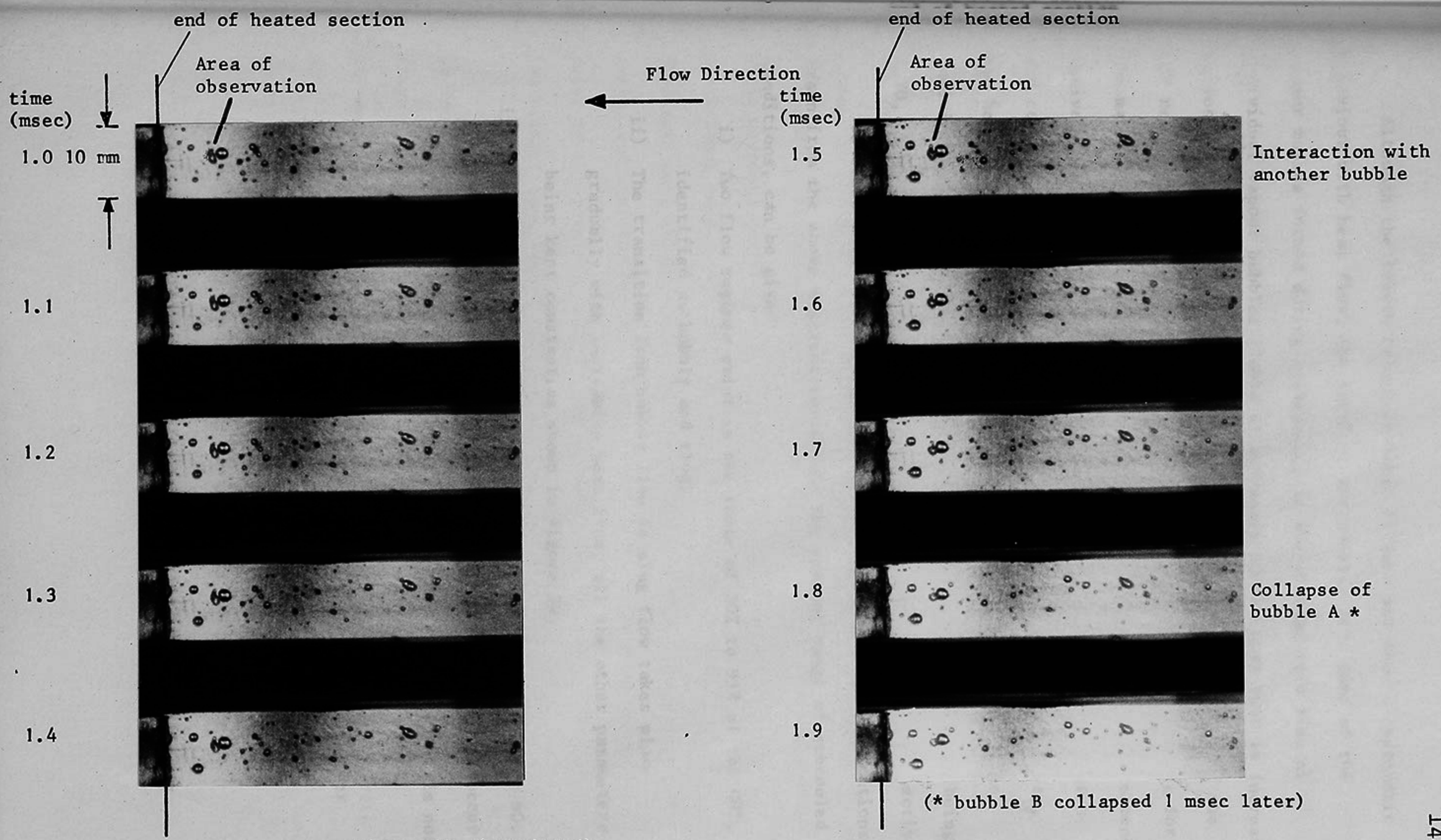


Figure 63 (continued)

Although the fourth column in Table 11 does not show a systematic behaviour with heat flux, the ratio of the average life time of the vapour masses formed during coalescence to the average life time of individual vapour bubbles (Table 4) increases as the heat flux is increased, the ratios being 1.44, 1.59, 1.65 and 1.66 for 70%, 80%, 90% and 95% of the CHF respectively. The fifth column in Table 11 presents the results for the maximum diameter of the vapour masses formed during bubble coalescence, derived by measuring the maximum projected area of these vapour masses and calculating the equivalent diameters of circles having such areas. It can be observed that the size of these vapour masses compared to the individual maximum bubble diameter is relatively large, the ratios being 1.70, 2.13, 2.00 and 2.00 for 70%, 80%, 90% and 95% of the CHF respectively.

To close this section, a summary of the most important observations drawn from the above descriptions within the present range of subcooled conditions, can be given:

i) Two flow regimes exist in the range of 30% to 95% of the CHF, identified as bubbly and slug.

ii) The transition from bubbly flow to slug flow takes place gradually with increasing heat flux, all the other parameters being kept constant, as shown in Figure 59.

iii) The flow regime is not affected by wall thickness, Figure 60.

iv) The present study gives clear evidence that burnout can occur throughout the range of flow conditions, showing that it is not associated with a particular flow regime; Figure 60.

v) The cine films showed that the boiling surfaces were never blanketed by bubbles.

vi) Nucleation persists at all flow patterns and is shown to exist under the large vapour clots in the slug regime, Figure 59 (d).

vii) Bubble coalescence exists at heat fluxes as low as 30% of the CHF, but increases with increasing heat flux. Both the life time and the maximum dimension of the vapour masses formed during bubble coalescence are greater than those values for individual bubbles.

II. Critical heat flux experiments

For the range of conditions studied, presented in Table 1, a systematic investigation of the CHF was carried out. The experimental procedure adopted, fully described in Chapter Two, was to fix both the inlet water bulk temperature and the mass-velocity, and apply direct current to the test specimens at a level generally ranging from 30% to 50% of the CHF. Slight increments in power were applied to the test surfaces until physical destruction occurred. Tests were conducted at the same operational conditions for the stainless steel surfaces of three different wall thicknesses. At burnout, melting took place across the entire width of the heated strips and the last steady value recorded prior to the physical destruction of the test surfaces was taken to be the burnout heat flux or CHF.

The arithmetic means of the CHF values for repeat tests are presented in Table 12. The reproducibility obtained in these tests is ±5% with respect to the given average values. Detailed tabulated data for the 70 CHF determinations giving flow-velocity, inlet subcooling, test-section wall thickness, wall superheat, burnout location length and type of failure (see section II.5.) are presented in Appendix E.

Table 12. Critical heat flux results.
System pressure: atmospheric. Water/stainless steel strips (150 mm long x 10 mm wide).
Geometry: a channel of rectangular cross-section with one side electically heated.
D_H = 7 mm; L_H = 150 mm. Flow direction: vertical upflow.

FLOW VELOCITY v(m/sec)	INLET SUBCOOLING $\Delta T_{sub_{in}}$ (^oK)	TEST SECTION WALL THICKNESS					
		δ = 0.08 mm		δ = 0.13 mm		δ = 0.20 mm	
		RUN NUMBER	AVERAGE CRITICAL HEAT FLUX $\emptyset_c$ (MW/m^2)	RUN NUMBER	AVERAGE CRITICAL HEAT FLUX $\emptyset_c$ (MW/m^2)	RUN NUMBER	AVERAGE CRITICAL HEAT FLUX $\emptyset_c$ (MW/m^2)
0.8	80	1	3.50	10	5.04	19	5.46
	50	2	2.92	11	3.84	20	4.01
	20	3	1.59	12	2.18	21	2.29
1.7	80	4	4.92	13	6.60	22	7.12
	50	5	3.80	14	4.89	23	5.48
	20	6	2.13	15	2.66	24	2.98
2.0	80	7	5.54	16	7.16	25	8.00
	50	8	4.54	17	5.44	26	6.22
	20	9	2.49	18	3.03	27	3.59

1. Effect of inlet subcooling on CHF

The experimental results are illustrated in Figure 64 where the critical heat flux has been plotted against inlet subcooling with the mass-velocity as parameter. The non-linear relationship between CHF and inlet subcooling, typical of short-length geometries [50,57], can be observed. Macbeth [31] pointed out that this non-linearity is found to be associated with bubbly or slug flow regimes, and this is confirmed by the present flow pattern observations. For a given wall thickness at constant mass-velocity, the CHF was observed to increase sharply with subcooling. The CHF values were found to be 2.2 to 2.5 times greater at $80^{o}K$ of inlet subcooling than those at $20^{o}K$, with no systematic change associated with mass-velocity or wall thickness.

2. Effect of mass-velocity on CHF

In order to establish the dependence of the CHF on mass-velocity, the experimental data of Figure 64 have been replotted in Figure 65 for each wall thickness as CHF against mass-velocity with the level of inlet subcooling as parameter: the increase in CHF with mass-velocity is quite significant. Within the present range of mass-velocities, 800 to 2000 Kg/m^2sec, a linear relationship between CHF and mass-velocity has been found. The best drawn straight lines in Figure 65 fitted the experimental data within 5%. The effect of mass-velocity on CHF was particularly marked at high inlet subcoolings.

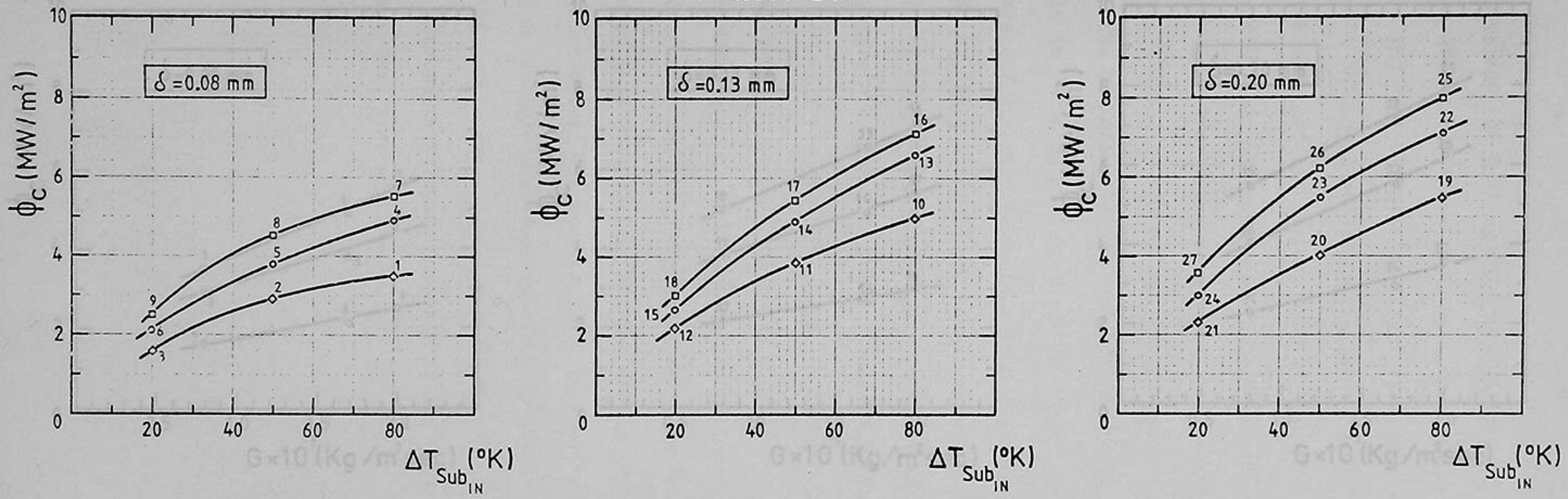
3. Effect of test-section wall thickness on CHF

Unlike the effects of inlet subcooling and mass-velocity on CHF, little attention has been focussed on the effect of wall thickness on CHF in subcooled flow boiling. This is, perhaps, the first systematic study directed to clarify the matter.

The data of Table 12 are replotted in Figure 66 as CHF against wall thickness, with the mass-velocity as parameter, showing substantial increases in CHF with increasing wall thickness. The increases observed

WATER / STAINLESS STEEL

P=1.013 bar

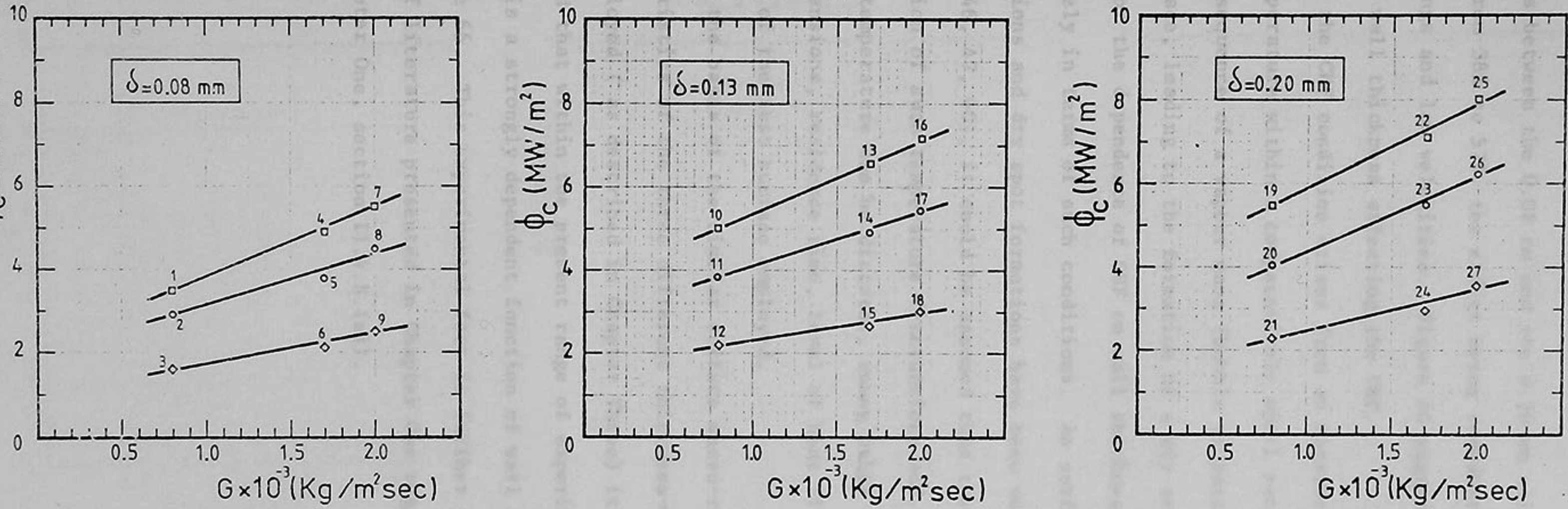


Geometry: Rectangular Channel heated on one side
D_H = 7 mm ; L_H = 150 mm ; Vertical upflow
Boiling Surface Dimensions : 150 × 10 × δ(mm)

FIGURES ADJACENT TO DATA POINTS DENOTE RUN NUMBER

Symbol	$G \times 10^{-3}$ (Kg/m²sec)
◇	0.8
○	1.7
□	2.0

Figure 64. Critical heat flux as a function of inlet subcooling.



Geometry: Rectangular Channel heated on one side
D_H=7 mm ; L_H=150 mm ; Vertical upflow
Boiling Surface Dimensions : 150 × 10 × δ(mm)

FIGURES ADJACENT TO DATA POINTS DENOTE RUN NUMBER

Symbol	$\Delta T_{sub_{in}}$ (°K)
◇	20
○	50
□	80

Figure 65. Critical heat flux as a function of mass-velocity.

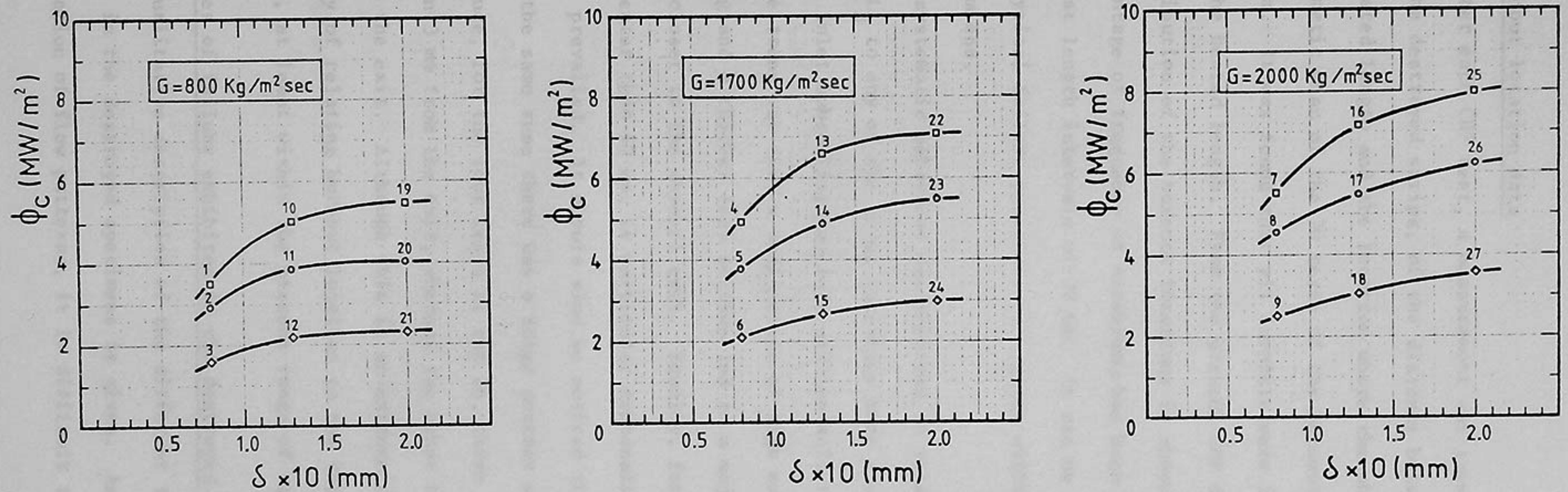
in CHF as between the 0.08 mm and the 0.20 mm wall thickness, ranged from 38% to 57%, the effect being somewhat higher at high subcoolings and low velocities. Figure 66 suggests a limiting value of wall thickness affecting the CHF.

As the CHF condition arises from an extraordinary rise in wall temperature within a comparatively small surface area, which is a consequence of a vapour mass (bubble or patch) insulating the surface, leading to the formation of a dry area, a possible reason for the dependence of CHF on wall thickness might be given intuitively in terms of such conditions. As surface temperature fluctuations and dry spot formations have been verified in boiling [18-20, 46, 47, 60], it could be assumed that the depth of penetration of such temperature fluctuations and the rate of increase in wall temperature can be dictated, among other things (vapour mass dimensions, residence time, level of heat flux), by the thermal capacity of the test surface employed.

On the basis of the similar surface macro-roughness and surface characteristics of the three different thickness-walled surfaces here employed (as described in Chapter Three) it is therefore concluded that within the present range of experimental conditions, the CHF is a strongly dependent function of wall thickness, as illustrated in Figure 66. This experimental fact is further supported by the survey of literature presented in Chapter One regarding this effect, (see Chapter One, section II.4.B.(a)).

WATER / STAINLESS STEEL

P=1.013 bar



Geometry: Rectangular Channel heated on one side
D_H=7 mm ; L_H=150 mm ; Vertical upflow
Boiling Surface Dimensions : 150 × 10 × δ(mm)

FIGURES ADJACENT TO DATA POINTS DENOTE RUN NUMBER

Symbol	$\Delta T_{sub_{in}}$ (°K)
◇	20
○	50
□	80

Figure 66. Critical heat flux as a function of test-section wall thickness.

4. Burnout location data

After each CHF test, a measurement was taken, along the centre line of the destroyed strips, of the distance between the downstream end of the heated length and the location where the physical failure occurred. The arithmetic mean of the 70 tests of the burnout location was found to be 15.2 mm. It was found that all burnouts were located in the downstream half of the heated length. From the present CHF data (see Appendix E), the distribution of the burnout locations is shown in Figure 67, where the percentage of frequency of occurrence has been plotted against burnout location at length intervals of 20 mm. It can be observed that 71.4% of the physical failure positions took place within 20 mm from the downstream end.

No systematic behaviour was observed to relate burnout location distance L_B to any of the three variables here studied, namely, mass-velocity, inlet subcooling and test section wall thickness; the only noticeable trend was that a combination of high mass-velocity, high inlet subcooling and a thicker test section led to a major proportion of burnouts closer to the channel exit. Equally, for the six tests whose L_B was greater than 50 mm, no particular combination of the above variables prevailed. It should also be noticed that even for repeat tests of the same runs there was a large scatter on burnout location. For instance, for the four tests of run 26, three burnout locations lay within 3 mm from the exit, whereas the other burnout occurred 56 mm away from the exit. Although this is an extreme example, it shows the difficulty of relating burnout location to the three variables above mentioned, at least within the present range of variations.

5. Types of failure exhibited in the destroyed test sections

A qualitative description of the different types of failure exhibited in the destroyed specimens is given. As with the classification of flow patterns, it is difficult to place absolute limits

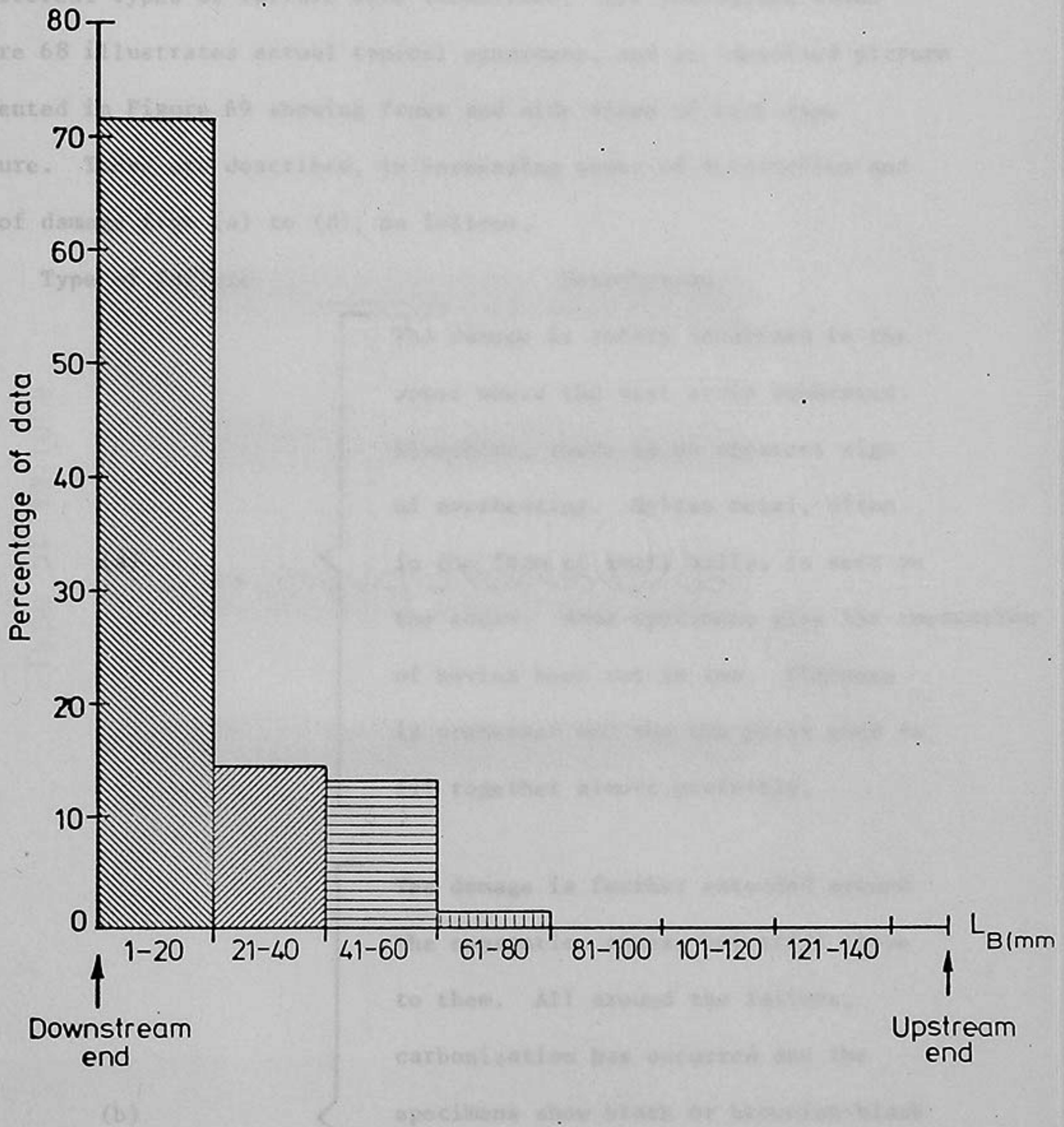
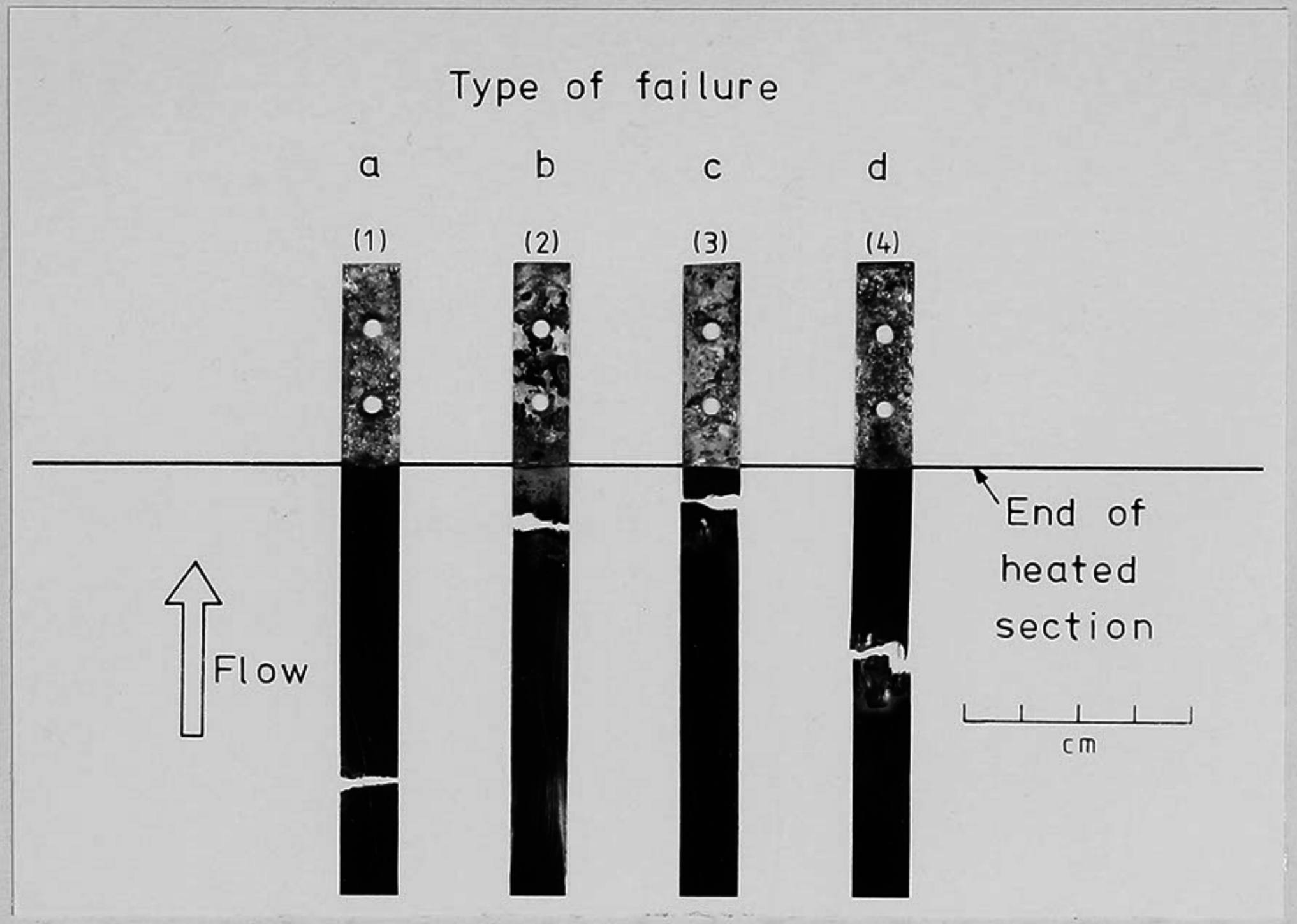


Figure 67, Distribution of burnout location data.

upon different characteristics and the description therefore depends largely on the observer's interpretation. Nevertheless, as some interesting and distinctive features are shown in the destroyed surfaces, it is fruitful to point out such differences. In classifying the types of failure, two basic factors were taken into consideration: the extent of the damage and the deformation of the test sections. Accordingly, four different types of failure were identified. The photograph shown in Figure 68 illustrates actual typical specimens, and an idealized picture is presented in Figure 69 showing front and side views of each type of failure. These are described, in increasing order of deformation and extent of damage from (a) to (d), as follows,

Type of failure	Description
(a)	The damage is totaly localized in the zones where the test strip separated. Elsewhere, there is no apparent sign of overheating. Molten metal, often in the form of small balls, is seen on the edges. Some specimens give the impression of having been cut in two. Flatness is preserved and the two parts seem to fit together almost perfectly.
(b)	The damage is further extended around the separation zones, but still close to them. All around the failure, carbonization has occurred and the specimens show black or brownish-black coloration, with yellowish areas surrounding them. The surfaces still preserve their original flatness but would fit together with difficulty.



(1) Run / Test 5-13

(2) Run / Test 13-33

(3) Run / Test 3-8

(4) Run / Test 8-22

Figure 68 Types of failure exhibited in destroyed test sections.

(c) Damage is much more extensive. Larger affected areas are observed and carbonization zones have greatly spread out from the failure. Areas of various colour tonalities around the failure are observed, the closer to the burnout the darker, from black to yellowish. The specimens are bent near the failure, sometimes exhibiting a wavy-like deformation. In a few of this type, pinholes some distance away from the actual failure were observed. Rough estimates of the equivalent diameters of the pinholes (i.e. the diameter corresponding to a circle having the pinhole areas) ranged from 1 to 2.5 mm. The surfaces would not fit together at all.

(d) The damage is very extensive. Severe carbonization occurred and the large burnouts suggest bursting. The zones of discolouration have spread further. The specimens are greatly deformed over fairly large areas close to the failure.

Appendix E gives the type of failure observed in each of the 70 burn-out tests, and Figure 70 shows the distribution of the types of failure. The highest proportion of the total number of failures was 45.7% and corresponded to type (b). It was observed that the type of failure (a) did not occur either at a mass-velocity of 800 $Kg/m^2 sec$ or with a surface of 0.20 mm in wall thickness. As far as inlet subcooling is concerned, the proportion of failures types (a) and (b) increased with

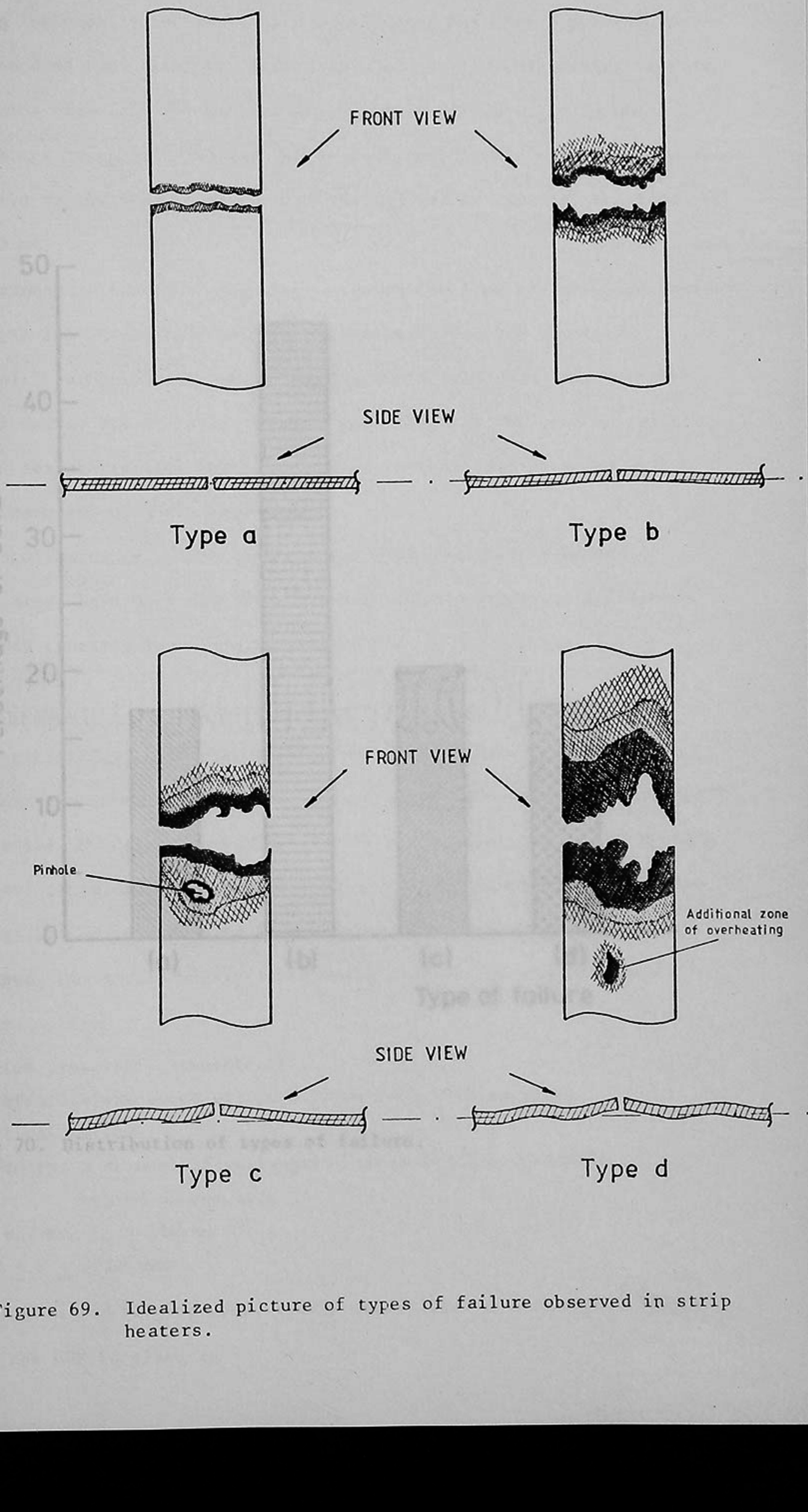


Figure 69. Idealized picture of types of failure observed in strip heaters.

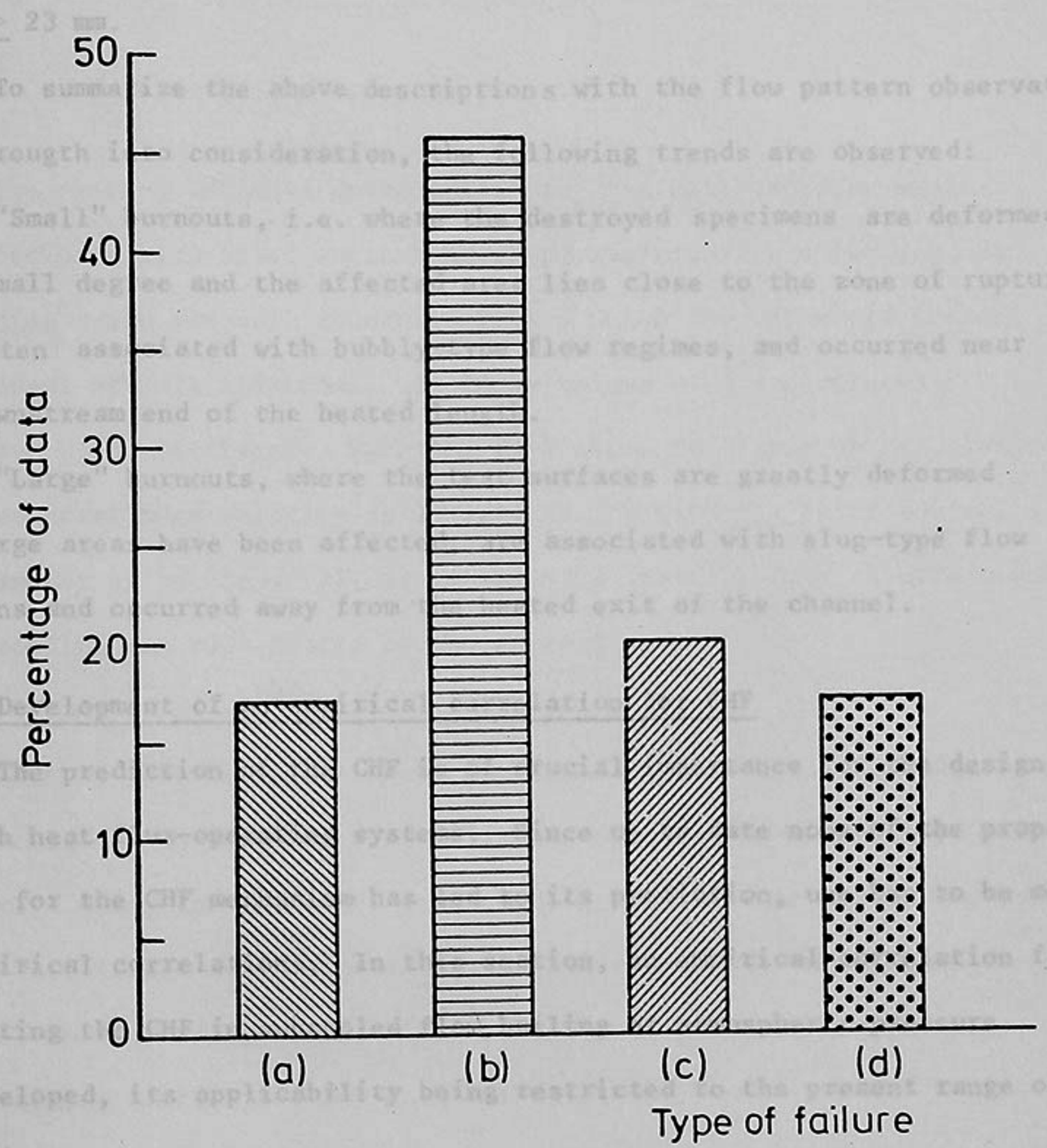


Figure 70. Distribution of types of failure.

increasing subcooling, whereas the percentage of failures types (c) and (d) increased as subcooling was decreased. It is also interesting to note that failures type (a), (b) and (c) were located within L_B = 20 mm, the percentage being 75%, 84% and 86% respectively within that distance range, while on the other hand, 83% of the failures of type (d) occurred at $L_B \geq 23$ mm.

To summarize the above descriptions with the flow pattern observations also brougth into consideration, the following trends are observed:

"Small" burnouts, i.e. where the destroyed specimens are deformed to a small degree and the affected area lies close to the zone of rupture, are often associated with bubbly-type flow regimes, and occurred near the downstream end of the heated length.

"Large" burnouts, where the test surfaces are greatly deformed and large areas have been affected, are associated with slug-type flow patterns and occurred away from the heated exit of the channel.

6. Development of an empirical correlation for CHF

The prediction of the CHF is of crucial importance for the design of high heat flux-operating systems. Since up to date none of the proposed models for the CHF mechanism has led to its prediction, use has to be made of empirical correlations. In this section, an empirical correlation for predicting the CHF in subcooled flow boiling at atmospheric pressure is developed, its applicability being restricted to the present range of conditions:

System pressure: atmospheric
Water/stainless steel strips (150 mm long x 10 mm wide)
Vertical upflow
Geometry: a channel of rectangular cross-section uniformly heated on one side
D_H = 7 mm; L_H = 150 mm
$0.8 \leq \delta \leq 0.20$ (mm)

For a liquid flowing under stable conditions in a uniformly heated channel, the CHF is given as

$$\emptyset_c = \text{fn}\ (\Delta T_{sub_{in}},\ v,\ P,\ D_H,\ L_H) \qquad (4\text{-}2)$$

Since during the present investigation both the system pressure and the channel geometry have been kept constant and the CHF has been found to be a dependent function of wall thickness, equation (4-2) takes the form

$$\emptyset_c = \text{fn}\ (\Delta T_{sub_{in}},\ v,\ \delta) \qquad (4\text{-}3)$$

The present CHF data when plotted as critical heat flux against wall thickness with inlet subcooling as parameter, Figure 66, suggest a limiting value for wall thickness beyond which the CHF would become independent of wall thickness. As these values of δ are unknown, they have to be predicted. When the data shown in Figure 66 are plotted for a constant mass-velocity as $\emptyset_c$ against $1/\delta$ with the inlet subcooling as parameter as in Figure 71, it is observed that the data at each level of subcooling are well fitted by the expression

$$\emptyset_c = a(1-e^{-b\delta}) \qquad (4\text{-}4)$$

Each of the nine curves shown in Figure 66 was replotted using this procedure, as shown in Figure 71, and equation (4-4) was applied for each curve using the method of least squares in order to obtain the values of the coefficient a and exponent b in each case. The values of $\emptyset_\infty$, i.e. the corresponding values of $\emptyset_c$ at $1/\delta = 0$, were calculated using the resulting expressions for each curve.

Subsequently, at a constant mass-velocity for each of the three levels of inlet subcooling, the ratio of actual $\emptyset_c$ to $\emptyset_\infty$ was computed and plotted against wall thickness as shown in Figure 72. It was found that a single expression

$$\eta = \frac{\emptyset_c}{\emptyset_\infty} = 1-e^{-c\delta} \qquad (4\text{-}5)$$

fitted all the data reasonably. The value of the exponent c in equation (4-5) was found to be 12 after applying the least squares method. Equation

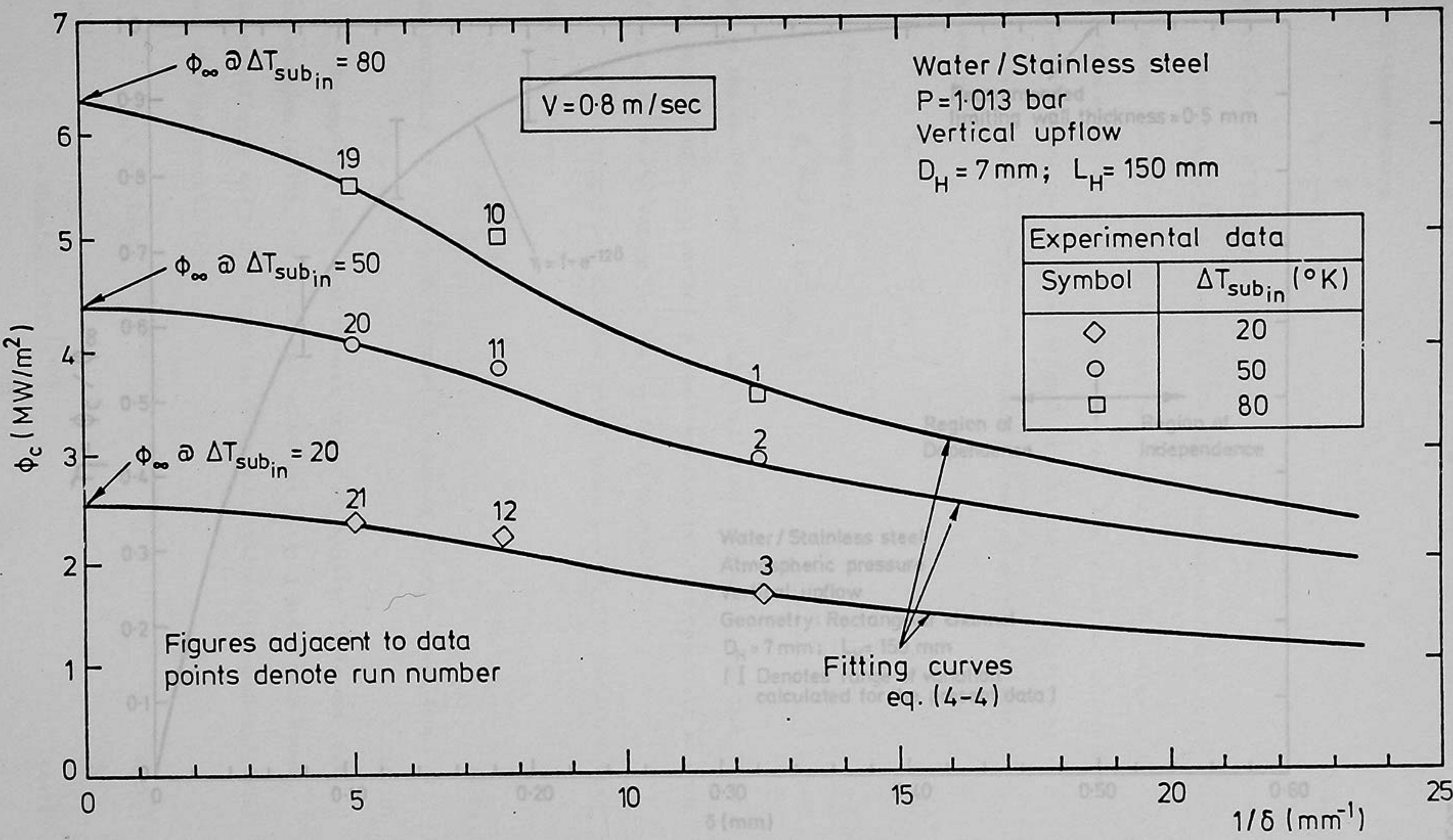


Figure 71. Critical heat flux against 1/δ.

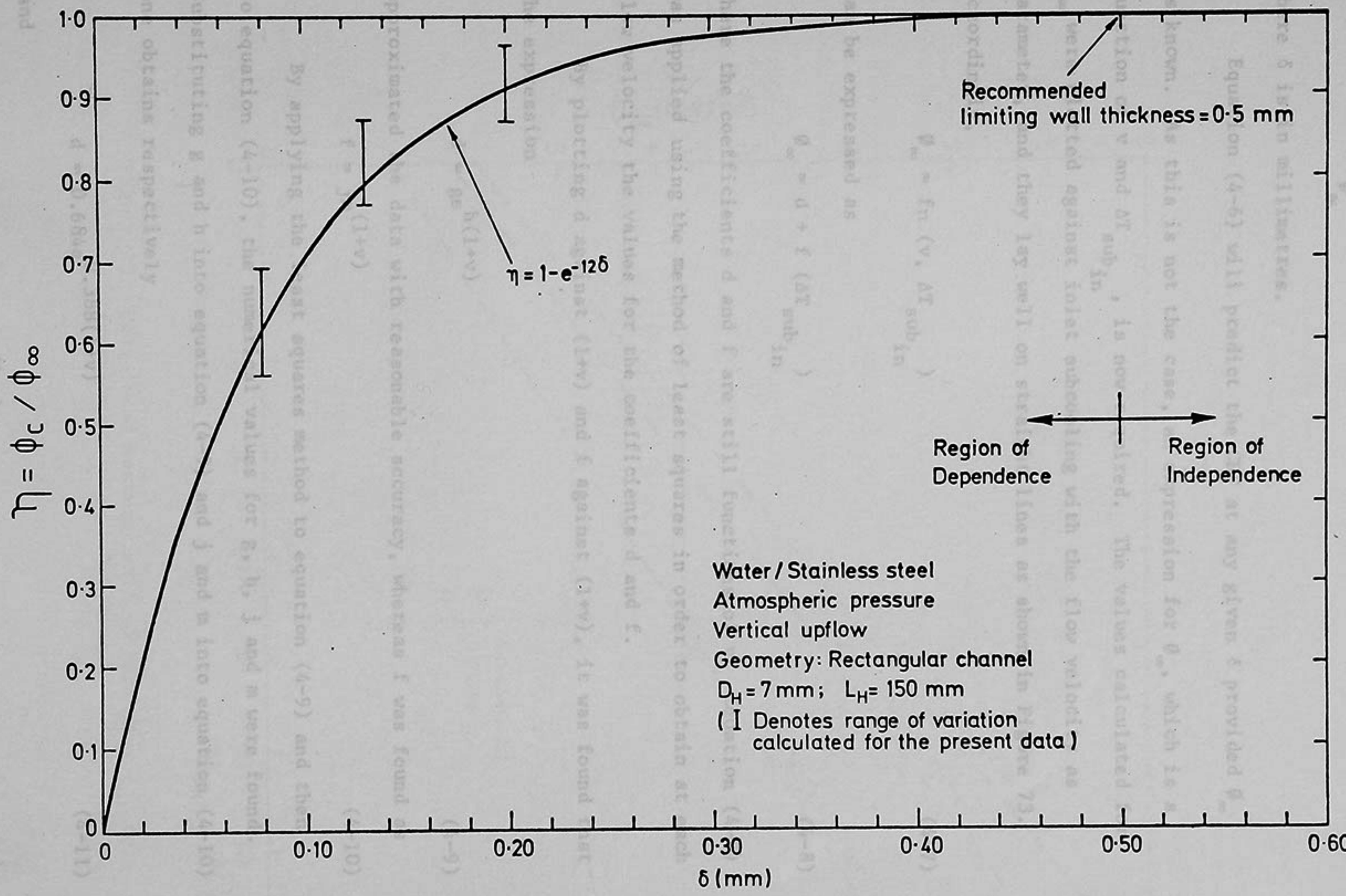


Figure 72. Normalized critial heat flux η as a function of wall thickness.

(4-5) then becomes

$$\eta = \frac{\phi_c}{\phi_\infty} = 1-e^{-12\delta} \qquad (4-6)$$

where δ is in millimetres.

Equation (4-6) will predict the CHF at any given δ provided ϕ_∞ is known. As this is not the case, an expression for ϕ_∞, which is a function of v and $\Delta T_{sub_{in}}$, is now required. The values calculated for ϕ_∞ were plotted against inlet subcooling with the flow velocity as parameter, and they lay well on straight lines as shown in Figure 73. Accordingly,

$$\phi_\infty = fn\ (v,\ \Delta T_{sub_{in}}) \qquad (4-7)$$

can be expressed as

$$\phi_\infty = d + f\ (\Delta T_{sub_{in}}) \qquad (4-8)$$

where the coefficients d and f are still functions of v. Equation (4-8) was applied using the method of least squares in order to obtain at each flow velocity the values for the coefficients d and f.

By plotting d against (1+v) and f against (1+v), it was found that the expression

$$d = ge^{h(1+v)} \qquad (4-9)$$

approximated the data with reasonable accuracy, whereas f was found as

$$f = jm^{(1+v)} \qquad (4-10)$$

By applying the least squares method to equation (4-9) and then to equation (4-10), the numerical values for g, h, j and m were found. Substituting g and h into equation (4-9) and j and m into equation (4-10) one obtains respectively

$$d = 0.684e^{0.388(1+v)} \qquad (4-11)$$

and

$$f = 0.0454(1.207)^{(1+v)} \qquad (4-12)$$

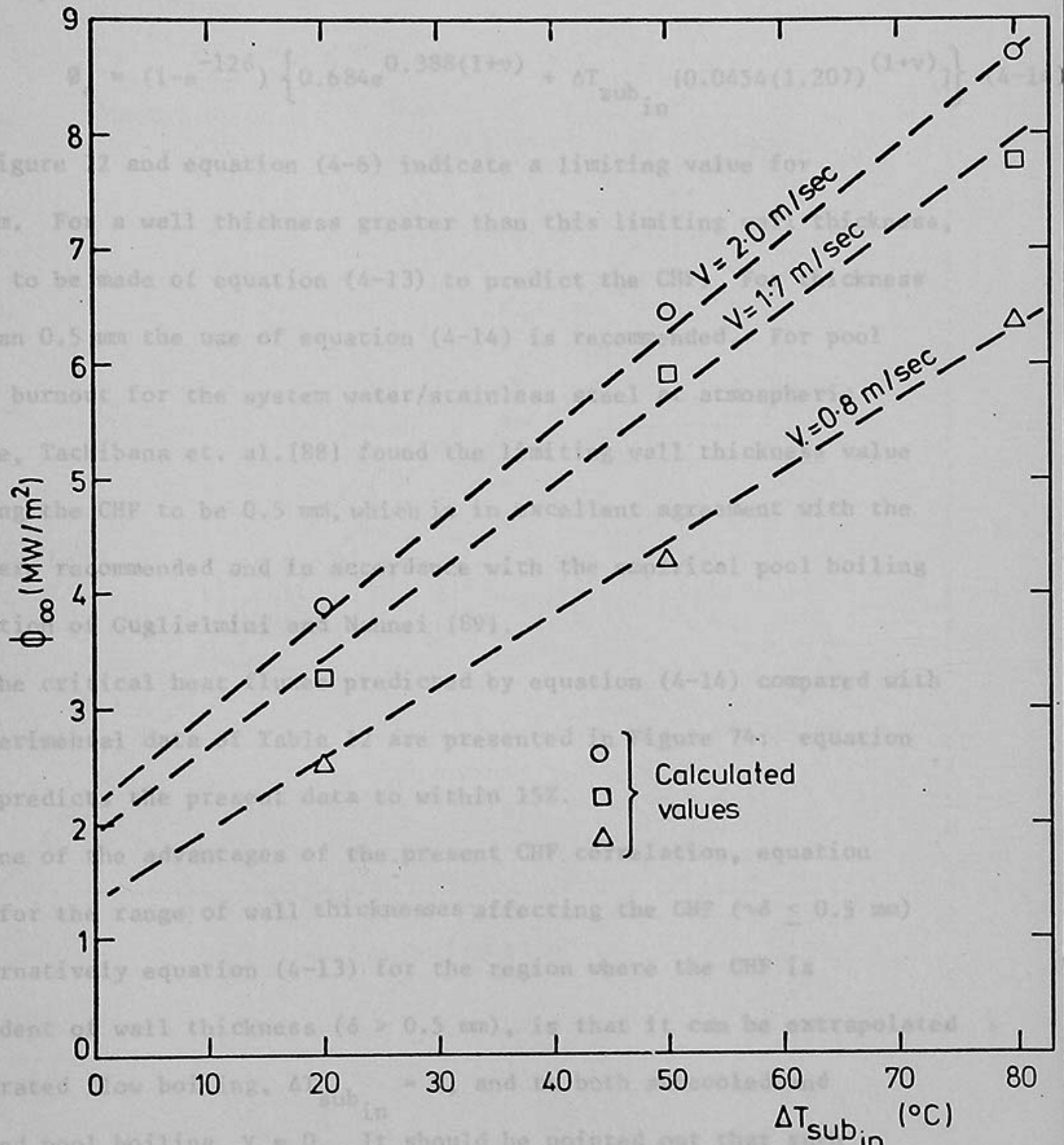


Figure 73. Calculated maximum critical heat flux ϕ_∞, as a function of inlet subcooling.

Substituting (4-11) and (4-12) into equation (4-8) yields

$$\phi_\infty = 0.684e^{0.388(1+v)} + [0.0454(1.207)^{(1+v)}]\Delta T_{sub_{in}} \qquad (4\text{-}13)$$

where ϕ_∞ is in MW/m^2, v is in m/sec and $\Delta T_{sub_{in}}$ is in ^oK.

Substituting equation (4-13) into equation (4-6) the CHF is finally expressed as

$$\phi_c = (1-e^{-12\delta})\left\{0.684e^{0.388(1+v)} + \Delta T_{sub_{in}}[0.0454(1.207)^{(1+v)}]\right\} \qquad (4\text{-}14)$$

Figure 72 and equation (4-6) indicate a limiting value for $\delta \sim 0.5$ mm. For a wall thickness greater than this limiting wall thickness, use has to be made of equation (4-13) to predict the CHF. For thickness less than 0.5 mm the use of equation (4-14) is recommended. For pool boiling burnout for the system water/stainless steel at atmospheric pressure, Tachibana et. al.[88] found the limiting wall thickness value affecting the CHF to be 0.5 mm, which is in excellent agreement with the value here recommended and in accordance with the empirical pool boiling correlation of Guglielmini and Nannei [89].

The critical heat fluxes predicted by equation (4-14) compared with the experimental data of Table 12 are presented in Figure 74: equation (4-14) predicts the present data to within 15%.

One of the advantages of the present CHF correlation, equation (4-14) for the range of wall thicknesses affecting the CHF ($\sim\delta \leq 0.5$ mm) or alternatively equation (4-13) for the region where the CHF is independent of wall thickness ($\delta > 0.5$ mm), is that it can be extrapolated to saturated flow boiling, $\Delta T_{sub_{in}} = 0$, and to both subcooled and saturated pool boiling, $v = 0$. It should be pointed out that such an extraploation is restricted to systems at atmospheric pressure with rectangular channel geometries for water-stainless steel combination. Rohsenow [5] has summarized well known pool boiling burnout correlations and recommends for saturated pool boiling the following correlations:

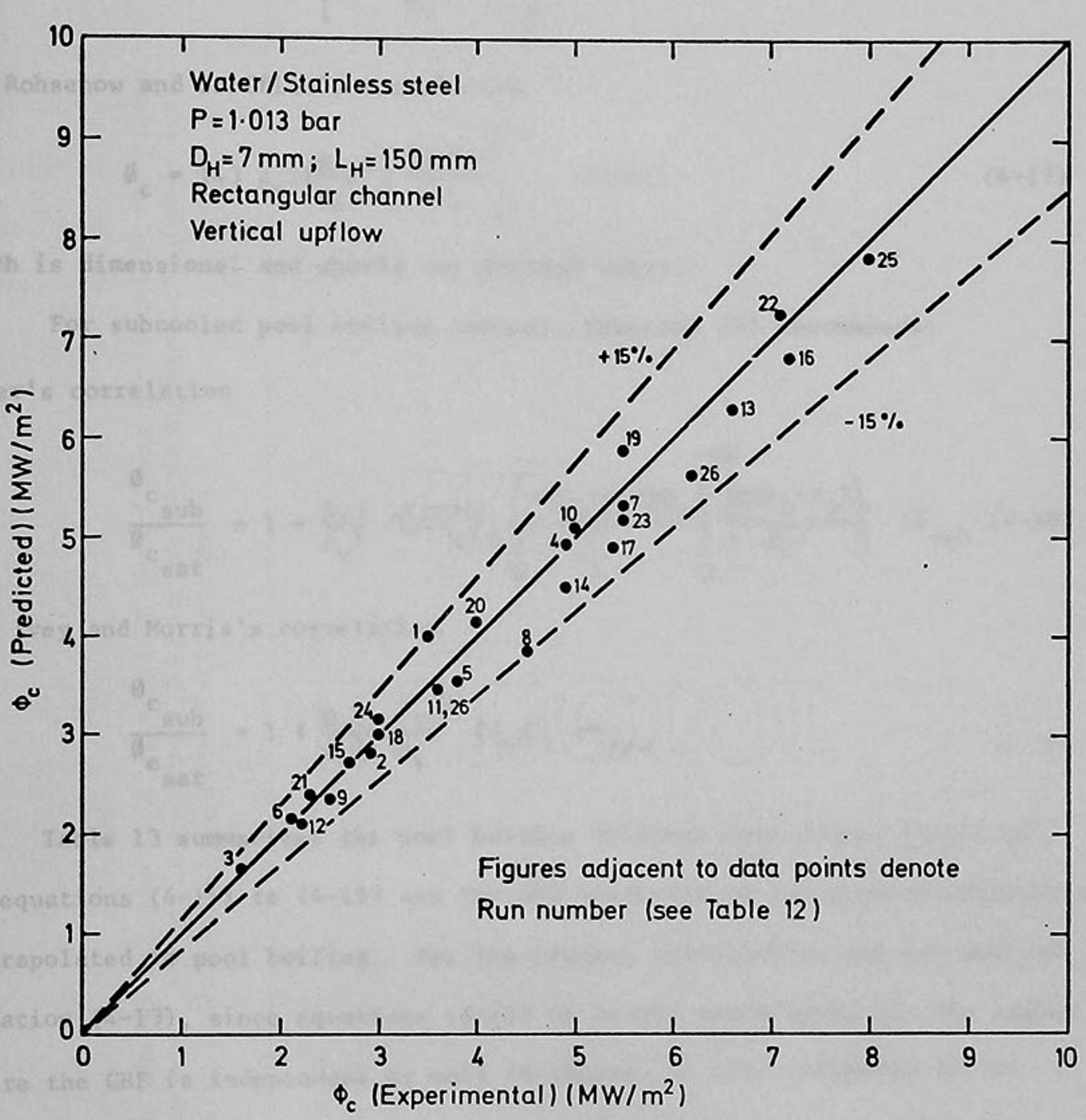


Figure 74. Comparison between experimental critical heat fluxes and those predicted by the present correlation, equation (4-14).

Zuber's correlation

$$\emptyset_c = 0.13\ \rho_v \lambda \left[\frac{\sigma(\rho_1-\rho_v)gg_c}{\rho_v^2}\right]^{\frac{1}{4}} \left[\frac{\rho_1}{\rho_1+\rho_v}\right]^{\frac{1}{2}} \quad (4\text{-}15)$$

Kutateladze's correlation

$$\emptyset_c = 0.16\rho_v \lambda \left[\frac{\sigma(\rho_1-\rho_v)gg_c}{\rho_v^2}\right]^{\frac{1}{2}} \quad (4\text{-}16)$$

and Rohsenow and Griffith's correlation

$$\emptyset_c = 143\ \rho_v \lambda \left(\frac{g}{g_c}\right)^{\frac{1}{4}} \left[\frac{\rho_1-\rho_v}{\rho_v}\right]^{0.6} \quad \text{(ft/hr)} \quad (4\text{-}17)$$

which is dimensional and should use British units.

For subcooled pool boiling burnout, Rohsenow [5] recommends:

Zuber's correlation

$$\frac{\emptyset_{c_{sub}}}{\emptyset_{c_{sat}}} = 1 + \frac{5.3}{\rho_v \lambda} \sqrt{(k\rho C_p)_1} \left[\frac{\sigma(\rho_1-\rho_v)gg_c}{\rho_v^2}\right]^{-1/8} \left[\frac{g(\rho_1-\rho_v)}{g_c\sigma}\right] \Delta T_{sub} \quad (4\text{-}18)$$

and Ivey and Morris's correlation

$$\frac{\emptyset_{c_{sub}}}{\emptyset_{c_{sat}}} = 1 + \frac{0.1}{\rho_v \lambda} \left(\frac{\rho_v}{\rho_1}\right)^{\frac{1}{4}} (C_p\rho)_1 \Delta T_{sub} \quad (4\text{-}19)$$

Table 13 summarizes the pool boiling critical heat fluxes predicted by equations (4-15) to (4-19) and the CHF predicted by the present correlation extrapolated to pool boiling. For the present correlation, use was made of equation (4-13), since equations (4-15) to (4-19) would apply for the region where the CHF is independent of wall thickness, as wall thickness is not included in any of them. It can be observed that the present correlation compares favourably with all the above correlations, especially with those for subcooled pool boiling.

Table 13. Comparison between the pool boiling critical heat fluxes predicted by the present correlation and those predicted by well known pool boiling burnout correlations. System: water/stainless steel; atmospheric pressure.

Subcooling $\Delta T_{sub_{in}}$ (^oK)	Critical Heat Flux, ϕ_c (MW/m^2)					
	Saturated Pool Boiling			Subcooled Pool Boiling		Subcooled and Saturated Pool Boiling. Present correlation. eq. (4-13)
	Zuber eq.(4-15)	Kutateladze eq.(4-16)	Rohsenow-Griffith eq.(4-17)	Zuber eq.(4-18)	Ivey-Morris eq.(4-19)	
0	1.10	1.34	1.35	—	—	1.01
20	—	—	—	2.25	2.14	2.10
50	—	—	—	3.96	3.71	3.75
80	—	—	—	5.68	5.27	5.39

CHAPTER FIVE

ANALYSIS OF NUCLEATE FLOW BOILING HEAT TRANSFER

I. Introduction

In the survey of the literature presented in Chapter One, sections I.2. and I.3., it was shown that none of the contributions of the proposed models for nucleate boiling heat transfer can alone account for the high heat transfer rates observed in boiling. It was also concluded, consistently with the experimental evidence, that the combination of microlayer evaporation, surface quenching and single-phase convective components appears to be the most appropriate integrated model for the mechanism of nucleate boiling heat transfer. Such a model is now presented for nucleate flow boiling heat transfer extended to the fully-developed nucleate boiling region, in which for the first time the overlap in the areas of influence is taken into consideration. The proposed model gives explicit expressions for the heat flux attributed to the above three components, whose addition yields the total heat flux in nucleate flow boiling, and eliminates the inconsistencies shown by previous models (see Chapter One, section I.3.). It must be emphasized that as information about maximum bubble diameter, frequency of bubble emission, nucleation site density, waiting and growth times, wall superheat and spatial distribution of nucleation sites from experiment or estimation from appropriate correlations is required, the model cannot be used alone as a predictive method.

II. A proposed model for nucleate flow boiling heat transfer

1. Basic assumptions

The development of the present model is based on the following assumptions, and extrapolation beyond the range of application, unless properly modified, is not recommended. It has been assumed that:

1) The total heat flux in subcooled nucleate flow boiling is given by the sum of the microlayer evaporation flux, the surface quenching

component and the single-phase forced convection contribution. These three components act independently over portions of the total surface area;

2) bubble shape is hemispherical;

3) bubble growth-collapse is symmetrical with respect to time;

4) the fraction F of surface area affected by bubbles is less than unity,

$$F = \frac{\pi}{4} D_m^2 n_s < 1 ;$$

5) depending on nucleation site density and spatial distribution of nucleation sites, some areas of influence will overlap;

6) there are statistical average values for the maximum bubble diameter and frequency of bubble emission, having the same values for sites in close proximity as for isolated sites;

7) there is no overlap in the maximum bubble projected areas, and

8) the level of bubble coalescence is insignificant.

Most of the above assumptions are self-explanatory, but it is worth commenting on some of them. Assumption 2) implies that the bubbles are hemispherical throughout their life time, growing and collapsing while attached to the heating surface. This however, has to be justified by reference to the work of other experimenters, since in the present study the boiling surface was filmed only from above and not simultaneously in side and plan views. Direct support is found in the work of Gunther [9] who in fact observed the bubbles to be hemispheres in subcooled flow boiling of water. Indirect evidence is provided by the generally observed tendency for rapidly growing bubbles to be hemispherical [27]. In the present study of the bubble parameters - Chapter Three, section II.2.B.-, it was found that the vast majority of the measured bubbles reached their maximum size within 0.3 msec. Further evidence can also be found in the work of Cooper et.al. [27], who in studying bubble shape and changes in

shape during bubble growth, found the ratio of bubble diameter to bubble height to be a function of the Jakob number. The authors defined a dimensionless time as

$$t^+ = \frac{t\sigma^2}{b^6 \rho_1^2} \tag{5-1}$$

where t is the time under consideration and

$$b = Ja\sqrt{\alpha_1} \tag{5-2}$$

Figure 75, reproduced from reference [27], shows the ratio bubble diameter to bubble height plotted against t^+. For the present case t^+ lies between 10^{-4} and 10^{-3}, at which values such a ratio is 2, implying that the bubbles are hemispheres. The values calculated for the parameters required in equation (5-1) are tabulated in Table 14 for the present bubble parameters (see Table 4). It should be pointed out that this latter approach is only regarded as an indirect justification since the conditions of the present investigation and the study of Cooper et.al. [27] are quite different. The latter study dealt with single bubbles growing under zero initial velocity field and uniform superheat under different gravitational fields.

Table 14. Values calculated for t^+ based on t_L.

RUN/FILM	$\emptyset$ (MW/m^2)	% CHF	Ja	$bx10^2$ ($m/sec^{\frac{1}{2}}$)	b^6x10^9 (m^6/sec^3)	t_Lx10^3 (sec)	$t_L^+x10^4$
4-70	3.44	70	82.6	3.40	1.56	0.39	9.38
4-80	3.94	80	85.3	3.52	1.89	0.37	7.34
4-90	4.43	90	89.2	3.68	2.47	0.34	5.16
4-95	4.67	95	90.1	3.71	2.62	0.32	4.58

Assumption 3) is supported by the present observations regarding bubble growth rate, Figure 41, which closely resembles a parabolic growth rate. Assumption 4) implies, consistently with the photographic evidence, that

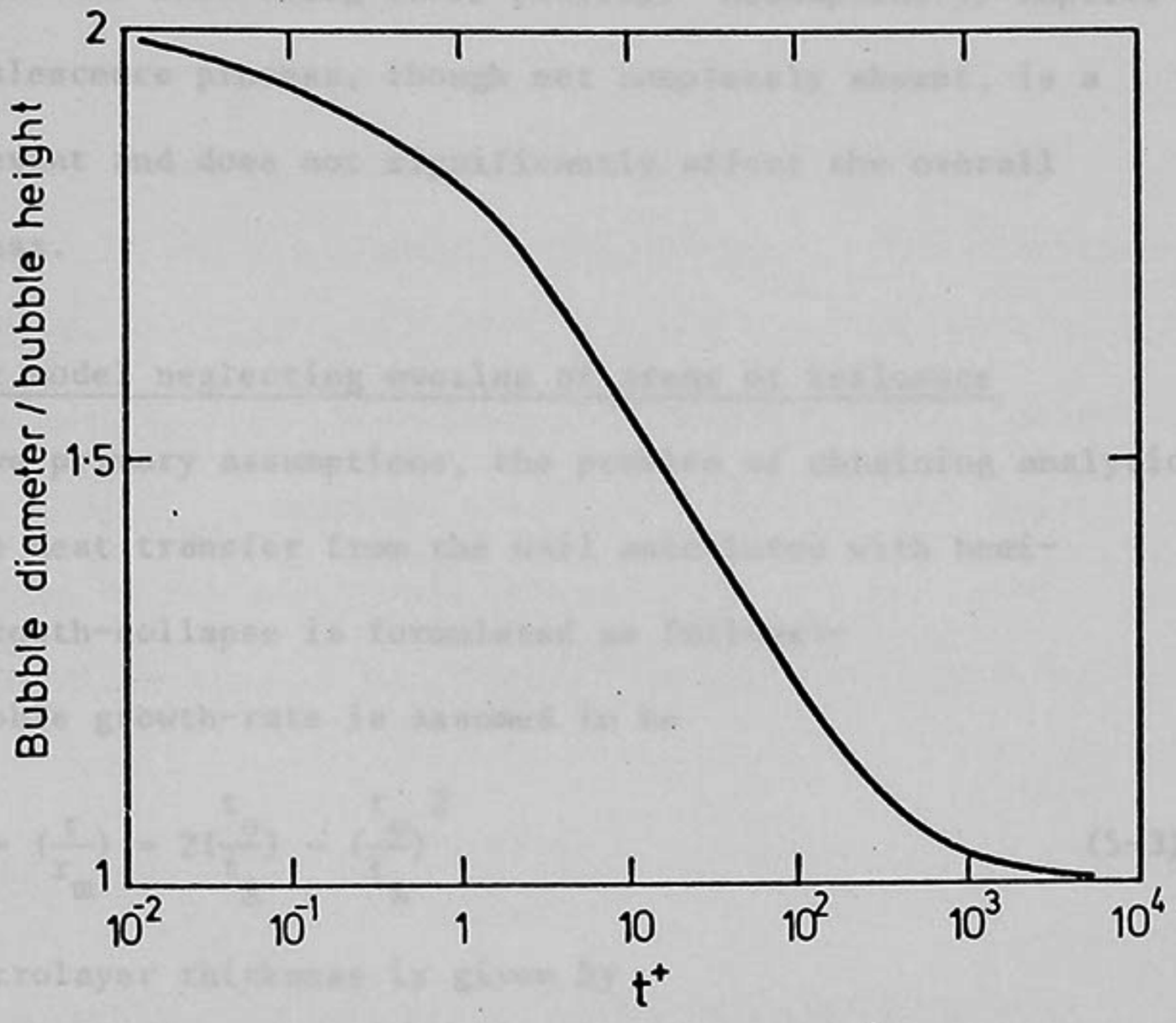


Figure 75 Bubble shape variation with t^+. (Redrawn from Cooper et. al.[27]; data points omitted for clarity).

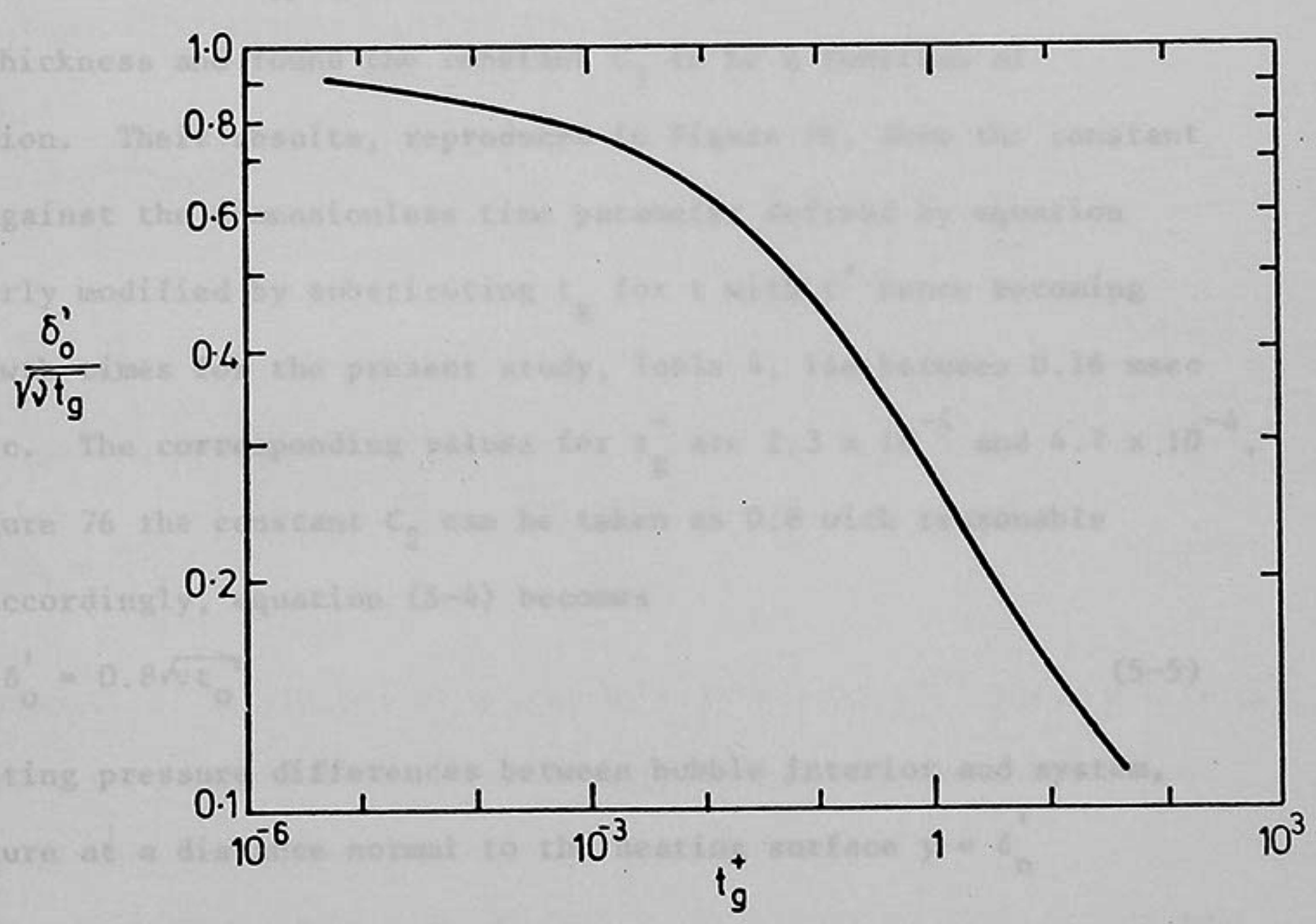


Figure 76 Initial microlayer thickness as a funtion of t_g^+. (Redrawn from [27]; data points omitted for clarity).

bubble population are far from being close-packing. Assumption 8) implies that the bubble coalescence process, though not completely absent, is a rather infrequent event and does not significantly affect the overall heat transfer process.

2. Heat transfer model neglecting overlap of areas of influence

From the above primary assumptions, the problem of obtaining analytical expressions for the heat transfer from the wall associated with hemispherical bubble growth-collapse is formulated as follows:-

The bubble growth-rate is assumed to be

$$r(t_o) = \left(\frac{r}{r_m}\right) = 2\left(\frac{t_o}{t_g}\right) - \left(\frac{t_o}{t_g}\right)^2 \qquad (5\text{-}3)$$

and the initial microlayer thickness is given by

$$\delta'_o = fn(r) = fn\,(t_o) = C_2\sqrt{\nu t_o} \qquad (5\text{-}4)$$

Cooper et.al. [27] applied dimensional analysis to the initial microlayer thickness and found the constant C_2 to be a function of surface tension. Their results, reproduced in Figure 76, show the constant C_2 plotted against the dimensionless time parameter defined by equation (5-1), properly modified by substituting t_g for t with t^+ hence becoming t_g^+. The growth times for the present study, Table 4, lie between 0.16 msec and 0.20 msec. The corresponding values for t_g^+ are 2.3×10^{-4} and 4.7×10^{-4}, and from Figure 76 the constant C_2 can be taken as 0.8 with reasonable accuracy. Accordingly, equation (5-4) becomes

$$\delta'_o = 0.8\sqrt{\nu t_o} \qquad (5\text{-}5)$$

Neglecting pressure differences between bubble interior and system, the temperature at a distance normal to the heating surface $y = \delta'_o$ becomes T_{sat} ($\Delta T_{sat} = 0$); but the effect is not felt at the wall until $\sim C_3(\delta'^2_o/\alpha)$ seconds later. This can be approximated by assuming no effect for a time $t_d = C_3\,\delta'^2_o/\alpha$, and then a linear temperature gradient across the microlayer. Substitution of equation (5-5) into the latter

expression for t_d yields

$$t_d = C_3\ \delta'^2_o/\alpha = C_3\ (0.64)\ \nu t_o/\alpha = C_3\ (0.64)\ P_r\ t_o \qquad (5\text{-}6)$$

The modes of heat transfer at the wall for this idealized model are depicted in Figure 77 (a) for a complete bubble cycle. The numerical value of constant C_3 is obtained by initially regarding the microlayer as the region $0<x'<L$ at zero initial temperature; $x' = 0$ maintained at zero temperature and $x' = L$ at T_{sat}, constant for $t > 0$. Carslaw and Jaeger [90] give the solution of the heat conduction equation for the total quantity of heat which has crossed the plane $x' = 0$ from $t = 0$ to $t = t$ for this case as

$$q = \frac{4k\Delta T_{sat}\ t^{\frac{1}{2}}}{\alpha^{\frac{1}{2}}} \sum_{n=0}^{\infty} \text{ierfc}\ \frac{(2n+1)L}{2\sqrt{\alpha t}} \qquad (5\text{-}7)$$

Multiplying equation (5-7) by L/t, it can be rearranged to give

$$\bar{Q} = \frac{4}{\sqrt{\tau}} \sum_{n=0}^{\infty} \text{ierfc}\ \frac{1}{2\sqrt{\tau}}\ (2n+1) \qquad (5\text{-}8)$$

where $\bar{Q}$ and τ are dimensionless parameters given by

$$\bar{Q} = \frac{qL}{k\Delta T_{sat}\ t} \qquad (5\text{-}9)$$

and

$$\tau = \frac{\alpha t}{L^2} \qquad (5\text{-}10)$$

From equation (5-6)

$$C_3 = \frac{\alpha t_d}{\delta'^2_o} \qquad (5\text{-}11)$$

Equation (5-8) is plotted as $\bar{Q}$ against τ in Figure 78. For $\tau \equiv C_3 = 0.6$, it is observed that equation (5-8) can be approximated by the dashed line.

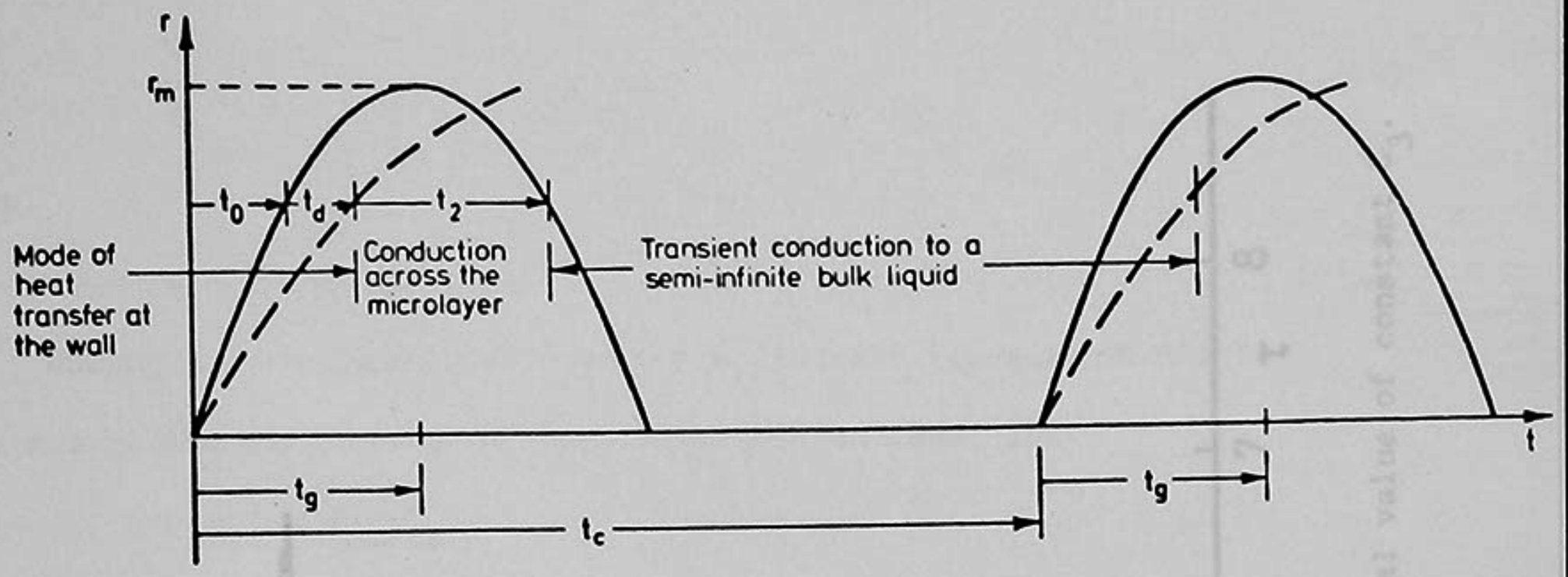
Equation (5-6) then takes the form

$$t_d = C_3(0.64)\ Prt_o = 0.384\ Prt_o \qquad (5\text{-}12)$$

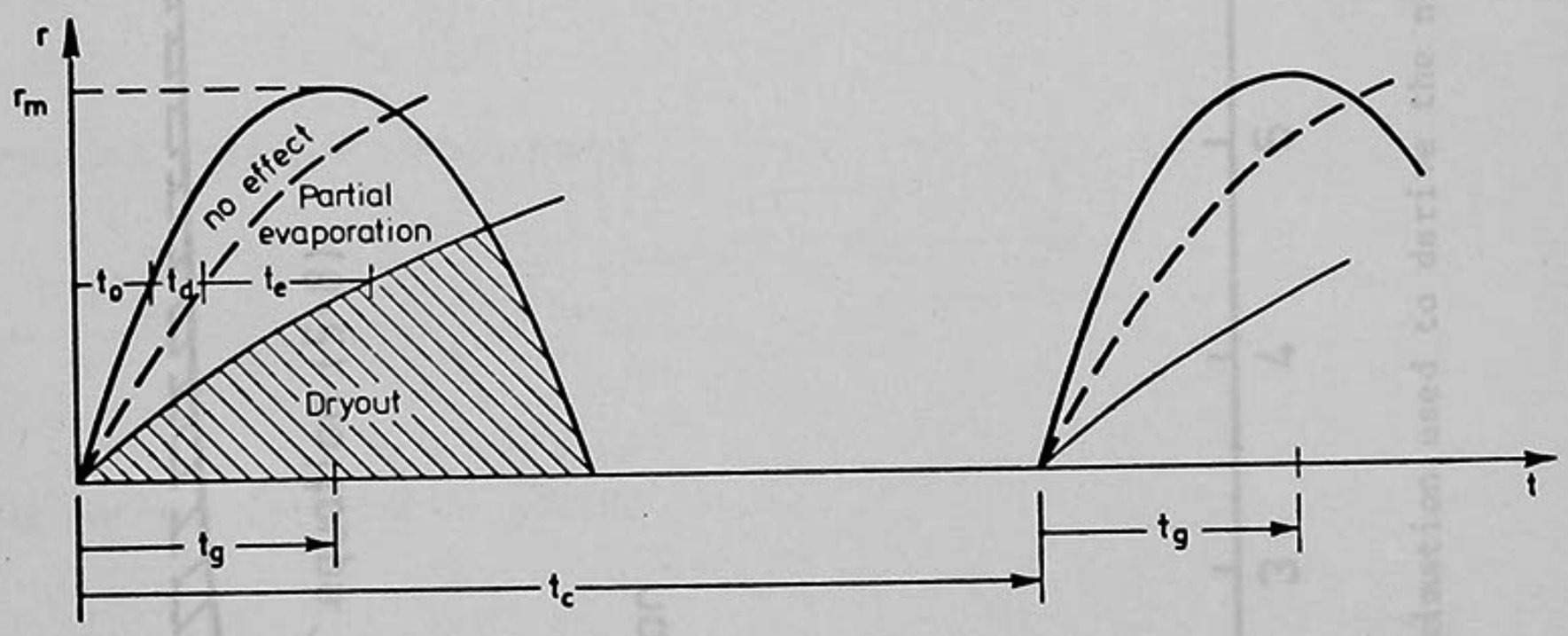
The time during which there is conduction across the microlayer, Figure 77(a), is

$$t_2 = 2(t_g - t_o) - t_d = 2t_g - t_o(2+0.384Pr) \qquad (5\text{-}13)$$

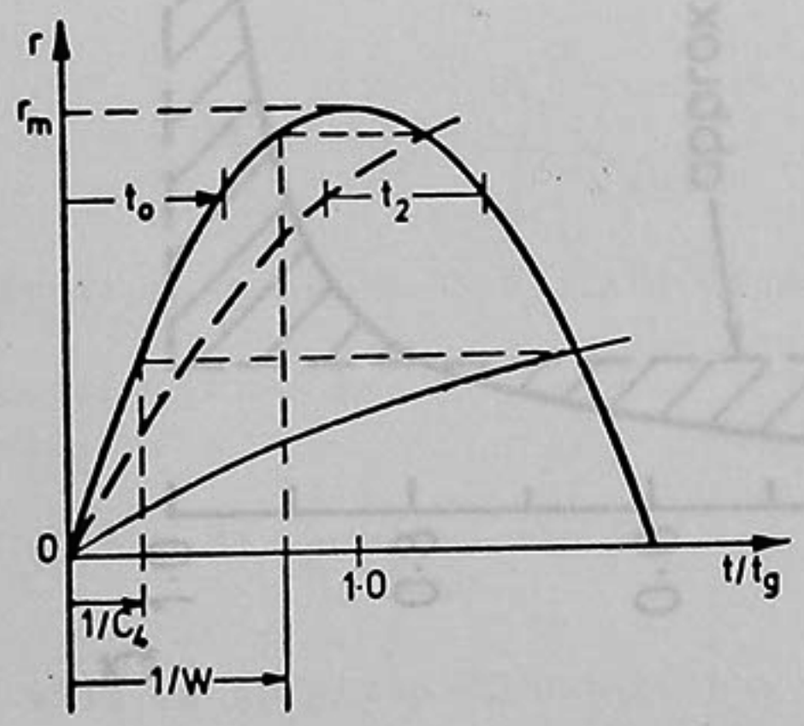
$$t_2 = 0 \text{ at } t_o = t_g - t_d/2$$



(a) Modes of heat transfer at the heated wall.



(b) Processes occurring during the lifetime of a bubble.



(c) Time intervals for the operation of the heat transfer modes.

Figure 77 Heat transfer from the wall associated with hemispherical bubble growth-collapse.

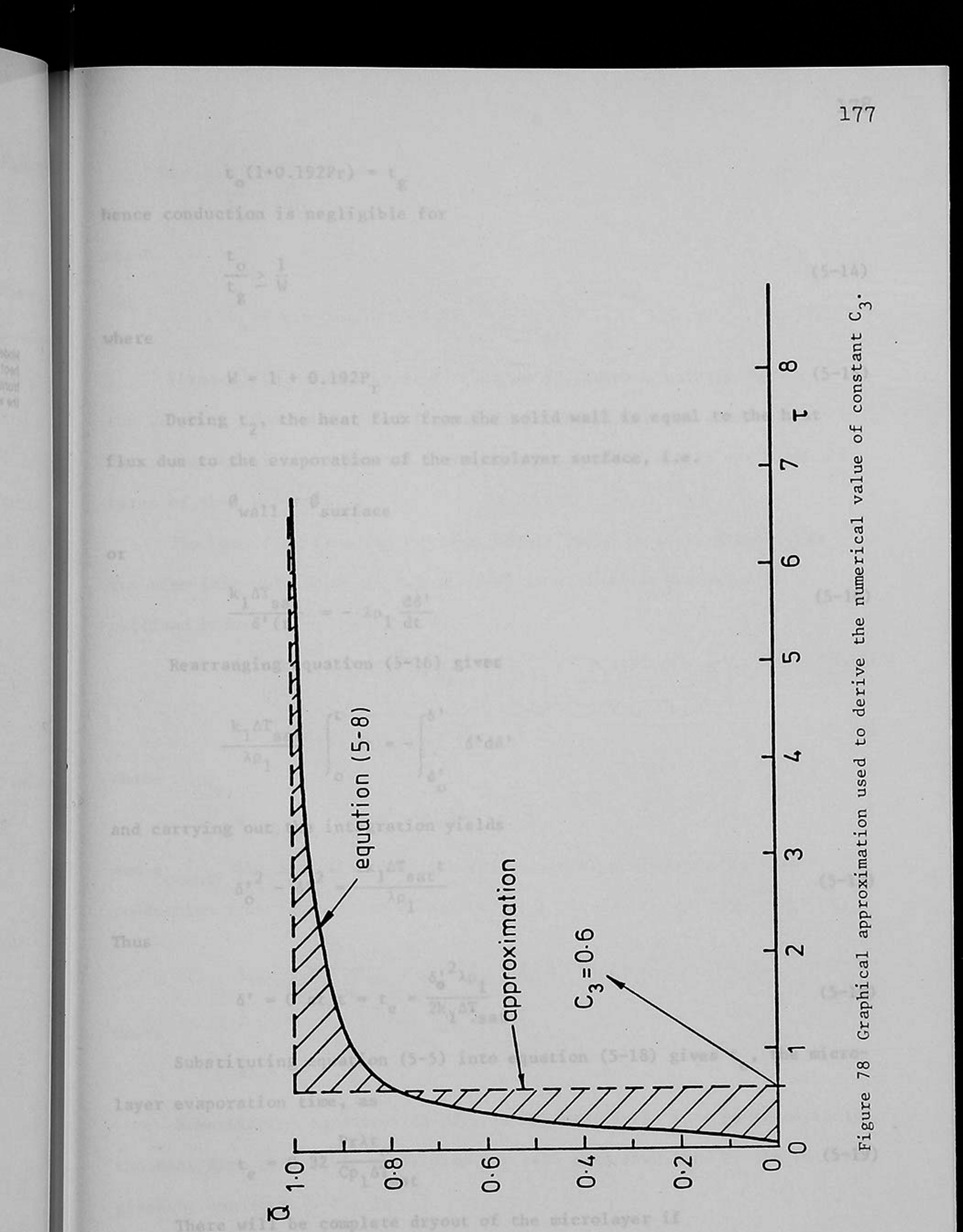


Figure 78 Graphical approximation used to derive the numerical value of constant C_3.

$$t_o(1+0.192Pr) = t_g$$

hence conduction is negligible for

$$\frac{t_o}{t_g} \geq \frac{1}{W} \tag{5-14}$$

where

$$W = 1 + 0.192P_r \tag{5-15}$$

During t_2, the heat flux from the solid wall is equal to the heat flux due to the evaporation of the microlayer surface, i.e.

$$\phi_{wall} = \phi_{surface}$$

or

$$\frac{k_1 \Delta T_{sat}}{\delta'(t)} = - \lambda \rho_1 \frac{d\delta'}{dt} \tag{5-16}$$

Rearranging equation (5-16) gives

$$\frac{k_1 \Delta T_{sat}}{\lambda \rho_1} \int_o^t dt = - \int_{\delta'_o}^{\delta'} \delta' d\delta'$$

and carrying out the integration yields

$$\delta_o'^2 - \delta'^2 = \frac{2k_1 \Delta T_{sat} t}{\lambda \rho_1} \tag{5-17}$$

Thus

$$\delta' = 0 \text{ at } t = t_e = \frac{\delta_o'^2 \lambda \rho_1}{2k_1 \Delta T_{sat}} \tag{5-18}$$

Substituting equation (5-5) into equation (5-18) gives t_e, the microlayer evaporation time, as

$$t_e = 0.32 \frac{Pr \lambda t_o}{Cp_1 \Delta T_{sat}} \tag{5-19}$$

There will be complete dryout of the microlayer if

$$t_d + t_e \leq 2(t_g - t_o) \tag{5-20}$$

Substitution of equations (5-12) and (5-19) into equation (5-20) results in

$$\frac{t_o}{t_g} \leq \frac{1}{C_4} \tag{5-21}$$

where

$$C_4 = 1 + 0.192Pr + 0.16 \frac{Pr\lambda}{Cp_1 \Delta T_{sat}} \tag{5-22}$$

Figure 77(b) shows the heat transfer processes occurring during the lifetime of a bubble, and Figure 77(c) illustrates the time intervals at which the assumed modes of heat transfer are in operation in terms of the ratio t/t_g.

The heat flow from the wall per bubble cycle is then obtained for the time intervals shown in Figure 77(c) in a stepwise procedure as outlined below:

(1) For $0 \leq \frac{t_o}{t_g} \leq \frac{1}{C_4}$ (5-23)

$$q = 2\pi r dr \, (q_{evap(1)} + q_{tcond}) \tag{5-24}$$

where

$$q_{evap(1)} = \lambda \rho_1 \delta'_o = 0.8\lambda\rho_1 \sqrt{\nu_1 t_o} \tag{5-25}$$

and q_{tcond}, the heat flow due to surface quenching assuming transient conduction from the wall to a semi-infinite liquid for the time $t_c - t_2$, is

$$q_{tcond} = \frac{2k_1 \Delta T}{(\pi\alpha_1)^{\frac{1}{2}}} \left[t_c - 2t_g + t_o \, (2+0.384Pr) \right]^{\frac{1}{2}} \tag{5-26}$$

where

$$\Delta T = T_w - T_b$$

Substituting equations (5-22), (5-25) and (5-26) into equation (5-24), the heat flow per bubble cycle from the wall area specified by the interval given by equation (5-23) is

$$q_a = 2\pi \int_o^{t_g/C_4} r(t_o) \frac{dr}{dt_o} \left\{ 0.8\lambda\rho_1 \sqrt{\nu_1 t_o} + \frac{2k\Delta T}{(\pi\alpha)^{\frac{1}{2}}} \left[t_c - 2t_g + t_o(2+0.384Pr) \right]^{\frac{1}{2}} \right\} dt_o$$

(5-27)

(2) For the time interval

$$\frac{1}{C_4} \leq \frac{t_o}{t_g} \leq \frac{1}{W} \tag{5-28}$$

the heat flow from the wall per bubble cycle is given by equation (5-24) modified as

$$q = 2\pi r dr \, (q_{evap(2)} + q_{t_{cond}}) \tag{5-29}$$

where

$$q_{evap(2)} = \lambda \rho_1 (\delta'_o - \delta') \tag{5-30}$$

$$\delta' = \delta'_o \left(1 - \frac{t_2}{t_e}\right)^{\frac{1}{2}} \tag{5-31}$$

and $q_{t_{cond}}$ is as given by equation (5-26).

Substituting equations (5-15), (5-26) and (5-30) into equation (5-29), the heat flow during the time interval given by equation (5-28) is

$$q_b = 2\pi \int_{t_g/C_4}^{tg/w} r(t_o) \frac{dr}{dt_o} \left\{ \lambda \rho_1 (\delta'_o - \delta') + \frac{2k\Delta T}{\sqrt{\pi \alpha_1}} \left[t_c - 2t_g + t_o (2 + 0.384 Pr) \right]^{\frac{1}{2}} \right\} dt_o \tag{5-32}$$

(3) For the time interval

$$\frac{1}{W} < \frac{t_o}{t_g} \leq 1 \tag{5-33}$$

the heat flow is calculated only by transient conduction from the wall to a semi-infinite liquid for the time $t = t_c$. Therefore, the heat flow for the time interval given by equation (5-33) is

$$q_c = 2\pi \int_{t_g/w}^{t_g} r(t_o) \frac{dr}{dt_o} \left[\frac{2k\Delta T}{\sqrt{\pi \alpha_1}} t_c^{\frac{1}{2}} \right] dt_o \tag{5-34}$$

The addition of equations (5-27), (5-32) and (5-34), when integrated, will yield the heat flow from the wall over the projected surface area of a bubble.

For radial distances greater than $r_m = Dm/2$, i.e., over the area of influence around a nucleation site, instantaneous quenching and then

transient conduction for the time $t = t_c = t_L + t_w$ is assumed, over the area

$$K(\frac{\pi}{4}D_m^2) - (\frac{\pi}{4}D_m^2) = (K-1)\frac{\pi D_m^2}{4} \tag{5-35}$$

The corresponding heat flux for this annular-shaped surface area is given by

$$\phi_{NB_i} = 2\sqrt{(k\rho Cp)_l f/\pi}(T_w-T_b)(K-1)\frac{\pi D_m^2}{4} n_s \tag{5-36}$$

Equation (5-36) is in fact equation (1-13) modified by introducing (K-1) instead of K. Equation (5-36) may also be expressed as

$$\phi_{NBi} = 2\sqrt{(k\rho Cp)_l f/\pi}\ (T_w-T_b)\ [\beta-F] \tag{5-37}$$

where β is the fraction of the total surface area involved in boiling

$$\beta = KF = KA_b\ n_s = K(\frac{\pi D_m^2}{4})\ n_s \tag{1-14}$$

The heat transfer for the fraction of the total surface area not involved in any of the above areas, i.e. $(1-\beta)$ is calculated as forced convection. For the present case, the forced convection contribution is obtained by applying the empirical correlation of James et.al. [63], equation (3-1). Accordingly

$$\phi_{FC_{(1-\beta)}} = \phi_{FC}\ (1-\beta) \tag{5-38}$$

where ϕ_{FC} is the heat flux due to forced convection before correction for area, as given in equation (3-1).

A. Heat flow under bubbles per unit of time over the total surface area

The heat flow from the wall under the bubbles is obtained by adding the solutions to equations (5-27), (5-32) and (5-34). The detailed procedure is presented in Appendix F. The integration and addition of these equations yields:

$$\phi_{UB} = [(q_5+q_6) + (q_7+q_{32})]n_s\ f \tag{5-39}$$

where

$$q_5 = \frac{\gamma\sqrt{t_c}\,t_g}{4W^4}\ (W^4 - 2W^2 + 4W - 1) \tag{5-40}$$

$$q_6 = \frac{\gamma}{315 t_g^3 W^4} \left\{ t_c^{3/2} \left[t_g^3 (126W^2-135W+35) - 3t_g^2 t_w (14W^2-18W+5) \right.\right.$$
$$\left.\left. - 6t_g t_w^2 (3W-1) - 2t_w^3 \right] + 2t_w^{5/2} \left[21t_g^2 W^2 + 9t_g W t_w + t_w^2 \right] \right\} \quad (5\text{-}41)$$

$$q_7 = \frac{2\xi\sqrt{t_g}}{315 W^{9/2}} (126W^2-135W+35) \quad (5\text{-}42)$$

$$q_{32} = \frac{-2\xi E\sqrt{t_g}}{315 W^{3/2} (E+2W)^4} \left\{ \left(\frac{E}{W}\right)^3 (126W^2-135W+35) + 6\left(\frac{E}{W}\right)^2 \right.$$
$$\left. (154W^2-171W+45) + 84\left(\frac{E}{W}\right) (26W^2-33W+9) + 840(2W^2-3W+1) \right\} \quad (5\text{-}43)$$

ξ and γ are dimensional parameters defined by

$$\xi = 3.2\pi r_m^2 \sqrt{\nu_1}\, \lambda \rho_1 \quad (5\text{-}44)$$

and

$$\gamma = \frac{8k_1\sqrt{\pi}\, r_m^2}{\sqrt{\alpha_1}} \left(\frac{\Delta T}{t_g}\right) \quad (5\text{-}45)$$

W and E are dimensionless quantities, the former defined by equation (5-15) and the latter given by

$$E = 0.32 \frac{Pr\lambda}{Cp_1 \Delta T_{sat}} \quad (5\text{-}46)$$

The heat flow due to the microlayer evaporation is given by the sum of q_7 and q_{32}, given by equations (5-42) and (5-43) respectively, whereas the addition of q_5 and q_6, equations (5-40) and (5-41), represents the heat flow obtained by surface quenching.

It should be stressed that the validity of the above heat transfer model is restricted to the isolated bubble regime, since the preceding analysis does not take into consideration the overlap of areas of influence. Therefore, in the absence of overlap, the addition of the heat fluxes given by equations (5-36), (5-38) and (5-39) will give the total heat flux during nucleate flow boiling.

3. Heat transfer model considering overlap of areas of influence

In the fully developed nucleate boiling region, the nucleation site densities become so high, that there will be overlap in the bubble areas of influence. Overlap and interference between bubble sites may affect (i) the wall superheat required for nucleation, (ii) bubble growth and (iii) the rate of heat transfer from the wall. Point (i) was discussed in Chapter Three (section II.3.) where from the deactivation/reactivation process of nucleation sites, it was found that nucleation close to an exising site was greatly diminished; no information seems to be available about point (ii). Here only point (iii) is considered, assuming a constant value for the parameter K.

In order to estimate the effect of overlap on nucleate boiling heat transfer, the preceding model must be modified. The assumptions made in section 1. are retained here. Overlap of bubble projected areas is neglected, so overlapping will affect only the surrounding areas of influence, where heat transfer proceeds entirely by surface quenching. Consequently equation (5-39) still applies but equations (5-36) and (5-38) need to be modified.

A. Analysis

When the areas of influence overlap, the fraction of surface area affected by boiling is reduced from $\beta = n_s K A_b$ to $\beta_a = x\beta$. The consequent reduction in boiling flux is offset by the enhanced rate of heat transfer in the overlapping areas, which are now subjected to quenching by more than one bubble site, i.e. at a higher frequency than otherwise. Considering binary overlap only, i.e. ignoring the possibility that more than two areas of influence cover the same area, the overlapping area fraction $\beta(1-x)$ will be subjected to quenching by two bubble sites instead of one. The heat transfer during a period $t_c = 1/f$ depends on the delay time t between quenches,

$$q_{tc} = \frac{2k\Delta T}{(\pi\alpha)^{\frac{1}{2}}} \left[t^{\frac{1}{2}} + (t_c - t)^{\frac{1}{2}} \right] \qquad (5\text{-}47)$$

If adjacent sites have the same frequency but are completely independent on their phase relationships, so that all times t in the interval 0 to t_c are equally probable, the mean heat transfer on the overlapping areas is

$$\bar{q}_{tc} = \frac{2k_1\Delta T}{(\pi\alpha_1)^{\frac{1}{2}}} \frac{1}{t_c} \int_o^{t_c} \left[t^{\frac{1}{2}} + (t_c - t)^{\frac{1}{2}} \right] dt$$

$$\bar{q}_{tc} = \frac{4}{3} \left[\frac{2k_1\Delta T}{(\pi\alpha_1)^{\frac{1}{2}}} \right] t_c^{\frac{1}{2}} \tag{5-48}$$

thus the corresponding heat flux is

$$\phi_{ov} = \frac{4}{3} (2) \sqrt{(k\rho Cp)_1 \, f/\pi} \quad (\Delta T) \left[\beta - A_b n_s \right] (1-x)$$

or

$$\phi_{ov} = (1-x)\frac{4}{3} \phi_{NB_i} \tag{5-49}$$

where ϕ_{NB_i} is given by equation (5-36).

Equation (5-49) represents the boiling flux in the overlapping areas only. In order to obtain the boiling heat flux corresponding to the total fraction of actual boiling area β_a involved, excluding the heat flux attributed to the fraction of bubble projected areas $n_s A_b$ which is given by equation (5-39), the heat flux of the remaining fraction of actual boiling area, which is expressed as

$$\phi = \left[x - (1-x) \right] \phi_{NB_i} \tag{5-50}$$

should be added to equation (5-39).

Addition of equations (5-49) and (5-50) yields

$$\phi_b = \left(\frac{2x+1}{3}\right) \phi_{NB_i} \tag{5-51}$$

The consequent reduction in boiling area produces an increase in the fraction of area not involved in boiling from $(1-\beta)$ to $(1-\beta x)$, so that the forced convection contribution becomes

$$\phi_{FC_{(1-\beta_a)}} = \phi_{FC} \, (1-\beta x) \tag{5-52}$$

where ϕ_{FC} is given by equation (3-1).

In the absence of overlapping, the ratio x of actual boiling area to nominal boiling area is equal to unity and equations (5-51) and (5-52) become equations (5-37) and (5-38) respectively.

The total heat flux when there is overlap in the areas of influence is finally expressed as the addition of equations (5-39), (5-51) and (5-52)

$$\emptyset_T = \emptyset_{UB} + (\frac{2x+1}{3})\ \emptyset_{NBi} + \emptyset_{FC}\ (1-\beta_a) \qquad (5-53)$$

where

$$\beta_a = x\beta \qquad (5-54)$$

B. Prediction of overlap

The model of surface quenching for nucleate boiling heat transfer has been extended beyond the isolated bubble regime only at the expense of introducing the variable x which must be determined either from experimental measurements of bubble site positions or from some assumption about their spatial distribution. For an assumed random distribution of nucleation sites on the boiling surface, it can be shown (see Appendix G) that for large populations, x is given by

$$x = (1-e^{-\beta})/\beta \qquad (5-55)$$

β depends on the site density and bubble projected area- both obtainable experimentally - and K. Although K is often taken to be 4 in pool boiling studies, there is no theoretical basis for this value and different values may apply under different conditions. In the present study, for the spatial distribution of nucleation sites for run 4, from 70% to 95% of the CHF, shown in Figures 43 and 44, measurements of the actual boiling area at three different values of K, namely 4, 4.8 and 6, were carried out and the results are tabulated in Table 15 and presented graphically in Figures 79 to 81. Figures 82 and 83 show the actual boiling area drawn for the above four distributions of nucleation sites at K = 4.8.

It can be observed, Figure 79, that as K is increased x decreases,

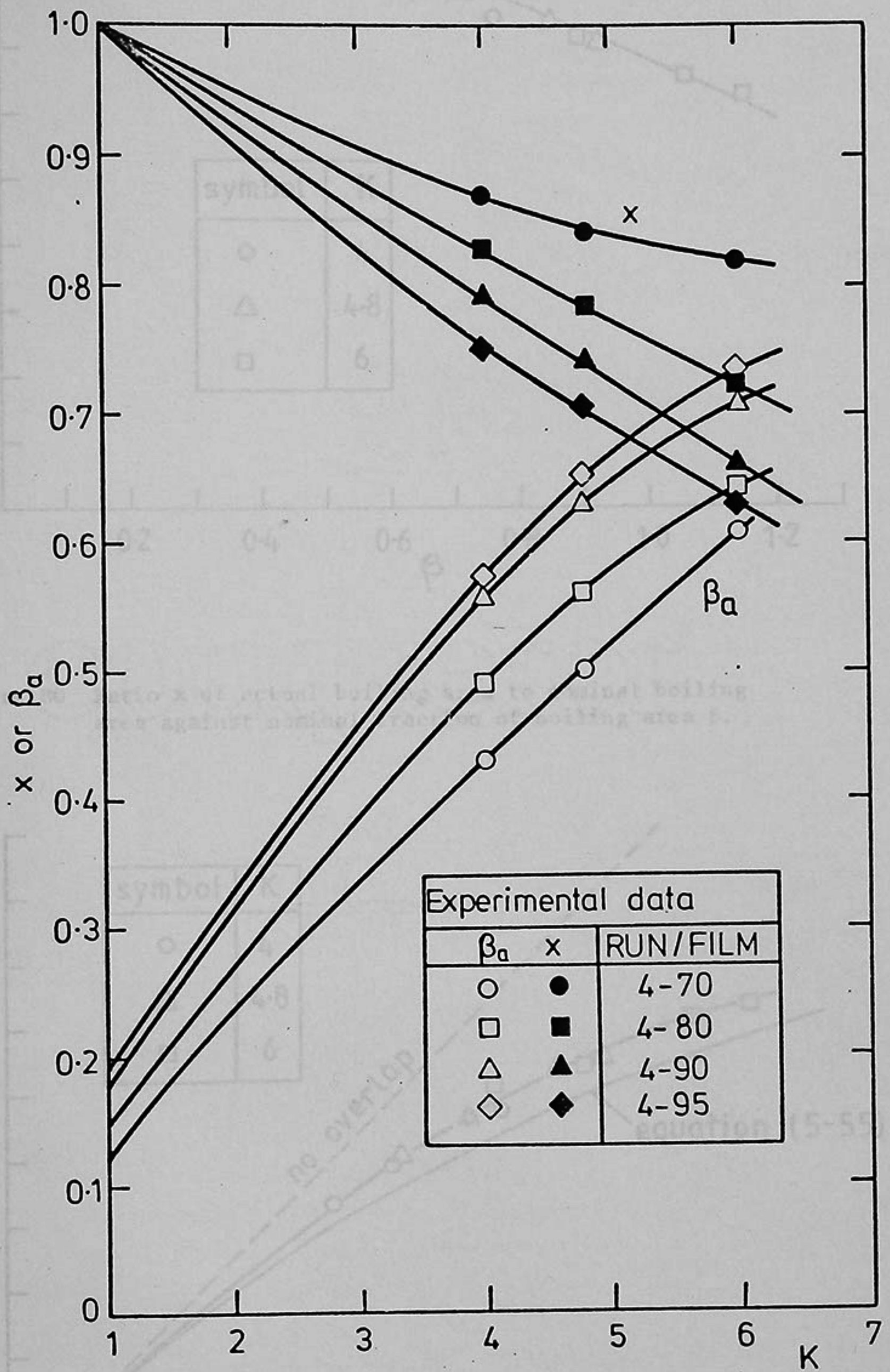


Figure 79 Actual fraction of boiling area as a function of K.

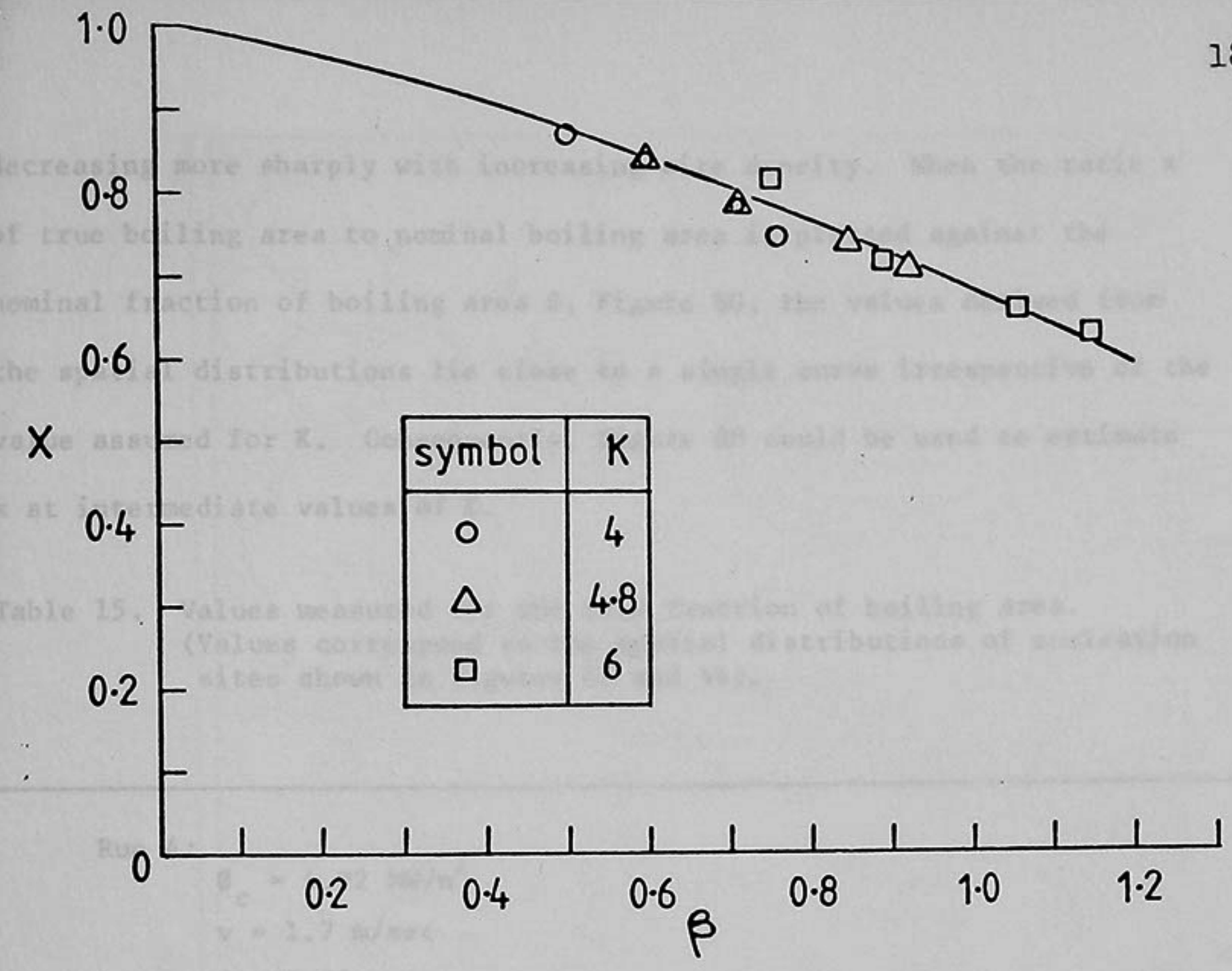


Figure 80 Ratio x of actual boiling area to nominal boiling area against nominal fraction of boiling area β.

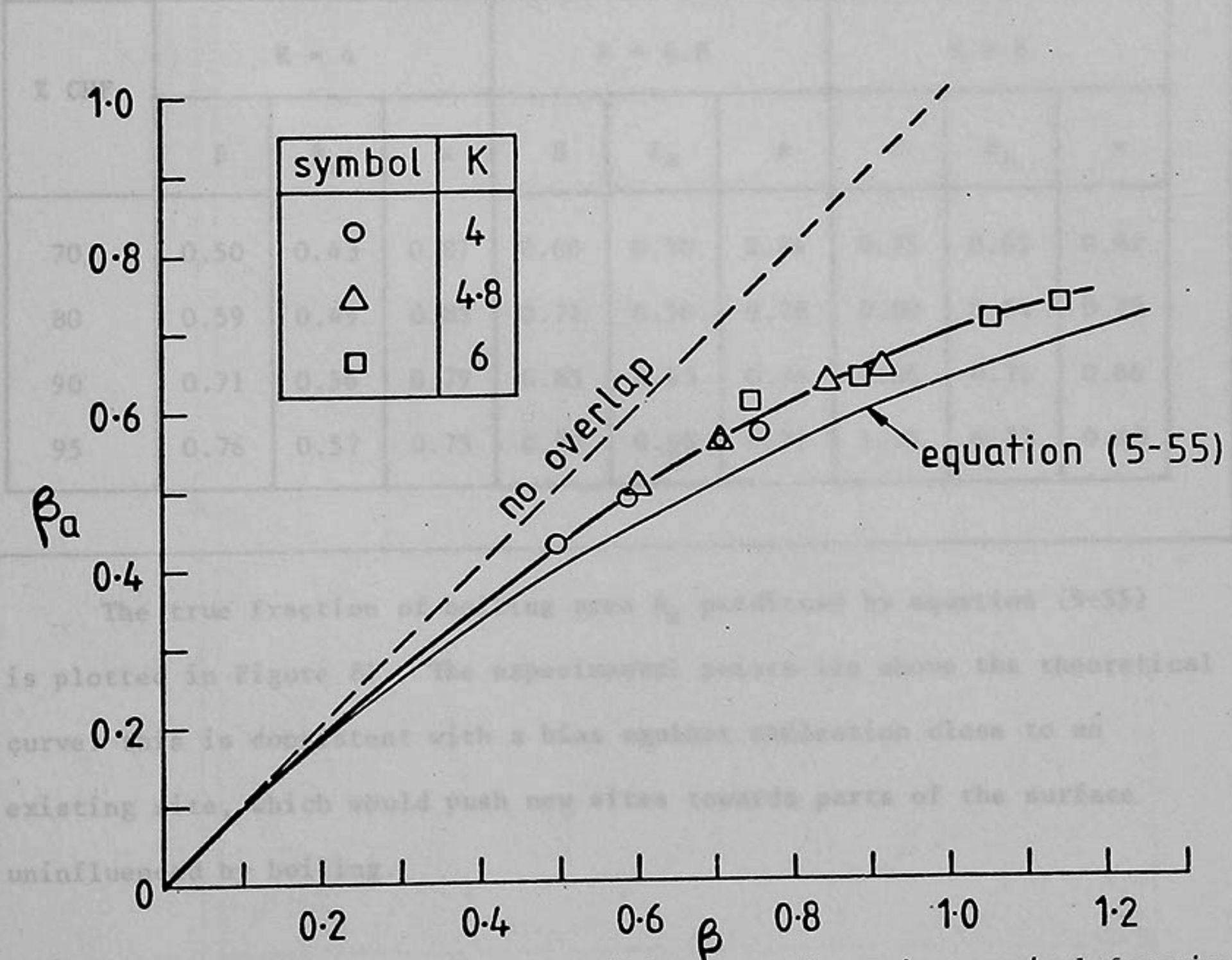


Figure 81 Actual fraction of boiling area β_a against nominal fraction of boiling area β.

decreasing more sharply with increasing site density. When the ratio x of true boiling area to nominal boiling area is plotted against the nominal fraction of boiling area β, Figure 80, the values derived from the spatial distributions lie close to a single curve irrespective of the value assumed for K. Consequently, Figure 80 could be used to estimate x at intermediate values of K.

Table 15. Values measured for the true fraction of boiling area. (Values correspond to the spatial distributions of nucleation sites shown in Figures 43 and 44).

Run 4:

$\emptyset_c = 4.92$ MW/m^2

$v = 1.7$ m/sec

$\delta = 0.08$ mm

$\Delta T_{sub_{in}} = 80^{o}K$

% CHF	K = 4			K = 4.8			K = 6		
	β	β_a	x	β	β_a	x	β	β_a	x
70	0.50	0.43	0.87	0.60	0.50	0.84	0.75	0.61	0.82
80	0.59	0.49	0.83	0.71	0.56	0.78	0.89	0.64	0.72
90	0.71	0.56	0.79	0.85	0.63	0.74	1.06	0.71	0.66
95	0.76	0.57	0.75	0.92	0.65	0.71	1.15	0.73	0.63

The true fraction of boiling area β_a predicted by equation (5-55) is plotted in Figure 81. The experimental points lie above the theoretical curve: this is consistent with a bias against nucleation close to an existing site, which would push new sites towards parts of the surface uninfluenced by boiling.

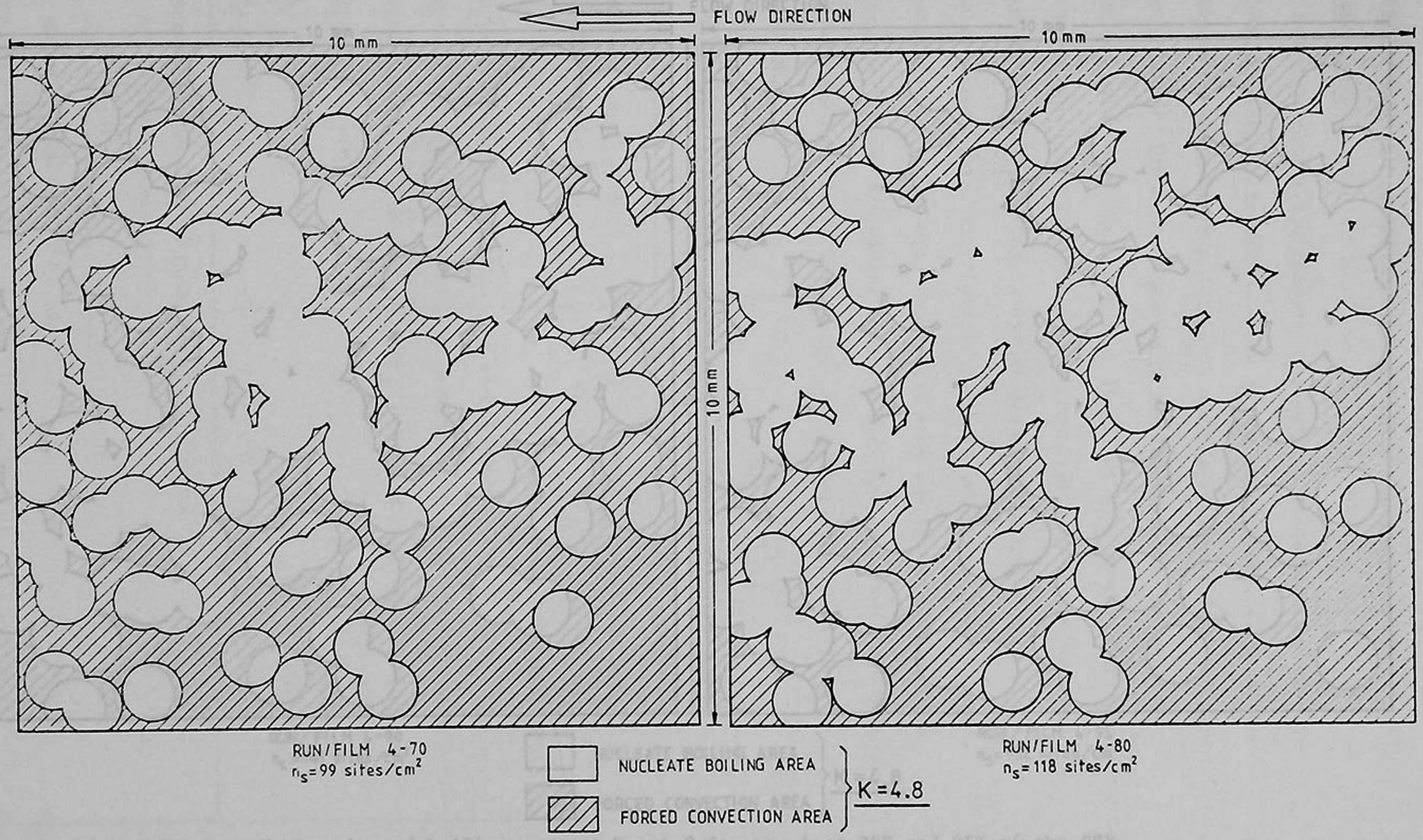


Figure 82 Actual fraction of boiling area at K = 4.8 for run 4 at 70% and 80% of the CHF.

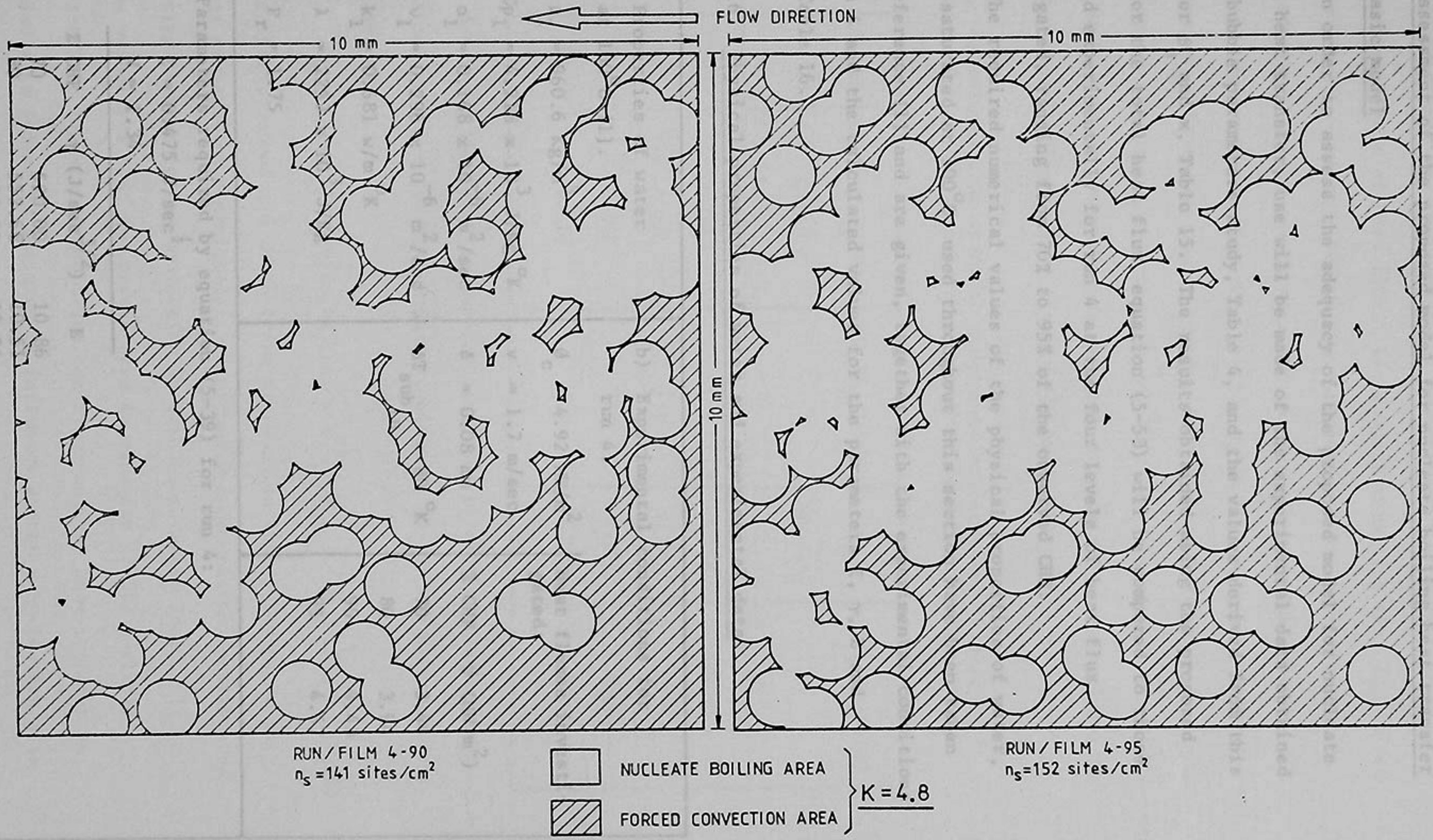


Figure 83 Actual fraction of boiling area at K = 4.8 for run 4 at 90% and 95% of the CHF.

III. Assessment of the proposed model for nucleate boiling heat transfer

1. Basic model

In order to assess the adequacy of the proposed model for nucleate boiling heat transfer, use will be made of the experimental data obtained in the bubble parameters study, Table 4, and the values derived from this study for β_a and x, Table 15. The results obtained using the proposed model for the total heat flux, equation (5-53) will be compared to those obtained experimentally for run 4 at the four levels of heat flux investigated, ranging from 70% to 95% of the observed CHF.

The required numerical values of the physical properties of water, liquid saturated at 100°C, used throughout this section have been taken from reference [1] and are given, together with the experimental conditions for run 4 and the calculated values for the parameters ξ, γ, E and W, in Table 16.

Table 16. Physical properties of water and experimental data

(a) Properties of water at 100°C [1].

$\rho_l = 960.6$ Kg/m^3

$Cp_l = 4.218 \times 10^3$ J/Kg °K

$\alpha_l = 0.168 \times 10^{-6}$ m^2/sec

$\nu_l = 0.296 \times 10^{-6}$ m^2/sec

$k_l = 0.681$ w/m °K

$\lambda = 2257 \times 10^3$ J/Kg

$P_r = 1.75$

(b) Experimental conditions for run 4:

$\emptyset_c = 4.92$ MW/m^2

$v = 1.7$ m/sec

$\delta = 0.08$ mm

$\Delta T_{sub_{in}} = 80$ °K

Heat fluxes investigated:

% CHF	$\emptyset$ (MW/m^2)
70	3.44
80	3.94
90	4.43
95	4.67

(c) Parameters required by equation (5-39) for run 4:

$\xi = 0.475$ J/sec$^{\frac{1}{2}}$

$W = 1.34$

% CHF	γ (J/sec$^{3/2}$)	E
70	520.00	10.86
80	552.68	10.51
90	608.65	10.06
95	648.46	9.96

Table 17 summarizes the calculated heat transfer under the bubbles $\emptyset_{UB}$ at the four levels of heat flux. It is worth recalling that $\emptyset_{UB}$, given by equation (5-39), is comprised of two components: microlayer evaporation heat transfer and surface quenching. The results given in Table 17 show that the microlayer evaporation contribution $\emptyset_M$ to the experimental total heat fluxes, $\emptyset_{TE}$, is rather small, ranging from 1.9% to 2.7%, with a slight increase with increasing heat flux. This result confirms the hypothesis that at low pressures and high subcoolings the microlayer evaporation contribution to heat transfer is negligible [16].

Table 17. Calculated heat transfer under bubbles, equation (5-39), including the microlayer evaporation contribution, Run 4.

$\emptyset_{TE}$ MW/m^2	% CHF	$\emptyset_M=(q_7+q_{32})fn_s$ (MW/m^2)	$(\emptyset_M/\emptyset_{TE})x100$	$\emptyset_{UB}$ (MW/m^2)	$(\emptyset_{UB}/\emptyset_{TE})x100$
3.44	70	0.064	1.9	0.555	16.1
3.94	80	0.076	1.9	0.693	17.6
4.43	90	0.101	2.3	0.898	20.3
4.67	95	0.126	2.7	1.056	22.6

To determine the relative importance of the three different assumed contributions to the total heat transfer, equation (5-53) can alternatively be expressed as:

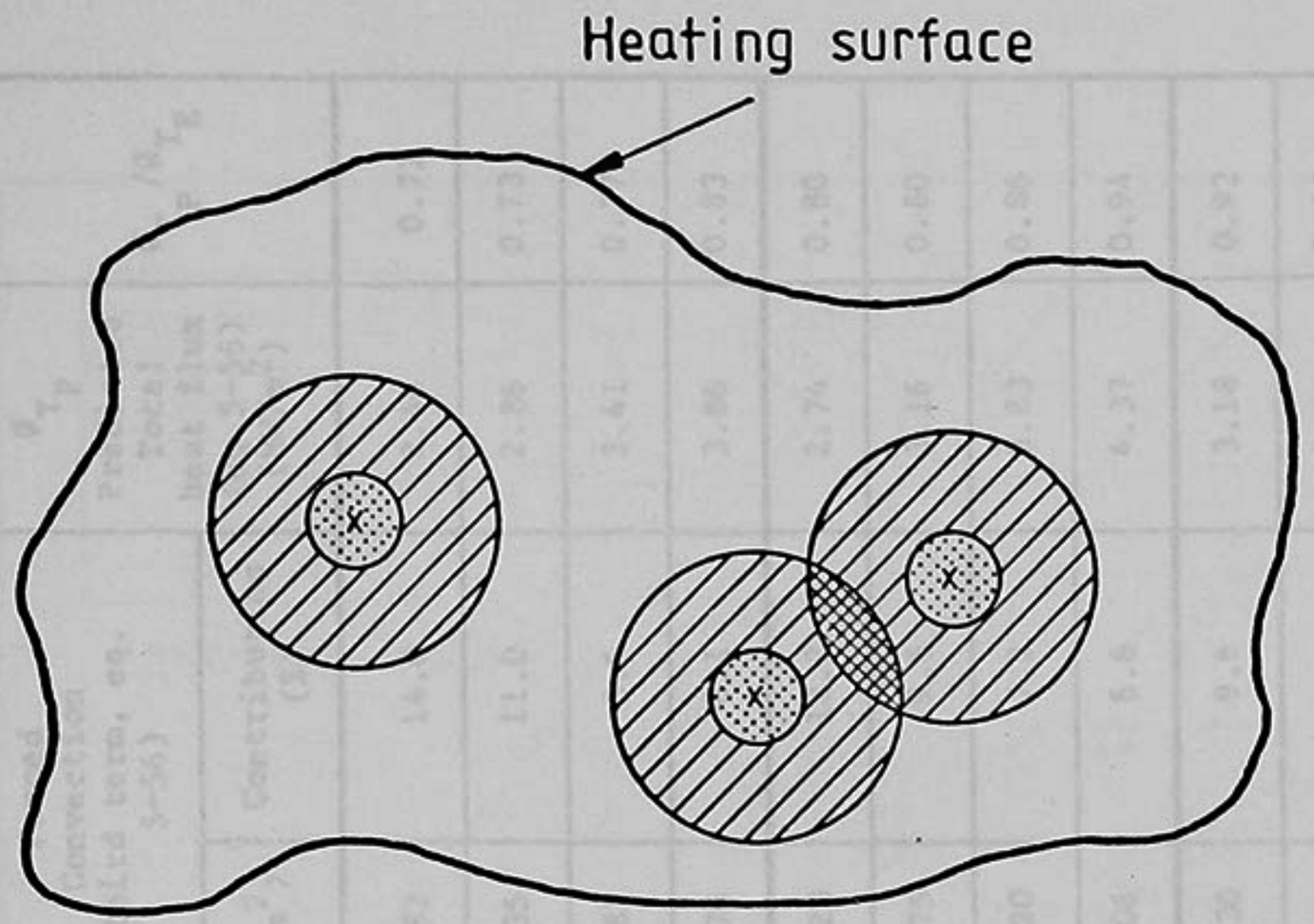
$$\emptyset_T = (q_7+q_{32})fn_s + \left[(q_5+q_6)fn_s + \left(\frac{2x+1}{3}\right)\emptyset_{NBi}\right] + \emptyset_{FC}\,(1-\beta_a) \quad (5\text{-}56)$$

The first, second and third terms of equation (5-56) represent the microlayer evaporation contribution, the transient conduction contribution, and the single-phase forced convection contribution respectively. It should be emphasised that the second term in equation (5-56) includes the under-bubble transient conduction contribution, the heat transfer in the annular area formed by the area of influence around a nucleation site

minus the maximum bubble projected area, and the enhanced heat transfer in the overlapping areas of influence. Figure 84 shows the areas where the assumed heat transfer mechanisms operate.

Table 18 summarizes the results for the total heat fluxes predicted by equation (5-56) at the three values of K, namely 4, 4.8 and 6, and gives the ratio of predicted total heat flux to experimental total heat flux, and the relative contribution to heat transfer by the above three components calculated by dividing each of the three terms of equation (5-56) by the experimental total heat flux. It can be observed that at any of the three values of K, the major contribution to the total heat flux arises from the transient conduction mechanism, accounting, depending on K and the level of heat flux, for 55% to 98% of the total heat flux. When the total heat fluxes are calculated using the present model, the results obtained give not just the right order of magnitude at any of the three values of K but a reasonably good fit between the experimental and predicted heat fluxes. A very good fit, ±8%, is obtained when K = 6, as shown in Figure 85. However, the correctness of K = 6 has to be justified. For this purpose, use can be made of the deactivation/reactivation process of nucleation sites observed with increasing heat flux, a process broadly discussed in Chapter Three. A value of K in the vicinity of 6, which implies a diameter of influence $D_i = 2.45D_m$, is fully justified: the great majority of nucleation sites deactivated during an increase in heat flux, were found to be associated with the activation of a new site within two bubble radii. At 2.45 bubble radii, the proportion of deactivated sites due to this cause, i.e. thermal interference, is at least 80%.

Since the components of this model cannot be tested independently, uncertainty regarding one may affect the results that can be drawn from the others, and consequently these uncertainties have to be analysed. The theoretical modelling of the microlayer evaporation flux is admittedly a gross simplification of a very complex process which if the model were



Area:	Heat transfer mechanism:
Maximum bubble projected area.	Microlayer evaporation and transient conduction.
Annular area. (maximum bubble projected area subtracted from the area of influence.)	Transient conduction.
Overlap of areas of influence.	Enhanced transient conduction.
Area unaffected by boiling.	Single-phase forced convection.

Figure 84 Areas of operation for the proposed nucleate boiling heat transfer model.

Table 18. Total heat fluxes predicted by equation (5-56) at various values of K for run 4.

K	% CHF	$\emptyset_{T_E}$ Experimental total heat flux (MW/m^2)	Microlayer Evaporation (first term, eq. 5-56)		Transient Conduction (second term, eq. 5-56)		Forced Convection (third term, eq. 5-56)		$\emptyset_{T_P}$ Predicted Total heat flux (eq.5-56) (MW/m^2)	$\emptyset_{T_P}/\emptyset_{T_E}$
			(MW/m^2)	Contribution (%)	(MW/m^2)	Contribution (%)	(MW/m^2)	Contribution (%)		
4	70	3.44	0.064	1.9	1.912	55.6	0.482	14.0	2.46	0.72
	80	3.94	0.076	1.9	2.334	59.2	0.435	11.0	2.86	0.73
	90	4.43	0.101	2.3	2.919	65.9	0.381	8.6	3.41	0.77
	95	4.67	0.126	2.7	3.364	72.0	0.376	8.1	3.86	0.83
4.8	70	3.44	0.064	1.9	2.252	65.5	0.423	12.3	2.74	0.80
	80	3.94	0.076	1.9	2.710	68.8	0.375	9.5	3.16	0.80
	90	4.43	0.101	2.3	3.381	76.3	0.320	7.2	3.83	0.86
	95	4.67	0.126	2.7	3.914	83.8	0.306	6.6	4.37	0.94
6	70	3.44	0.064	1.9	2.773	80.6	0.330	9.6	3.18	0.92
	80	3.94	0.076	1.9	3.242	82.3	0.307	7.8	3.63	0.92
	90	4.43	0.101	2.3	3.978	89.8	0.251	5.7	4.32	0.98
	95	4.67	0.126	2.7	4.597	98.4	0.236	5.1	4.93	1.06

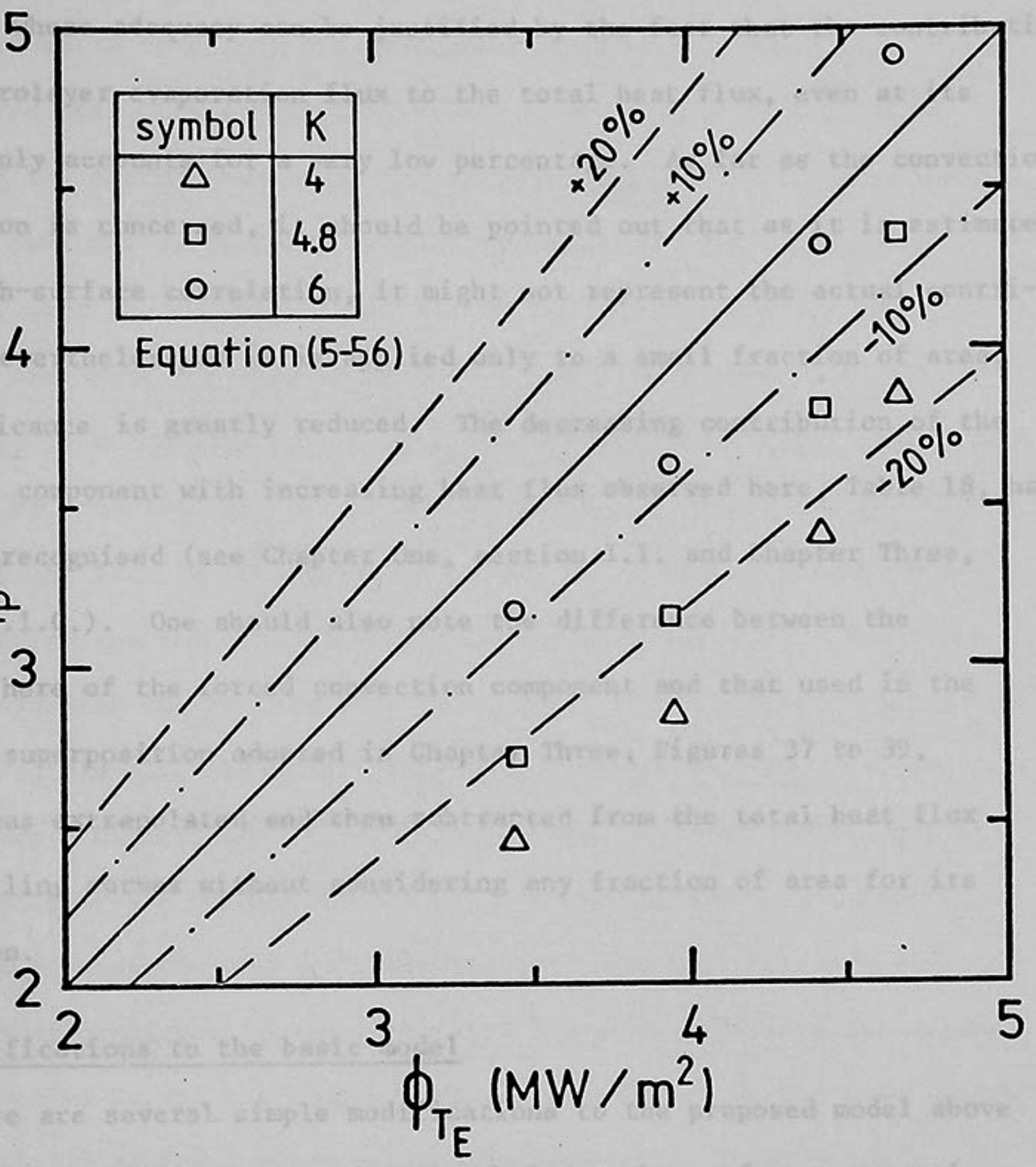


Figure 85 Comparison between experimental total heat fluxes and those predicted by the present model.

required to predict bubble dynamics might be important. However, it was necessary to make this simplification in order to arrive at an explicit expression whose adequacy can be justified by the fact that the contribution of the microlayer evaporation flux to the total heat flux, even at its maximum, only accounts for a very low percentage. As far as the convection contribution is concerned, it should be pointed out that as it is estimated from smooth-surface correlation, it might not represent the actual contribution. Nevertheless, as it is applied only to a small fraction of area, its significance is greatly reduced. The decreasing contribution of the convective component with increasing heat flux observed here, Table 18, has been long recognised (see Chapter One, section I.1. and Chapter Three, section II.1.C.). One should also note the difference between the treatment here of the forced convection component and that used in the method of superposition adopted in Chapter Three, Figures 37 to 39, where it was extrapolated and then subtracted from the total heat flux in the boiling curves without considering any fraction of area for its application.

2. Modifications to the basic model

There are several simple modifications to the proposed model above for nucleate boiling heat transfer, two being perhaps of more general interest. Neglecting the microlayer evaporation contribution, the under-bubble heat transfer would proceed by the usual transient conduction mechanism. The first modification to the model leads to the well-known composite mechanism of surface quenching which implies no overlapping at all, and gives the total heat flux as

$$\emptyset_T = \emptyset_{NB} + \emptyset_{FC}\ (1-\beta) \qquad (1\text{-}13)$$

The second modification considers overlap of area of influence but no enhanced heat transfer on the overlapping areas, i.e. simply a reduction in the fraction of boiling area from β to $x\beta$ and the consequent increase in the fraction of area not affected by boiling from $(1-\beta)$ to $(1-\beta x)$. In this

case, the total heat flux becomes

$$\emptyset_T = \emptyset_{NB}\, x + \emptyset_{FC}\, (1-\beta x) \qquad (5\text{-}57)$$

It is worth recalling the difference between $\emptyset_{NB}$ and $\emptyset_{NBi}$. The former gives the boiling heat flux over the whole area of influence (including the maximum bubble projected area) while the latter gives the heat flux over the surrounding area of the maximum bubble projected area, i.e. over the annulus formed by subtracting the maximum bubble projected area from the area of influence, as illustrated in Figure 84.

Table 19 summarizes the results of the calculated total heat fluxes predicted by equations (1-13) and (5-57) and their respective deviations at each of the four levels of heat flux for the three different values of K, given as the ratio of predicted to experimental total heat flux. The corresponding values according to equation (5-56), already given in Table 18, are also shown for comparison. It can be seen that equation (5-57) gives a higher level of deviations from the experimental values, under-predicting the measured total heat fluxes by 35% to 21% over the range of K considered here, although it gives the smallest variation in the ratios of predicted to experimental total heat fluxes at any of the three values of K over the four levels of heat flux. On the other hand, equation (1-13) at K = 4 gives comparable results to those given by equation (5-56); as K is increased, a better fit is obtained when equation (5-56) is applied, and, at K = 6 it gives the closest fit of all.

Assuming that the basic concept of the surface quenching mechanism is correct, the variations in the ratios of predicted to experimental total heat fluxes shown in Table 19 using any of the above three equations, suggest a possible dependency of K on the level of heat flux - or alternatively on any related variable such as nucleation site density or Jakob number ——. This suggestion could be confirmed by carrying out simple calculations using equations (1-13) and (5-56) to obtain optimum values of K, i.e. those values of K which give an exact fit to the measured heat fluxes. This was done, the procedure being to vary K at a given level of

Table 19. Total heat fluxes predicted by the modified models of nucleate boiling heat transfer.

% CHF	ϕ_{T_E} Experimental total heat flux (MW/m^2)	K = 4						K = 4.8						K = 6					
		Predicted total heat flux ϕ_{T_p} (MW/m^2)			ϕ_{T_p}/ϕ_{T_E}			Predicted total heat flux ϕ_{T_p} (MW/m^2)			ϕ_{T_p}/ϕ_{T_E}			Predicted total heat flux ϕ_{T_p} (MW/m^2)			ϕ_{T_p}/ϕ_{T_E}		
		Eq (1-13)	Eq (5-57)	Eq (5-56)	Eq (1-13)	Eq (5-57)	Eq (5-56)	Eq (1-13)	Eq (5-57)	Eq (5-56)	Eq (1-13)	Eq (5-57)	Eq (5-56)	Eq (1-13)	Eq (5-57)	Eq (5-56)	Eq (1-13)	Eq (5-57)	Eq (5-56)
70	3.44	2.50	2.29	2.46	0.73	0.66	0.72	2.83	2.51	2.74	0.82	0.73	0.80	3.32	2.88	3.18	0.97	0.84	0.92
80	3.94	2.93	2.58	2.86	0.74	0.65	0.73	3.35	2.79	3.16	0.85	0.71	0.80	3.97	3.10	3.63	1.01	0.79	0.92
90	4.43	3.54	2.98	3.41	0.80	0.67	0.77	4.08	3.24	3.83	0.92	0.73	0.86	4.94	3.51	4.32	1.12	0.79	0.98
95	4.67	4.10	3.30	3.86	0.88	0.71	0.83	4.74	3.62	4.37	1.02	0.78	0.94	5.84	3.92	4.93	1.25	0.84	1.06

heat flux and to calculate the total heat flux until the obtained value coincided with the experimental one. Figure 86 shows the calculated optimum values of K plotted against level of heat flux. With both equations, (1-13) and (5-56), there is an apparent tendency for K to decrease with increasing heat flux. The deduction of such a functional variation in K is not attempted here since no data for the bubble parameters at lower heat fluxes are available. Nevertheless, Figure 86 strongly suggests a dependency of K on heat flux which could well represent the subject of future research, in which attention would be focussed on the interactions between close-spaced bubbles; this in turn would throw light on the actual definition of K, since to date it represents a gross simplification of a very complex - unknown - process of flow dynamics and heat transfer in the vicinity of a bubble.

Particularly relevant to the validity of the surface quenching model is the process of bubble coalescence. The model will start to break down when the level of bubble coalescence becomes significant, since parts of the surface will be subjected to different mechanisms of heat transfer, for instance in small volumes of liquid trapped below vapour patches, Figure 13.

3. Effect of overlap on boiling heat flux

The effect of overlap on the boiling heat flux can be quantified as follows. If the microlayer evaporation contribution is neglected, equation (5-56) becomes

$$\phi_T = \phi_{NB} \left(\frac{2x+1}{3}\right) + \phi_{FC} \left(1-\beta_a\right) \qquad (5\text{-}58)$$

in which the boiling flux is given by

$$\phi_b = \phi_{NB} \left(\frac{2x+1}{3}\right)$$

or alternatively expressed as

$$\frac{\phi_b}{\phi_{NB}} = \frac{2x+1}{3} \qquad (5\text{-}59)$$

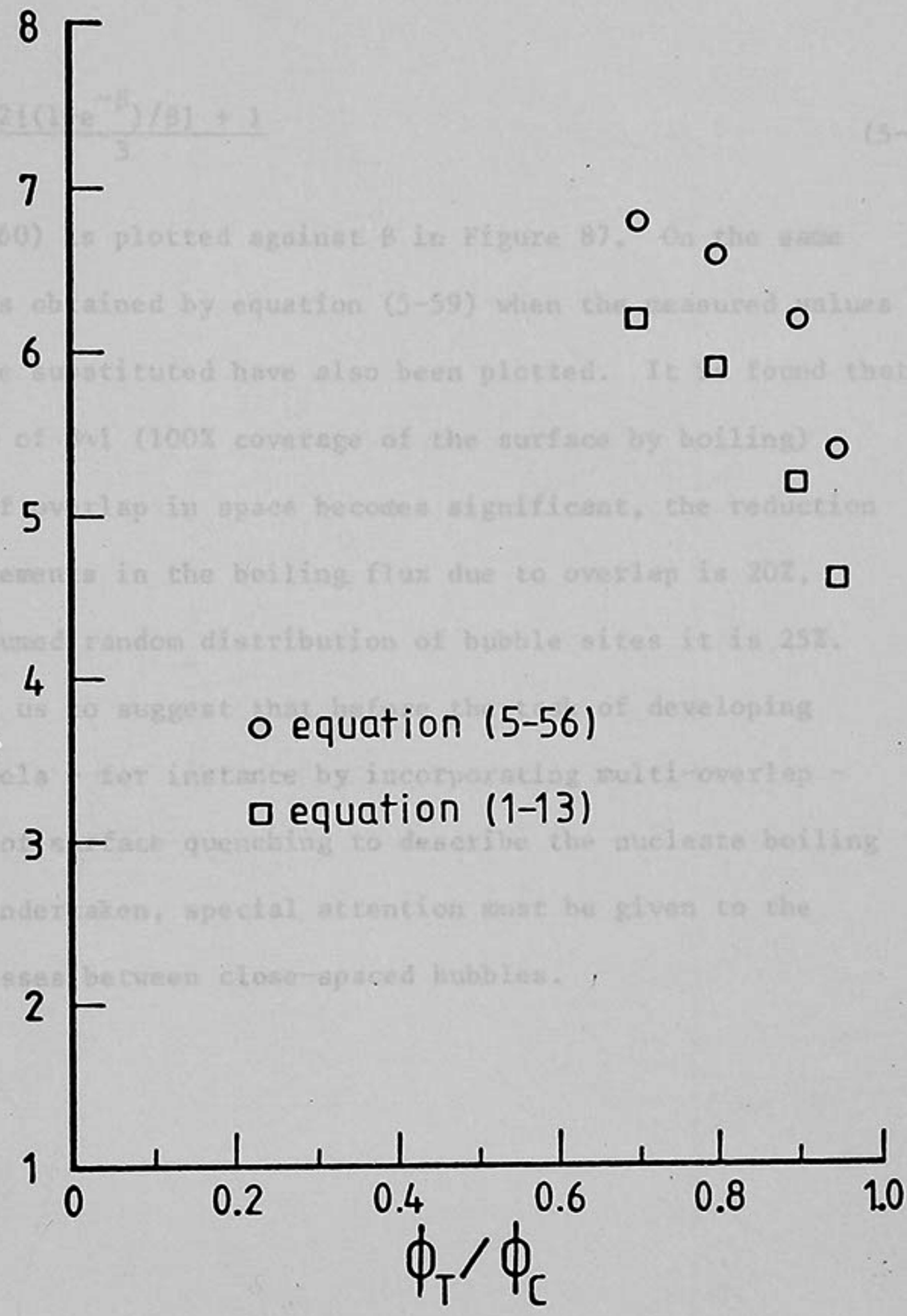


Figure 86 Apparent decrease in the parameter K with increasing heat flux.

For an assumed random distribution of nucleation sites, the expression for x, equation (5-55), can be substituted into equation (5-59) to give

$$\frac{\phi_b}{\phi_{NB}} = \frac{2[(1-e^{-\beta})/\beta] + 1}{3} \qquad (5\text{-}60)$$

Equation (5-60) is plotted against β in Figure 87. On the same Figure, the results obtained by equation (5-59) when the measured values of x, Table 15, are substituted have also been plotted. It is found that even in the region of $\beta \sim 1$ (100% coverage of the surface by boiling) where the effect of overlap in space becomes significant, the reduction from actual measurements in the boiling flux due to overlap is 20%, whereas for an assumed random distribution of bubble sites it is 25%. These results lead us to suggest that before the task of developing more elaborate models - for instance by incorporating multi-overlap - using the concept of surface quenching to describe the nucleate boiling heat transfer is undertaken, special attention must be given to the interference processes between close-spaced bubbles.

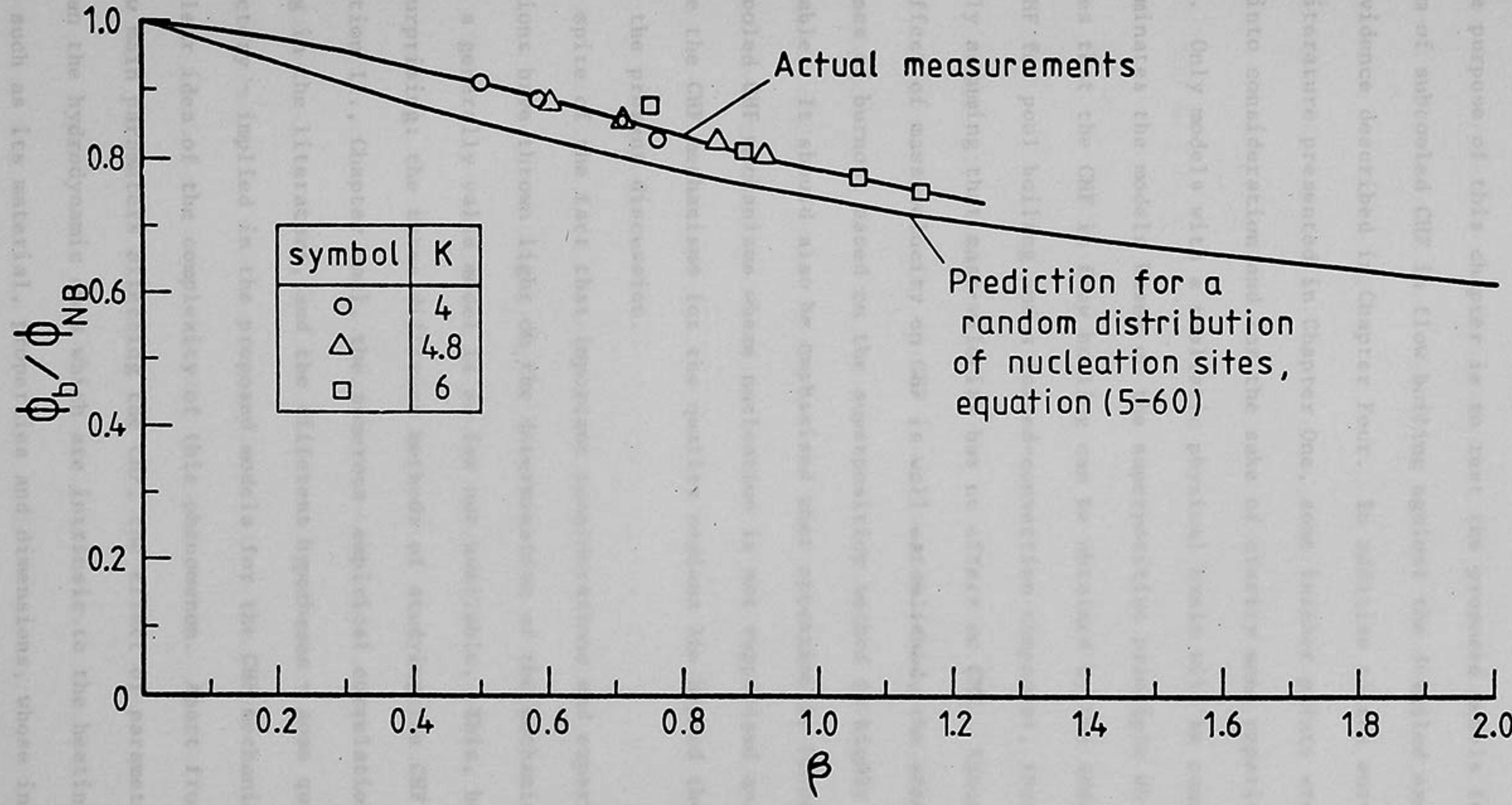


Figure 87 Reduction in boiling flux due to overlap.

C H A P T E R S I X

ANALYSIS OF CRITICAL HEAT FLUX

I. Introduction

The purpose of this chapter is to test the proposed models for the mechanism of subcooled CHF in flow boiling against the detailed experimental evidence described in Chapter Four. In addition to the survey of the literature presented in Chapter One, some further points are brought into consideration and for the sake of clarity some repetitions are made. Only models with a realistic physical basis will be considered; this eliminates the models based on the superposition principle which postulates that the CHF in flow boiling can be obtained by the addition of the CHF for pool boiling and a forced-convection component, thus implicitly assuming that mass-velocity has no effect on CHF. Since the marked effect of mass-velocity on CHF is well established, the adequacy of analyses of burnout based on the superposition method is highly questionable. It should also be emphasised that attention is focussed on the subcooled CHF mechanisms where nucleation is not suppressed and therefore the CHF mechanisms for the quality regions lie beyond the scope of the present discussion.

In spite of the fact that important considerations and experimental observations have thrown light on the determination of the mechanism of burnout, a generally valid model is so far not available. This, however, is not surprising: the three different methods of studying the CHF (see section II., Chapter One), the numerous empirical correlations appearing in the literature, and the different hypotheses - some quite contradictory - implied in the proposed models for the CHF mechanism, give a clear idea of the complexity of this phenomenon. Apart from the well-know main parameters affecting the CHF, the effect of parameters other than the hydrodynamic ones which are intrinsic to the heating surface, such as its material, properties and dimensions, whose influence

on burnout has been more generally observed, introduce further complexity into the determination of burnout. The effect of this latter group of parameters on CHF receives strong support in the literature. For instance, evidence that indicates a definite dependence of CHF on heater properties is provided by the experimental study of Knoebel et al [91] who reported CHF determinations with water and heavy water flowing through a vertical annular channel formed by an aluminium outer tube with both stainless steel and aluminium heated tubes within the range of conditions

$$5 \text{ m/sec} \leq v \leq 20 \text{ m/sec}$$

$$500 \text{ mm} \leq L_H \leq 610 \text{ mm}$$

$$13 \text{ mm} \leq D_{heater} \leq 54 \text{ mm}$$

$$4^{o}C \leq \Delta T_{sub} \leq 89^{o}C$$

$$2 \text{ bar} \leq P \leq 6 \text{ bar}$$

They observed CHF's 20% greater for aluminium than for stainless steel at the same operating conditions. Although this increase in CHF for aluminium might at first be thought to be attributable to the difference in thermal properties (higher thermal diffusivity for aluminium), this has proved not to be the case: Tachibana and co-workers [88] carried out pool boiling burnout tests with horizontally-placed metallic strips made of different materials in saturated water at atmospheric pressure. Among the various materials tested were stainless steel, aluminium and copper. Their tests showed that stainless steel and copper had similar CHF values whereas for aluminium the measured CHF values were systematically higher (~20%). Since the thermal diffusivity of copper is greater than for aluminium and the CHF's for stainless steel and copper were similar, this clearly indicates that the increase in CHF for aluminium cannot possibly be attributed to bulk thermal properties. Tachibana et al attributed this difference in behaviour to interfacial properties between the solid and liquid, their physico-chemical affinity. They pointed out the possibility that aluminium might have higher superheating properties

conductive to the Leidenfrost condition because of the good affinity of aluminium oxide and water.

With the above evidence and the observed wall thickness effect on CHF (Chapter Four) the ideal theoretical formulation of the CHF problem involves the solution of equation (6-1)

$$\emptyset_c = \text{fn } (\Delta T_{sub}, G, P, D_H, L_H, \delta, \text{fluid and solid properties}) \quad (6\text{-}1)$$

Equation (6-1) excludes the so-called secondary factors affecting CHF (described in Chapter One), since conclusive evidence to relate the magnitude of such parameters to the CHF conditions has not been demonstrated. This implies that the effect of secondary factors on CHF, such as surface roughness, surface tension, liquid purity and heating method, do not influence the occurrence of CHF.

The strict examination of the validity of a given model for the mechanism of CHF for a liquid flowing under stable conditions in a uniformly heated section would involve assessing: (i) whether it correctly represents the physical situation, (ii) its capability to explain the well-known tendencies of the main parameters affecting it and the effect of parameters of non-hydrodynamic nature, (iii) the correctness of the assumptions involved in its derivation, (iv) the adequacy of its mathematical formulation, and (v) its consistency with the experimental evidence over the whole region of its applicability.

Because of the time required for detailed analyses of cine-films taken at conditions near burnout, Appendix D, it is only possible to consider here one set of experimental data, Table 3, the conditions being:

(Run 4)

$\emptyset_C = 4.92$ MW/m^2	Water/stainless steel
$v = 1.7$ m/sec	Atmospheric pressure
$\delta = 0.08$ mm	Vertical upflow
$\Delta T_{sub_{in}} = 80^oK$	Rectangular channel uniformly heated on one side
	$L_H = 150$ mm; $D_H = 7$mm

Heat flux levels:

RUN-FILM	Ø (MW/m^2)	% CHF
4-70	3.44	70
4-80	3.94	80
4-90	4.43	90
4-95	4.67	95

The quantitative results from the photographic analyses of this set of cine-films are presented in Tables 4 and 11.

Since the present discussion is limited to the above conditions, it is not possible to comment on the validity of the proposed CHF models over the full range of conditions possible. However, it should be pointed out that no evidence in the empirical correlation of CHF against variables such as flow velocity, inlet subcooling and wall thickness was found (Figures 64 - 66) to suggest a sudden change in CHF mechanism.

II. Critical Heat Flux models

Some well-known models for the mechanism of subcooled CHF in flow boiling reported in the literature have been reviewed in Chapter One. They can be summarized as follows:-

(1) Models which assume the presence of a vapour bubble blanket close to the heating surface which at the critical condition prevents the inflow of "cold" liquid from the core, resulting in the dryout of the superheated liquid film under the bubble blanket, which in turn causes the extraordinary increase in surface wall temperature that leads to burnout, [8,39,41-43].

(2) A model based on slug flow pattern, which assumes the formation of a dry spot on the heater surface due to the breakdown of a superheated liquid layer, caused by the interaction of a nucleating bubble with the passage of vapour clots, promoting a localised increase in the

wall temperature. As the vapour clot moves, it passes the site and the dry spot is quenched by a liquid slug. This sequence of events is repeated, causing a local cyclical rise in temperature and quenching of the heater surface. At the CHF it is then postulated that the temperature rise is greater than the temperature drop during quenching, until eventually, the Leidenfrost condition is reached, resulting in burnout [40].

(3) A model which postulates the formation of a dry patch underneath a growing bubble which arises from the evaporation of the micro-layer with a consequent sharp increase of the heater temperature in the dry area. At the critical condition, the dry patch stabilizes and the wall temperature reaches the Leidenfrost condition at which rewetting is prevented, causing burnout [45].

(4) A model which describes the critical condition as arising from the isolation of a thin liquid layer due to bubble coalescence, which at burnout evaporates rapidly resulting in the formation of a dry area with the consequent increase in surface wall temperature sufficient to reach the Leidenfrost band of temperatures and therefore causing burnout, [49].

Regarding the liquid film dryout hypothesis implied in the first group of models, the concept of a vapour bubble blanket arises from the assumption that numerous vapour bubbles covering the boiling surface are arranged in a closed-packed condition. Evidence which contradicts the necessity of a close-packing bubble condition for burnout is provided by the present photographic study of the flow structure near the CHF, described in detail in Chapters Three and Four. It seems that this concept is entirely based on photographic studies near burnout, in which the boiling surface was filmed only in side view [41]. It is not difficult to imagine that the presence of a small number of well-

spaced bubbles distributed over the heating surface could lead to incorrect interpretations, since it would be sufficient to have only a few bubbles close to the camera to obscure the field of view and to prevent the true location of farther bubbles being accurately known. Only when filming takes place normal to the heating surface is it possible to determine the actual distribution of bubbles, although - certainly - a side view provides the required information regarding the bubble shape. Since the bubble blanket hypothesis implied in the models of group (1) is not consistent with the present observations, they are not applicable to the present case.

Models (2), (3) and (4) all involve a localised temporary dryout of the surface, differing as to how this condition is initiated, and as to whether single or repeated events are required to reach some critical (Leidenfrost) value for temperature, generally denoting a wall surface temperature at which contact between solid and liquid is prevented. However, particulary for a flow boiling situation it is not a well-defined quantity, and present knowledge seems to be rather limited [92]. For the case of pool boiling, there exist a number of studies reported in the literature regarding the Leidenfrost phenomenon, and although there seems to be general good agreement on the minimum value for Leidenfrost temperature (often reported to vary between 230^{o}C and 250^{o}C for water-stainless steel at atmospheric pressure [93,94]), significant differences have been observed, associated with surface conditions. Baumeister, et al, quoted in [2], reported a difference in Leidenfrost temperature of 75^{o}C lower for the same surface when freshly used and after it had been used several times. The existence of liquid-solid contact, pointed out in [2], adds further uncertainty to the definition of the Leidenfrost temperature.

As far as model (2) is concerned, it assumes the necessary condition for the flow pattern at burnout to be slug flow. However, there is no substantiated basis to relate the flow pattern to the CHF: the present

study, (Chapter Four, section I.1) and several other photographic investigations near burnout [44,48] reveal that although under certain conditions the flow regime can in fact be indentified as slug, under other conditions only bubbly flow is observed, thus demonstrating that a slug flow pattern is not essential for the onset of burnout. Apart from the fact that a quantitative formulation of this model is not available it does not represent the present physical conditions and therefore it cannot be applied to this case.

The hypothesis behind model (3) is neither contradicted nor substantiated with the present experimental evidence. However, since the assumed formation of dry patches under nucleating bubbles leading to an increase in the wall temperature of sufficiently high magnitude to promote burnout has never been identified in flow boiling, this model can only remain as a possible alternative; it cannot possibly be used quantitatively.

Regarding the CHF model (4), the hypothesis on which it is based is supported by several photographic studies of boiling near burnout [60,87] and by the present observations which show the increasing tendency of bubbles to coalesce in regions near burnout and both the life time and maximum projected dimensions of the vapour masses formed by bubble coalescence to be greater than those values for individual bubbles (see section I.2, Chapter Four). Nevertheless, the assumed residence time of the vapour mass used in that model - 0.1 and 0.2 seconds - necessary to reach the Leidenfrost range of temperatures is two orders of magnitude greater than those observed in the present study at comparable conditions. It would seem, therefore, that such a discrepancy - which does not call into question the hypothesis that burnout can be associated with the process of bubble coalescence -, nullifies the general application of the quantitative formulation of this model for CHF.

Since the above proposed models for the mechanism of subcooled CHF in flow boiling are not consistent with the present evidence, it is clear that another mechanism prevails under these conditions. In the following section a possible alternative is formulated.

III. A possible alternative for the CHF mechanism

The model pictures the CHF condition as arising from the formation of small vapour patches on the heater surface, which insulate the surface, preventing contact between it and the liquid bulk, and therefore causing a local temperature rise in the wall surface.

The above assumption is consistent with the experimental evidence, which indicates that:

(a) small vapour patches form rapidly (small in comparison with the width of the test section);

(b) the vapour patches are mostly located near the downstream end of the heating surface;

(c) the frequency of vapour patch formation increases with increasing heat flux, and

(d) both the life time and maximum dimensions of the vapour patches, compared to those values for individual bubbles, increase as the heat flux is increased.

Since the vapour patches last longer than single bubbles, surface dryout under the patches is most likely. The localised formation of vapour patches rules out system pressure instabilities as a possible cause for their occurrence. This is consistent with the localised burnouts exhibited in destroyed specimens (see sections II.4 and II.5, Chapter Four). The most likely source of vapour patch formation is the coalescence of a few individual vapour bubbles from closely-spaced nucleation sites, possibly with evaporation of trapped liquid.

Under the above conditions, the alternative routes to burnout are:

(i) Stabilisation (or continuous growth) of the vapour patch, or

(ii) repeated growth/collapse of vapour pathes over the same surface location.

Alternative (i) implies a wall surface overheating occurring as a single event, whereas alternative (ii) would produce a gradual overheating in increasing cycles.

Since the analysis of stabilisation/growth of a vapour patch involves the prediction of bubble coalescence and liquid trapping evaporation and two - or even three - dimmensional transient conduction in the wall plus convection in the liquid and vapour, alternative (i) represents a major problem and such a complex formulation is not attempted here. Instead, we will consider the events occurring immediately after the collapse of a vapour patch: if they increase the probability of a second vapour patch forming, then alternative (ii), i.e. the cyclical path to failure, is possible; otherwise, the growth of the first patch must be the cause for burnout.

1. Analysis

The quantitative analysis of the probability of the formation of a second vapour patch in the vicinity of the original vapour patch is carried out for a specified heat flux, $\emptyset_c$, local bulk liquid temperature, wall thickness, average measured wall temperature, and observed patch life time, all these variables known from experiment. The corresponding experimental data are:

Run 4

$\emptyset_c = 4.92 \times 10^6$ w/m^2

$T_b = 37^oC$

$\delta = 0.08$ mm

$\overline{T}_w = 130^oC$

$t_i = 1$ msec

The local bulk liquid temperature is calculated using the liquid enthalpy rise (heat balance) at the burnout location for run-test 4-11

(Appendix E). The insulation time of 1 msec is consistent with the experimental observations regarding the life time of vapour patches, as described in Chapter Four, section I.2. It should also be recalled that the values given in Table 11 (bubble coalescence data for run 4 as a function of heat flux) are the arithmetic mean values of a series of measurements, but that individual life times of these vapour patches were found to vary between 0.5 and 1.2 msec.

The quantitative formulation is carried out as follows:

A. Initial conditions. The surface wall temperature is at a mean (measured) value, $\overline{T}_w$, with parabolic temperature distribution in the solid.

B. Insulation of the surface by vapour patch. The vapour patch forms, the surface is suddenly insulated, and therefore the wall temperature at that location rises to a first maximum temperature, T_{M_1}. Elsewhere, nucleation continues maintaining the wall surface at $\overline{T}_w$.

Since the model implies a sudden insulation of the boiling surface on a local basis, the analysis can be approximated by the one-dimensional heat conduction equation for the slab $0 < X_s < 2\delta$, with an internal heat generation rate $\dot{q}$ per unit of volume, constant for $t > 0$ and T_o initial temperature.

The unsteady-state heat conduction equation for the above case is

$$\frac{\partial^2 T}{\partial X_s^2} - \frac{1}{\alpha}\frac{\partial T}{\partial t} = \frac{\dot{q}}{k} \qquad (6\text{-}2)$$

with initial conditions

$$t = 0,\ T_o = \frac{\dot{q}\delta X_s}{k} - \frac{\dot{q}X_s^2}{2k} + \overline{T}_w \qquad (6\text{-}3)$$

and boundary conditions

$$\frac{dT}{dX_s} = 0 \text{ at } X_s = 0 \text{ and } X_s = 2\delta, \text{ for } t > 0 \qquad (6\text{-}4)$$

The general solution of equation (6-2) with conditions (6-3) and (6-4) is given in Appendix H. The results obtained for ΔT_w^+ within $0.2 \leq \tau_i \leq 2.0$ are presented graphically in Figure 88, where ΔT_W^+, τ_i and ε are non-dimensional parameters defined as

$$\Delta T_W^+ = \frac{(T-\bar{T}_w)k_s}{\emptyset\delta} \tag{6-5}$$

$$\tau_i = \frac{\alpha_s t_i}{\delta^2} \tag{6-6}$$

$$\varepsilon = \frac{X_s}{\delta} \tag{6-7}$$

where $(T-\bar{T}_w)$ represents the wall temperature rise $(\equiv T_{M_1} - \bar{T}_w)$ during the insulation time t_i and δ is the wall thickness.

The particular solution to equation (6-2), of interest here, at $X_s = 0$, i.e. the wall temperature rise on the boiling surface - also given in Appendix H - is graphically shown in Figure 89.

Taking t_i = 1 msec and $\emptyset = 4.92 \times 10^6 W/m^2$ and using equation (6-6) and Figure 89, the first maximum wall temperatures, as a function of wall thickness, shown in Figure 90(a), are obtained, where it can be observed that as wall thickness decreases, the maximum wall temperature increases. This indicates that a given heat flux which could cause an increase in wall temperature high enough to promote burnout for a thin wall, would not reach an equivalent level of surface wall temperature with a thicker surface. This is consistent with the experimental evidence regarding the marked effect of wall thickness on CHF, Figure 66.

C. Quenching of the surface by the liquid bulk. The vapour patch collapses after a period of insulation time t_i, (i.e. the life time of the vapour patch) then cold liquid at local bulk temperature T_b contacts the surface and the interface temperature falls to T_{Q_1}, first quenching temperature.

Since only short times are of interest, the quenching temperature after the collapse of the vapour patch can be obtained by assuming

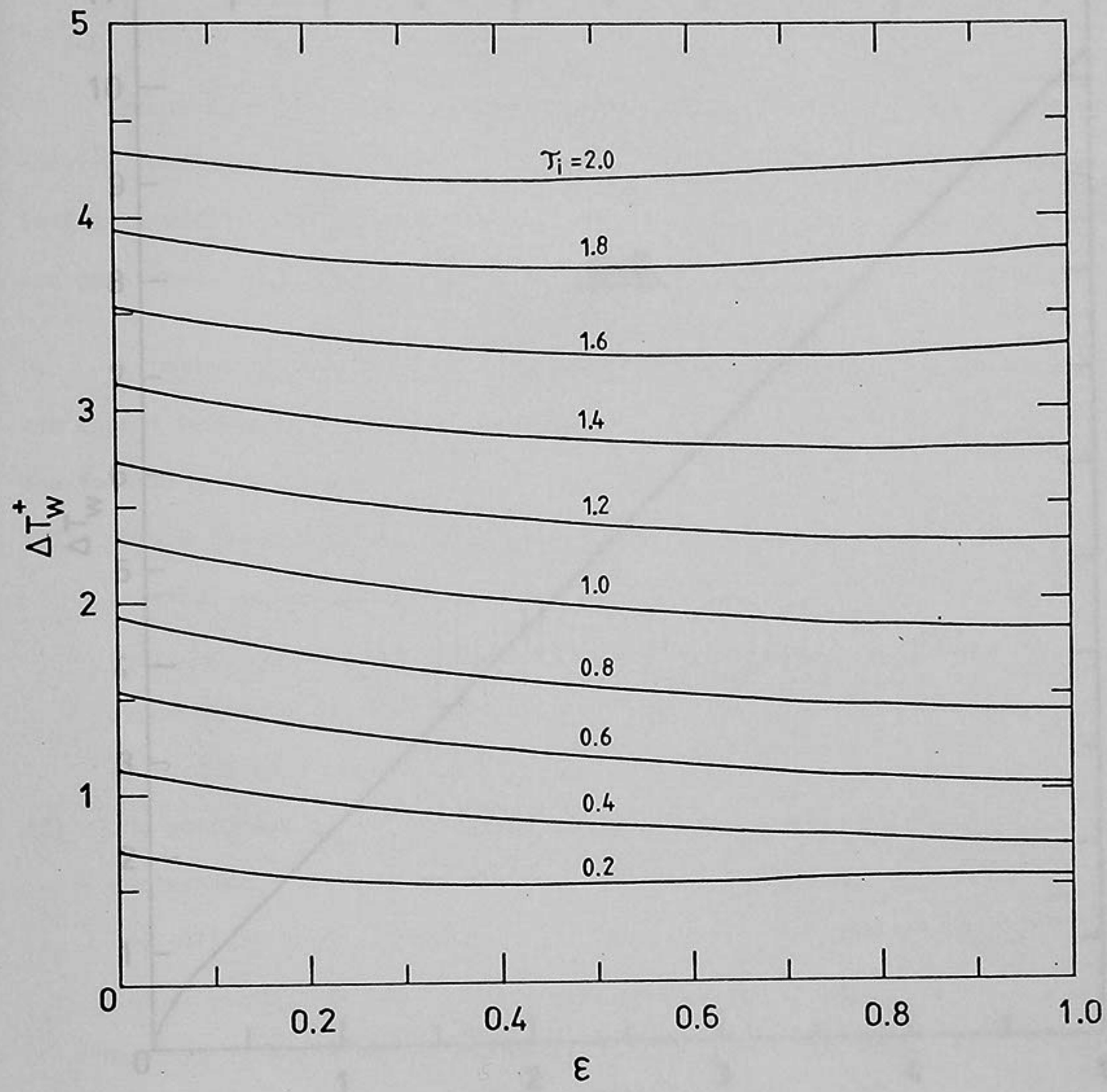


Figure 88 Temperature distribution in a solid with internal heat generation subjected to sudden insulation.

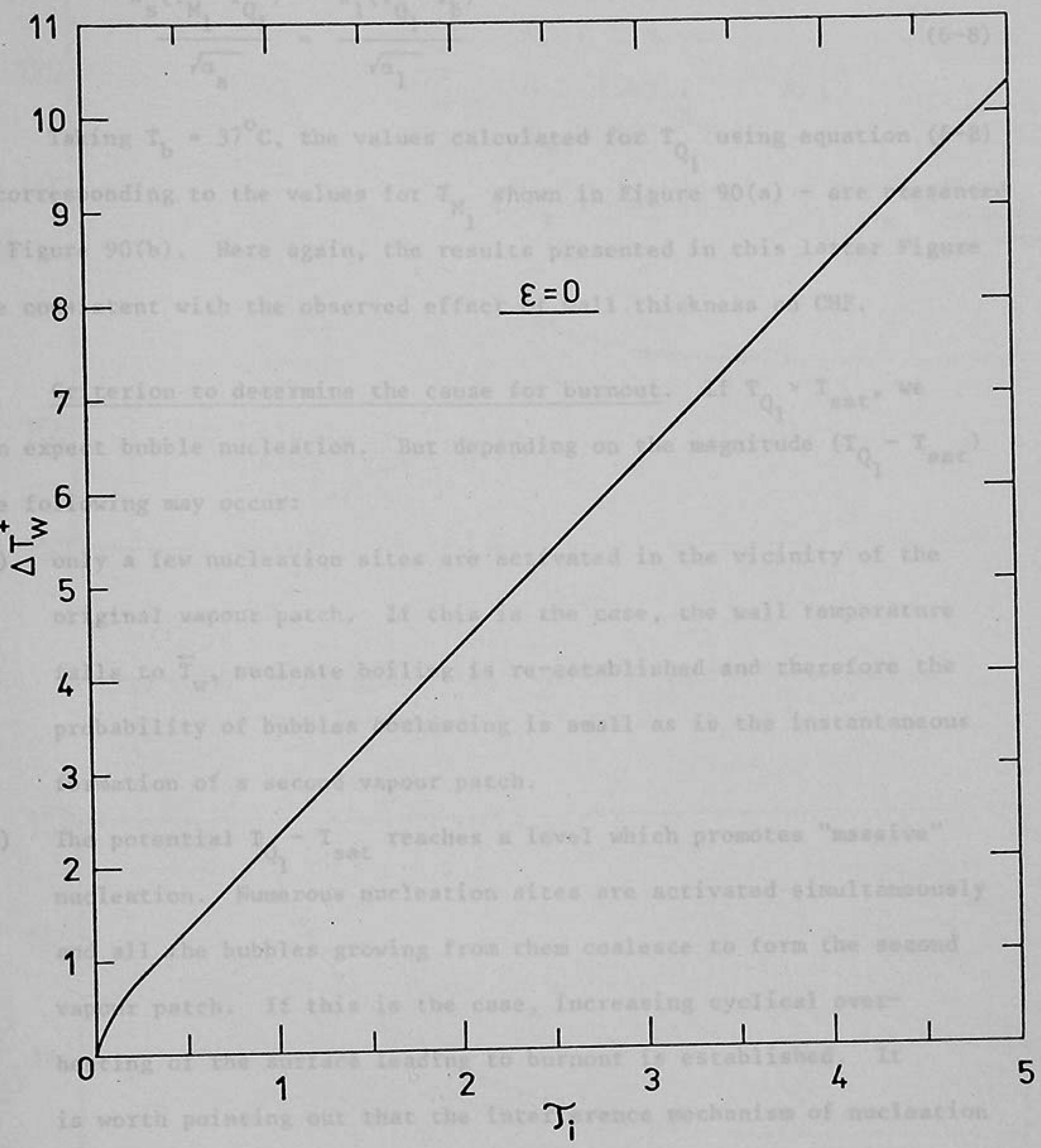


Figure 89 Wall temperature rise at the heater surface as a function of time.

contact between semi-infinite bodies, thus

$$\frac{k_s(T_{M_1} - T_{Q_1})}{\sqrt{\alpha_s}} = \frac{k_1(T_{Q_1} - T_b)}{\sqrt{\alpha_1}} \qquad (6\text{-}8)$$

Taking $T_b = 37^{\circ}C$, the values calculated for T_{Q_1} using equation (6-8) - corresponding to the values for T_{M_1} shown in Figure 90(a) - are presented in Figure 90(b). Here again, the results presented in this latter Figure are consistent with the observed effect of wall thickness on CHF.

D. Criterion to determine the cause for burnout. If $T_{Q_1} > T_{sat}$, we can expect bubble nucleation. But depending on the magnitude $(T_{Q_1} - T_{sat})$ the following may occur:

(1) only a few nucleation sites are activated in the vicinity of the original vapour patch. If this is the case, the wall temperature falls to $\overline{T}_w$, nucleate boiling is re-established and therefore the probability of bubbles coalescing is small as is the instantaneous formation of a second vapour patch.

(2) The potential $T_{Q_1} - T_{sat}$ reaches a level which promotes "massive" nucleation. Numerous nucleation sites are activated simultaneously and all the bubbles growing from them coalesce to form the second vapour patch. If this is the case, increasing cyclical overheating of the surface leading to burnout is established. It is worth pointing out that the interference mechanism of nucleation sites described in Chapter Three, section II.3. only applies for gradual increases in heat flux.

To elucidate the above two possibilities, use will be made of Hsu's nucleation model [95] and the experimental data on nucleation site density of the gas nucleation tests described in section II.1.A. of Chapter Three - Figure 33 -, the experimental data for run 4 given above, and the results obtained from the bubble parameters study listed on Table 4. The method of calculation is illustrated in Figures 91 and 92, and the

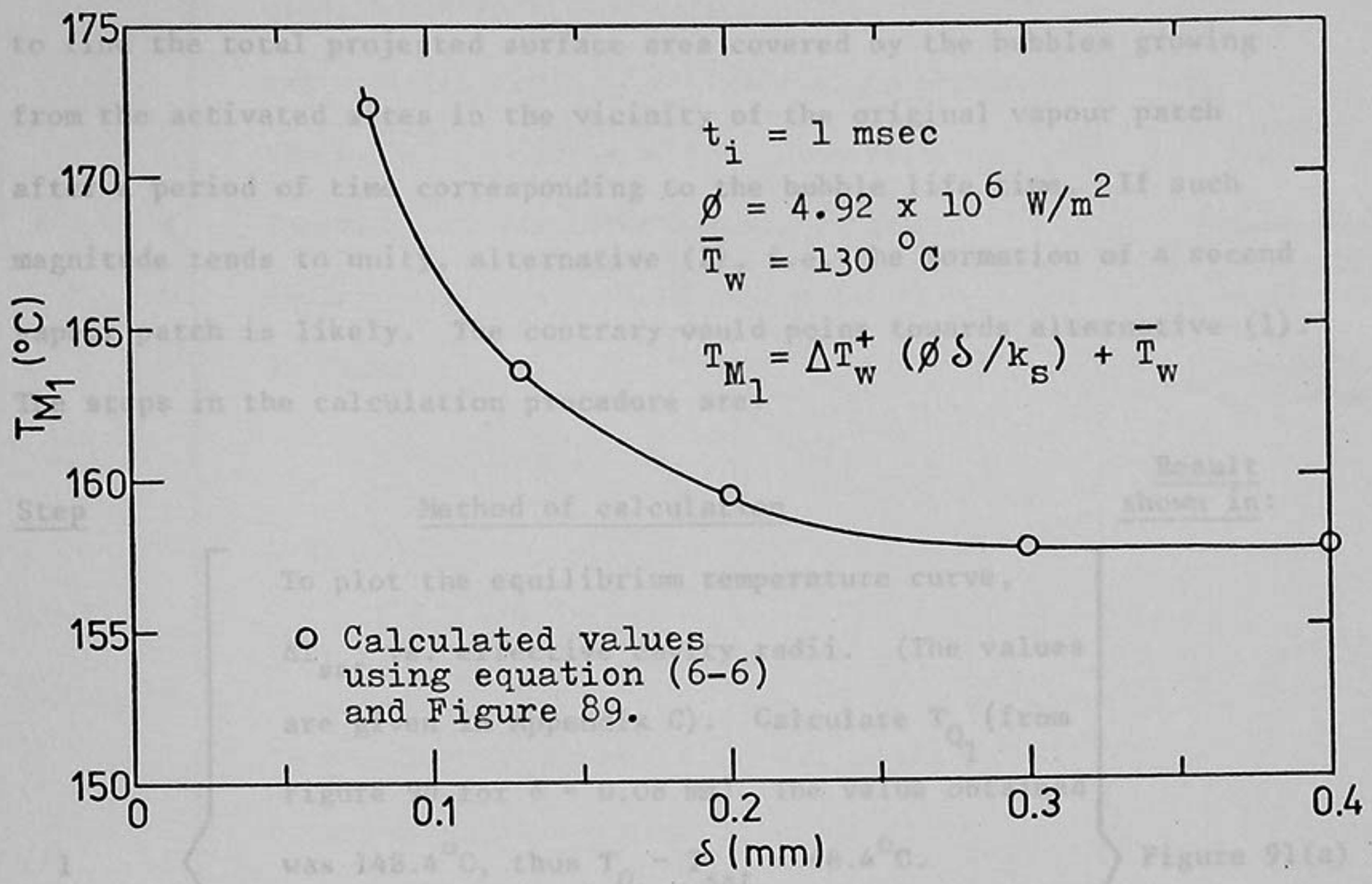


Figure 90(a) The effect of wall thickness on the first maximum wall temperature.

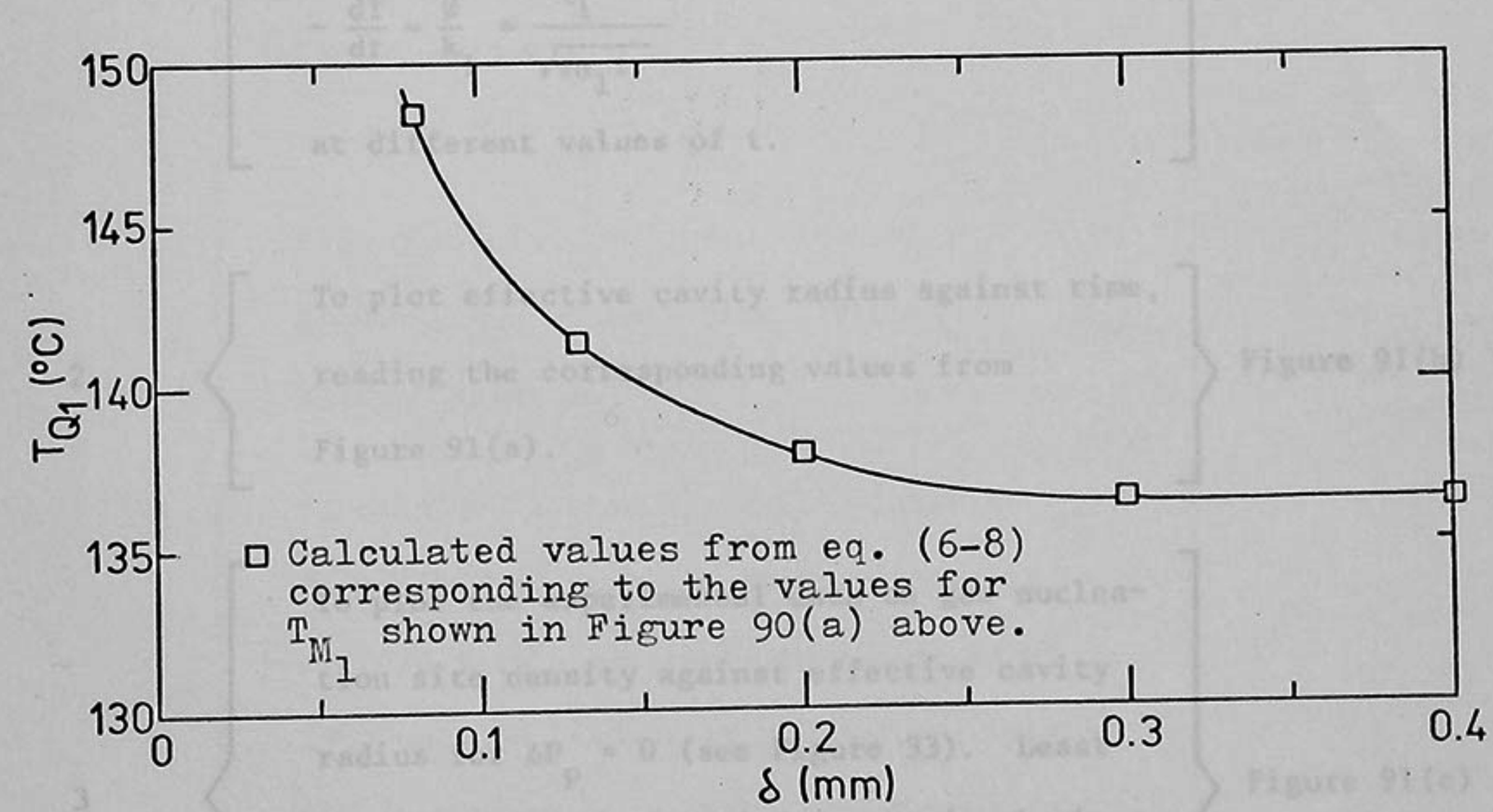


Figure 90(b) The effect of wall thickness on the first quenching wall temperature.

criterion adopted to decide which of the two possibilities above applies is to find the total projected surface area covered by the bubbles growing from the activated sites in the vicinity of the original vapour patch after a period of time corresponding to the bubble life time. If such magnitude tends to unity, alternative (2), i.e. the formation of a second vapour patch is likely. The contrary would point towards alternative (1). The steps in the calculation procedure are:

Step	Method of calculation	Result shown in:
1	To plot the equilibrium temperature curve, ΔT_{sat} vs. effective cavity radii. (The values are given in Appendix C). Calculate T_{Q_1} (from Figure 90 for δ = 0.08 mm). The value obtained was 148.4°C, thus $T_{Q_1} - T_{sat}$ = 48.4°C. Trace the straight lines shown with slope (transient conduction is assumed) $-\frac{dT}{dr} = \frac{\phi}{k_1} = \frac{T_{Q_1} - T_b}{\sqrt{\pi \alpha_1 t}}$ at different values of t.	Figure 91(a)
2	To plot effective cavity radius against time, reading the corresponding values from Figure 91(a).	Figure 91(b)
3	To plot the experimental data on gas nucleation site density against effective cavity radius for ΔP_p = 0 (see Figure 33). Least square method was applied to obtain the best fitting curve which was used to extrapolate outside the experimental range.	Figure 91(c)

4

An assumed bubble growth rate function was used, based on r_{max} (maximum bubble radius) extrapolated to T_{Q_1} from Table 4, to obtain the bubble projected surface area as a function of time. The assumed function, supported by the experimental data shown in Figure 41, is

$$r = r_m\left[2\left(\frac{t}{t_g}\right) - \left(\frac{t}{t_g}\right)^2\right]$$

thus

$$A_b(t) = \pi r_m^2\left[2\left(\frac{t}{t_g}\right) - \left(\frac{t}{t_g}\right)^2\right]^2$$

Figure 92(a)

5

To obtain from Figure 91(b), for various values of time, the size range of active sites $r_{e_{min}}$ and $r_{e_{max}}$. Enter with these values in Figure 91(c) to obtain the number of sites activated at the given time. Evaluate

$$N_G = n_{g_{min}} - n_{g_{max}}$$

thus obtaining the number of bubbles growing, N_G, at each time. Plot N_G against time.

Figure 92(b)

6

To consider period t_L (extrapolated to T_{Q_1} from Table 4) from the start of nucleation divided into j intervals in Figure 92(b). Take each ΔN_G from Figure 92(b), multiply by the instantaneous surface area from Figure 92(a), thus obtaining curves for the instantaneous fraction of surface area covered. Plot each of the j curves against time and obtain the total surface area covered at t_L by summing up all the instantaneous fraction of areas at each t_j.

Figure 92(c)

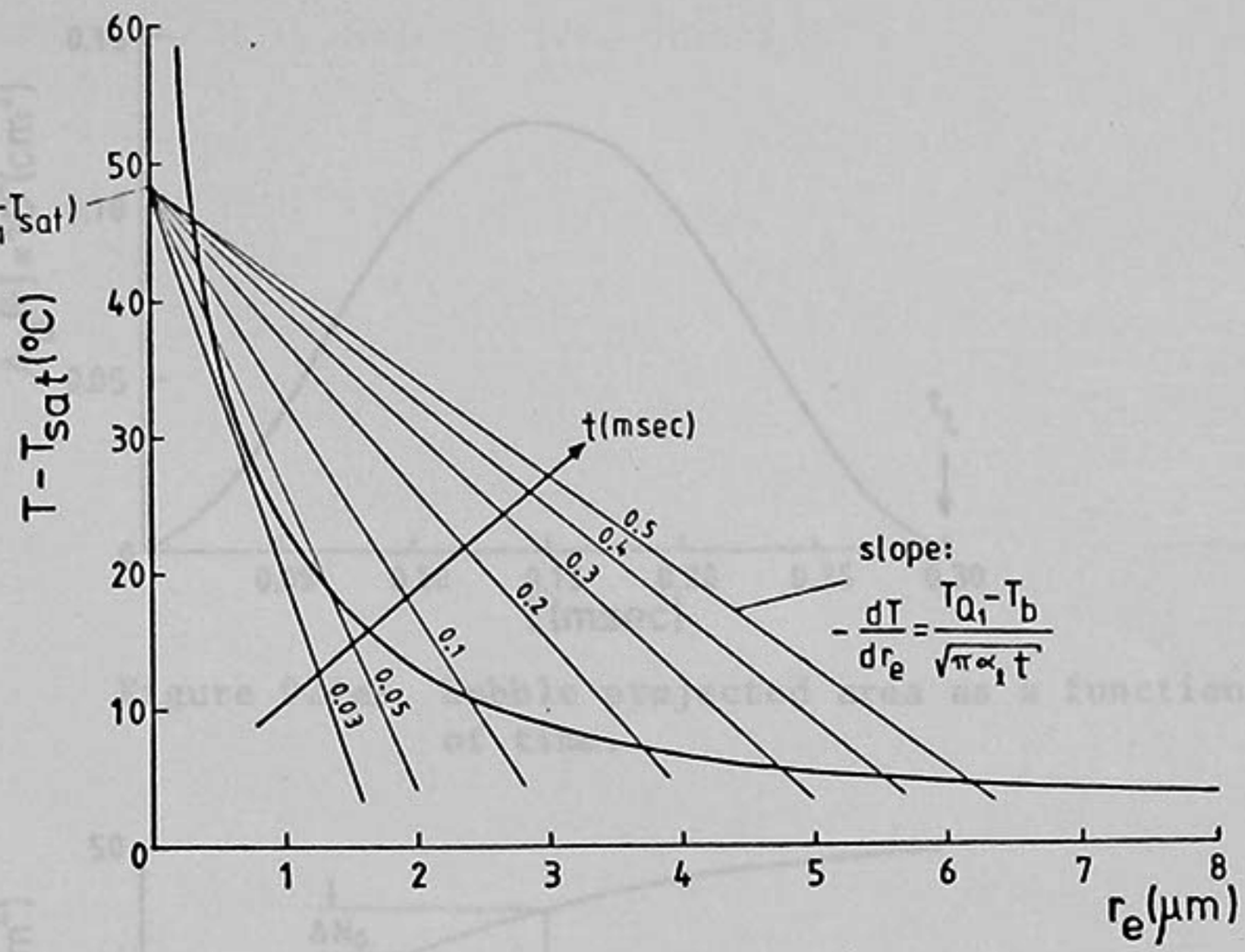


Figure 91(a) Wall superheat as a function of effective cavity radii.

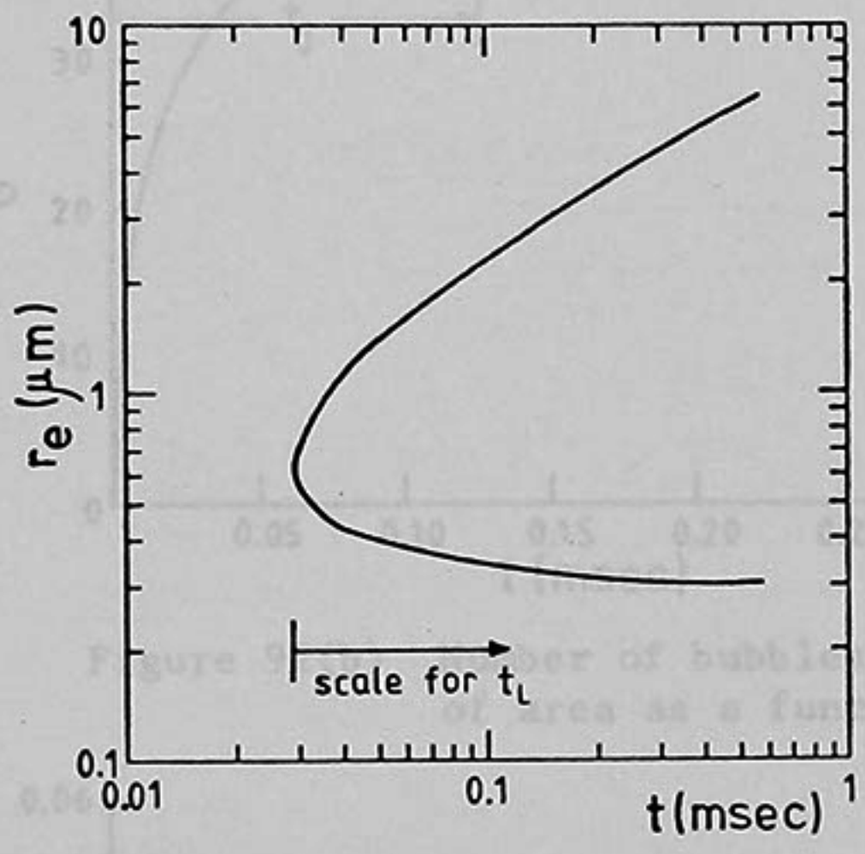


Figure 91(b) Effective cavity radius as a function of time.

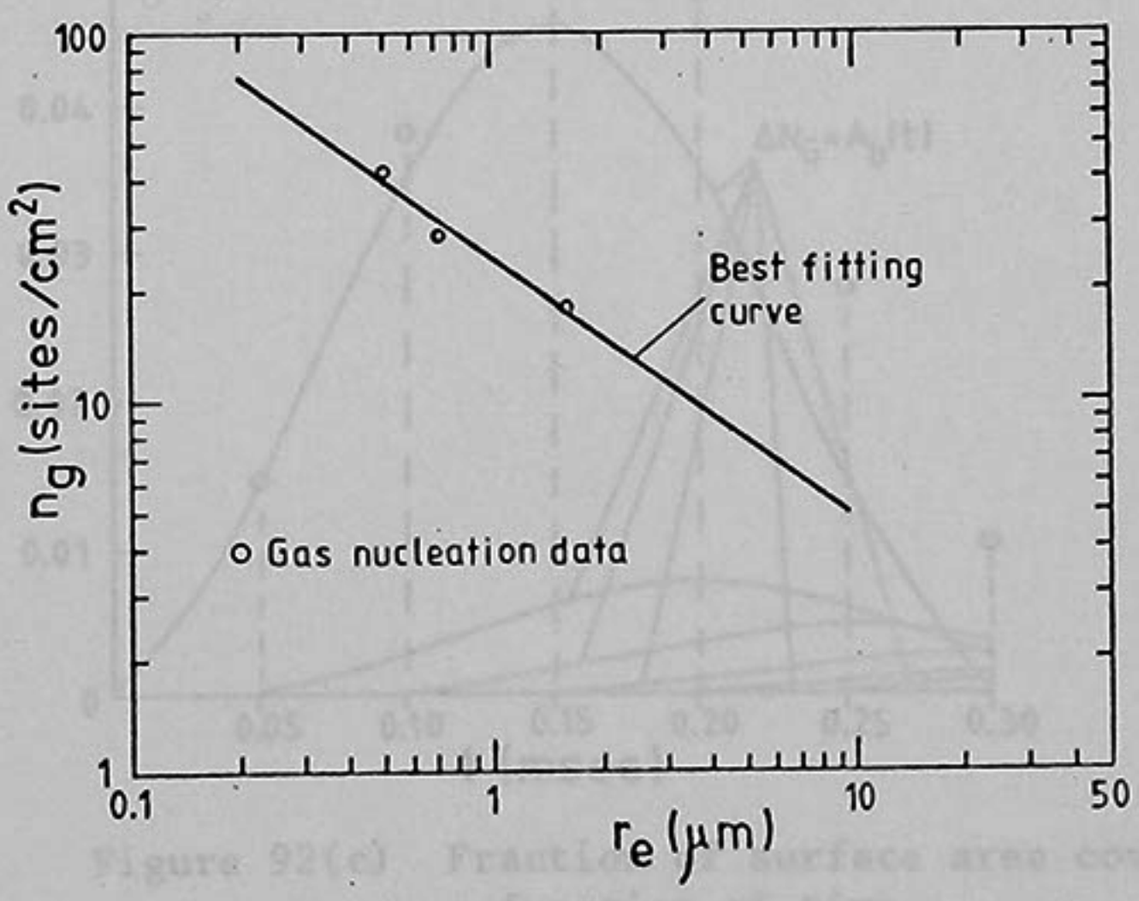


Figure 91(c) Experimental gas nucleation density data.

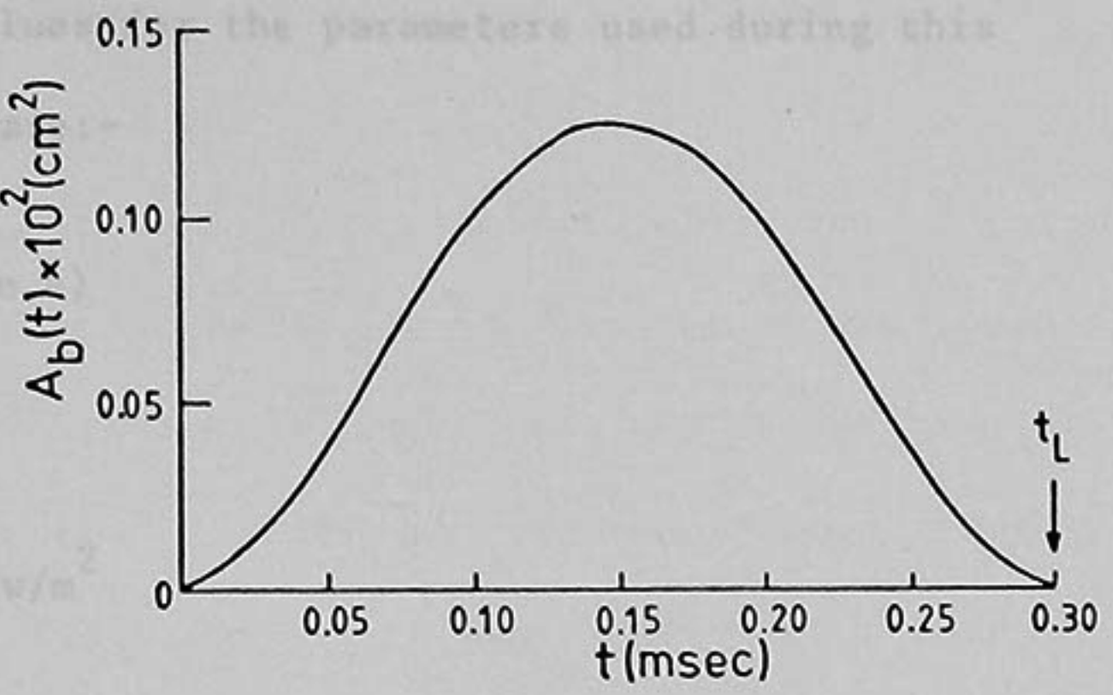


Figure 92(a) Bubble projected area as a function of time.

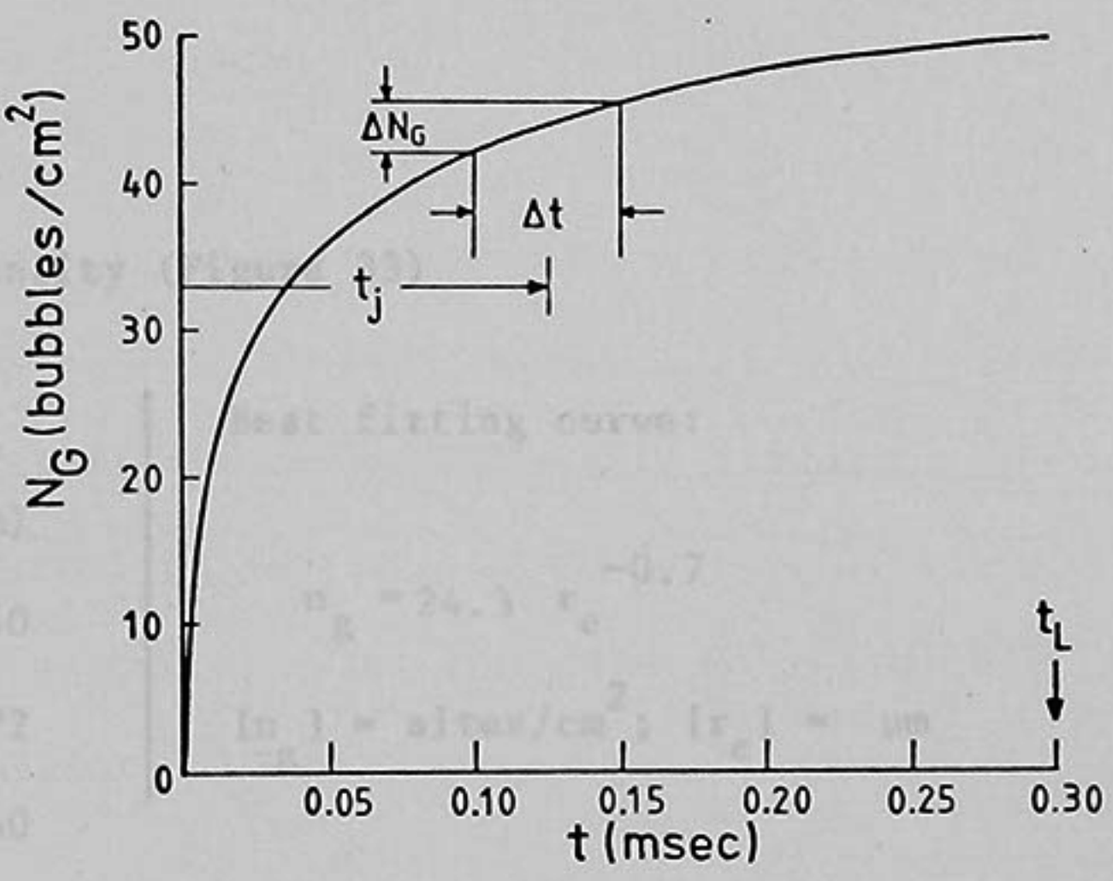


Figure 92(b) Number of bubbles growing per unit of area as a function of time.

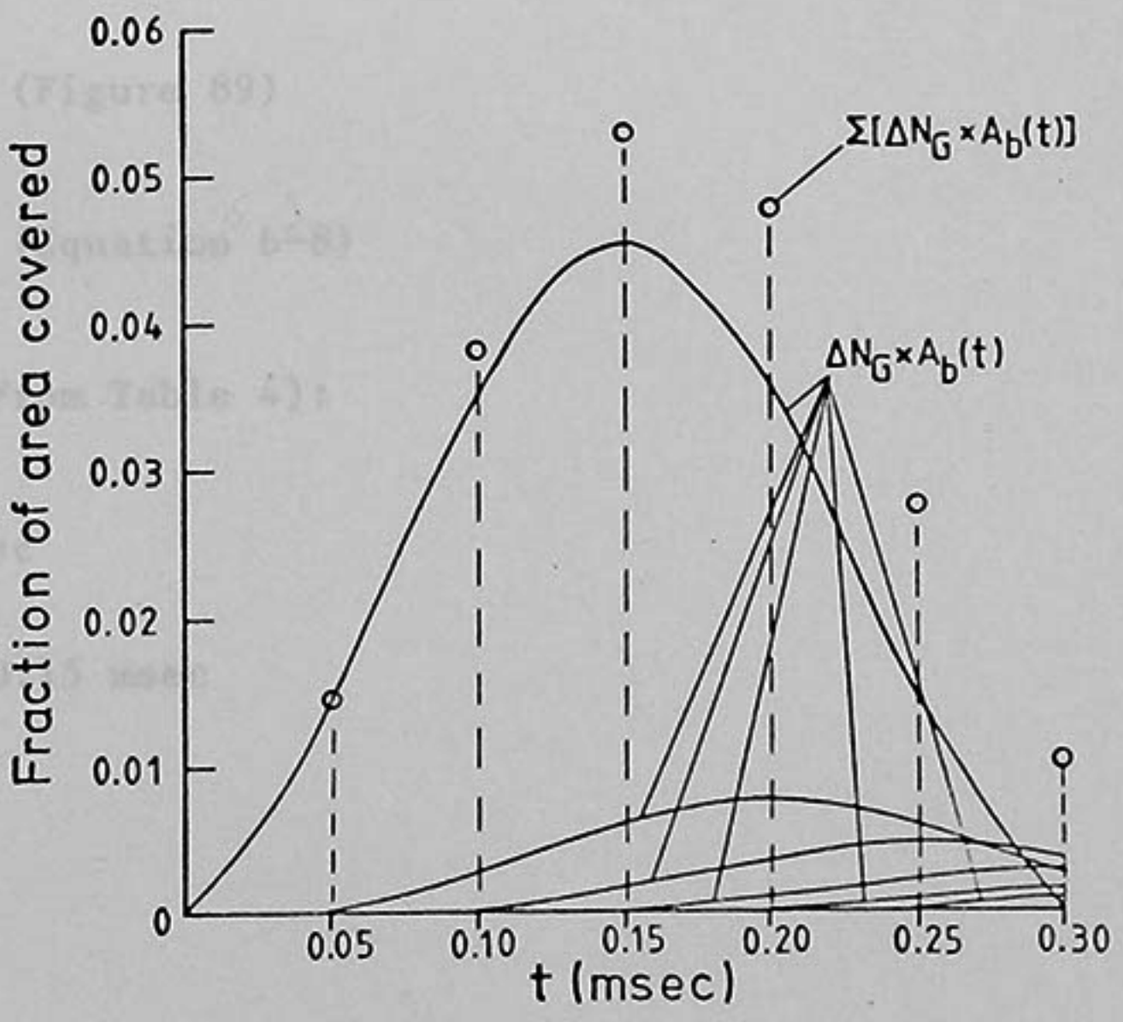


Figure 92(c) Fraction of surface area covered as a function of time.

The numerical values for the parameters used during this calculating procedure are:-

Experimental Data (Run 4)

$\overline{T}_w = 130^oC$

$\emptyset_c = 4.92 \times 10^6$ w/m^2

$\delta = 0.08$ mm

$T_b = 37^oC$

$t_i = 1$ msec

Gas nucleation site density (Figure 33)

n_g (sites/cm^2)	r_e (μm)
42	0.50
28	0.72
18	1.60

Best fitting curve:

$$n_g = 24.3\ r_e^{-0.7}$$

$[n_g]$ = sites/cm^2; $[r_e]$ = μm

Calculated quantities:

$T_{M_1} = 173.2^oC$ (Figure 89)

$T_{Q_1} = 148.4$ (Equation 6-8)

Extrapolated values (From Table 4):

$t_L = 0.30$ msec

$t_g = t_L/2 = 0.15$ msec

$r_m = 0.2$ mm

With the above information, the method of calculation was applied. A first estimate was carried out dividing the bubble lifetime into 6 broad intervals in Figure 92(b), and the total fraction of surface area was calculated. Then j was increased first to 15 and subsequently to 30, but since the difference in results was not significant, a repeat calculation at finer intervals aiming at improving accuracy was not attempted: for an insulation time for a vapour patch of 1 msec the total fraction of surface area covered was only 0.01. The whole exercise was repeated at j = 15 assuming an insulation time of 2 msec and the corresponding value for the fraction of surface area covered was found to be 0.021.

The above results, according to the proposed alternatives for burnout, lead us therefore to conclude that the most likely cause for burnout is the stabilisation/growth of a single vapour patch. The conditions promoting such a process are yet to be elucidated. Further experimental studies directed at determining the mechanism(s) of bubble coalescence may be fruitful.

CHAPTER SEVEN

SUMMARY AND CONCLUSIONS

I. Summary and Conclusions

An experimental investigation of the flow boiling of water at atmospheric pressure was undertaken, including a high-speed cine photographic study of the flow structure near the Critical Heat Flux (CHF). Experimental tests from single-phase forced convection to burnout were conducted at several combinations of flow velocities and inlet subcoolings for water flowing upwards through a vertical channel of rectangular cross-section electrically and uniformly heated on one wall only, with a glass window forming the opposite wall, Figure 20. Detailed descriptions of the experimental apparatus, the high-speed cine photographic equipment and tests procedures were presented in Chapter Two. The ranges of parameters investigated were as follows:

System pressure : atmospheric.

Test section geometry : a channel of rectangular cross-section (12mm x 5 mm); D_H = 7 mm.

Test surface (Figure 19):

Material - Stainless steel

Heated length - 150 mm

Width - 10 mm

Wall thickness - 0.08 mm to 0.20 mm

Water flow velocity : 0.8 m/sec to 2.0 m/sec

Inlet subcooling : $20^{o}K$ to $80^{o}K$

Within the above range of experimental conditions, the following conclusions can be drawn from the present study:

1. Single-phase forced convection

Measured heat transfer coefficients in the single-phase forced

convection region at Reynolds numbers, based on the mean hydraulic diameter of the test channel (D_H=7 mm), in the range 10^4 to 6 x 10^4, were found to be in close agreement (± 7%) with the empirical correlation of James et al [63], equation (3-1), developed for ducts of rectangular cross-section. The inadequacy of well-known correlations developed for tubular geometries, equations (3-2) to (3-4), often applied to channels of rectangular cross-section using the mean hydraulic diameter concept, pointed out in [63] and [67], was substantiated by the present data.

2. Nucleate boiling heat transfer

Seventy tests of 27 different experimental runs (Table 1) were conducted from nucleate boiling up to burnout (physical destruction). In the resulting boiling curves, Figures 29 to 31, the exponent n in the heat flux-wall superheat relationship over the fully-developed nucleate boiling region

$$\Delta T_{sat} = \psi \, \phi^n \qquad (3\text{-}5)$$

ranged from 0.25 to 0.44, lying within the range of values reported elsewhere [1]. The values predicted by the empirical correlation of Bergles and Rohsenow [68] for the onset of boiling, equation (3-6), coincided to within ±2 ^{o}K with the experimental values shown in the boiling curves, Figures 29 to 31.

The position of the boiling curve was found to be affected by wall thickness, when all the other parameters were kept constant. At a given heat flux, the wall superheat became higher as wall thickness decreased, and this difference in wall superheat tended to increase as the heat flux was increased. The increases in wall superheat as between the 0.20 mm and the 0.08 mm wall thickness ranged from 4% to 25%. Alternatively, at a given wall superheat, the heat flux became higher as wall thickness increased, Table 2. The observed effect of wall thickness on the position of the boiling curves could not be attributed to differences either in roughness or in surface nucleation conditions between the surfaces of the three

different thicknesses, since their roughness (Figure 32) and nucleation conditions in the gas nucleation tests (Figure 33), were similar and with no systematic variation which might be attributable to wall thickness.

At constant heat flux, wall thickness and flow velocity, the wall superheat reduced with increasing inlet subcooling. The change in wall superheat as between the 20 ^{o}K and the 80 ^{o}K inlet subcooling ranged from 3% to 10%, Figure 39. Since this was found to be a secondary effect, the basic assumption $\phi = fn(\Delta T_{sat})$ is a good approximation.

Flow velocity, in the range 0.8 m/sec to 2.0 m/sec, did not seem to affect the wall superheat, and experimental data lay reasonably well on a single curve, with all the other parameters kept constant, Figure 37. This behaviour supports the hypothesis that the contribution to heat transfer of the convective component, compared to the highly efficient mode of heat transfer operating at nucleate boiling, is negligible.

For a set of four high-speed cine films, out of a total of thirty three (all taken at 10,000 frames per second), a complete quantitative analysis of the bubble parameters in bubbly flow was carried out. For the same heating surface under the same conditions of flow and subcooling (Run 4, Table 1) with varying levels of heat flux ranging from 70% to 95% of the average measured CHF, the following parameters were determined: maximum bubble diameter, waiting time, bubble growth time, bubble life time, frequency of bubble emission, bubble population density, nucleation site density, spatial distribution of nucleation sites and separation distance between pairs of nearest-neighbour nucleation sites. The average values for these parameters were listed in Table 4. It was found, Figure 40, that with increasing heat flux:

Maximum bubble diameter remained constant, bubble life time decreased slightly, waiting time decreased sharply, frequency of bubble emission and bubble population density increased, nucleation site density increased and separation distance between pairs of nearest-neighbour sites decreased.

At the four levels of heat flux maximum bubble diameter data and waiting

time data fitted well with a Normal distribution, whereas frequency of bubble emission data and separation distance between pairs of nearest-neighbour sites data followed neither Poisson nor Normal distributions.

A deactivation/reactivation process of nucleation sites with increasing heat flux was observed: some sites at a lower heat flux were deactivated at the next higher level of heat flux and some of these even reactivated at a still higher heat flux. An individual site activation history was established, Figure 55, and a site deactivation mechanism was proposed. It was found that in the great proportion of sites, deactivation during an increase in heat flux was due to thermal interference: the deactivation of a nucleation site seems to be associated with the activation of a new site within its vicinity which makes conditions less favourable at existing sites (Chapter Three, section II. 3.). The statistical method of determining spatial distribution of local active nucleation sites based on the Poisson probability law, equation (3-19), is not adequate to discern interference effects since the results obtained are markedly dependent on the number of local areas into which the total surface area of observation is divided, Figure 54. To observe the occurrence of interference effects use should be made of probability distributions based on the separation distance between pairs of nearest-neighbour sites, Figure 51.

A model for nucleate boiling heat transfer was proposed which extends to the fully-developed nucleate boiling region where the areas of bubble influence overlap. The model, expressed explicitly by equation (5-56), allows for the overlapping areas of bubble influence and assumes that the total heat flux in nucleate boiling is given by the sum of the microlayer evaporation flux, a surface quenching component and the single-phase forced convection contribution. These components act independently over portions of the total surface area, Figure 84. The surface quenching model was extended beyond the isolated bubble regime by introducing the ratio x of true fraction of boi-

ling area β_a to nominal fraction of boiling area β, since when the areas of bubble influence overlap, the fraction of surface area affected by boiling is reduced from $\beta = n_s K A_b$ to $\beta_a = x\beta$. The consequent reduction in boiling flux is offset by an assumed enhanced rate of heat transfer in the overlapping areas which are subjected to quenching by more than one bubble site, at a higher frequency.

Measurements of the actual boiling area at three different values assumed for K (empirical factor defining the area of bubble influence), ranging from 4 to 6, were carried out for the spatial distributions of nucleation sites for run 4 from 70% to 95% of the CHF, shown in Figures 43 and 44. Making use of the bubble parameters data, Tabla 4, the adequacy of the proposed model, which considers binary overlap only, was assessed: with a constant value for K of 6, the model fitted the experimental data to within ±8%, Figure 85. The major contribution to the total heat flux arose from surface quenching, accounting (at K = 6) at the four levels of heat flux for from 81% to 98% of the total heat flux, the single-phase forced convection contribution ranged from 5% to 10%, whereas the microlayer evaporation contribution was found to be very small, 2% to 3%.

When both the present model-incorporating the effect of overlap of the areas of bubble influence in heat transfer- and the simple surface quenching mechanism, equation (1-13), were used to estimate the optimum values of K, i.e. those values which could give an exact fit to the measured heat fluxes, a tendency for K to decrease with increasing heat flux was observed, Figure 86. This indicates a likely dependence of K on heat flux or any other related variable such as Jakob number or wall superheat.

3. Critical heat flux

The high-speed cine photographic study of the flow structure at different levels of heat flux within the present range of experimental conditions revealed that:

i) Two flow regimes exist in the range 30% to 95% of the measured

critical heat fluxes, these being identified as bubbly and slug. (The corresponding flow regimes and conditions for the complete set of cine films are tabulated in Appendix D) ;

ii) there is a gradual transition from bubbly to slug flow with increasing heat flux, all the other parameters being kept constant, (Figure 59);

iii) the flow regime is not affected by wall thickness, (Figure 60);

iv) burnout is not associated with a particular flow regime, (Figure 60);

v) the boiling surfaces are never completely blanketed by bubbles;

vi) nucleation persists at all flow patterns and is observed under large vapour clots in the slug flow regime, (Figure 59 (d));

vii) bubble coalescence occurs at heat fluxes as low as 30% of the CHF, Figure 63, but the frequency of coalescence events, Table 11, increases with increasing heat flux. Both the life time and the size of the vapour masses formed by bubble coalescence, compared to corresponding values for individual bubbles, increase with increasing heat flux, and

viii) small vapour patches, mostly localised near the downstream end of the heating surface, form rapidly. Some of these vapour patches seem to grow with time, to reach a stage of apparent constant size and to collapse as a single unit. Others, on the other hand, seem to reach a maximum size and grow smaller, and then to break into smaller vapour masses, collapsing subsequently (Chapter Four, section I.2.).

Seventy experimental CHF tests to physical destruction were carried out. Table 12 lists the arithmetical means of the CHF values for repeat tests. The effect of wall thickness on CHF was systematically investigated and within the present range of conditions, Table 1, increases in CHF as between the 0.08mm and the 0.20mm wall thickness, ranged from 38% to 57%, the effect being somewhat higher at high subcoolings and low flow velocities, Figure 66.

An empirical expression for CHF, equation (4-14), was developed, including wall thickness as a parameter. The expression correlated the experi-

mental data to within 15%, Figure 74, and indicated a limiting value for wall thickness affecting the CHF ($\sim$ 0.5 mm). Beyond this value of wall thickness, the correlation predicted the CHF to be independent of this parameter. Neglecting the effect of wall thickness on CHF was considered as a potential source of disagreement among existing correlations. The correlation was extrapolated to pool boiling burnout, and when it was compared to the CHF obtained using well-known pool boiling burnout correlations, good agreement was observed, Table 13.

Some well-known models proposed for the mechanism of CHF were tested against detailed experimental observations under particular conditions of high subcooling. They were found to be inconsistent with the experimental evidence. Under these conditions, two alternative routes to burnout arose (Chapter Six, section III.) :

(1) Stabilisation (or continuous growth) of a vapour patch, or

(2) repeated growth/collapse of vapour patches over the same surface location.

The events occurring immediately after the collapse of a vapour patch were quantitatively analysed. A one-dimensional conduction model was formulated to predict the wall surface temperature rise due to the insulation of the heating surface by a vapour patch, Appendix H. The wall surface temperature after the collapse of the vapour patch was calculated using semi-infinite body theory, equation (6-8). By making use of Hsu's nucleation model [95] and experimental data on gas nucleation site density, Figure 33, and the experimental data for Run 4, Tables 4 and 11, the surface area covered by bubbles growing from the activated sites in the vicinity of the original vapour patch was calculated; the method of calculation was described step by step in Chapter Six. The fraction of surface blanketed by bubbles was very small, leading to the conclusion that the most likely cause for burnout is the stabilisation/growth of a vapour patch.

II. Future work

To extend the present work, and to throw further light on the determination of the mechanisms of nucleate boiling heat transfer and critical heat flux, a programme of work for the immediate future is briefly outlined in the following paragraphs.

There are several areas where our present knowledge seems to be particularly limited and further work is required:

1) The actual definition of the parameter K;

2) the mechanism(s) of bubble coalescence;

3) the origin of vapour patches;

4) the temperature fluctuations experienced by the boiling surface;

5) the identification of dry areas in flow boiling when metallic surfaces are used;

6) the stability of nucleation sites in the long term, and

7) the conditions leading to vapour patch stabilisation/growth.

The information accumulated during the development of this study could help to elucidate points 3,6 and 7 mentioned above. Although frame by frame analyses of the cine films are highly time-consuming, they could provide substantial information. By pursuing a further analysis of the four sections of films so far analysed (Run 4, 70% to 95% CHF), the stability of the nucleation sites already identified could be studied in detail. The conditions prior to and during the formation of vapour patches could be determined in the cine film corresponding to Figure 59(b) for instance.

The study of points 1, 2, 5 and 6 would require further experiments:

To determine the functional variation of K with heat flux, similar analyses to those described in chapters Three and Five would be necessary: flow boiling experiments in conjunction with high-speed cine photography under the same operating conditions for the same surface at varying levels of heat flux ranging from low fluxes (10-20% of CHF) up to regions close to burnout.

The study of the mechanism(s) of bubble coalescence would necessitate the design of a test channel in which the heating surface could be filmed simultaneously in side and front views. Here the study would have to be confined to high subcoolings/low heat fluxes so that the bubbles did not obscure the view.

The verification of temperature fluctuations and the formation of dry areas would require the development of a fast-response temperature measuring device, capable of being embodied in the solid without altering the conditions of the heating surface and perturbing the flow of heat and fluid. The deposition of a thin-film resistance thermometer at the rear face of thin test surfaces would be pursued.

REFERENCES

[1] Collier, J.G. "Convective boiling and condensation", McGraw-Hill Book Company, U.K. Ltd. (1972).

[2] Hsu, Y.Y. and Graham, R.W. "Transport processes in boiling and two-phase systems", McGraw-Hill Book Company, New York (1976).

[3] Butterworth, D. and Hewitt, G.F. (Editors) "Two-phase flow and heat transfer", Oxford University Press (1977).

[4] Tong, L.S. "Boiling heat transfer and two-phase flow" John Wiley & Sons, Inc.; New York (1965).

[5] Rohsenow, W.M., Section 13 "Boiling" in "Handbook of heat transfer" edited by Rohsenow, W.M. & Hartnett, J.P. McGraw-Hill Book Co.; New York (1973).

[6] Rohsenow, W.M. & Clark J.A. "A study of the mechanism of boiling heat transfer" Trans. ASME, 73:609 (1951).

[7] Rohsenow, W.M. "A method of correlating heat transfer data for surface boiling of liquids" Trans. ASME, 74:969 (1952).

[8] Bankoff, S.G. "On the mechanism of subcooled nucleate boiling. Parts I and II". Chem. Eng. Prog. Symp. Series, 57 (32):156 (1961).

[9] Gunther, F.C. "Photographic study of surface boiling heat transfer with forced convection" Trans. ASME, 73:115 (1951).

[10] Kast, W. "Importance of nucleation activation and nonstationary heat transport for the heat transfer in nucleate boiling and dropwise condensation" Chem. Eng. Tech. 36(9):933 (1964).

[11] Forster, K.E. & Greif, R. "Heat transfer to a boiling liquid - mechanism and correlations" Trans. ASME, J.Heat Transfer 81:43 (1959).

[12] Graham, R.W. & Hendricks, R.C. "Assessment of convection, conduction and evaporation in nucleate boiling" NASA, Report TN D-3943 (1967).

[13] Bankoff, S.G. "A note on latent heat transport in nucleate boiling" AIChE Journal, 8(1):63 (1962).

[14] Rallis, C.J. & Jawurek, H.H. "Latent heat transport is saturated nucleate boiling" Int.J.Heat & Mass Transfer, 7:1051 (1964).

[15] Han, C.Y & Griffith, P. "The mechanisms of heat transfer in nucleate pool boiling" Int. J. Heat & Mass Transfer, 8:887 (1965).

[16] Mikic, B.B. & Rohsenow, W.M. "A new correlation of pool boiling data including the effect of surface characteristics" Trans. ASME, J. Heat Transfer, 91:245 (1969).

[17] Bankoff, S.G.; Colahan, W.J. & Bartz, D.R. "Summary of conference on bubble dynamics and boiling heat transfer" Memo 20-137 Jet Propulsion Lab., Calif. Institute of Technology, (1956).

[18] Moore, F.D. & Mesler, R.B. "The measurement of rapid surface temperature fluctuations during nucleate boiling of water". AIChE Journal, 7:620 (1961).

[19] Cooper, M.G. & Lloyd, A.J.P. "Miniature thin film thermometers with rapid response" J. Sci. Inst. 42:791 (1965).

[20] Sharp, R.R. "The nature of liquid film evaporation during nucleate boiling", NASA, Report TN D-1997 (1964).

[21] Jawurek, H.H. "Simultaneous determination of microlayer geometry and bubble growth in nucleate boiling" Int. J. Heat & Mass Transfer, 12:843 (1969).

[22] Voutsinos, C.M. & Judd, R.L. "Laser interferometric investigation of the microlayer evaporation phenomenon" Trans. ASME, J. Heat Transfer, 97(1):88 (1975).

[23] Cooper, M.G. "The microlayer and bubble growth in nucleate pool boiling" Int. J. Heat & Mass Transfer, 12:915 (1969).

[24] van Ouwerkerk, H.J. "The rapid growth of a vapour bubble at a liquid-solid interface" Int. J. Heat & Mass Transfer, 14:1415 (1971).

[25] Cooper, M.G. & Merry, J.M.D. "A general expression for the rate of evaporation of a layer of liquid on a solid body" Int. J. Heat & Mass Transfer, 16:1811 (1973).

[26] Robin, T.T. & Snyder, N.W. "Bubble dynamics in subcooled nucleate boiling based on the mass-transfer mechanism" Int. J. Heat & Mass Transfer, 13:305 (1970).

[27] Cooper, M.G.; Judd, A.M. & Pike, R.A. "Shape and departure of single bubbles growing at a wall" Paper PB-1, VI Int. Heat Transfer Conference, 1:115 (1978); Toronto, Canada.

[28] Judd, R.L. & Hwang, K.S. "A comprehensive model for nucleate pool boiling heat transfer including microlayer evaporation" Trans. ASME, J. Heat Transfer, 98(4):623 (1976).

[29] Rohsenow, W.M. "Heat transfer with evaporation", Chapter 4 in "Heat transfer, a symposium" Eng. Research Institue, Univ. of Michingan Press, Ann Arbor, Mich. (1952).

[30] Singh, A.; Mikic, B.B. & Rohsenow, W.M. "Relative behaviour of water and organics in boiling" Paper PB-9, VI Int. Heat Transfer Conf., 1:163 (1978); Toronto, Canada.

[31] Macbeth, R.V. "The burnout phenomenon in forced convection boiling" Adv. in Chem.Eng. 7:207 (1968).

[32] Tong, L.S. "Boiling crisis and critical heat flux" USAEC, Critical Review Series, Report TID-25887 (1972).

[33] Hewitt, G.F. "Critical heat flux: a review" Paper No. C1, European Two-phase flow Meeting, Harwell, England (June 1974).

[34] Hewitt, G.F. "Critical heat flux in flow boiling" Proc VI Int. Heat Transfer Conf.; Toronto, Canada (1978).

[35] Bećker, K.M. "An analytical and experimental study of burnout conditions in vertical round ducts" A.B. Atomenergi, Report AE-178, Sweden (1965).

[36] McAdams, W.H. et al "Heat transfer at high rates to water with surface boiling" Indust. & Eng. Chem. 41(9):1945 (1949).

[37] Macbeth, R.V. "An appraisal of forced convection burnout data" Proc. Inst. Mech. Engrs. (London) 180: Part 3C: 37 (1965-66).

[38] Levy, S. "Prediction of the CHF in forced convection flow" USAEC, Report GEAP-3961 (1962).

[39] Chang, Y.P. "Some possible critical conditions in nucleate boiling" Trans. ASME, J.Heat Transfer, 85:89 (1963).

[40] Fiori, M.P. & Bergles, A.E. "Model of critical heat flux in sub-cooled flow boiling" Report No. DSR 70281-56, MIT, Dept. Mech. Eng. (1968).

[41] Tong, L.S. et al "Influence of axially non-uniform heat flux on DNB" Chem. Eng. Prog. Symp. Series, 62:35 (1966).

[42] Kutateladze, S.S. & Leont'ev, A.I. "Some applications of the asymptotic theory of the turbulent boundary layer" Proc. 3rd. Int. Heat Transfer Conf., Paper 81, 3 :1 (1966) Chicago.

[43] Tong, L.S. "Boundary-layer analysis of the flow boiling crisis" Int. J. Heat & Mass Transfer, 11:1208 (1968).

[44] Kirby, G.J., et al "An investigation into a possible mechanism of subcooled burnout" UKAEA, Report AEEW-M725 (1966).

[45] Kirby, G.J., et al "A visual study of forced convection boiling. Flow patterns and burnout for a round test section. Part 2". UKAEA, Report AEEW-R 506 (1967).

[46] Torikai, K., Et al "Boiling heat transfer and burnout mechanism in boiling-water cooled reactor" Paper No. 28/P/580 3rd United Nat. Int. Conf. on the Peaceful uses of Atomic Energy (1964).

[47] Torikai, K. & Yamazaki, T. "The contact area of boiling bubbles on the heating surface" Bull. JSME, 8:660 (1965).

[48] Tong, L.S. et al "A photographic study of subcooled boiling flow and DNB of Freon-113 in a vertical channel" ASME paper 66-WA/HT-39 (1966).

[49] van der Molen, S.B. & Galjee, F.W.B.M. "The boiling mechanism during burnout phenomena in subcooled two-phase water flows" Paper FB-19, VI Int. Heat Transfer Conf. Toronto, Canada, 1:381 (1978).

[50] Lee, D.H. "An experimental investigation of forced convection burnout in high pressure water. Part III: Long tubes with uniform and non-uniform axial heating" UKAEA, Report AEEW-R 355 (1965).

[51] Barnett, P.G. "An investigation into the validity of certain hypotheses implied by various burnout correlations" UKAEA, Report AEEW-R 214 (1963).

[52] Bergles, A.E. "Subcooled burnout in tubes of small diameter" ASME paper 63-WA-182 (1963).

[53] Griffith, P. "Correlation of nucleate boiling burnout data" ASME paper 57-HT-21 (1957).

[54] Aladyev, I.T., et al "Boiling crisis in tubes" Int. Developments in heat transfer, ASME, paper 28 (1961).

[55] Tippets, F.E. "Critical heat flux and flow pattern characteristics of high pressure boiling water in forced convection" Trans. ASME, J. Heat Transfer 86:12 (1964).

[56] Vliet. G.C. & Leppert, G. "Critical heat flux for nearly saturated water flowing normal to a cylinder" Trans. ASME, J. Heat Transfer, 86: 59 (1964).

[57] Hewitt, G.F. et al "Burnout and film flow in the evaporation of water in tubes" Proc. Inst. Mech. Engrs. (London) 180: Part 3C: 206 (1965-66).

[58] Gambill, W.R. "Generalized prediction of burnout heat flux for flowing subcooled, wetting liquids" AIChE preprint 17, 5th Nat. Heat Transf. Conf.; Houston, U.S.A. (1962).

[59] Tong, L.S., et al "New correlations predict DNB conditions" Nucleonics, 21:43 (1963)

[60] Kirby, D.B. & Westwater, J.W. "Bubble and vapour behaviour on a heated horizontal plate during pool boiling near burnout" Chem. Eng. Prog. Symp. Ser. 61(57):238 (1965).

[61] Holman, J.P. "Heat Transfer" McGraw-Hill Book Co., 3rd Edition. Kogakusha Company Ltd., Tokyo (1972).

[62] Eddington, R.I. "Comparison between gas and vapour bubble nucleation at a heater surface" D.Phil. Thesis, Oxford University (1978).

[63] James, D.D. et al "Forced convection heat transfer in asymmetrically heated ducts of rectangular cross-section" Proc. 3rd. Int. Heat Transfer Conference; Vol. I. pp 85 (1966)

[64] Sieder, E.N. & Tate, G.E. "Heat transfer and pressure drop of liquids in tubes" Indust.and Eng. Chem., 28(12):1429 (1936).

[65] Dittus, F.W. and Boelter, L.M.K. "Heat transfer in automobile radiators of the tubular type" Univ. of Calif., Publications in Engineering, 2:443 (1930).

[66] Colburn, A.P. "A method of correlating forced convection heat transfer data and a comparison with fluid friction" Trans. AIChE, 29:174 (1933).

[67] Kenning, D.B.R. and Kao, Y.S. "Convective heat transfer to water containing bubbles: enhancement not dependent on thermo-capillarity" Int. J. Heat & Mass Transfer, 15:1709 (1972).

[68] Bergles, A.E. and Rohsenow, W.M. "The determination of forced-convection surface-boiling heat transfer" Trans. ASME, J. of Heat Transfer, 86: 365 (1964).

[69] Grigoriev, V.A. et al, Trudy, M.E.I. (Trudy-Moskovskogo Energetichescogo Instituta) Series 198, pp. 3 (1974). (In Russian).

[70] Corty, C. and Foust, A.S. "Surface variables in nucleate boiling" Chem. Eng. Prog. Symp. Series 51(17):1 (1955).

[71] Kurihara, H.M. & Myers, J.E. "The effect of superheat and surface roughness on boiling coefficients" AIChE Journal, 6:83 (1960).

[72] Marto, P.J. & Rohsenow, W.M. "Effects of surface conditions on nucleate pool boiling of sodium" Trans. ASME, J.Heat Transfer, 88(2):196 (1966).

[73] Eddington, R.I. & Kenning, D.B.R. "The prediction of flow boiling bubble populations from gas bubble nucleation experiments", Proceedings VI Int. Heat Transfer Conf., Toronto,Canada (August 1978).

[74] Bernath, L. "A theory of local-boiling burnout and its application to existing data" Chem. Eng. Prog. Symposium Series 56(30):95(1960).

[75] Grigoriev, V.A. et al, Trudy M.E.I.(Trudy-Moskovskogo Energetichescogo Instituta), Series 268, pp. 53 (1975). (In Russian).

[76] Judd, R.L. & Merte, H. Jr. "Evaluation of nucleate boiling heat flux predictions at varying levels of subcooling and acceleration", Int. J. of Heat and Mass Transfer, 15:1075 (1972).

[77] Tolubinsky, V.I. & Kostanchuk, D.M. "Vapour bubbles growth rate and heat transfer intensity at subcooled water boiling", Paper B2.8, IV Int. Heat Transfer Conf., Vol. V, Paris (1970).

[78] Gaertner, R.F. & Westwater, J.W. "Population of active sites in nucleate boiling heat transfer", Chem. Eng. Prog. Symp. Series, 56(30:39 (1960).

[79] Sultan, M. & Judd, R.L. "Spatial distribution of active sites and bubble flux density" Trans. ASME, J. Heat Transfer 100(1):56 (1978).

[80] Freund, J.E. "Modern Elementary Statistics", 3rd Edition, Prentice Hall Inc., New Jersey (1967).

[81] Kreyzig, E. "Advanced Engineering Mathematics", 3rd Edition, John Wiley and Sons,Inc., New York (1972).

[82] Heading, J. "Mathematical methods in Science and Engineering", 2nd Edition, Edward Arnold Ltd., London (1971).

[83] von Ceumern, W. C. Chapter 3 in "Heat Transfer in Boiling" edited by Hahne, E. & Grigull, U. Academic Press, New York (1977).

[84] Gaertner, R.F. "Distribution of active sites in the nucleate boiling of liquids" Chem. Eng. Prog. Symp. Series 59(41):52 (1963).

[85] Kenning, D.B.R. Private communication, Dept. of Eng. Science, University of Oxford, (October 1978).

[86] Bergles, A.E. et al, "Critical heat flux and flow pattern observations for low-pressure water boiling in tubes" Trans. ASME, J. Heat Transfer 89:69 (1967).

[87] Gaertner, R.F. "Photographic study of nucleate pool boiling on a horizontal surface". Trans. ASME, J. Heat Transfer 87:17 (1965).

[88] Tachibana, F. et al, "Non-hydrodynamic aspects of pool boiling burnout" J. Nucl. Sci. & Technol. 4:121 (1967).

[89] Guglielmini, G. & Nannei, E. "On the effect of heating wall thickness on pool boiling burnout" Int. J. of Heat & Mass Transfer, 19:1073 (1976).

[90] Carslaw, H.S. and Jaeger, J.C. "Conduction of heat in solids", 2nd edition, Oxford University Press, Oxford (1973).

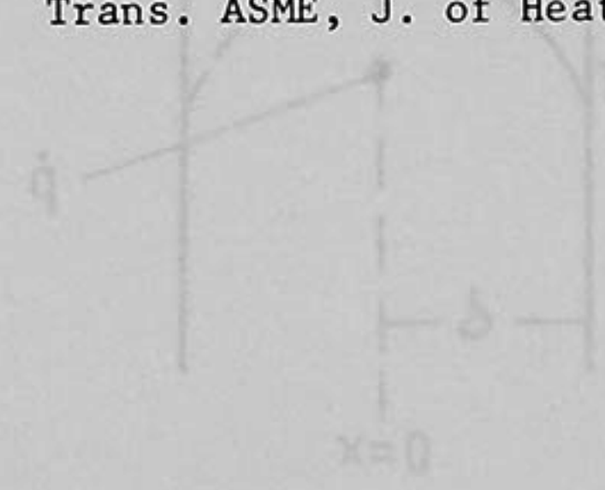
[91] Knoebel, D.H. et al "Forced-convection subcooled critical heat flux. D_2O and H_2O coolant with aluminum and stainless steel heaters". USAEC Report DP-1306, E.I. Du Pont de Nemours and Co. (Feb. 1973).

[92] Kenning, D.B.R. Chapters 7 and 8 in "Two-phase flow and heat transfer" edited by Butterworth, D. and Hewitt, G.F. Oxford University Press (1977).

[93] Henry, R.E. "A correlation for the minimum film boiling temperature". AIChE, Symp. Ser. 70(138):81 (1974).

[94] Gottfried, B.S.; Lee, C.J. & Bell, K.J. "The Leidenfrost phenomena: film boiling and liquid droplets on a flat plate", Int. J. Heat & Mass Transfer, 9:1167 (1966).

[95] Hsu, Y.Y. "On the size range of active nucleation cavities on a heating surface". Trans. ASME, J. of Heat Transfer 84:207 (1962).

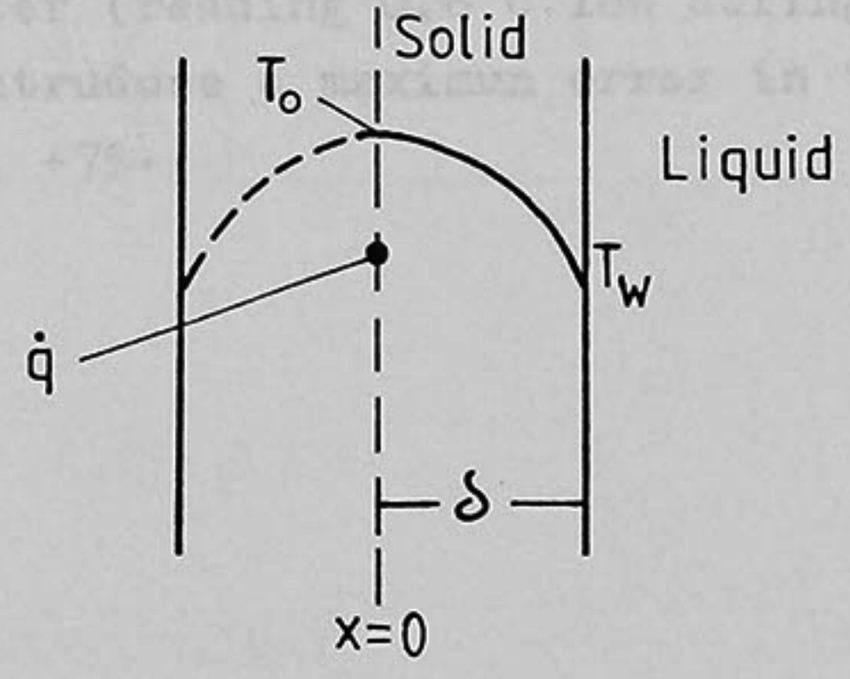


APPENDIX A

Temperature Drop Across the Test Section Wall

The correction for the temperature drop across the test section wall is formulated as the steady-state one-dimensional heat conduction equation for a heater of thickness 2δ with uniform internal heat generation rate $\dot{q}$ and both sides at wall temperature T_w. Assuming no heat losses through the back of the test section and constant thermal conductivity of the solid, the temperature T_o at the midplane of such a heater is given by Holman[61] as:

$$T_o - T_w = \frac{\dot{q}\delta^2}{2k_s} \qquad \text{(A-1)}$$



where

T_o = temperature at the back of the test section (measured temperature)

T_w = surface wall temperature.

k_s = thermal conductivity of solid heater.

δ = heater wall thickness.

$\dot{q}$ = internal heat generation rate per unit of volume (W/m^3)

APPENDIX B

Estimates of Experimental Errors

The heat fluxes during the present tests were calculated on the basis of the power input to the test section from voltage and current determinations which could be measured very accurately by the Fenlow 501 Digital Voltmeter. However, it is estimated that the uncertainty of ± 1.7% in the heat transfer area produces a maximun error of ±2% in the heat flux.

The wall superheat was calculated from the wall temperature measured by thermocouples calibrated to ±0.1°C. When corrected by the temperature drop across the wall (see appendix A), the uncertainty of ±5% in the thermal conductivity of the stainless steel and the further potential error in the platinum resistance thermometer (reading 0.6°C low during calibration) reported in [62], intruduce a maximun error in the calculated wall superheats of -8%, +7%.

APPENDIX C

Effective Cavity Radii as a Function of ΔP^*

T_w (°C)	ΔT_{sat} (°C)	P_s (bar)	ΔP (bar)	ΔP ($\times 10^{-3}$ N/m^2)	σ ($\times 10^{3}$ N/m)	r_e (μm)
100	0	1.013	0	0	58.8	∞
105	5	1.21	0.19	18.7	57.8	6.18
108	8	1.34	0.33	32.7	57.2	3.50
110	10	1.43	0.42	42.0	56.8	2.71
113	13	1.57	0.56	55.7	56.2	2.02
115	15	1.68	0.67	66.7	55.8	1.67
118	18	1.85	0.84	83.7	55.2	1.32
120	20	1.98	0.97	97.2	54.8	1.13
123	23	2.16	1.15	114.7	54.2	0.95
125	25	2.30	1.29	128.7	53.8	0.84
128	28	2.52	1.51	150.7	53.2	0.71
130	30	2.70	1.69	168.8	52.8	0.63
133	33	2.92	1.91	190.7	52.2	0.55
135	35	3.10	2.09	208.7	51.8	0.50
138	38	3.40	2.39	238.7	51.2	0.43
140	40	3.61	2.60	260.1	50.8	0.39

$$r_e = \frac{2\sigma}{\Delta P}; \quad \text{(eq.(3-7))}$$

r_e = effective cavity radius,
σ = surface tension at T_w,
P_s = saturation pressure at T_w,
P = system pressure = 1.013 bar, (or final pressure),
$\Delta P = P_s - P$.

* Property values taken from ref. [1]

APPENDIX D

Observed Flow Patterns in the High-Speed Cine Films

Run/Film	δ (mm)	G (Kg/m^2sec)	$\Delta T_{sub_{in}}$ (°K)	ϕ (MW/m^2)	%CHF	X_e (%)	Flow Pattern*
1-90	0.08	800	80	3.15	90	- 9.6	B
10-90	0.13	800	80	4.50	90	- 7.4	B
19-90	0.20	800	80	4.95	90	- 6.6	B
3-90	0.08	800	20	1.44	90	- 1.3	TBS
12-90	0.13	800	20	1.98	90	- 0.4	S
21-30	0.20	800	20	0.69	30	- 2.6	B
21-60	0.20	800	20	1.38	60	- 1.4	TBS
21-90	0.20	800	20	2.07	90	- 0.3	S
4-70	0.08	1700	80	3.44	70	-12.2	B
4-80	0.08	1700	80	3.94	80	-11.8	B
4-90	0.08	1700	80	4.43	90	-11.4	B
4-95	0.08	1700	80	4.67	95	-11.2	B
13-70	0.13	1700	80	4.62	70	-11.2	B
13-80	0.13	1700	80	5.28	80	-10.7	B
13-90	0.13	1700	80	5.94	90	-10.2	B
13-95	0.13	1700	80	6.27	95	-10.0	B
22-90	0.20	1700	80	6.39	90	- 9.9	B
23-70	0.20	1700	50	3.72	70	- 6.4	B
6-70	0.08	1700	20	1.47	70	- 2.6	B
6-80	0.08	1700	20	1.68	80	- 2.4	B
6-90	0.08	1700	20	1.89	90	- 2.3	B
6-95	0.08	1700	20	2.00	95	- 2.2	B
15-70	0.13	1700	20	1.89	70	- 2.3	B
15-80	0.13	1700	20	2.16	80	- 2.0	TBS
15-90	0.13	1700	20	2.43	90	- 1.8	S
15-95	0.13	1700	20	2.57	95	- 1.7	S
24-90	0.20	1700	20	2.70	90	- 1.6	S
7-90	0.08	2000	80	4.95	90	-11.6	B
16-90	0.13	2000	80	6.48	90	-10.5	B
25-90	0.20	2000	80	7.20	90	-10.1	B
9-90	0.08	2000	20	2.25	90	- 2.2	S
18-90	0.13	2000	20	2.70	90	- 1.9	S
27-90	0.20	2000	20	3.24	90	- 1.6	S

* B= Bubbly flow
TBS= Transition from bubbly to slug flow.
S= Slug flow.

APPENDIX E

Critical Heat Flux Data

Water/Stainless steel

System pressure: atmospheric

Geometry: a rectangular channel with one side uniformily heated;
D_H = 7mm

Strips heated dimensions: 150mm x 10mm

Flow direction: vertical upflow.

Run/Test	δ (mm)	v (m/sec)	$\Delta T_{sub_{in}}$ (°K)	ΔT_{sat} (°K)	L_B (mm)	Type of Failure	ϕ_c (MW/m^2)
1-1	0.08	0.8	80.3	30.8	50	b	3.63
1-2	0.08	0.8	79.6	-	53	b	3.35
1-3	0.08	0.8	80.1	30.2	31	d	3.51
2-4	0.08	0.8	50.3	30.2	3	b	2.96
2-5	0.08	0.8	50.3	-	3	c	2.92
2-6	0.08	0.8	50.0	29.9	1	b	2.87
3-7	0.08	0.8	19.8	28.5	16	c	1.62
3-8	0.08	0.8	21.1	-	6	c	1.59
3-9	0.08	0.8	20.2	28.8	2	b	1.57
4-10	0.08	1.7	80.1	31.0	54	b	4.95
4-11	0.08	1.7	79.6	-	31	b	4.89
5-12	0.08	1.7	49.6	30.9	32	a	3.84
5-13	0.08	1.7	48.6	-	55	a	3.79
5-14	0.08	1.7	49.8	30.4	29	b	3.77
6-15	0.08	1.7	20.2	27.5	54	c	2.17
6-16	0.08	1.7	20.0	27.8	37	d	2.08
7-17	0.08	2.0	79.6	31.9	2	a	5.48
7-18	0.08	2.0	79.8	31.6	1	a	5.52
7-19	0.08	2.0	80.1	32.1	2	a	5.61
8-20	0.08	2.0	49.8	31.9	1	a	4.52
8-21	0.08	2.0	50.3	32.4	46	a	4.61
8-22	0.08	2.0	49.8	31.6	31	d	4.48
9-23	0.08	2.0	20.2	28.0	15	a	2.49
9-24	0.08	2.0	20.0	28.4	9	c	2.38
9-25	0.08	2.0	19.5	28.7	14	d	2.61
10-26	0.13	0.8	79.8	30.0	19	b	5.20
10-27	0.13	0.8	78.1	-	13	b	4.88
11-28	0.13	0.8	50.3	28.4	10	c	3.92
11-29	0.13	0.8	48.2	-	5	b	3.75
12-30	0.13	0.8	19.5	26.0	34	d	2.10
12-31	0.13	0.8	19.5	-	47	d	2.25
13-32	0.13	1.7	79.8	31.1	2	b	6.55
13-33	0.13	1.7	79.6	-	10	b	6.60
13-34	0.13	1.7	80.1	30.8	2	b	6.66
14-35	0.13	1.7	49.6	29.5	2	b	4.83
14-36	0.13	1.7	49.8	-	3	b	4.94

APPENDIX E (continued)

Run/Test	δ (mm)	v (m/sec)	$\Delta T_{sub_{in}}$ (°K)	ΔT_{sat} (°K)	L_B (mm)	Type of failure	ϕ_c (MW/m^2)
15-37	0.13	1.7	19.8	27.4	7	c	2.55
15-38	0.13	1.7	20.4	-	11	c	2.77
16-39	0.13	2.0	79.8	33.9	1	a	7.31
16-40	0.13	2.0	80.3	34.2	1	a	7.16
16-41	0.13	2.0	80.1	33.6	2	b	7.20
16-42	0.13	2.0	79.8	33.5	1	a	6.98
17-43	0.13	2.0	50.0	33.8	2	b	5.52
17-44	0.13	2.0	49.8	32.9	2	a	5.36
18-45	0.13	2.0	19.8	27.6	6	c	3.02
18-46	0.13	2.0	20.4	27.1	2	b	2.97
18-47	0.13	2.0	20.0	27.8	1	b	3.11
19-48	0.20	0.8	79.8	29.0	5	b	5.55
19-49	0.20	0.8	79.8	-	31	d	5.37
19-50	0.20	0.8	80.1	29.3	2	b	5.46
20-51	0.20	0.8	50.3	26.7	1	c	4.04
20-52	0.20	0.8	49.3	-	1	c	3.97
21-53	0.20	0.8	20.0	25.7	12	c	2.38
21-54	0.20	0.8	21.8	-	43	c	2.20
22-55	0.20	1.7	79.6	32.0	1	b	7.13
22-56	0.20	1.7	79.6	-	1	b	7.01
22-57	0.20	1.7	80.8	-	1	b	7.21
23-58	0.20	1.7	50.3	28.8	1	b	5.41
23-59	0.20	1.7	50.0	-	7	d	5.54
24-60	0.20	1.7	20.2	26.6	37	d	2.92
24-61	0.20	1.7	22.0	-	65	d	3.04
25-62	0.20	2.0	79.8	33.8	1	b	7.95
25-63	0.20	2.0	80.1	34.2	1	b	8.04
26-64	0.20	2.0	49.3	32.7	2	b	6.17
26-65	0.20	2.0	50.0	31.9	3	b	6.25
26-66	0.20	2.0	50.5	32.5	56	d	6.31
26-67	0.20	2.0	49.8	32.1	1	b	6.14
27-68	0.20	2.0	20.7	27.6	23	d	3.60
27-69	0.20	2.0	20.0	28.0	2	b	3.62
27-70	0.20	2.0	19.8	28.2	5	c	3.55

APPENDIX F

Heat Flow under Bubbles per unit of Time over the Total Surface Area

1. Integration of equations (5-27), (5-32) and (5-34).

(A) Integration of equation (5-27).

$$q_a = 2\pi \int_0^{t_g/c_4} r(t_o) \frac{dr}{dt_o} \left\{ 0.8 \lambda \rho_l \sqrt{\nu_l t_o} + \frac{2 k_l \Delta T}{(\pi \alpha_l)^{1/2}} \left[t_c - 2t_g + t_o (2 + 0.384 P_r) \right]^{1/2} \right\} dt_o \qquad (5\text{-}27)$$

The assumed bubble growth-rate, equation (5-3), is

$$r(t_o) = 2 r_m \left(\frac{t_o}{t_g} \right) - r_m \left(\frac{t_o}{t_g} \right)^2 \qquad (5\text{-}3)$$

and its derivative

$$\frac{dr}{dt_o} = \frac{2 r_m}{t_g} \left(1 - \frac{t_o}{t_g} \right) \qquad (F\text{-}1)$$

Substituting equations (5-3) and (F-1) into equation (5-27) gives

$$q_a = \frac{4\pi r_m^2}{t_g} \int_0^{t_g/c_4} \left[\frac{2t_o}{t_g} - \frac{3t_o^2}{t_g^2} + \frac{t_o^3}{t_g^3} \right] \left\{ 0.8 \lambda \rho_l \sqrt{\nu_l t_o} + \frac{2 k_l \Delta T}{(\pi \alpha_l)^{1/2}} \left[t_c - 2t_g + t_o (2 + 0.384 P_r) \right]^{1/2} \right\} dt_o \qquad (F\text{-}2)$$

Equation (F-2) can be divided into two equations

$$q_a = q_1 + q_2 \qquad (F\text{-}3)$$

where q_1 gives the heat transfer due to the evaporation of the microlayer and q_2 represents the heat flow due to transient conduction. Thus

$$q_1 = \frac{4\pi r_m^2}{t_g} \int_0^{t_g/c_4} \left[\frac{2t_o}{t_g} - \frac{3t_o^2}{t_g^2} + \frac{t_o^3}{t_g^3} \right] \left(0.8 \lambda \rho_l \sqrt{\nu_l t_o} \right) dt_o \qquad (F\text{-}4)$$

Carrying out the integration of equation (F-4) and after some algebraic manipulations q_1 is finally obtained as

$$q_1 = \frac{2\xi\sqrt{t_g}}{315\, C_4^{9/2}}\left[126\,C_4^2 - 135\,C_4 + 35\right] \qquad (F\text{-}5)$$

where

$$C_4 = 1 + 0.192\,P_r + 0.16\,\frac{P_r\,\lambda}{c_{p_l}\,\Delta T_{sat}} \qquad (5\text{-}22)$$

$$\xi = 3.2\pi\, r_m^2\, \nu_l^{1/2}\, \lambda\, \rho_l \qquad (5\text{-}44)$$

q_2 is expressed as

$$q_2 = \frac{4\pi r_m^2}{t_g}\int_0^{t_g/C_4}\left(\frac{2t_o}{t_g} - \frac{3t_o^2}{t_g^2} + \frac{t_o^3}{t_g^3}\right)\left\{\frac{2k_l\Delta T}{\sqrt{\alpha_l \pi}}\left[t_c - 2t_g + t_o(2 + 0.384\,P_r)\right]^{1/2}\right\} dt_o \qquad (F\text{-}6)$$

Substituting:

$$t_w = t_c - 2t_g \qquad (F\text{-}7)$$

$$C_5 = 2 + 0.384\ Pr \qquad (F\text{-}8)$$

and

$$\gamma = \frac{8k_l\Delta T\sqrt{\pi}\, r_m^2}{t_g\sqrt{\alpha_l}} \qquad (5\text{-}45)$$

into equation (F-6) and separating terms yields

$$q_2 = \frac{2\gamma}{t_g}\int_0^{t_g/C_4} t_o\,(C_5 t_o + t_w)^{1/2}\, dt_o - \frac{3\gamma}{t_g^2}\int_0^{t_g/C_4} t^2\,(C_5 t_o + t_w)^{1/2}\, dt_o$$
$$+ \frac{\gamma}{t_g^3}\int_0^{t_g/C_4} t_o^3\,(C_5 t_o + t_w)^{1/2}\, dt_o \qquad (F\text{-}9)$$

Equation (F-9) can alternatively be expressed as

$$q_2 = q_{21} + q_{22} + q_{23} \qquad (F\text{-}10)$$

where

$$q_{21} = \frac{2\gamma}{t_g} \int_0^{t_g/c_4} t_o \left(c_5 t_o + t_w\right)^{1/2} dt_o \qquad \text{(F-11)}$$

Integration of equation (F-11) gives

$$q_{21} = \frac{4\gamma}{15 t_g c_5} \left[\left(3 \frac{t_g}{c_4} c_5 - 2t_w\right) c_6^{3/2} + 2t_w^{5/2} \right] \qquad \text{(F-12)}$$

where

$$c_6 = t_g(c_5/c_4) + t_w \qquad \text{(F-13)}$$

$$q_{22} = \frac{-3\gamma}{t_g^2} \int_0^{t_g/c_4} t_o^2 \left(c_5 t_o + t_w\right)^{1/2} dt_o \qquad \text{(F-14)}$$

Integration of equation (F-14) gives

$$q_{22} = \frac{2\gamma}{35 c_5^3 t_g^2} \left\{ 8t_w^{7/2} - \left[15c_5^2 \left(\frac{t_g}{c_4}\right)^2 - 12 c_5 t_w \left(\frac{t_g}{c_4}\right) + 8t_w^2 \right] c_6 \right\} \qquad \text{(F-15)}$$

From equation (F-9), the remaining term, q_{23}, is then given by

$$q_{23} = \frac{\gamma}{t_g^3} \int_0^{t_g/c_4} t_o^3 \left(c_5 t_o + t_w\right)^{1/2} dt_o \qquad \text{(F-16)}$$

Integrating equation (F-16) yields

$$q_{23} = \frac{2\gamma}{315 c_5^4 t_g^3} \left\{ c_6^{3/2} \left[35 c_5^3 \left(\frac{t_g}{c_4}\right)^3 - 30 c_5^2 \left(\frac{t_g}{c_4}\right)^2 t_w + 24 c_5 \left(\frac{t_g}{c_4}\right) t_w^2 - 16 t_w^3 \right] + 16 t_w^{9/2} \right\} \qquad \text{(F-17)}$$

q_a is then finally given as

$$q_a = q_1 + q_{21} + q_{22} + q_{23} \qquad \text{(F-18)}$$

where q_1, q_{21}, q_{22} and q_{23} are given by equations (F-5), (F-12), (F-15) and (F-17) respectively.

(B) Integration of equation (5-32).

$$q_b = 2\pi \int_{t_g/C_4}^{t_g/W} r(t_o) \frac{dr}{dt_o} \left\{ \lambda \rho_l (\delta_o' - \delta') + \frac{2 k_l \Delta T}{\sqrt{\pi \alpha_l}} \left[t_w + t_o C_5 \right]^{1/2} \right\} dt_o \qquad (5\text{-}32)$$

where the fist term accounts for the partial evaporation of the microlayer and the second term represents the transient conduction contribution.

The term $\lambda \rho_l (\delta_o' - \delta')$ is given as

$$\lambda \rho_l (\delta_o' - \delta') = \lambda \rho_l \left\{ \delta_o' - \delta_o' \left(1 - \frac{t_2}{t_e} \right)^{1/2} \right\} \qquad (F\text{-}19)$$

where

$$\delta_o' = 0.8 \sqrt{\nu_l t_o} \qquad (5\text{-}5)$$

$$t_2 = 2\, t_g - t_o\, C_5 \qquad (5\text{-}13)$$

$$t_e = 0.32 \, \frac{Pr \;\; \lambda}{C_{p_l} \;\; \Delta T_{sat}} \, t_o \qquad (5\text{-}19)$$

$$\delta' = \delta_o' \left(1 - \frac{t_2}{t_e} \right)^{1/2} \qquad (5\text{-}31)$$

Equation (5-19) can be expressed as

$$t_e = E\, t_o \qquad (F\text{-}20)$$

where

$$E = 0.32 \, \frac{Pr \, \lambda}{C_{p_l} \Delta T_{sat}} \qquad (5\text{-}46)$$

Substituting equations (5-5), (5-13) and (F-20) into equation (F-19) gives

$$\lambda \rho_l (\delta_o' - \delta') = \lambda \rho_l \left\{ 0.8 \sqrt{\nu_l t_o} \left[1 - \left(1 - \frac{2 t_g - t_o C_5}{E t_o} \right)^{1/2} \right] \right\} \qquad (F\text{-}21)$$

Equation (F-21) can be rearranged to give

$$\lambda \rho_l (\delta_o' - \delta') = 0.8 \lambda \rho_l \nu_l^{1/2} \left\{ t_o^{1/2} - \frac{1}{E^{1/2}} \left[t_o (E + C_5) - 2 t_g \right]^{1/2} \right\} \qquad (F\text{-}22)$$

Substitution of equations (5-3), (F-1) and (F-22) into equation (5-32), q_b becomes

$$q_b = \frac{\xi}{t_g}\int_{t_g/C_4}^{t_g/w}\left(\frac{2t_o}{t_g}-\frac{3t_o^2}{t_g^2}+\frac{t_o^3}{t_g^3}\right)\left\{t_o^{1/2}-\frac{1}{E^{1/2}}\left[t_o(E+C_5)-2t_g\right]^{1/2}\right\}dt_o$$

$$+\gamma\int_{t_g/C_4}^{t_g/w}\left(\frac{2t_o}{t_g}-\frac{3t_o^2}{t_g^2}+\frac{t_o^3}{t_g^3}\right)\left[C_5t_o+t_w\right]^{1/2}dt_o \qquad (F-23)$$

Following a similar procedure as in section (A) above,

$$q_b = q_3 + q_4 \qquad (F-24)$$

where q_3 is given as

$$q_3 = \frac{2\xi}{t_g^2}\int_{t_g/C_4}^{t_g/w} t_o^{3/2}\,dt_o - \frac{3\xi}{t_g^3}\int_{t_g/C_4}^{t_g/w} t_o^{5/2}\,dt_o + \frac{\xi}{t_g^4}\int_{t_g/C_4}^{t_g/w} t_o^{7/2}\,dt_o$$

$$-\frac{2\xi}{t_g^2E^{1/2}}\int_{t_g/C_4}^{t_g/w} t_o\left[t_o(E+C_5)-2t_g\right]^{1/2}dt_o+\frac{3\xi}{t_g^2E^{1/2}}\int_{t_g/C_4}^{t_g/w} t_o^2\left[t_o(E+C_5)-2t_g\right]^{1/2}dt_o$$

$$-\frac{\xi}{t_g^4E^{1/2}}\int_{t_g/C_4}^{t_g/w} t_o^3\left[t_o(E+C_5)-2t_g\right]^{1/2}dt_o \qquad (F-25)$$

Equation (F-25) can be expressed as

$$q_3 = q_{31} + q_{32} \qquad (F-26)$$

q_{31} is given by

$$q_{31} = \frac{2\xi}{t_g^2}\int_{t_g/C_4}^{t_g/w} t_o^{3/2}\,dt_o - \frac{3\xi}{t_g^3}\int_{t_g/C_4}^{t_g/w} t_o^{5/2}\,dt_o + \frac{\xi}{t_g^4}\int_{t_g/C_4}^{t_g/w} t_o^{7/2}\,dt_o \qquad (F-27)$$

Integration of equation (F-27) yields

$$q_{31} = \frac{2\xi\sqrt{t_g}}{315\,w^{9/2}}\left(126w^2-135w+35\right) - \frac{2\xi\sqrt{t_g}}{315\,C_4^{9/2}}\left(126C_4^2-135C_4+35\right) \qquad (F-28)$$

It follows from equation (F-26) that

$$q_{32} = \frac{-2\xi}{t_g^2E^{1/2}}\int_{t_g/C_4}^{t_g/w} t_o\left[t_o(E+C_5)-2t_g\right]^{1/2}dt_o+\frac{3\xi}{t_g^3E^{1/2}}\int_{t_g/C_4}^{t_g/w} t_o^2\left[t_o(E+C_5)-2t_g\right]^{1/2}dt_o$$

$$-\frac{\xi}{t_g^2E^{1/2}}\int_{t_g/C_4}^{t_g/w} t_o^3\left[t_o(E+C_5)-2t_g\right]^{1/2}dt_o \qquad (F-29)$$

Integration of equation (F-29) after some algebraic manipulations reduces to give

$$q_{32} = \frac{-2\xi E\sqrt{t_g}}{315 W^{3/2}(E+2W)^4}\left\{\left(\frac{E}{W}\right)^3(126W^2-135W+35)+6\left(\frac{E}{W}\right)^2(154W^2-171W+45)\right.$$

$$\left.+84\left(\frac{E}{W}\right)(26W^2-33W+9)+840(2W^2-3W+1)\right\} \qquad (5-43)$$

From equation (F-23), q_4 is expressed as

$$q_4 = \gamma\int_{t_g/c_4}^{t_g/w}\left(\frac{2t_o}{t_g}-\frac{3t_o^2}{t_g^2}+\frac{t_o^3}{t_g^3}\right)\left[t_o c_5 + t_w\right]^{1/2} dt_o \qquad (F-30)$$

Separating terms in equation (F-30), it takes the form

$$q_4 = q_{41} + q_{42} + q_{43} \qquad (F-31)$$

where

$$q_{41} = \frac{2\gamma}{t_g}\int_{t_g/c_4}^{t_g/w} t_o\left(t_o c_5 + t_w\right)^{1/2} dt_o \qquad (F-32)$$

$$q_{42} = -\frac{3\gamma}{t_g^2}\int_{t_g/c_4}^{t_g/w} t_o^2\left(t_o c_5 + t_w\right)^{1/2} dt_o \qquad (F-33)$$

$$q_{43} = \frac{\gamma}{t_g^3}\int_{t_g/c_4}^{t_g/w} t_o^3\left(t_o c_5 + t_w\right)^{1/2} dt_o \qquad (F-34)$$

Integration of equations (F-32), (F-33) and (F-34) gives respectively

$$q_{41} = \frac{\gamma}{15W^2 t_g}\left\{2(3t_g - t_w)t_c^{3/2} - \left[3\left(\frac{c_5}{c_4}\right)t_g - 2t_w\right]c_6^{3/2}\right\} \qquad (F-35)$$

$$q_{42} = \frac{\gamma}{140 W^3 t_g^2}\left\{\left[15t_g^2\left(\frac{c_5}{c_4}\right)^2 - 12\left(\frac{c_5}{c_4}\right)t_g t_w + 8t_w^2\right]c_6^{3/2}\right.$$

$$\left.-4\left[15t_g^2 - 6t_g t_w + 2t_w^2\right]t_c^{3/2}\right\} \qquad (F-36)$$

$$q_{43} = \frac{\gamma}{2530\, w^4 t_g^3} \left\{ 8 t_c^{3/2} \left[35 t_g^3 - 15 t_g^2 t_w + 6 t_g t_w^2 - 3 t_w^3 \right] \right.$$

$$\left. - \left[35 \left(\frac{c_5}{c_4} \right)^3 t_g^3 - 30 \left(\frac{c_5}{c_4} \right)^2 t_g^2 t_w + 24 \left(\frac{c_5}{c_4} \right) t_g t_w^2 - 16 t_w^3 \right] c_6^{3/2} \right\} \quad \text{(F-37)}$$

q_b is then given as

$$q_b = q_{31} + q_{32} + q_{41} + q_{42} + q_{43} \quad \text{(F-38)}$$

where q_{31}, q_{32}, q_{41}, q_{42} and q_{43} are given by equations (F-28), (5-43), (F-35), (F-36) and (F-37) respectively.

(C) Integration of equation (5-34).

$$q_c = 2\pi \int_{t_g/w}^{t_g} r(t_o) \frac{dr}{dt_o} \left[\frac{2 k_l \Delta T}{\sqrt{\pi \alpha_l}} t_c^{1/2} \right] dt_o \quad \text{(5-34)}$$

Substitution of equations (5-3) and (F-1) into equation (5-34) yields

$$q_c = \gamma \sqrt{t_c} \int_{t_g/w}^{t_g} \left(\frac{2t_o}{t_g} - \frac{3t_o^2}{t_g^2} + \frac{t_o^3}{t_g^3} \right) dt_o \quad \text{(F-39)}$$

carrying out the integration of equation (5-39) gives

$$q_c = q_5 = \frac{\gamma \sqrt{t_c}\, t_g}{4 w^4} \left(w^4 - 2w^2 + 4w - 1 \right) \quad \text{(5-40)}$$

2. Addition of the solutions to equations (5-27), (5-32) and (5-34).

The addition of equations (F-18), (F-38) and (F-40) will give the heat flow from the wall under the bubbles. Carrying out the addition and clearing the terms yields

$$q_{UB} = q_5 + q_6 + q_7 + q_{32} \quad \text{(F-40)}$$

where q_5 and q_{32} are given by equations (5-40) and (5-43) respectively, whereas q_6 and q_7 are expressed as

$$q_6 = \frac{\gamma}{315 t_g^3 W^4} \left\{ t_c^{3/2} \left[t_g^3 (126W^2 - 135W + 35) - 3 t_g^2 t_w (14W^2 - 18W + 5) \right.\right.$$

$$\left.\left. - 6 t_g t_w^2 (3W - 1) - 2 t_w^3 \right] + 2 t_w^{5/2} \left[21 t_g^2 W^2 + 9 t_g W t_w + t_w^2 \right] \right\} \quad (5\text{-}41)$$

$$q_7 = \frac{2\xi\sqrt{t_g}}{315 W^{9/2}} (126W^2 - 135W + 35) \quad (5\text{-}42)$$

The heat flow under the bubbles per unit of time over the total surface area is finally obtained as

$$\phi_{UB} = [(q_5 + q_6) + (q_7 + q_{32})] n_s f \quad (5\text{-}39)$$

APPENDIX G

Prediction of the ratio x of actual boiling area to nominal boiling area for an assumed random distribution of nucleation sites.

It is imagined a large area A partly covered by N discs, each of area b, placed randomly over A.

$$\left.\begin{aligned} &\frac{b}{A} = Z << 1 \\ 1 \geq\ &\frac{Nb}{A} = NZ \geq 0 \\ &\text{and } A \longrightarrow \infty \end{aligned}\right\} \qquad (G\text{-}1)$$

the fraction of the area A covered by discs β_a, can be derived as follows:

For n=1, n denoting the number of discs, the fraction of surface covered is

$$\frac{b}{A} = Z \qquad (G\text{-}2)$$

and the fraction of surface uncovered is

$$\frac{A-b}{A} = 1-Z = y_1 \qquad (G\text{-}3)$$

For n=2, i.e. placing another site assuming that a fraction of area of the new disc is overlapped with the previous one, the newly covered surface is by_1,
and the fraction of surface covered is now

$$\frac{by_1}{A} = Zy_1 \qquad (G\text{-}4)$$

thus the total fraction of covered area is

$$\text{Eq.}(G\text{-}3) + \text{Eq.}(G\text{-}4) = Z+Zy_1 = Z(1+y_1) = 1-y_2 \qquad (G\text{-}5)$$

For n=3,

newly covered surface = by_2

so the fraction of newly covered surface is

$$\frac{by_2}{A} = Zy_2 \qquad (G-6)$$

hence the total fraction of covered surface is

$$= Z+Zy_1+Zy_2 = Z(1+y_1+y_2) = 1-y_3 \qquad (G-7)$$

Similarly, for

n=N-1 the total fraction of covered surface is

$$=Z+Zy_1 + Zy_2 + \ldots + y_{N-2} = Z(1+y_1+y_2+\ldots+y_{N-2}) = 1-y_{N-1} \qquad (G-8)$$

at n=N such fraction is

$$=Z(1+y_1 + y_2 +\ldots+y_{N-1}) = 1-y_N \qquad (G-9)$$

From eqs. (G-8) and (G-9)

$$1-y_{N-1} + Zy_{N-1} = 1-y_N$$

so

$$y_N = y_{N-1}\,(1-Z) \qquad (G-10)$$

From eq. (G-10),

$$\left.\begin{aligned} y_2 &= y_1\,(1-Z) \\ y_3 &= y_2\,(1-Z) = y_1\,(1-Z)(1-Z) = y_1\,(1-Z)^2 \\ y_4 &= y_3\,(1-Z) = y_1\,(1-Z)^3, \text{ etc.} \end{aligned}\right\} \qquad (G-11)$$

Substituting (G-11) into eq. (G-9), the total fraction of surface covered when N discs are placed is

$$\beta_a = 1-y_N = Z\left\{1+y_1 + y_1(1-Z) + y_1(1-Z)^2+\ldots+y_1(1-Z)^{N-2}\right\} \qquad (G-12)$$

Rearranging eq. (G-12) yields

$$\beta_a = 1-y_N = Z\left\{1+y_1\left[1+(1-Z) + (1-Z)^2 +\ldots+(1-Z)^{N-2}\right]\right\} \quad (G-13)$$

Substituting eq. (G-3) into eq. (G-13) gives

$$\beta_a = 1-y_N = Z\left\{1+(1-Z)\left[1+(1-Z) + (1-Z)^2+\ldots+ (1-Z)^{N-2}\right]\right\} \quad (G-14)$$

the terms $(1-Z)^m$ can be expanded as

$$(1-Z)^m = 1-mZ + \frac{m(m-1)}{2!} Z^2 - \frac{m(m-1)(m-2)}{3!} Z^3 +\ldots+$$

$$(\pm 1)^r \frac{m(m-1)\ldots(m-r+1)}{r!} + \ldots \quad (G-15)$$

Using the expansion (G-15) and then summing the finite series for the coefficients Z^m, eq. (G-14) becomes

$$\beta_a = 1-y_N = Z\left\{1+(1-Z)(N-1)\left[1- \frac{Z(m-2)}{2!} + \frac{Z^2(m-2)(m-3)}{3!}\right.\right.$$

$$\left.\left. - \frac{Z^3 (m-2)(m-3) (m-4)}{4!} + \ldots\right]\right\} \quad (G-16)$$

For $Z<<1$ and $N>>1$,

$$\beta_a = 1-y_N = ZN\left[1 - \frac{ZN}{2!} + \frac{(ZN)^2}{3!} - \frac{(ZN)^3}{4!} + \ldots\right] \quad (G-17)$$

$\therefore$

$$\beta_a = (1-e^{-ZN}) \quad (G-18)$$

Substituting $\beta = ZN$ into eq. (G-18) gives

$$\left.\begin{aligned} \beta_a &= 1-e^{-\beta} \\ \text{or} \quad x &= (1-e^{-\beta})/\beta \end{aligned}\right\} \quad (5\text{-}55)$$

APPENDIX H

Solution of the One-dimensional Unsteady-state Heat Conduction Equation for a Solid with Internal Heat Generation subjected to Sudden Insulation

One-dimensional heat conduction equation for the slab $0 < X_s < 2\delta$ with internal heat generation rate $\dot{q}$ per unit of volume, constant for $t > 0$ and T_o initial temperature.

The heat conduction equation for the above case is

$$\frac{\partial^2 T}{\partial X_s^2} - \frac{1}{\alpha}\frac{\partial T}{\partial t} = -\frac{\dot{q}}{k} \qquad (H-1)$$

with initial conditions

$$\text{at } t=0 \,,\; T_o = \frac{\dot{q}\delta X_s}{k} - \frac{\dot{q}X_s^2}{2k} + T_w \qquad (H-2)$$

and boundary conditions

$$\frac{dT}{dX_s} = 0 \text{ at } X_s = 0 \text{ and } X_s = 2\delta \,, \text{ for } t > 0 \qquad (H-3)$$

The above partial differential equation, (H-1), can be transformed into an ordinary differential equation by applying the Laplace Transformation method [90] :

$$L_o\left[\frac{\partial^2 T}{\partial x^2}\right] - \frac{1}{\alpha} L_o\left[\frac{\partial T}{\partial t}\right] = -L_o\left[\frac{\dot{q}}{k}\right]$$

where L_o denotes Laplace transformation, yielding

$$\frac{d^2\bar{T}}{dX_s^2} - \frac{p}{\alpha}\bar{T} = -\frac{1}{\alpha}T_o - \frac{\dot{q}}{pk} \qquad (H-4)$$

The general solution to equation (H-4) is

$$\bar{T} = A_1 e^{-\sqrt{\frac{p}{\alpha}}X_s} + A_2 e^{\sqrt{\frac{p}{\alpha}}X_s} + \frac{1}{p}\left(\frac{\dot{q}\delta X_s}{k} - \frac{\dot{q}X_s^2}{2k}\right) + \frac{\alpha\dot{q}}{p^2 k} + \frac{T_w}{p} \qquad (H-5)$$

Differentiation of equation (H-5) gives

$$\frac{d\bar{T}}{dX_s} = -A_1\sqrt{\frac{p}{\alpha}}\, e^{-\sqrt{\frac{p}{\alpha}}X_s} + A_2\sqrt{\frac{p}{\alpha}}\, e^{\sqrt{\frac{p}{\alpha}}X_s} + \frac{\dot{q}}{pk}(\delta - X_s) \qquad (H-6)$$

Solving the subsidiary equation (H-5) with boundary conditions

$$\frac{d\bar{T}}{dX_s} = 0 \text{ at } X_s = 0 \text{ and } X_s = 2\delta \,, \; t > 0$$

and using (H-6) gives the constants A_1 and A_2 as

$$A_1 = \frac{\dot{q}\delta}{pk\sqrt{\frac{p}{\alpha}}}\left[\frac{1}{\left(1-e^{-2\sqrt{\frac{p}{\alpha}}\delta}\right)}\right] \qquad (H-7)$$

$$A_2 = \frac{\dot{q}\delta}{pk\sqrt{\frac{p}{\alpha}}}\left[\frac{1}{\left(1-e^{-2\sqrt{\frac{p}{\alpha}}\delta}\right)} - 1\right] \qquad (H-8)$$

Substituting equations (H-7) and (H-8) into equation (H-5), using the expansion

$$\left(1-e^{-2\sqrt{\frac{p}{\alpha}}\delta}\right)^{-1} = 1 + \sum_{n=1}^{\infty} e^{-2\sqrt{\frac{p}{\alpha}}\delta n} \qquad (H-9)$$

and carrying out the algebraic manipulations, yields

$$\bar{T} = \frac{\phi\sqrt{\alpha}}{p^{3/2}k}\left[\sum_{n=1}^{\infty} e^{-\sqrt{\frac{p}{\alpha}}(2\delta n - x_s)} + \sum_{n=1}^{\infty} e^{-\sqrt{\frac{p}{\alpha}}(2\delta n + x_s)} + e^{-\sqrt{\frac{p}{\alpha}}x_s}\right]$$

$$+ \frac{\phi\alpha}{p^2 k\delta} + \frac{1}{p}\left[\frac{\phi x_s}{k} - \frac{\phi x_s^2}{2k\delta}\right] + \frac{T_w}{p} \qquad (H-10)$$

where the heat flux, $\phi = \dot{q}\delta$

Inversion of equation (H-10), taking the corresponding functions from reference [90] , yields after some algebraic simplifications:

$$\Delta T_w^+ = \tau_i + \varepsilon - \frac{1}{2}\varepsilon^2 + \frac{2}{\sqrt{\pi}}\sqrt{\tau_i}\left\{\sum_{n=1}^{\infty}\left[e^{\left(-\frac{n^2}{\tau_i} + \frac{\varepsilon n}{\tau_i} - \frac{\varepsilon^2}{4\tau_i}\right)} - \sqrt{\pi}\left(\frac{n}{\sqrt{\tau_i}} - \frac{\varepsilon}{2\sqrt{\tau_i}}\right)\operatorname{erfc}\left(\frac{n}{\sqrt{\tau_i}} - \frac{\varepsilon}{2\sqrt{\tau_i}}\right)\right.\right.$$

$$+ e^{\left(-\frac{n^2}{\tau_i} - \frac{\varepsilon n}{\tau_i} - \frac{\varepsilon^2}{4\tau_i}\right)} - \sqrt{\pi}\left(\frac{n}{\sqrt{\tau_i}} + \frac{\varepsilon}{2\sqrt{\tau_i}}\right)\operatorname{erfc}\left(\frac{n}{\sqrt{\tau_i}} + \frac{\varepsilon}{2\sqrt{\tau_i}}\right)\Bigg]$$

$$\left. + e^{\left(-\frac{\varepsilon^2}{4\tau_i}\right)} - \sqrt{\pi}\left(\frac{\varepsilon}{\sqrt{\tau_i}}\right)\operatorname{erfc}\left(\frac{\varepsilon}{2\sqrt{\tau_i}}\right)\right\} \qquad (H-11)$$

where ΔT_w^+, τ_i and ε are non-dimensional parameters defined as

$$\Delta T_w^+ = \frac{(T - \bar{T}_w)\,k_s}{\phi\delta} \qquad (H-12)$$

$$\tau_i = \frac{\alpha_s t_i}{\delta^2} \qquad (H-13)$$

and

$$\varepsilon = \frac{X_s}{\delta} \qquad (H-14)$$

$(T-\bar{T}_w)$ represents the temperature rise during the insulation time t_i; δ is the wall thickness, α_s and k_s are the thermal diffusivity and thermal conductivity of the solid respectively, and n is a positive integer.

A computer programme was written to obtain the numerical values for ΔT_w^+. n was normally varied from n=1 to n=30, since both the exponential functions and the complementary error function, erfc, involved in the summation converged rapidly at low values of n. The numerical values for the complementary error function were obtained by linear interpolation within the programme from values tabulated in Appendix II of reference [90]. The results for ΔT_w^+ at $0.2 \leq \tau_i \leq 2.0$ are shown in Figure 88.

The particular solution to equation (H-11) at $X_s=0$, i.e. at the surface, is readily obtained as

$$\Delta T_w^+ = \tau_i + \frac{2}{\sqrt{\pi}}\sqrt{\tau_i}\left\{1 + 2\sum_{n=1}^{\infty}\left[e^{\left(-\frac{n^2}{\tau_i}\right)} - \sqrt{\pi}\left(\frac{n}{\sqrt{\tau_i}}\right)\operatorname{erfc}\left(\frac{n}{\sqrt{\tau_i}}\right)\right]\right\} \qquad (H-15)$$

and it is graphically shown in Figure 89.